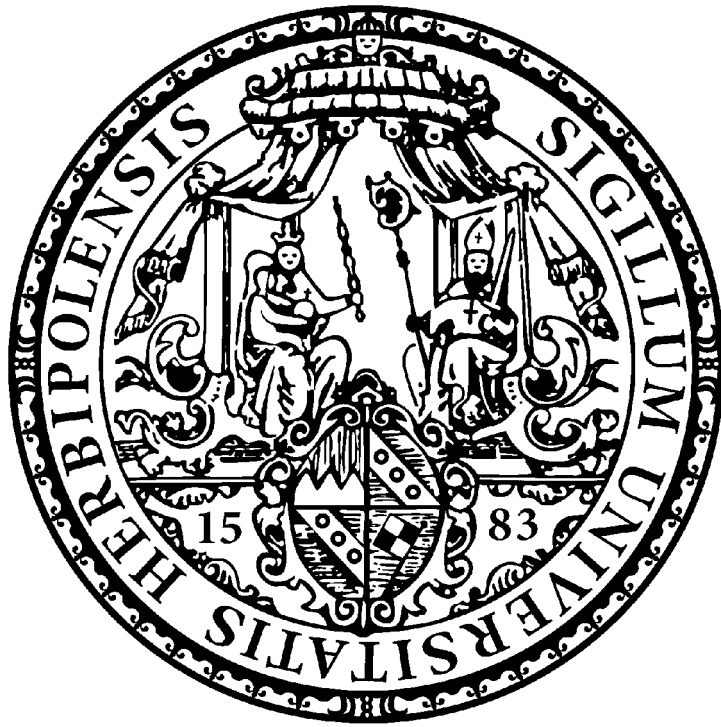


Information-Theoretical Studies on Time-Dependent Quantum Systems



Dissertation

zur Erlangung des naturwissenschaftlichen Doktorgrades
der Julius-Maximilians-Universität Würzburg

vorgelegt von

Peter Schürger

aus Prichsenstadt

Würzburg, 2024

Information-Theoretical Studies on Time-Dependent Quantum Systems

Dissertation

zur Erlangung des naturwissenschaftlichen Doktorgrades
der Julius-Maximilians-Universität Würzburg

vorgelegt von

Peter Schürger

aus Prichsenstadt

Würzburg, 2024

Eingereicht bei der Fakultät für Chemie und Pharmazie am

01. Februar 2024

Gutachter der schriftlichen Arbeit

1. Gutachter: Prof. Dr. Volker Engel

2. Gutachter: Prof. Dr. Bernd Engels

Prüfer des öffentlichen Promotionskolloquiums

1. Prüfer: Prof. Dr. Volker Engel

2. Prüfer: Prof. Dr. Bernd Engels

3. Prüfer: Prof. Dr. Holger Helten

4. Prüfer: Prof. Dr. Christoph Lambert

5. Prüfer: Prof. Dr. Roland Mitric

Datum des öffentlichen Promotionskolloquiums

15. März 2024

Doktorurkunde ausgehändigt am

The present work was conducted at the Faculty of Chemistry and Pharmacy of the Julius-Maximilians University, Würzburg under the supervision of Prof. Dr. Volker Engel.

This semi-cumulative thesis contains reprinted peer-reviewed scientific publications. Please note that the indexation of the references in these are not identical to the indexation of the references from the additional chapters in this thesis.

List of Publications

- [1] Schürger, P., Schaupp, T., Kaiser, D., Engels, B., Engel, V.: Wave packet dynamics in an harmonic potential disturbed by disorder: Entropy, uncertainty, and vibrational revivals. *The Journal of Chemical Physics*. 156, 054303 (2022).
- [2] *Schürger, P., Renziehausen, K., Schaupp, T., Barth, I., Engel, V.: Time-Dependent Expectation Values from Integral Equations for Quantum Flux and Probability Densities. *The Journal of Physical Chemistry A*. 126, 8964–8975 (2022).
- [3] Schürger, P., Engel, V.: Information Theoretical Approach to Coupled Electron-Nuclear Wave Packet Dynamics: Time-Dependent Differential Shannon Entropies. *The Journal of Physical Chemistry Letters*. 14, 334–339 (2023).
- [4] Schürger, P., Engel, V.: Differential Shannon Entropies Characterizing Electron-Nuclear Dynamics and Correlation: Momentum-Space Versus Coordinate-Space Wave Packet Motion. *Entropy*. 25, 970 (2023).
- [5] Schürger, P., Engel, V.: Differential Shannon entropies and correlation measures for Born–Oppenheimer electron–nuclear dynamics: numerical results and their analytical interpretation. *Phys. Chem. Chem. Phys.* 25, 28373–28381 (2023).
- [6] Schürger, P., Engel, V.: On the relation between nodal structures in quantum wave functions and particle correlation. *AIP Advances*. 13, 125307 (2023).
- [7] *Schürger, P., Engel, V.: Differential Shannon entropies and mutual information in a curve crossing system: Adiabatic and diabatic decompositions (to be published). *J. Chem. Theory Comput.* (2024).
- [8] *Endres, L., Klopff J., Schürger, P., Braunschweig, H., Helten, H., Finze, M., Fantuzzi, F., Engels, B.: Benchmark of geometrical, NMR, and ESR parameters for boron-containing compounds (to be published). (2024).

* *These papers are not contained in this thesis.*

Contents

Contents	I
List of Abbreviations	III
List of Figures	IV
List of Tables	V
1 Introduction	1
2 Quantum Mechanical Concepts	6
2.1 Fundamentals of quantum dynamics	6
2.2 The Born-Oppenheimer approximation	9
2.3 Adiabatic expansion	11
2.4 Wigner representation	12
3 Information-Theoretical Concepts	14
3.1 Mean values and variances	14
3.2 Definition of the differential Shannon entropy	14
3.3 Properties of the differential Shannon entropy	15
3.4 Unit convention for differential Shannon entropy	17
3.5 BBM inequality	18
3.6 Mutual information	19
3.7 Covariance and linear correlation coefficient	20
3.8 Entropies from decomposed densities	23
3.9 Entropy of Gaussians	25
4 Numerical Methods	28
4.1 Grid	28
4.2 Split-operator method	29
4.3 Relaxation method	30
4.4 Velocity-Verlet algorithm	32
5 Entropy in a Disordered Harmonic Oscillator	34
5.1 Entropy of the undisturbed harmonic oscillator	35
5.1.1 Coherent and squeezed states	36
5.1.2 Entropy of harmonic eigenstates	40

5.1.3	Entropy of the classical HO in a microcanonical ensemble	44
5.1.4	Discussion and classical limit	46
5.2	Harmonic oscillator with disorder	47
5.2.1	Model and methods	47
5.2.2	Short-time behavior	52
5.2.3	Long-time behavior	55
5.3	Energy dependence of entropy for long times	61
5.3.1	Dephased densities	62
5.3.2	Numerical simulation and high energy limit	67
5.4	Conclusion	71
6	Information-Theoretical Approach to Coupled Electron-Nuclear Dynamics	73
6.1	Model and setup	74
6.2	Overview over the information-theoretical approach to coupled electron-nuclear dynamics	77
6.3	Reprinted publications	86
6.3.1	Information Theoretical Approach to Coupled Electron- Nuclear Wave Packet Dynamics: Time-Dependent Differential Shannon Entropies [3]	87
6.3.2	Differential Shannon entropies and correlation measures for Born–Oppenheimer electron– nuclear dynamics: numerical results and their analytical interpretation [5]	93
6.3.3	Differential Shannon Entropies Characterizing Electron– Nuclear Dynamics and Correlation: Momentum- Space Versus Coordinate-Space Wave Packet Motion [4]	102
6.3.4	On the relation between nodal structures in quantum wave functions and particle correlation [6]	125
7	Summary	136
8	Zusammenfassung	138
9	References	140
10	Listing of Author Contributions	146
11	Acknowledgements	150

List of Abbreviations

BBM	B ialynicki- B irula M ycielski
BEC	B ose- E instein C ondensate
BO	B orn- O ppenheimer
DFT	D ensity F unctional T heory
DSE	D ifferential S hannon E ntropy
HO	H armonic O scillator
HUP	H eisenberg U ncertainty P inciple
KL	K ullback- L eibler
MD	M olecular D ynamics
MI	M utual I nformation

List of Figures

1.1	Example for an efficient communication.	3
3.1	Mutual information in the Ven-diagram representation.	20
5.1	Position, momentum and entropy sum as well as widths and uncertainty product of a Gaussian in an harmonic oscillator.	39
5.2	Difference of $S_{sum,n}^{EF}$ (eq. (5.29)) and $S_{sum,n}^{EF,asympt}$ (eq. (5.35)) as well as the logarithmic regression (eq. (5.37) and eq. (5.38)).	43
5.3	Entropy sum of the eigenstates of the harmonic oscillator plotted vs the energy, together with various approximations described in the text.	47
5.4	Different realizations of the disorder potential.	48
5.5	Upper panel: Energy eigenvalues derived from potentials (a), (b) and (c), respectively. Lower panel: Spacing between the energy eigenvalues as deviations from to the harmonic spacing.	50
5.6	Decomposition of the initial wave function in energy eigenstates: Shown is the occupation of different states.	52
5.7	Quantum mechanical and classical position density for early times 0-10 T	53
5.8	Quantum mechanical and classical entropies and uncertainty product for times 0-20 T	54
5.9	Quantum mechanical and classical entropies and uncertainties for $t = 100 T - 130 T$	56
5.10	Quantum and classical density for different times. In the bottom panel the initial density is compared to the density at the approximate revival time $t = 118 T$	57
5.11	Quantum (top) and classical density (bottom) for $t = 100 T - 130 T$	58
5.12	Top panel: Entropy sum in potential (b). Bottom panel: Entropy sum plotted against the modulo of time.	61
5.13	Classical dephasing in phase-space. Left: Initial density, sampled from the quantum coherent state. Right: Dephased density.	64
5.14	Averaged entropy sum for late times $t \gg T_{th}$ obtained by classical and quantum dynamics.	69
5.15	Distribution of coefficients $ c_n ^2$ for different excitations x_0	70
6.1	The Shin-Metiu model: A mobile electron and a mobile nucleus interact with two fixed nuclei.	75
6.2	Schematic comparison: The soft Coulomb potential is approximately harmonic for small values of x	80

List of Tables

5.1	Scaling constants of the harmonic oscillator.	36
5.2	Entropies derived from harmonic oscillator eigenfunctions. Numerically exact values are compared to different approximations.	42
5.3	Parameters of the three different disorder potential parametrizations.	48
5.4	Parameters of the numerical simulation.	50
5.5	Energy eigenvalues and expansion coefficients of the states with the largest expansion coefficients c_n in potential (b).	60
6.1	Overview of the definitions of the investigated quantities.	84
6.2	Overview of the analytic results derived within the Born-Oppenheimer adiabatic ansatz.	85
6.3	Overview of the analytic results derived from the diabatic ansatz.	85
6.4	Copyright statements of the respective papers.	86

1 Introduction

In 1926, Erwin Schrödinger formulated the time-dependent Schrödinger equation [9]

$$i\hbar\frac{\partial\Psi(x,t)}{\partial t} = \hat{H}\Psi(x,t), \quad (1.1)$$

describing the dynamics of a particle with a wave function $\Psi(x,t)$ determined by the Hamilton operator \hat{H} . Hereby, the quantum particle has no defined location, but is found at position x with probability $\rho(x)dx$, where $\rho(x) = |\Psi(x,t)|^2$. Since eq. (1.1) is solvable exactly only for a few systems [10], theoretical efforts for analytical approximations and numerical algorithms to solve eq. (1.1) are asked for. A non-standard ansatz is to study the density distribution obtained from $\Psi(x,t)$ using entropy, and this is the main topic of the present thesis.

The concept of entropy is very important in physics and chemistry. However, there is more than one definition of entropy. In classical thermodynamics, for example, the entropy of a microcanonical ensemble is defined as [11]

$$S = k_B \ln \Omega_{\text{mic}}, \quad (1.2)$$

where k_B is the Boltzmann constant and Ω_{mic} the microcanonical partition function. This entropy is used to define the temperature of the system and thermodynamic equilibrium. This entropy is essential to define the second law of thermodynamics: In isolated systems entropy can only grow or remain the same, but it can not decrease. [11]

In quantum thermodynamics, the von-Neumann entropy is used to calculate the entropy of a system. It is defined as

$$S = -k_B \text{Tr}(\hat{\rho} \ln \hat{\rho}), \quad (1.3)$$

where $\hat{\rho}$ is the density operator of the quantum state. This entropy is basis independent due to the trace-operation. If the quantum state is in an eigenstate of $\hat{\rho}$, which is a pure state, the von-Neumann entropy vanishes [12]. Following [13], the entropy production is

$$\frac{dS(t)}{dt} = -k_B \text{Tr}(\dot{\hat{\rho}} \ln \hat{\rho} + \dot{\hat{\rho}}), \quad (1.4)$$

where the second term on the right hand side is zero since $\text{Tr}\hat{\rho}=1$. If the considered system is an isolated quantum system, the time evolution is unitary and the entropy production

vanishes,

$$\frac{dS(t)}{dt} = \frac{ik_B}{\hbar} \text{Tr}([\hat{H}, \hat{\rho}] \ln \hat{\rho}) = \frac{ik_B}{\hbar} \sum_{i,j} \langle i | [\hat{H}, \hat{\rho}] | j \rangle \langle j | \ln \hat{\rho} | i \rangle = 0, \quad (1.5)$$

where the von-Neumann equation was used. The last step is trivial by taking $|i\rangle$ and $|j\rangle$ as eigenstates of $\hat{\rho}$. Thus, the von-Neumann entropy is constant. However, pure states as well as isolated systems can show very interesting dynamics. For example, the eigenstate thermalization hypothesis was stated, which implies that isolated systems can show some form of thermalization [14].

A different approach to entropy, which, among other things, allows to analyze the dynamics of isolated systems and pure states, is to use an information-theoretical ansatz.

Information theory was pioneered by Claude Shannon in a seminal paper [15] in 1948. There, Shannon examined the information content of messages and random variable distributions using entropy,

$$S = -\kappa \sum_{i=1}^N p_i \ln[p_i], \quad (1.6)$$

where $\kappa > 0$ is some constant and p_i are the probabilities p_i , $i = 1, \dots, N$. To illustrate this, consider an experiment that has $N = 8$ possible events with the probabilities $p_1 > p_2 > p_3 > \dots > p_N$. If one wants to communicate the outcome of an experiment most efficiently, one should use the shortest possible signal to communicate that the most probable result occurred, the second shortest for the second most probable, and so on (e.g., in binary: 1,10,110,1110,11110,111110,111111, see also fig. 1.1). In other words: Less information is required to communicate that a highly probable event occurs, than a seldom one. It is possible to show that the optimal length of the signal is proportional to the logarithm of the corresponding probability, $l_i = -\kappa \ln p_i$ [16]. Then, eq. (1.6) is the average length of the message necessary to identify the result, $S = p_1 l_1 + p_2 l_2 + \dots + p_N l_N$. Consequently, if the entropy is small, more short messages are transmitted on average and thus the probability set is dominated by high likely outcomes. Hence, the outcomes are to some degree predictable. Conversely, if the entropy is large, the incoming messages are of similar length and the probability is spread over the outcomes. Here, less accurate predictions of the result can be made. The latter would constitute an extremal case in which all probabilities are identical $p_1 = p_2 = p_3 = \dots = p_N = \frac{1}{N}$. Then, the messages are of equal length and the entropy is $S \sim \ln N$. Hence, the entropy reveals information about the respective probability set: It can be used as a measure of uncertainty of a discrete

probability distribution.

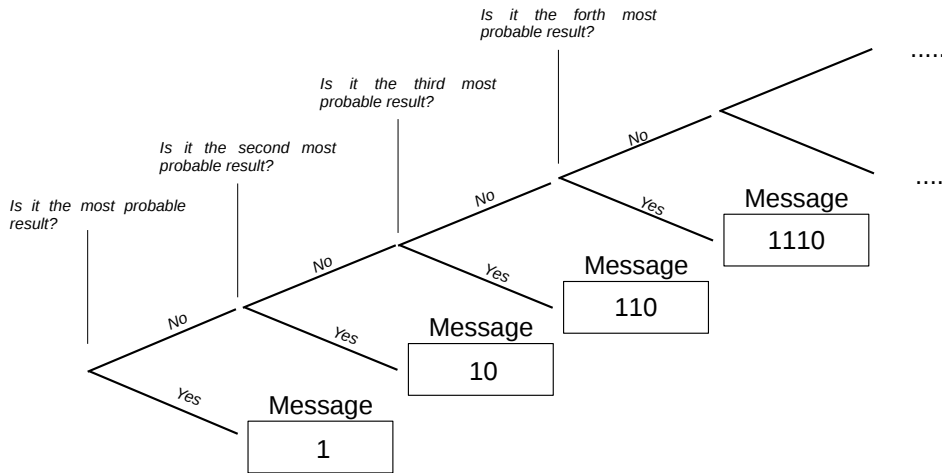


Figure 1.1: Example for an efficient communication of the result of an experiment with probabilities that can be ordered as $p_1 > p_2 > p_3 > p_4 > \dots$.

The definition in eq. (1.6) can be extended to continuous probability distributions $\rho(x)$ [15]

$$S = -\kappa \int dx \rho(x) \ln[\rho(x)], \quad (1.7)$$

which is called the *differential Shannon entropy* (DSE), a more rigorous definition is given later in this thesis, see sec. 3.2. As its discrete version, the differential Shannon entropy is used as a measure for uncertainty: It assumes low values for distributions with a high degree of predictability and high values for distributions with high uncertainty. If the continuous probability distribution is a position density, predictability and uncertainty relates to the (de-)localization of the density and is thus an interesting property to study. However, the differential Shannon entropy loses various properties in comparison to the discrete one. For example, while the discrete entropy eq. (1.6) is positive semidefinite, the differential Shannon entropy can take any value between $-\infty$ and ∞ . Therefore, the DSE is not absolute, but a relative measure. Using these entropies, Shannon defined another important quantity in [15]: the mutual information (MI). This is a measure that can be computed from the entropies and quantifies the correlation between two random variables.

The information-theoretical measures presented above are used in a variety of research areas. For example, they are applied in cryptography [17] and economics [18]. However, there are also numerous applications in physics and quantum chemistry. Here,

the information-theoretic approach is used to grasp properties that cannot, or are only poorly, described with conventional methods. It is important to stress that information-theoretical quantities like differential Shannon entropy and mutual information are not observables, it is not possible to measure them. Instead, they can be used to process measured or simulated data, e.g., to quantify correlation, localization or dispersion, and link its strength to the occurring effects. For example, due to its relation to localization, differential Shannon entropy has been used to study chemical properties such as reactivity [19–21] and aromaticity [22], see also ref. [23] for a review. Information-theoretical measures have been discussed in the context of chemical dynamics, e.g. in [24–26]. Differential Shannon entropies were applied to study stationary states in various potentials [27–30], to predict avoided crossings [31–33] and to analyze correlation effects [34–40]. Isolated quantum systems were studied within the information-theoretical framework in [13, 41]. Differential Shannon entropies are also used in the context of MD simulations (MD, molecular dynamics). This is extensively discussed in ref. [42].

In this thesis, we apply the information-theoretic approach in the context of quantum dynamics and wave packet motion: Information-theoretic measures are calculated from position and momentum densities, which are obtained from time-dependent quantum wave functions. The aim of this thesis is to benchmark, analyze and interpret these quantities and relate their features to the wave packet dynamics. Firstly, this is done for the harmonic oscillator (HO) with and without static disorder. In the unperturbed HO, the analytical study of coherent and squeezed states reveals time-dependent entropy expressions related to the localization of the wave function. In the disordered HO, entropies from classical and quantum dynamics are compared for short and long times. In the quantum case, imprints of wave packet revivals are found in the entropy. Then, the energy dependence of the entropy for very long times is discussed. Secondly, this is done for correlated electron-nuclear motion. Here, entropies derived from the total, electronic and nuclear density, respectively, are calculated in position and momentum space for weak and strong adiabatic electronic coupling. The correlation between electron and nucleus is investigated using different correlation measures, where some of these functions are sensitive to the nodal structure of the wave function. An analytic ansatz to interpret the information-theoretical quantities is applied as well.

This thesis is structured as follows. Initially, fundamental quantum dynamical concepts are presented in sec. 2. The differential Shannon entropy and other information-theoretical concepts are defined in sec. 3. The employed numerical methods are explained in sec. 4. The discussion of entropy in an harmonic oscillator with and without disorder

is found in sec. 5. An information-theoretical approach to coupled electron-nuclear dynamics is given in sec. 6. Finally, the summary is given in English and German in sec. 7 and sec. 8, respectively.

2 Quantum Mechanical Concepts

In the first half of the 20-th century, the works of many scientists like Max Planck, Albert Einstein, Werner Heisenberg and Erwin Schrödinger led to the development of quantum mechanics. In particular, equations were found, that govern the dynamics of electrons and nuclei. In the following section, this and other basic concepts of quantum mechanics are presented.

2.1 Fundamentals of quantum dynamics

The heart of quantum dynamics is the time-dependent Schrödinger equation [9],

$$i\hbar \frac{\partial}{\partial t} |\Psi(t)\rangle = \hat{H} |\Psi(t)\rangle. \quad (2.1)$$

It describes the time evolution of a quantum state $|\Psi(t)\rangle$ in a system defined by the Hamilton operator \hat{H} . The Hamilton operator itself is the sum of the kinetic energy operator \hat{T} and the potential energy operator \hat{V} , $\hat{H} = \hat{T} + \hat{V}$. The quantum state $|\Psi(t)\rangle$ is a complex vector in Hilbert space and is normalized by the scalar product with itself

$$\langle \Psi(t) | \Psi(t) \rangle = 1. \quad (2.2)$$

To solve the time-dependent Schrödinger equation, we introduce the time evolution operator \hat{U} , which acts on the quantum state as $|\Psi(t)\rangle = \hat{U}(t, t_0) |\Psi(t_0)\rangle$. The time-dependent Schrödinger equation is then

$$i\hbar \frac{\partial}{\partial t} \hat{U}(t, t_0) |\Psi(t_0)\rangle = \hat{H} \hat{U}(t, t_0) |\Psi(t_0)\rangle. \quad (2.3)$$

The time derivative is acting on the operator $\hat{U}(t, t_0)$ while the state is time-independent, so that formally

$$i\hbar \frac{\partial}{\partial t} \hat{U}(t, t_0) = \hat{H} \hat{U}(t, t_0). \quad (2.4)$$

Symbolically, we can write this as

$$\frac{1}{\hat{U}(t, t_0)} \frac{\partial}{\partial t} \hat{U}(t, t_0) = -\frac{i}{\hbar} \hat{H}. \quad (2.5)$$

Integrating this over time yields a logarithm due to the fraction on the left hand side and an factor of $t - t_0$ for time-independent Hamiltonians, as we assume here:

$$\ln \hat{U}(t, t_0) = \frac{-i}{\hbar} \int dt \hat{H} \rightarrow \ln \hat{U}(t, t_0) = \frac{-i}{\hbar} \hat{H}(t - t_0). \quad (2.6)$$

Thus, the time evolution operator for time-independent Hamiltonians is given as

$$\hat{U}(t, t_0) = \hat{U}(t - t_0) = e^{-\frac{i}{\hbar} \hat{H}(t-t_0)}. \quad (2.7)$$

A complete orthonormal basis set $|a\rangle$ has the properties of

$$\text{a) completeness } \sum_a |a\rangle \langle a| = 1, \quad \text{and b) orthonormality } \langle a|a'\rangle = \delta_{a,a'}, \quad (2.8)$$

where $\delta_{a,a'} = 1$ for $a = a'$ and $\delta_{a,a'} = 0$ for $a \neq a'$ is the Kronecker Delta. To express the quantum state $|\Psi(t)\rangle$ in such a basis, the state is projected onto the respective basis set $|a\rangle$:

$$|\Psi(t)\rangle = \sum_a |a\rangle \langle a|\Psi(t)\rangle = \sum_a |a\rangle \Psi_a(t), \quad (2.9)$$

where $\Psi_a(t) = \langle a|\Psi(t)\rangle$ is a vector component in the basis $|a\rangle$. The population of state $|a\rangle$ is then given as the absolute square of the vector components

$$p_a = |\langle a|\Psi(t)\rangle|^2 = |\Psi_a(t)|^2. \quad (2.10)$$

The Hamilton operator is a unitary operator acting on the quantum states. Unitary means in particular that the operator has eigenvectors, that are a complete orthonormal basis set for the respective Hilbert space, and that its eigenvalues are real. The eigenvalue equation of the Hamiltonian is known as the time-independent Schrödinger equation:

$$\hat{H} |n\rangle = E_n |n\rangle, \quad (2.11)$$

where $|n\rangle$ are the energy eigenstates and E_n the eigenenergies of the system. The expansion in eigenstates $|n\rangle$ of the Hamilton operator is

$$|\Psi(t)\rangle = \sum_n |n\rangle \langle n|\Psi(t)\rangle = \sum_n |n\rangle c_n(t), \quad (2.12)$$

where $c_n(t) = \langle n | \Psi(t) \rangle$, and the population of the eigenstate $|n\rangle$ is $p_n = |c_n(t)|^2$. Combining this result with the time evolution operator yields

$$|\Psi(t)\rangle = \sum_n |n\rangle \langle n | U(t, t_0) | \Psi(t_0) \rangle = \sum_n c_n(t_0) e^{-\frac{i}{\hbar} E_n(t-t_0)} |n\rangle. \quad (2.13)$$

Thus, time evolution of time-independent Hamiltonians just adds a phase to the respective energy eigenfunction.

For continuous basis sets as in position and momentum space, the definitions completeness and orthonormality are extended by introducing integrals instead of sums and the delta-distribution instead of the Kronecker delta:

$$\int dx |x\rangle \langle x| = 1, \quad \text{and} \quad \langle x | x' \rangle = \delta(x - x'), \quad (2.14)$$

$$\int dp |p\rangle \langle p| = 1, \quad \text{and} \quad \langle p | p' \rangle = \delta(p - p'). \quad (2.15)$$

The basis expansion in position and momentum space, respectively, yields

$$|\Psi(t)\rangle = \int dx |x\rangle \langle x | \Psi(t) \rangle = \int dx |x\rangle \Psi(x, t), \quad (2.16)$$

$$|\Psi(t)\rangle = \int dp |p\rangle \langle p | \Psi(t) \rangle = \int dp |p\rangle \Psi(p, t). \quad (2.17)$$

The vector components $\Psi(x, t)$ and $\Psi(p, t)$ are referred to as the wave functions of state $|\Psi(t)\rangle$ in position or momentum space, respectively. To switch between momentum- and position-space basis, we use that both are complete orthonormal basis sets of the same Hilbert space:

$$|\Psi(t)\rangle = \int dx |x\rangle \langle x | \int dp |p\rangle \langle p | \Psi(t) \rangle = \int dx |x\rangle \Psi(x, t), \quad (2.18)$$

where $\langle x | p \rangle$ is an eigenvector of the momentum operator represented in position space. The basis set $|p\rangle$ is given as the result of the eigenvalue equation for the momentum operator \hat{P} with eigenvalues p and eigenvectors $|p\rangle$:

$$\hat{P} |p\rangle = p |p\rangle. \quad (2.19)$$

In position-space basis, $\hat{P} = -i\hbar\nabla$ and the equation is

$$\langle x | \hat{P} |p\rangle = \hat{P} \langle x | p \rangle = -i\hbar\nabla \langle x | p \rangle = p \langle x | p \rangle. \quad (2.20)$$

In one dimension, $\langle x|p\rangle = \frac{1}{\sqrt{2\pi\hbar}}e^{ipx/\hbar}$, thus the state vector is

$$|\Psi(t)\rangle = \int dx |x\rangle \int dp \frac{e^{ipx/\hbar}}{\sqrt{2\pi\hbar}} \Psi(p, t) = \int dx |x\rangle \Psi(x, t). \quad (2.21)$$

From this we see that $\Psi(p, t)$ is the Fourier transform of $\Psi(x, t)$:

$$\int dp \frac{e^{ipx/\hbar}}{\sqrt{2\pi\hbar}} \Psi(p, t) = \Psi(x, t). \quad (2.22)$$

The same arguments hold for the position-space component in momentum space:

$$\int dx \frac{e^{-ipx/\hbar}}{\sqrt{2\pi\hbar}} \Psi(x, t) = \Psi(p, t). \quad (2.23)$$

The Fourier relationship between position- and momentum-space wave function is therefore intrinsic to quantum mechanics. From calculating the position-space wave function one receives the position-space probability density

$$|\langle x|\Psi(t)\rangle|^2 = \rho(x, t), \quad (2.24)$$

as well as the momentum-space probability density

$$|\langle p|\Psi(t)\rangle|^2 = \left| \int dx \langle p|x\rangle \langle x|\Psi(t)\rangle \right|^2 = \rho(p, t). \quad (2.25)$$

The probability p_x to find the quantum state in the spatial interval $[x, x + dx]$ is $p_x = \rho(x, t)dx$. Analogously, the probability that the quantum state has momentum $[p, p + dp]$ is $p_p = \rho(p, t)dp$. Due to the normalization condition, the probability densities are normalized to one, i.e. $\int dx \rho(x, t) = \int dp \rho(p, t) = 1$. In contrast to probabilities, probability densities are in general not dimensionless but carry the inverse unit of its associated observable.

2.2 The Born-Oppenheimer approximation

The Born-Oppenheimer approximation is of great importance in quantum chemistry. It simplifies the dynamics of coupled electron-nuclei systems by solving the problem in two steps. First, adiabatic movement of the electron in the background field of the nuclei is assumed, i.e. the electron is in an eigenstate which is parametric in the nuclear positions. Secondly, the eigenenergy of this eigenfunction is an effective potential for the nucleus. Historically, these approximations were justified by Born and Oppenheimer by an expan-

sion of the Hamiltonian in terms of $\sqrt{m/M}$, where m is the electron mass and M is the averaged mass of the nuclei [43]. Born and Oppenheimer show, that the electronic eigenenergy takes the role of a potential for the nuclei up to second order in $\sqrt{m/M}$, while coupling effects occur in fourth order. Since the electron mass is very small compared to nuclei masses, the mass ratio is very small as well and the expansion is assumed to hold in a large variety of cases.

Intuitively, the approximation are reasonable from a classical point of view: Due to the large mass difference of the electron and the nuclei, the inertia and thus the associated timescales of both kinds of motion are very different. While the electron may see the nuclei as static during its timescale, the nuclei sees the electron moving fast and is thus effectively reacting to the averaged position of the electron. This consideration is close to the approach which is presented in modern quantum chemistry books [12, 44, 45]. Starting with the complete Hamiltonian of a not specified molecular system, the Hamiltonian is

$$\hat{H}\Psi(r, R) = (\hat{T}_e + \hat{T}_{nuc} + \hat{V}_e(r) + \hat{V}_{nuc}(R) + \hat{V}_{int}(r, R))\Psi(r, R), \quad (2.26)$$

where r and R are vectors of electronic and nuclear coordinates, respectively, and \hat{T} and \hat{V} label electronic and nuclear momentum and potential energy operators. Furthermore, $\hat{V}_{int}(r, R)$ describes the interaction of electrons and nuclei. The electronic Schrödinger equation is defined as

$$\hat{H}_e\varphi(r; R) = (\hat{T}_e + \hat{V}_e(r) + \hat{V}_{nuc}(R) + \hat{V}_{int}(r; R))\varphi(r; R), \quad (2.27)$$

where $\varphi(r; R)$ is the electronic wave function, which depends parametrically on the nuclear coordinates R . Comparing this to the full Schrödinger equation (2.26), we see that the kinetic energy of the nuclei is neglected in this step, which is approximated to be constant from the point of view of the electron. The electronic wave function is in an eigenstate of eq. (2.27), $\varphi_n(r; R)$, with energy $V_n(R)$. This enters in to the nuclear Schrödinger equation, which reads

$$\hat{H}_{nuc}\Phi(R) = [\hat{T}_{nuc} + V_n(R)]\Phi(R). \quad (2.28)$$

The nuclear Hamiltonian only depends on R and is solved by the wave function $\Phi(R)$, $\hat{H}_{nuc}\Phi(R) = E_n\Phi(R)$. Thus, $V_n(R)$ acts as a potential for the nuclear wave function. The full wave function is the product of the nuclear and the electron wave function

$$\Psi(r, R) = \Phi(R)\varphi_n(r; R). \quad (2.29)$$

As we can see, in the Born-Oppenheimer approximation the wave function factorizes into an electronic and a nuclear part. By plugging this into the complete Schrödinger equation (2.26), we see which contributions are neglected in detail. While the electronic operators act exclusively on the electronic wave function and allow a separation of electronic and nuclear equations, the nuclear kinetic operator acts on the nuclear as well as the electronic wave function and generates terms, which were not considered. Explicitly, they are the last two terms of

$$\begin{aligned} \hat{T}_{nuc}\Phi(R)\varphi_n(r; R) &= \sum_i^N \frac{-\hbar^2}{2M_i} (\varphi_n(r; R)\nabla^2\Phi(R) \\ &\quad + 2\nabla\varphi_n(r; R)\nabla\Phi(R) + \Phi(R)\nabla^2\varphi_n(r; R)), \end{aligned} \quad (2.30)$$

where we consider a system with N nuclei and ∇ summarizes the derivatives for the nuclei coordinates R . The first occurring term is the kinetic energy of the nuclei, while the last two terms are neglected. In particular, $\nabla\varphi_n(r; R)$ and $\nabla^2\varphi_n(r; R)$ are in general considered to be small, since it is expected that the eigenfunctions of the electronic Hamiltonian change only slowly under change of R .

An example, where the Born-Oppenheimer approximation breaks down, is an *avoided crossing*: For a single coordinate R , different eigenvalues $V_n(R)$ of electronic eigenfunctions with the same symmetry cannot cross [12], but they can come arbitrarily close to each other. At these points, terms in eq. (2.30) become large so that they cannot be neglected anymore and the approximation breaks down.

2.3 Adiabatic expansion

The electronic eigenfunctions $\varphi_n(r; R)$ obtained from solving the electronic Schrödinger equation (2.27) form a complete orthonormal basis at each nuclear configuration R , thus it is possible to expand a molecular wave function in what is referred to as the adiabatic representation [12]:

$$\Psi(r, R) = \sum_n^\infty \Phi_n(R)\varphi_n(r; R). \quad (2.31)$$

When inserting this into the Schrödinger equation, a set of coupled equations is obtained:

$$\begin{aligned} \sum_n^\infty H_{mn}(R)\Phi_n(R) &= \sum_n^\infty \{(T_N + V_n(R))\delta_{nm} + 2T_{mn}^{(1)}(R) \cdot \nabla + T_{mn}^{(2)}(R)\}\Phi_n(R) \\ &= E\Phi_m(R) \end{aligned} \quad (2.32)$$

where coupling terms occur:

$$T_{mn}^{(1)}(R) = \langle \varphi_m | \nabla \varphi_n \rangle_r \quad \text{and} \quad T_{mn}^{(2)}(R) = \langle \varphi_m | \nabla^2 \varphi_n \rangle_r. \quad (2.33)$$

The Born-Oppenheimer approximation corresponds to only taking one diagonal term into account. We can also expand the expectation values of an operator \hat{O} in the adiabatic basis:

$$\begin{aligned} \langle \Psi(r, R) | \hat{O} | \Psi(r, R) \rangle &= \sum_{nm}^{\infty} \int dr \int dR \Phi_n^*(R) \varphi_n^*(r; R) \hat{O} \Phi_m(R) \varphi_m(r; R) \\ &= \sum_{nm}^{\infty} O_{nm}, \end{aligned} \quad (2.34)$$

where O_{nm} are matrix elements in the adiabatic basis. In particular, the probability density is:

$$\begin{aligned} \rho(r, R) &= |\Psi(r, R)|^2 = \left| \sum_n^{\infty} \Phi_n(R) \varphi_n(r; R) \right|^2 \\ &= \sum_{nm}^{\infty} \rho_{nm}^a(r, R), \end{aligned} \quad (2.35)$$

with matrix elements

$$\rho_{nm}^a(r, R) = \Phi_n^*(R) \varphi_n^*(r; R) \Phi_m(R) \varphi_m(r; R). \quad (2.36)$$

Using eq. (2.36), one can define adiabatic decompositions of the nuclear and electron density as well:

$$\rho_{nm}^{nuc}(R) = \int dr \rho_{nm}^a(r, R) \quad \text{and} \quad \rho_{nm}^{el}(r) = \int dR \rho_{nm}^a(r, R). \quad (2.37)$$

2.4 Wigner representation

The Wigner distribution function of a wave function $\psi(x)$ is defined as [12, 46]

$$f_W(p, q) = \frac{1}{2\pi\hbar} \int_{-\infty}^{\infty} ds e^{\frac{i}{\hbar}ps} \psi^*\left(q - \frac{s}{2}\right) \psi\left(q + \frac{s}{2}\right). \quad (2.38)$$

It was initially proposed by Wigner in 1932 to study quantum correction terms to classical dynamics [47]. The Wigner density is normalized to unity

$$\int_{-\infty}^{\infty} dpdq f_W(p, q) = 1. \quad (2.39)$$

Integrating out p or q , respectively, the momentum and position density are recovered:

$$\int_{-\infty}^{\infty} dp f_W(p, q) = |\psi(x)|^2 = \rho(x), \quad (2.40)$$

$$\int_{-\infty}^{\infty} dq f_W(p, q) = |\psi(p)|^2 = \rho(p), \quad (2.41)$$

where $\psi(p)$ is the Fourier transformation of $\psi(x)$. Due to equations (2.39),(2.40) and (2.41), the Wigner function is often compared with the classical phase space distribution. For example, this is since if the wave function is a Gaussian wave packet, the Wigner function is a Gaussian phase space distribution [12]. Also, if the potential $V(x)$ of a system only includes up to second order terms in x , the governing equation of $f_W(p, q)$ becomes the classical Liouville equation, which determines the time evolution of classical phase space distributions [46, 48]. However, for potentials including higher-order terms, the dynamics begin to differ. On top of that, the Wigner function of arbitrary wave functions is not positive semidefinite and can assume negative values, therefore the interpretation as a density distribution is difficult.

3 Information-Theoretical Concepts

In this section, information-theoretical concepts are presented that are relevant in the course of the present thesis. This includes the definition of the mean value, variance, differential Shannon entropy (DSE) and the correlation measures mutual information, covariance and linear correlation coefficient. Entropies from decomposed densities are discussed as well. Finally, the differential Shannon entropy of Gaussian densities is calculated.

3.1 Mean values and variances

The mean value $\langle x \rangle$ and the variance σ_X^2 of a continuous probability distribution $\rho(x)$ of a random variable X are [49]

$$\langle x \rangle = \int dx \rho(x) x, \quad (3.1)$$

$$\sigma_X^2 = \int dx \rho(x) (x - \langle x \rangle)^2. \quad (3.2)$$

The width Δx of $\rho(x)$ is defined as the square root of the variance,

$$\Delta x = \sqrt{\sigma_X^2} = \sigma_X. \quad (3.3)$$

3.2 Definition of the differential Shannon entropy

The differential Shannon entropy is a continuous extension of the (discrete) Shannon entropy. Both concepts were introduced by Claude Shannon in [15] as a mathematical tool to analyze probabilities. The Shannon entropy of a discrete distribution of random variables X is [16, 50]

$$S^{discrete}[X] = - \sum_i^N p_i \ln(p_i), \quad (3.4)$$

where p_i $i = 1, \dots, N$ are probabilities of the outcomes x_1, \dots, x_N of the random variable and it holds that $\sum_i^N p_i = 1$.

The differential Shannon entropy generalizes the concept as follows.

Consider a continuous probability distribution $\rho(X_1, X_2, \dots, X_d)$ of a set of d continuous random variables X_i , $i = 1, \dots, d$. The differential Shannon entropy is defined as the d -dimensional integration over the support set G of all random variables X_i [16, 50],

$$S[X_1, X_2, \dots, X_d] = - \int_G dx^d \rho(X_1, X_2, \dots, X_d) \ln(\rho(X_1, X_2, \dots, X_d)). \quad (3.5)$$

Here, square brackets denote that $S[X_1, X_2, \dots, X_d]$ is a functional of the density distribution of the listed random variables. The density distribution is normalized to unity on the support set G , $\int_G dx^d \rho(X_1, X_2, \dots, X_d) = 1$.

In the context of this thesis, ρ is interpreted as the diagonal entries of the density operator $|\rho\rangle\langle\rho|$ in an continuous orthonormal basis set $|a\rangle$,

$$\rho(a) = \langle a|\rho\rangle\langle\rho|a\rangle, \quad (3.6)$$

where $|a\rangle$ are eigenvectors of an observable \hat{A} . Therefore, the differential Shannon entropy relates to the amount of information accessible by the measurement of the operator \hat{A} . Hence, the differential Shannon entropy of a quantum state depends on the basis it is measured in. [41]

If the basis $|a\rangle$ is discrete, the discrete Shannon entropy $S = -\sum_a p_a \ln(p_a)$ is recovered and if in particular the basis are pure states of the system, the Shannon entropy is equal to the von-Neumann entropy.

3.3 Properties of the differential Shannon entropy

Extending the definition of the Shannon entropy to be able to measure continuous random variable distributions amounts to replacing the discrete probabilities p_i , $i = 1, N$ by a normalized probability density $\rho(X)$ and the summation by an integral over x . Schematically, for a one dimensional case, this means:

$$S^{discrete}[X] = - \sum_i^N p_i \ln(p_i) \rightarrow S[X] = - \int dx \rho(x) \ln(\rho(x)). \quad (3.7)$$

This heuristic substitution has severe implications for the properties of the entropy and is not as trivial as it seems. To do it more carefully, a continuous probability distribution $\rho(X)$ is approximated with N step functions of width dx , so that the probability for the result of the random variable X to be in the interval $[x_i, x_i + dx]$ is $p_i = \rho(x_i)dx$. The

Shannon entropy of this discrete distribution is

$$\begin{aligned}
 S^{discrete}[X] &= - \sum_i^N p_i \ln(p_i) = - \sum_i^N \rho(x_i) dx \ln(\rho(x_i) dx) \\
 &= - \sum_i^N dx \rho(x_i) \ln(\rho(x_i)) - \underbrace{\sum_i^N dx \rho(x_i) \ln(dx)}_{=1}. \tag{3.8}
 \end{aligned}$$

For $N \rightarrow \infty$ the discrete distribution becomes continuous and summation becomes a Riemann integral, assuming $\rho(x)$ is Riemann integrable. This yields

$$\begin{aligned}
 S[X] &= - \int dx \rho(x) \ln(\rho(x)) - \int dx \rho(x) \ln(dx) \\
 &= - \int dx \rho(x) \ln(\rho(x)) - \ln(dx), \tag{3.9}
 \end{aligned}$$

where the last term simplifies due to the normalization of $\rho(X)$. For $N \rightarrow \infty$, dx becomes infinitesimal small and thus, this expression formally diverges. Nevertheless, the left hand term is, in general, finite, and it is referred to as the differential Shannon entropy. The latter definition includes only a part of the formally correct entropy eq. (3.9) and thus its properties differ from the discrete one [16, 50].

(i) In contrast to the discrete Shannon entropy, the differential Shannon entropy is not positive semidefinite but can take values from $-\infty$ to ∞ . Consider for example the continuous uniform distribution $\rho(x) = \frac{1}{a}(1 - \Theta(x - a))$ which is $1/a$ when $x \in [0, a]$. The differential entropy is then

$$S = - \int_0^a dx \frac{1}{a} \ln\left(\frac{1}{a}\right) = \ln(a). \tag{3.10}$$

Thus, in this example, for $a > 1$ the differential entropy is positive, while it is negative for $a < 1$. The entropy becomes $-\infty$ for $a \rightarrow 0$, which can be interpreted as having complete information over the system, and the entropy becomes ∞ for $a \rightarrow \infty$, which means that we have no information over the system.

(ii) The differential entropy is invariant under coordinate shifts,

$$S[X] = - \int dx \rho(x) \ln(\rho(x)) = - \int dx \rho(x - a) \ln(\rho(x - a)). \tag{3.11}$$

(iii) The differential entropy is not scale invariant. Consider the transformation $Y = aX$. The probability densities transform as $\rho(y) = \frac{1}{|a|}\rho(x/a)$ and the entropies are

$$\begin{aligned} S[Y] &= - \int dx \frac{1}{|a|} \rho(x/a) \ln\left(\frac{1}{|a|} \rho(x/a)\right) = - \int dx \rho(x) \ln(\rho(x)) + \ln |a| \\ &= S[X] + \ln |a|. \end{aligned} \quad (3.12)$$

This can be extended to vector valued random variables \vec{X} transformed by an invertible square matrix A :

$$S[A\vec{X}] = S[\vec{X}] + \ln |\det A|. \quad (3.13)$$

(iv) As a consequence of (iii), if the random variable x has a unit [*unit*], the unit of the DSE becomes $[\ln(\textit{unit})]$. The unit convention for DSE in this thesis is given in the following section, sec. 3.4.

(v) Gaussian distributions maximize the entropy for a fixed variance. This means that in the set of distributions with variance σ the Gaussian distribution has the maximal entropy compared to the other elements.

3.4 Unit convention for differential Shannon entropy

The densities regarded in this thesis, i.e. position-, momentum- and phase-space densities, have units, and so do the considered entropies. Since, as described in the previous section, the absolute value of differential entropies depend on the unit system, we need to address this fact. As a convention, all entropy values are given in atomic units. To convert a position-space entropy from atomic units, indicated by the superscript [*a.u.*], into a different unit, the following applies:

$$\tilde{S}_x = S_x^{[a.u.]} + \ln(a_0^d) = S_x^{[a.u.]} + d \ln(a_0), \quad (3.14)$$

where \tilde{S}_x is the entropy in respect to the units in which the Bohr radius a_0 enters. Here, d is the dimension of the considered space. Analogous, the conversion for the momentum space entropy in atomic units $S_p^{[a.u.]}$ to arbitrary units is

$$\tilde{S}_p = S_p^{[a.u.]} + \ln \left[\left(\frac{E_h a_0 m_e}{\hbar} \right)^d \right] = S_p^{[a.u.]} + d \ln \left[\frac{\hbar}{a_0} \right], \quad (3.15)$$

where $E_h = 1$ is the Hartree energy and $m_e = 1$ is the electron mass. Finally, for the entropy sum the conversion is

$$\begin{aligned}\tilde{S}_{sum} &= \tilde{S}_x + \tilde{S}_p \\ &= S_x^{[a.u.]} + S_p^{[a.u.]} + \ln(a_0^d) + \ln\left[\left(\frac{\hbar}{a_0}\right)^d\right] \\ &= S_x^{[a.u.]} + S_p^{[a.u.]} + d \ln(\hbar),\end{aligned}\tag{3.16}$$

which is consistent, since it is associated with information in phase space. Note that $\hbar = 1$ in atomic units as well.

As implicitly stated in the definition of the entropies, in the calculation of all entropies the natural logarithm is applied. There are different definitions in the literature, where the logarithm of base 2 or base 10 is used. To clarify the use of the natural logarithm, sometimes the unit *nats* is used for entropy values. However, since we only use the natural one, this unit is dropped for better readability.

3.5 BBM inequality

Consider two d -dimensional variables X and P that are canonically conjugated, meaning that their distributions $\rho(x)$ and $\rho(p)$ are given by absolute squares of two functions

$$\rho(x) = |f(x)|^2 \quad \text{and} \quad \rho(p) = |g(p)|^2,\tag{3.17}$$

where both distributions $\rho(x)$ and $\rho(p)$ are normalized to unity. The functions $g(x)$ and $f(p)$ are related by a Fourier transformation

$$f(x) = \mathcal{FT}(g(p)) \quad \text{and} \quad g(p) = \mathcal{FT}^{-1}(f(x)).\tag{3.18}$$

Then, the sum of the entropies of both distribution is greater than a lower bound:

$$S[X] + S[P] \geq d \ln(\pi e).\tag{3.19}$$

This equation is based on works by Isidore Isaac Hirschman Jr. [51] and was proven by the mathematician William Beckner [52]. It was introduced in physical context by Iwo Białynicki-Birula and Jerzy Mycielski as an information-theoretical uncertainty relation for quantum mechanics [53] and is therefore referred to as the BBM inequality. This bound is stronger than the Heisenberg uncertainty principle in the sense that there is the

chain of uncertainties (simplified to $d = 1$ and $\hbar = 1$) [54, 55],

$$\sigma_X^2 \sigma_P^2 \geq \frac{1}{4\pi^2 e^2} e^{2(S[X]+S[P])} \geq \frac{1}{4}, \quad (3.20)$$

where σ_X^2 and σ_P^2 are the variances of the distributions $\rho(x)$ and $\rho(p)$, respectively. The first inequality of eq. (3.20) equation is related to the above noted property that Gaussian distributions maximize the entropy for fixed variances, while the second one follows directly from the BBM inequality.

3.6 Mutual information

Consider a system with two continuous random variables X and Y , which are distributed according to a density $\rho(x, y)$. By integrating out x or y respectively, one obtains the marginal densities $\rho(x)$ and $\rho(y)$. The mutual information (MI) is then defined as

$$I[X, Y] = S[X] + S[Y] - S[X, Y], \quad (3.21)$$

where $S[X]$ ($S[Y]$, $S[X, Y]$) is the entropy determined from $\rho(x)$ ($\rho(y)$, $\rho(x, y)$). Therefore it measures the information lost by integrating out the dependencies between X and Y . This is represented in a Ven-diagram in fig. 3.1, where the overlap is interpreted as the MI of both variables. If and only if the total density is a product of the marginal densities

$$\rho(X, Y) = \rho(X)\rho(Y), \quad (3.22)$$

the MI becomes zero, since then $S[X, Y] = S[X] + S[Y]$. Generally, when a density $\rho(x, y)$ factorizes like that, X and Y are considered to be stochastically independent.

The Kullback-Leibler divergence (KL divergence) of two densities is defined as [16]

$$D(\rho_1 || \rho_2) = \int dx \rho_1(x) \ln \left(\frac{\rho_1(x)}{\rho_2(x)} \right). \quad (3.23)$$

For this the support set of ρ_2 has to be contained in the support set of ρ_1 . The KL divergence is used as a distance measure between two probability distributions ρ_1 and ρ_2 and vanishes if both densities are identical. Note that it is not a distance in a mathematical sense, since it is not symmetric under exchange of ρ_1 and ρ_2 . The KL-divergence is unitless and invariant under scale transformations, in contrast to the differential entropy.

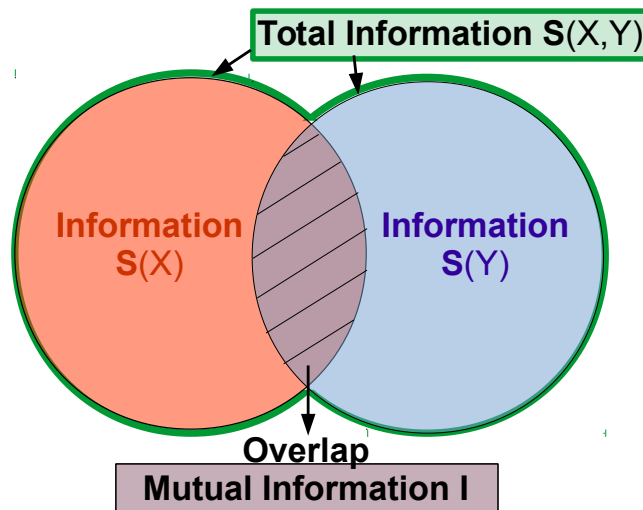


Figure 3.1: Mutual information in the Ven-diagram representation.

Using this, an equivalent form to write the MI is

$$I[X, Y] = \int dx dy \rho(x, y) \ln \left(\frac{\rho(x, y)}{\rho(x)\rho(y)} \right), \quad (3.24)$$

and therefore, it can also be interpreted as a Kullback-Leibler divergence. The MI is then the distance between the density $\rho(x, y)$ and the product of the marginal densities $\rho(x)\rho(y)$. If $\rho(x, y) = \rho(x)\rho(y)$, the distance and thus the MI is zero.

3.7 Covariance and linear correlation coefficient

The covariance of X and Y with respect to the same densities as used in sec. 3.6 is defined as [49]

$$\text{cov}(X, Y) = \langle (x - \langle x \rangle)(y - \langle y \rangle) \rangle = \int dx dy \rho(x, y)(x - \langle x \rangle)(y - \langle y \rangle), \quad (3.25)$$

and the (linear) correlation coefficient is defined as

$$\text{corr}(X, Y) = \frac{\text{cov}(X, Y)}{\sigma_X \sigma_Y} = \frac{\langle (x - \langle x \rangle)(y - \langle y \rangle) \rangle}{\sigma_X \sigma_Y}, \quad (3.26)$$

where σ_X and σ_Y are the variances of X and Y , respectively. The linear correlation coefficient takes values between -1 and 1, and a larger absolute value of the correlation coefficient is interpreted as a stronger correlation between X and Y . If $\text{corr}(X, Y) = 0$, X and Y are linearly uncorrelated, however, this does not imply $I[X, Y] = 0$, while the other direction is true. This means, the MI as well as correlation vanish, when the density

factorizes, but a vanishing correlation coefficient does not mean X and Y do not influence each other. Consider for example an arbitrary density $\rho(x, y)$ which is symmetric in x and has $\langle x \rangle = 0$. Then, the correlation coefficient is

$$\begin{aligned}
\text{corr}(X, Y) &\sim \text{cov}(X, Y) = \int dx dy \rho(x, y) x (y - \langle y \rangle) \\
&= \frac{1}{2} \left(\int dx dy \rho(x, y) x (y - \langle y \rangle) + \int dx dy \rho(x, y) (-x) (y - \langle y \rangle) \right) \\
&= \frac{1}{2} \left(\int dx dy \rho(x, y) x (y - \langle y \rangle) - \int dx dy \rho(x, y) x (y - \langle y \rangle) \right) \\
&= 0.
\end{aligned} \tag{3.27}$$

However, there are densities like $\sim \exp(-yx^2 - y^2)$ that do fulfill the requirements but do not factorize and thus have $I \neq 0$. The general understanding here is, that the MI does not only include linear correlations, but also higher ones. Linear meaning that both X and Y show up in eq (3.25) and (3.26) linearly.

In stochastic there are objects of interest called (joined) moments, which are defined as [49]

$$m_{kl} = \langle x^k y^l \rangle = \int dx dy \rho(x, y) x^k y^l. \tag{3.28}$$

From a physicist point of view, more interesting are the centralized moments

$$\tilde{m}_{kl} = \langle (x - \langle x \rangle)^k (y - \langle y \rangle)^l \rangle = \int dx dy \rho(x, y) (x - \langle x \rangle)^k (y - \langle y \rangle)^l. \tag{3.29}$$

We see that $\text{cov}(X, Y) = \tilde{m}_{11}$. Even though \tilde{m}_{11} may be zero, higher moments could be non-zero and therefore express an correlation between X and Y . Higher order moments are associated with long range interactions and large values of X (Y). The generating functional for the moments is [49]

$$\phi(\vec{s}) = \langle \exp(i\vec{s}\vec{Z}) \rangle = \int d\vec{Z} \rho(\vec{Z}) \exp(i\vec{s}\vec{Z}), \tag{3.30}$$

where $\vec{Z} = (X, Y)$ in the present case of two random variables. By taking appropriate derivatives of $\phi(\vec{s})$ and then evaluating the result at $\vec{s} = 0$ all moments can be constructed. Note that if the random variables are independent and the density factorizes, the generating functional factorizes as well. Also $\phi(\vec{s})$ depends only on the moments. We can

show this in the considered system of two random variables:

$$\begin{aligned}
 \phi(\vec{s}) &= \int d\vec{Z} \rho(\vec{Z}) \sum_{k=0}^{\infty} \frac{(is_1x + is_2y)^k}{k!} = \sum_{k=0}^{\infty} \frac{1}{k!} \int d\vec{Z} \rho(\vec{Z}) \sum_{l=0}^k \binom{k}{l} (is_1x)^l (is_2y)^{k-l} \\
 &= \sum_{k=0}^{\infty} \frac{1}{k!} \sum_{l=0}^k \binom{k}{l} (is_1)^l (is_2)^{k-l} \int d\vec{Z} \rho(\vec{Z}) x^l y^{k-l} \\
 &= \sum_{k=0}^{\infty} \frac{1}{k!} \sum_{l=0}^k \binom{k}{l} (is_1)^l (is_2)^{k-l} m_{l,k-l}. \tag{3.31}
 \end{aligned}$$

The generating functional is related directly to the density $\rho(X, Y)$ by a Fourier transformation

$$\rho(x, y) = \rho(\vec{Z}) = (2\pi)^2 \int d\vec{s} \phi(\vec{s}) \exp(-i\vec{s}\vec{Z}), \tag{3.32}$$

thus, the moments characterize the distribution completely:

$$m_{00}, m_{01}, \dots, m_{ij}, \dots \rightarrow \rho(m_{00}, m_{01}, \dots, m_{ij}, \dots). \tag{3.33}$$

Since the entropy is a functional of the density, the moments characterize the entropy as well:

$$m_{00}, m_{01}, \dots, m_{ij}, \dots \rightarrow S[X, Y] = S(m_{00}, m_{01}, \dots, m_{ij}, \dots), \tag{3.34}$$

and one can write the entropy in terms of the generating functional, without using the density explicitly at all:

$$S[X, Y] = \int dx dy (2\pi)^2 \int d\vec{s} \phi(\vec{s}) \exp(-i\vec{s}\vec{Z}) \ln((2\pi)^2 \int d\vec{s} \phi(\vec{s}) \exp(-i\vec{s}\vec{Z})). \tag{3.35}$$

By either shifting the distributions so that $\langle x \rangle = \langle y \rangle = 0$ or extending the formalism to the centralized moments, the relation to higher order correlation becomes even more apparent. Since the density and entropy can be written as a function of higher order correlations, i.e. the moments, the mutual information as a difference of entropies is a function of moments, in particular higher order moments, as well. Due to the logarithm the dependencies are generally not trivial.

3.8 Entropies from decomposed densities

In quantum physics, molecular wave functions are decomposed often in an adiabatic or an diabatic basis, see, e.g., sec. 2.3. To analyze the wave functions contributions in the respective states, we want to present a formalism that treats them information-theoretically. For this we assume the wave function of a coupled electron-nucleus pair. As in sec. 2.3, the nuclear coordinate is labeled as R and the electron coordinate as r , and the matrix elements of the density are

$$\rho_{nm}(r, R) = \Phi_n^*(R)\Phi_m(R)\varphi_n(r; R)\varphi_m(r; R), \quad (3.36)$$

Note that we assumed the electronic eigenfunction to be real. The decomposed nuclear and electron densities are

$$\rho_{nm}^{nuc}(R) = \int dr \rho_{nm}(r, R) \quad \text{and} \quad \rho_{nm}^{el}(r) = \int dR \rho_{nm}(r, R). \quad (3.37)$$

The off-diagonal terms of $\rho_{nm}^{nuc}(R)$ vanish due to the orthonormal electronic eigenfunctions, while that of $\rho_{nm}(r, R)$ and $\rho_{nm}^{el}(r)$ are complex. However, the diagonal terms of the densities are positive semidefinite and we use them to define

$$S_n[\rho_{nn}(r, R)] = - \int dR dr \rho_{nn}(r, R) \ln [\rho_{nn}(r, R)], \quad (3.38)$$

$$S_n^{nuc}[\rho_{nn}^{nuc}(R)] = - \int dR \rho_{nn}^{nuc}(R) \ln [\rho_{nn}^{nuc}(R)], \quad (3.39)$$

$$S_n^{el}[\rho_{nn}^{el}(r)] = - \int dr \rho_{nn}^{el}(r) \ln [\rho_{nn}^{el}(r)]. \quad (3.40)$$

We refer to them as *state specific entropies*. Note that the densities ρ_{nn} , ρ_{nn}^{el} and ρ_{nn}^{nuc} are not normalized to unity but their integral represents the population P_n of the respective state, i.e.

$$P_n = \int dR dr \rho_{nn}(r, R) = \int dr \rho_{nn}^{el}(r) = \int dR \rho_{nn}^{nuc}(R). \quad (3.41)$$

This makes it necessary to be careful with the interpretation of eq. (3.38)-(3.40), since this implies a different scaling behavior than the SDE of normalized densities.

Let us elaborate this shortly by using eq. (3.38), without loss of generality. Assuming we change coordinates using $r = Lx$, where L is some scale, the line-element and the density transform as

$$dr = Ldx, \quad \rho(r, R) = \rho'(x, R)/L. \quad (3.42)$$

Then, the differential Shannon entropy of the density $\rho(r, R)$ transforms as

$$\begin{aligned} S[\rho(r, R)] &= - \int dR dr \rho(r, R) \ln [\rho(r, R)] = - \int dR L dx \frac{\rho'(x, R)}{L} \ln \left[\frac{\rho'(x, R)}{L} \right] \\ &= S[\rho'(x, R)] + \ln(L) \int dR dx \rho'(x, R), \end{aligned} \quad (3.43)$$

which is, when the density is normalized to unity,

$$S[\rho(r, R)] = S[\rho'(x, R)] + \ln(L). \quad (3.44)$$

Therefore, if the differential entropy is zero for some density, it is possible to shift it to an arbitrary number using a coordinate transformation. However, by doing this, all DSEs of the system are shifted by the same value $\ln(L)$. But if the same transformation is considered in eq. (3.38), the entropies transform as

$$\begin{aligned} S_n[\rho_{nn}(r, R)] &= - \int dR dr \rho_{nn}(r, R) \ln [\rho_{nn}(r, R)] \\ &= - \int dR L dx \frac{\rho'_{nn}(x, R)}{L} \ln \left[\frac{\rho'_{nn}(x, R)}{L} \right] \\ &= S_n[\rho'_{nn}(x, R)] + \ln(L) \underbrace{\int dR dx \rho'_{nn}(x, R)}_{=P_n} \\ &= S_n[\rho'_{nn}(x, R)] + P_n \ln(L). \end{aligned} \quad (3.45)$$

Note that for $P_n = 0$, eq. (3.45) remains zero and is invariant under transformations. Regarding S_n , scaling as in eq. (3.45) is problematic: For a given scale transformations, "normal" DSEs shift relative to each other under transformations, so that the difference between two entropies stays constant. Differences between S_n do not stay constant but may even change sign. The difference ΔS_{nm} of S_n and S_m under the scale transformation from above is

$$\begin{aligned} \Delta S_{nm} &= S_n[\rho_{nn}(r, R)] - S_m[\rho_{nn}(r, R)] \\ &= S_n[\rho'_{nn}(x, R)] - S_m[\rho'_{nn}(x, R)] - (P_n - P_m) \ln(L) \\ &= \Delta S'_{nm} - (P_n - P_m) \ln(L). \end{aligned} \quad (3.46)$$

Thus $\Delta S'_{nm}$ depends on L and even can have the opposite sign as ΔS_{nm} . As a remark,

note that the sum of all S_n again scales like a "normal" DSE, since $\sum P_n = 1$:

$$\begin{aligned}
\sum_n^\infty S_n[\rho_{nn}(r, R)] &= \sum_n^\infty \left(- \int dR dx \rho'(x, R) \ln [\rho'(x, R)] + P_n \ln(L) \right) \\
&= \sum_n^\infty - \int dR dx \rho'(x, R) \ln [\rho(x, R)'] + \underbrace{\sum_n^\infty P_n}_{=1} \ln(L) \\
&= \sum_n^\infty S_n[\rho'_{nn}(x, R)] + \ln(L).
\end{aligned} \tag{3.47}$$

The above observations also apply to eq. (3.39) and (3.40) under similar transformations and have to be taken into account when interpreting the differential Shannon entropies from decomposed densities.

3.9 Entropy of Gaussians

Here, we calculate the entropy of a multidimensional Gaussian distribution, which is also referred to as multivariate normal distribution. The most general form of a multivariate normal distribution for n random variables $Z = (X_1, \dots, X_n)$ is [16]

$$\mathcal{N}(\mu, K) = \frac{1}{\sqrt{(2\pi^n)|K|}} \exp\left[\frac{1}{2}(Z - \mu)^T K^{-1}(Z - \mu)\right], \tag{3.48}$$

where μ is the vector of the averages of all random variables and K is the $n \times n$ covariance matrix

$$K_{ij} = \text{cov}[X_i X_j]. \tag{3.49}$$

Note that for $i = j$ the entries of K are the variances σ^2 . If the covariance matrix is diagonal, linear correlations vanish and the variables are independent in pairs. Let us calculate the entropy of this density explicitly. Recall the definition of the DSE, which reads

$$S[X, Y, \dots] = - \int dx dy \dots \rho(x, y, \dots) \ln \rho(x, y, \dots) \tag{3.50}$$

for d dimensional densities $\rho(x, y, \dots)$. The densities considered here are of form $\rho \sim n \exp(f(x, y, \dots))$, where $n^{-1} = \int dx dy \dots \exp(f(x, y, \dots))$, thus the entropy is

$$\begin{aligned}
 S[X, Y, \dots] &= - \int dx dy \dots n \exp(f(x, y, \dots)) \ln[n \exp(f(x, y, \dots))] \\
 &= - \ln n - \int dx dy \dots n \exp(f(x, y, \dots)) f(x, y, \dots) \\
 &= - \ln n - n \int dx dy \dots \lim_{a \rightarrow 1} \frac{d}{da} \exp(af(x, y, \dots)) \\
 &= - \ln n - n \lim_{a \rightarrow 1} \frac{d}{da} \int dx dy \exp(af(x, y, \dots)) \\
 &= - \ln n - n \lim_{a \rightarrow 1} \frac{d}{da} \frac{a^{-d/2}}{n} = - \ln n + \frac{nd}{2} \lim_{a \rightarrow 1} \frac{a^{-d/2-1}}{n} \\
 &= - \ln(n) + \frac{d}{2}. \tag{3.51}
 \end{aligned}$$

This calculation is possible for all $f(x, y, \dots)$ for which $\int dx dy \dots \exp(af(x, y, \dots)) = (a^{d/2}n)^{-1}$ is true for all $a > 0$. Let us now calculate the DSE for a two-dimensional Gaussian with $d = 2$, $Z = (X, Y)$ and

$$K = \begin{pmatrix} \sigma_X^2 & r\sigma_X\sigma_Y \\ r\sigma_X\sigma_Y & \sigma_Y^2 \end{pmatrix}, \tag{3.52}$$

where the linear correlation coefficient $\text{corr}(X, Y) = r$ occurs [16].

Using eq. (3.51), the total entropy yields

$$S[\mathcal{N}_2(\mu, K)] = - \ln(n) + \frac{d}{2} = \ln[2\pi e\sigma_X\sigma_Y\sqrt{1-r^2}]. \tag{3.53}$$

For $r \rightarrow 0$ the covariance matrix becomes diagonal and the entropy is $S = \ln[2\pi e\sigma_X\sigma_Y] = \frac{1}{2} \ln[2\pi e\sigma_X^2] + \frac{1}{2} \ln[2\pi e\sigma_Y^2] = S(X) + S(Y)$. We can use this to calculate the mutual information:

$$I[\mathcal{N}_2(\mu, K)] = -\frac{1}{2} \ln[(1-r^2)]. \tag{3.54}$$

Note that the Taylor expansion of the natural logarithm is for $|x| \leq 1$:

$$\ln(1-x) = -x - x^2/2 - x^3/3 + \dots \tag{3.55}$$

Since $|r| \leq 1$, it is possible to expand the mutual information in r :

$$I[\mathcal{N}_2(\mu, K)] = \frac{1}{2}r^2 + \frac{1}{4}r^4 + \frac{1}{6}r^6 + \dots \tag{3.56}$$

Therefore, for small $\text{corr}(X, Y)$, the MI behaves as $\sim r^2$. For $\text{corr}(X, Y) \rightarrow 1$ the argument of the logarithm goes to zero and the MI diverges.

4 Numerical Methods

In this thesis, problems are encountered that can not be treated analytically but require numerical approaches. The applied methods are presented in the following section.

4.1 Grid

There are many different types of numerical methods that are applied to solve the time-dependent Schrödinger equation [12, 56]. We here focus on grid based approaches, following [12]. Grid based means that the considered space, i.e. position-space, is discretized into intervals Δx . In general, it is sufficient to describe the space between a starting point x_{start} and an end point x_{end} on an equidistant grid so that

$$\Delta x = \frac{x_{end} - x_{start}}{N_x - 1}, \quad (4.1)$$

where N_x is the number of grid points, in which the interval $[x_{start}, x_{end}]$ is divided. The n -th grid point is then at position

$$x_n = (n - 1)\Delta x + x_{start}, \quad (4.2)$$

where $n \in \mathbb{N}$. Then, a continuous function $f(x)$ is approximated at the n -th grid point as

$$f(x) \approx f(x_n). \quad (4.3)$$

When treating operators being functions of only the momentum operator, it is advantageous to convert the discretized functions into the momentum-representation using the discretized Fourier transformation [57]. The Fourier transformation is the expansion of the respective function in a plane-wave basis. Since we consider a finite interval in position-space, the orthogonality requirement is

$$\delta_{k,k'} = \frac{1}{x_{end} - x_{start}} \int_{x_{start}}^{x_{end}} e^{-ikx} e^{ik'x} dx, \quad (4.4)$$

where $\delta_{k,k'}$ is the Kronecker delta and the prefactor ensures normalization. This is only possible for discrete momenta $k - k' = \frac{2\pi}{x_{end} - x_{start}} z$, $z \in \mathbb{Z}$, which implies

$$\Delta k = \frac{2\pi}{x_{end} - x_{start}}. \quad (4.5)$$

Therefore, the choice of the considered position-space domain $[x_{start}, x_{end}]$ determines the resolution in momentum-space. This results in the momentum space being periodic with period $2\pi/\Delta k$. Since the end and starting point can not be distinguished numerically, and since positive as well as negative momenta need to be represented, which results in a factor 1/2, the maximal representable momentum is [58]

$$k_{max} = \frac{1}{2} \left(\frac{2\pi}{\Delta x} - \Delta k \right). \quad (4.6)$$

4.2 Split-operator method

In sec 2.1 we showed that the time-dependent Schrödinger equation is solved by

$$\psi(x, t) = \hat{U}(t, t_0)\psi(x, t_0), \quad (4.7)$$

where $U(t, t_0)$ is the time evolution operator

$$\hat{U}(t, t_0) = e^{-i\hat{H}(t-t_0)/\hbar}. \quad (4.8)$$

Solving the problem numerically requires time to be discretized in time steps Δt . To propagate a wave function from the starting time t_0 to the final time t_{end} in N time steps Δt so that $N\Delta t = t - t_0$, the short-time propagator is introduced and applied N times

$$\hat{U}(t, t_0) = \prod_{i=1}^N e^{-i\hat{H}\Delta t/\hbar}. \quad (4.9)$$

Thus, a computational inexpensive but also sufficiently accurate implementation of this operator is needed. For this, remember that an operator in an exponential acts on the wave function as the Taylor expansion of the exponential. But if the wave function is expanded in the basis of the eigenstates of the operator in the exponential, the exponential of operators becomes an exponential of eigenvalues and is easy to evaluate numerically. However, since $\hat{H} = T(\hat{p}) + V(\hat{x})$ the wave function can be represented in either the basis of $T(\hat{p})$ or $V(\hat{x})$ but not both at the same time. A heuristic approach is to approximate the short time propagator as the product of two exponentials of the potential and the kinetic energy operator,

$$\hat{U}_{2nd}(\Delta t) = e^{-i\hat{H}\Delta t/\hbar} = e^{-i(T(\hat{p})+V(\hat{x}))\Delta t/\hbar} \approx e^{-iT(\hat{p})\Delta t/\hbar} e^{-iV(\hat{x})\Delta t/\hbar} + \mathcal{O}(\Delta t^2). \quad (4.10)$$

Using the latter operator, one first calculates the exponential of $V(\hat{x})$ acting on the wave function in position space, since $V(\hat{x})$ is diagonal there, and then switches to momentum

space where $T(\hat{p})$ is diagonal. To study the accuracy, the expansion of the approximation is calculated as

$$\begin{aligned}
 e^{-iT(\hat{p})\Delta t/\hbar}e^{-iV(\hat{x})\Delta t/\hbar} &= 1 - i[T(\hat{p}) + V(\hat{x})]\frac{\Delta t}{\hbar} \\
 &- \frac{1}{2}[T^2(\hat{p}) + T(\hat{p})V(\hat{x}) + V^2(\hat{x})]\frac{\Delta t^2}{\hbar^2} + \mathcal{O}(\Delta t^3). \quad (4.11)
 \end{aligned}$$

This is compared to the expansion of the exact short-time propagator, which is

$$\begin{aligned}
 e^{-i\hat{H}\Delta t/\hbar} &= 1 - i[T(\hat{p}) + V(\hat{x})]\frac{\Delta t}{\hbar} - \frac{1}{2}[T(\hat{p}) + V(\hat{x})]^2\frac{\Delta t^2}{\hbar^2} \\
 &+ \frac{1}{6}[T(\hat{p}) + V(\hat{x})]^3\frac{\Delta t^3}{\hbar^3} + \mathcal{O}(\Delta t^4). \quad (4.12)
 \end{aligned}$$

It can be seen that the error between equations (4.11) and (4.12) is in the second order of Δt . In order to increase accuracy, the product in eq. (4.10) is symmetrized:

$$\hat{U}_{SO}(\Delta t) = e^{-iV(\hat{x})\Delta t/2\hbar}e^{-iT(\hat{p})\Delta t/\hbar}e^{-iV(\hat{x})\Delta t/2\hbar}. \quad (4.13)$$

This is expanded to yield

$$\begin{aligned}
 &e^{-iV(\hat{x})\Delta t/2\hbar}e^{-iT(\hat{p})\Delta t/\hbar}e^{-iV(\hat{x})\Delta t/2\hbar} \\
 &= 1 - i[T(\hat{p}) + V(\hat{x})]\frac{\Delta t}{\hbar} - \frac{1}{2}[T^2(\hat{p}) + T(\hat{p})V(\hat{x}) + V(\hat{x})T(\hat{p}) + V^2(\hat{x})]\frac{\Delta t^2}{\hbar^2} \\
 &+ \frac{i}{6}[T^3(\hat{p}) + \frac{3}{2}V(\hat{x})T(\hat{p})V(\hat{x}) + \frac{3}{4}V^2(\hat{x})T(\hat{p}) + \frac{3}{2}V(\hat{x})T^2(\hat{p}) + \frac{3}{2}T^2(\hat{p})V(\hat{x}) \\
 &+ \frac{3}{4}T(\hat{p})V^2(\hat{x}) + V^3(\hat{x})]\frac{\Delta t^3}{\hbar^3} + \mathcal{O}(\Delta t^4). \quad (4.14)
 \end{aligned}$$

Hence, the second order error is canceled and the propagator eq. (4.13) is correct to third order in Δt . By applying this propagator consecutively to wave functions using sufficiently small Δt , reliable solutions to the time-dependent Schrödinger equation can be obtained. Since $\hat{U}_{SO}(\Delta t)$ "splits" the potential operator into two terms, this approach is called split-operator method. [59, 60]

4.3 Relaxation method

The relaxation method is a numerical method to find eigenstates of a Hamiltonian [61]. For this, the real time increment Δt is substituted by an imaginary time increment

$$\Delta t = -i\Delta\tau, \quad (4.15)$$

so that the short time propagator becomes

$$\hat{U}(-i\Delta\tau) = e^{-\hat{H}\Delta\tau/\hbar}. \quad (4.16)$$

To find the groundstate, the propagator is applied to a test wave packet $\psi(x, \tau)$. It is important that $\psi(x, \tau)$ contains the groundstate, $\langle \varphi_0(x) | \psi(x, \tau) \rangle \neq 0$, otherwise the relaxation method leads to convergence to lowest eigenstate contained in $\psi(x, \tau)$. After on step $\Delta\tau$ the test wave function becomes

$$\begin{aligned} \psi(x, \tau + \Delta\tau) &= \hat{U}(\Delta\tau)\psi(x, \tau) = \sum_i \langle \varphi_i(x) | \psi(x, \tau) \rangle e^{-\hat{H}\Delta\tau/\hbar} \varphi_i(x) \\ &= \sum_i \langle \varphi_i(x) | \psi(x, \tau) \rangle e^{-E_i\Delta\tau/\hbar} \varphi_i(x) \\ &= \sum_i \langle \varphi_i(x) | \psi(x, \tau) \rangle e^{-(E_0 + \Delta E_i)\Delta\tau/\hbar} \varphi_i(x) \\ &= e^{-E_0\Delta\tau/\hbar} (\langle \varphi_0(x) | \psi(x, \tau) \rangle \varphi_0(x) + \langle \varphi_1(x) | \psi(x, \tau) \rangle e^{-\Delta E_1\Delta\tau/\hbar} \varphi_1(x) + \\ &\quad + \langle \varphi_2(x) | \psi(x, \tau) \rangle e^{-\Delta E_2\Delta\tau/\hbar} \varphi_2(x) + \dots), \end{aligned} \quad (4.17)$$

using $E_i = E_0 + \Delta E_i$, where ΔE_i is the spacing between the $i-1$ -th and i -th eigenfunction and also $\Delta E_i > 0$ per definition. Assuming, without loss of generality, $E_0 > 0$, we see that at each step, the wave function is damped by $e^{-E_0\Delta\tau/\hbar}$ and inside the wave packet, each eigenfunction except the groundstate is dampened with $e^{-\Delta E_i\Delta\tau/\hbar}$. These observations require to renormalize the wave function after applying the propagator. Through the renormalization the coefficient of the groundstate eigenfunction $\langle \varphi_0(x) | \psi(x, \tau) \rangle$ grows with each step, while the other coefficients decreases and the test wave function converges to the groundstate.

If the wave function is close to the desired eigenfunction, $\psi(\tau, x) \sim \varphi_0(x)$, the eq. (4.17) becomes

$$\psi(x, \tau + \Delta\tau) \approx e^{-E_0\Delta\tau/\hbar} \langle \varphi_0(x) | \psi(x, \tau) \rangle \varphi_0(x) = e^{-E_0\Delta\tau/\hbar} \varphi_0(x), \quad (4.18)$$

and the absolute value of this equation is wave function is therefore

$$|\psi(x, \tau + \Delta\tau)|^2 = |e^{-E_0\Delta\tau/\hbar} \varphi_0(x)|^2 = e^{-2E_0\Delta\tau/\hbar} |\varphi_0(x)|^2 = e^{-2E_0\Delta\tau/\hbar}, \quad (4.19)$$

where we used that the eigenfunction is normalized to unity. This equation can be solved

for the eigenenergy of the groundstate E_0 , and we receive

$$E_0 = -\frac{\hbar}{2\Delta\tau} \ln |\psi(x, \tau + \Delta\tau)|^2. \quad (4.20)$$

It is possible to calculate eigenfunctions other than the groundstate by projecting out all states lower than the desired eigenstate out of the test function $\psi(\tau, x)$. To find the m -th wave function, one uses

$$\psi'(x, \tau) = \psi(x, \tau) - \sum_i^{m-1} \langle \varphi_i(x) | \psi(x, \tau) \rangle \varphi_i(x). \quad (4.21)$$

Of course this requires that eigenstates with quantum numbers lower than m have been found beforehand, which can be done by applying the method recursively.

4.4 Velocity-Verlet algorithm

A method to solve classical equations of motion numerically is the Verlet algorithm [10, 62, 63]. Here, one iteratively calculates classical trajectories from previous positions and the potential. For this the position of the classical particle is expanded up to the third order for small time steps dt and $-dt$:

$$r(t + dt) = r(t) + \dot{r}(t)dt + \frac{1}{2}\ddot{r}(t)dt^2 + \frac{1}{6}\dddot{r}(t)dt^3 + \mathcal{O}(dt^4), \quad (4.22)$$

$$r(t - dt) = r(t) - \dot{r}(t)dt + \frac{1}{2}\ddot{r}(t)dt^2 - \frac{1}{6}\dddot{r}(t)dt^3 + \mathcal{O}(dt^4). \quad (4.23)$$

The dots label derivatives in respect to time, i.e. $\dot{r}(t)$ and $\ddot{r}(t)$ are the velocity acceleration at time t , respectively. By adding both equations, odd order derivatives cancel and one obtains an equation for $r(t + dt)$ that is correct to third order:

$$r(t + dt) = 2r(t) - r(t - dt) + \ddot{r}(t)dt^2 + \mathcal{O}(dt^4). \quad (4.24)$$

The acceleration is hereby calculated from the potential $V(r)$ at each time step:

$$\ddot{r}(t) = -\frac{1}{m} \left. \frac{dV}{dr} \right|_{r=r(t)}. \quad (4.25)$$

For the initial time, the previous position $r(t - dt)$ is not known and it thus has to be estimated by $r(t - dt) = r(t) - \dot{r}(t)dt$ from eq. (4.22). However this algorithm may lead to inaccuracies, since $r(t)$ and $r(t - dt)$ are of a different order of magnitude as the term $\ddot{r}(t)dt^2$, which is of order dt^2 . The finite precession error of the difference $2r(t) - r(t - dt)$

compared to dt^2 can therefore result in truncation errors.

An improved version of this idea is the Velocity-Verlet algorithm [10, 63, 64]. Here, one calculates the position of the classical trajectories according to

$$r(t + dt) = r(t) + v(t)dt + \frac{1}{2}\ddot{r}(t)dt^2. \quad (4.26)$$

Additionally the velocity of the next time step is determined:

$$v(t + dt) = v(t)dt + \frac{\dot{r}(t + dt) + \dot{r}(t)}{2}dt. \quad (4.27)$$

The acceleration $\ddot{r}(t)$ is determined for each time step using (4.25). By iterating between equations (4.25), (4.26) and (4.27) classical trajectories can be calculated and reliable solutions to classical equations of motion can be found.

5 Entropy in a Disordered Harmonic Oscillator

This section is partially built on results published in [1].

The harmonic oscillator is one of the most important models in physics and chemistry. Its quadratic potential gives rise to equations of motion that are well understood in classical and quantum dynamics. In particular, it can be treated analytically and therefore provides an excellent starting point for approximate treatments. For example, in quantum chemistry, the vibrational modes of molecules are studied using an harmonic approximation. There, the Taylor expansion of the nuclear potential near the equilibrium geometry is truncated at the second order. Since the first order vanishes due to the equilibrium condition, the remaining potential is harmonic and can be treated much more easily. [65, 66] Furthermore, in the Marcus theory [67], the potentials of electron donor and acceptor are approximated to be harmonic, which allows to find an analytic expression for the electron transfer rate. For this theory Rudolph A. Marcus received the Nobel prize in 1992.

The harmonic oscillator is also used experimentally: In [68], Dries *et al.* studied the effects of impurities on a Bose-Einstein condensate (BEC) in an harmonic optical trap, with the intention to investigate dissipative transport of superfluids. This is important for understanding, for example, how BECs move in microchip traps and matter waveguides [69–72]. Numerical studies to this system have been carried out by Hsueh *et al.* in a series of papers, [13, 73–75], to gain insight into occurring effects, such as thermalization behavior and Anderson localization. In one of these publications, [13], the authors considered the rather general model of an excited wave function in an harmonic oscillator with static disorder potential. The group showed that differential Shannon entropies calculated from position- and momentum-space densities increase up to a maximum during the initial dynamics. They used this to define a time scale, the thermalization time, which is required to reach this maximum. The main result of [13] is how the system parameters translate into the thermalization time.

Stimulated by [13], in this section we investigate in detail the time-dependent differential Shannon entropies of wave packets in an unperturbed harmonic potential and an harmonic potential with random disorder. We relate the localization behavior of the wave function to the entropies and examine the disorder model in particular at long times, to study,

e.g., the imprint of revival dynamics on these information-theoretical measures: Due to the equal level spacing of the harmonic oscillator, the wave packet dynamics are periodic so that the initial state is recored in equal time intervals. However, anharmonicity, as the disorder potential, leads to dispersion of the wave packet. Nevertheless, (approximate) revivals of the initial quantum state are expected to be observed, especially since the system is isolated and the time evolution is unitary. Differential Shannon entropies proofed to be an excellent measure to indicate revival structures [76–78]. It is also interesting to compare entropies from quantum dynamics with those governed by classical equation of motions in order to highlight the quantum nature of observed effects. The results from this investigation are presented in the following section. Some of these results have been published in [1].

The section is structured as follows. In the first part, an information-theoretic approach is applied to wave packet dynamics by calculating differential Shannon entropies from quantum and classical position- and momentum-space densities of the harmonic oscillator. The aim is to apply and interpret these information-theoretical measures. Later, the model is expanded by adding anharmonicity in form of a static disorder potential to the system. This is based on the model treated in [13]. The entropies resulting from classical and quantum dynamics are investigated and compared. Finally, the energy dependence of the entropy for long times is discussed.

5.1 Entropy of the undisturbed harmonic oscillator

We calculate differential Shannon entropies from position- and momentum-probability densities in the harmonic oscillator. We consider the one-dimensional Hamiltonian

$$\hat{H} = \left[-\frac{\hbar^2}{2m} \frac{d^2}{dx^2} + \frac{1}{2} m \omega^2 x^2 \right]. \quad (5.1)$$

with mass m , and frequency ω . Scaled units are employed in the calculations, which are specified in tab. 5.1.

First, time-dependent studies are presented, where the entropy of coherent and squeezed states are calculated. Secondly, the entropy of stationary cases are reviewed, where the wave function is in an eigenstate of the Hamiltonian.

Table 5.1: Scaling constants of the harmonic oscillator.

Energy	$\epsilon_0 = \hbar\omega$
Time	$T = 2\pi/\omega$
Position	$l_0 = \sqrt{\frac{\hbar}{m\omega}}$
Momentum	$k_0 = l_0 m\omega$

5.1.1 Coherent and squeezed states

Gaussian states in the harmonic oscillator are special, since they remain Gaussian under time evolution. Additionally, Gaussians densities evolve classically identically [12]. There are two-different cases of Gaussians in the harmonic oscillator: Coherent and squeezed states. In coherent states, the width of the wave packet is constant, while in squeezed states the width oscillates. The time-dependent Schrödinger equation with a general Gaussian initial state in an harmonic potential was solved in [12], we here give the result as

$$\psi(x, t) = n \exp\left(-\frac{a_t}{2}(x - x_t)^2 + i\frac{p_t}{\hbar}(x - x_t) + i\gamma_t\right), \quad (5.2)$$

with norm n . The real valued parameters x_t and p_t are

$$x_t = x_0 \cos(\omega t) + \frac{p_0}{m\omega} \sin(\omega t), \quad (5.3)$$

$$p_t = p_0 \cos(\omega t) - m\omega x_0 \sin(\omega t), \quad (5.4)$$

and a_t and γ_t are complex valued, given as

$$a_t = a \frac{a_0 \cos(\omega t) + i a \sin(\omega t)}{i a_0 \sin(\omega t) + a \cos(\omega t)}, \quad (5.5)$$

$$\gamma_t = \frac{p_t x_t - p_0 x_0}{2\hbar} + \frac{i}{2} \ln \left(\frac{i a_0 \sin(\omega t) + a \cos(\omega t)}{a} \right), \quad (5.6)$$

where $a = m\omega/\hbar = \frac{1}{l_0^2}$ and x_0 and p_0 are the initial average position and momentum, respectively, so that at $t = 0$ the wave function reads

$$\psi(x, 0) = n \exp\left(-\frac{a_0}{2}(x - x_0)^2 + i\frac{p_0}{\hbar}(x - x_0) + i\gamma_0\right). \quad (5.7)$$

The width or variance of the Gaussian is [12]

$$\Delta x(t) = \sqrt{\int dx \psi^*(x, t)(x - x_t)^2 \psi(x, t)} = \frac{1}{2\sqrt{\text{Re}(a_t)}}, \quad (5.8)$$

which was solved by Gaussian integration methods. Therefore a_0 is related to the initial width of the wave function by $\Delta x_0 = 1/2\sqrt{a_0}$. For coherent states, $a_t = a_0 = a = m\omega/\hbar$ is constant for all times, while for squeezed states $a_0 \neq a$. Since we are interested in the density $\rho(x, t) = |\psi(x, t)|^2$, phases vanish, and we obtain

$$\begin{aligned} \rho(x, t) &= n^2 \exp\left(-\frac{a_t}{2}(x - x_t)^2 + i\frac{p_t}{\hbar}(x - x_t) + i\gamma_t\right) \\ &\quad -\frac{a_t^*}{2}(x - x_t)^2 - i\frac{p_t}{\hbar}(x - x_t) - i\gamma_t^*) \\ &= n^2 \exp\left(-\operatorname{Re}(a_t)(x - x_t)^2 - 2\operatorname{Im}(\gamma_t)\right). \end{aligned} \quad (5.9)$$

The expression $-2\operatorname{Im}(\gamma_t)$ is real valued and is thus absorbed in the new norm N

$$\rho(x, t) = N \exp(-\operatorname{Re}(a_t)(x - x_t)^2), \quad (5.10)$$

where we find

$$N^{-1} = \int \exp(-\operatorname{Re}(a_t)(x - x_t)^2) dx = \sqrt{\frac{\operatorname{Re}(a_t)}{\pi}} \quad (5.11)$$

by a standard Gaussian integration.

The differential Shannon entropy is now calculated using eq. 3.51:

$$S_x(t) = - \int dx \rho(x, t) \ln(\rho(x, t)) = \frac{1}{2} \ln \left[\frac{e\pi}{\operatorname{Re}(a_t)} \right]. \quad (5.12)$$

The position space entropy depends dynamically only on a_t . Since the logarithm is bijective, the position entropy is oscillating with the same period as $\operatorname{Re}(a_t)$ for squeezed states and is constant $S_x = \frac{1}{2} \ln(\frac{e\pi}{a})$ for coherent states. Comparing eq. (5.12) with the width of the Gaussian eq. (5.8), we see that the entropy oscillates in phase with Δx . Note that S_x becomes negative for $\operatorname{Re}(a_t) > e\pi$.

To determine the entropy in momentum space, $\psi(p, t)$ is calculated from eq. (5.2) by Fourier transform

$$\begin{aligned} \psi(p, t) &= \frac{n}{\sqrt{2\pi\hbar}} \int \exp\left(-\frac{a_t}{2}(x - x_t)^2 + i\frac{p_t}{\hbar}(x - x_t) + i\gamma_t\right) \exp(-i\frac{px}{\hbar}) dx \\ &= \frac{ne^{i\gamma_t + ip_t x_t}}{\sqrt{2\pi}} \int \exp\left(-\frac{a_t}{2}\left(x - \left(x_t - i\frac{p_t - p}{\hbar a_t}\right)\right)^2 - \frac{1}{2a_t}(x - x_t)^2 - i\frac{p_t - p}{\hbar}x_t\right) dx \\ &= n' \exp\left(-\frac{1}{2a_t\hbar}(p - p_t)^2 + i\frac{px_t}{\hbar} + i\gamma_t\right), \end{aligned} \quad (5.13)$$

with norm n' . The momentum probability is

$$\rho(p, t) = N \exp \left(-\frac{\operatorname{Re} a_t}{|a_t|^2 \hbar} (p - p_t)^2 \right), \quad (5.14)$$

where the norm N is

$$N = \sqrt{\frac{\operatorname{Re}(a_t)}{|a_t|^2 \pi \hbar}}. \quad (5.15)$$

Thus, the momentum entropy is, again using eq. 3.51:

$$S_p(t) = \frac{1}{2} \ln \left[\frac{|a_t|^2 e \pi \hbar}{\operatorname{Re}(a_t)} \right]. \quad (5.16)$$

The width in momentum space is [12]

$$\Delta p(t) = \sqrt{\int dp \psi^*(p, t) (p - p_t)^2 \psi(p, t)} = \frac{\hbar |a_t|}{2 \sqrt{\operatorname{Re}(a_t)}}, \quad (5.17)$$

thus, here as well, the oscillations of the width and the entropy are in phase. The momentum entropy becomes negative for $\operatorname{Re}(a_t) > |a_t|^2 e \pi$ and is constant for coherent states $S_p = \frac{1}{2} \ln(e \pi a)$.

The entropy sum is the sum of the position and momentum entropy:

$$\begin{aligned} S_{sum}(t) &= S_x(t) + S_p(t) \\ &= \frac{1}{2} \ln \left[\frac{e \pi}{\operatorname{Re}(a_t)} \right] + \frac{1}{2} \ln \left[\frac{|a_t|^2 e \pi \hbar}{\operatorname{Re}(a_t)} \right] \\ &= \ln \left[\frac{|a_t| e \pi}{\operatorname{Re}(a_t)} \right] + \ln \hbar. \end{aligned} \quad (5.18)$$

Since the real part of a number is always smaller or equal than its absolute value, $|a_t|/\operatorname{Re}(a_t) > 1$ for all times and therefore $\ln \left(\frac{|a_t| e \pi}{\operatorname{Re}(a_t)} \right)$ is always positive. The minimal value is reached for $|a_t|/\operatorname{Re}(a_t) = 1$ which is $S_{min} = \ln(e \pi) + \ln \hbar$. In particular this is fulfilled trivially by coherent states, where $S_x + S_p = \ln(e \pi) + \ln \hbar$. To see that the minimum agrees with the BBM inequality $S \geq \ln e \pi$ (sec. 3.5), we either have to rescale the momentum by $k = p/\hbar$ or, equivalently, consider eq. (5.18) in atomic units, so that ($\hbar = 1$). Then, the minimum is given as $S_{min} = \ln(e \pi)$, therefore coherent Gaussians saturate the entropic uncertainty relation.

We also find that the entropy sum eq. (5.18) is related to the product of the width of

the functions

$$S_{sum}(t) = \ln [2\Delta x(t)\Delta p(t)e\pi]. \quad (5.19)$$

To compare the oscillation period of the entropy sum, the term $|a_t|/\text{Re}(a_t)$ is simplified using eq. (5.5) and some algebra to obtain

$$\frac{|a_t|}{\text{Re}(a_t)} = \sqrt{1 + \frac{(a_0^2 - a^2)^2}{a_0^2 a^2} \frac{1}{8}(1 - \cos(4\omega t))}. \quad (5.20)$$

Thus the entropy sum is

$$S_{sum}(t) = \ln \left[e\pi \sqrt{1 + \frac{(a_0^2 - a^2)^2}{a_0^2 a^2} \frac{1}{8}(1 - \cos(4\omega t))} \right] \quad (5.21)$$

and therefore oscillates with four times the frequency of ω .

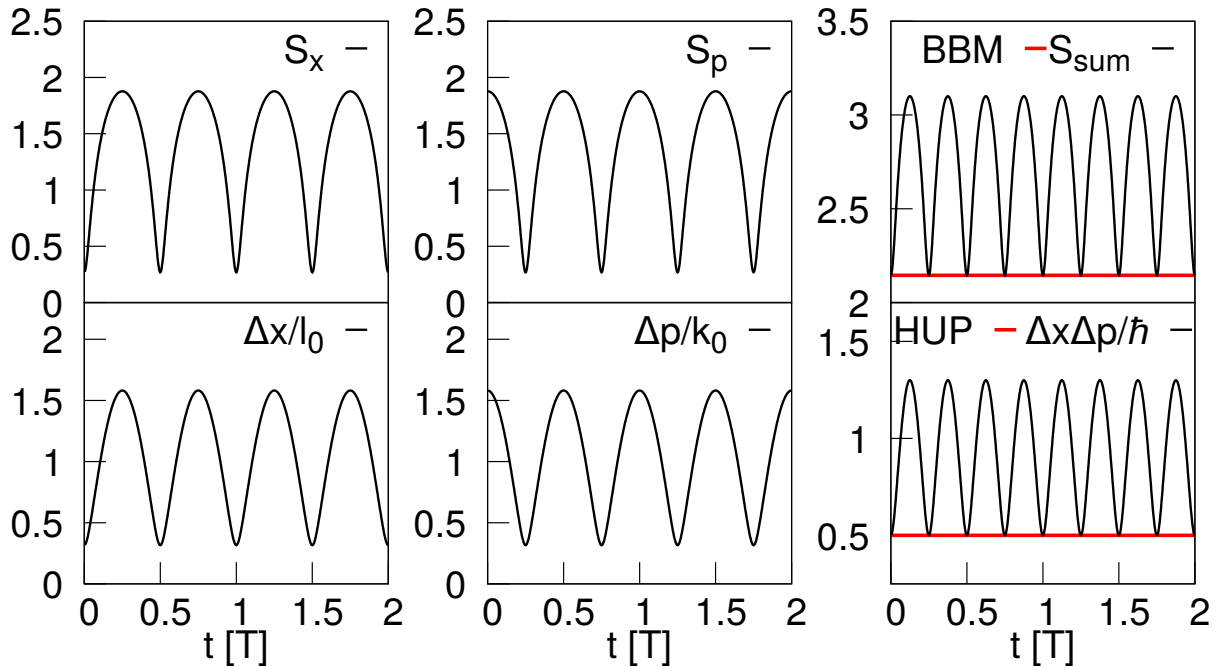


Figure 5.1: Position, momentum and entropy sum as well as widths and uncertainty product of a Gaussian in an harmonic oscillator. The lines in red show the limit given by the BBM inequality in the top right panel and the $x - p$ uncertainty (Heisenberg uncertainty principle, HUP) in the bottom right panel, respectively. Time is given in terms of the period T and the width in terms of $l_0 = \sqrt{\hbar/m\omega}$. Initial parameters are $a_0 = 5a$ and $x_0 = 5l_0$.

To illustrate the above discussed equation, an exemplary case is presented using the initial parameters $\omega = m = 1$, $a_0 = 5a$ and $x_0 = 5l_0$, where $l_0 = \sqrt{\hbar/a}$ is the associated

length scale of the harmonic oscillator (tab. 5.1). The results for the position space are shown in the left hand panels of fig. 5.1. Here, the time is given in terms of the period $T = 2\pi/\omega$. At $t = 0T$, the wave function has a small width and is highly localized. The information attainable about the wave function is therefore large in position space, which is associated with a low entropy. When the wave function passes the equilibrium point at $t = T/4$, the width and uncertainty of the wave function is maximal. Thus also the entropy reaches its maximum. At $t = T/2$, the classical turning point is reached and, due to symmetry, the mirrored situation as at $t = 0T$ occurs. The wave packet therefore localizes and repeats its dynamics periodically.

The momentum space entropy and width are shown in the middle panels of fig. 5.1. Since position- and momentum-space width are related by the uncertainty principle, the momentum width is large at $t = 0T$ and decreases as the position width increases. Thus Δp starts with a maximal value at $t = 0T$ and reaches its minima at $t = T/4$, which means it is phase-shifted with respect to Δx by $T/4$. The momentum space entropy assumes minima and maxima at the same times as Δp , in analogy with what is found in position space.

On the right hand side of fig. 5.1, the product of both uncertainties $\Delta x \Delta p$ (bottom panel) and the entropy sum (top panel) is displayed. Again, both panels show quite similar behavior. Each time Δx or Δp is minimal, the uncertainty product is minimal as well. In total, this leads to a twice as fast oscillation if compared to the position or momentum widths. This, in turn, determines the periodicity of the entropy sum, see eq. 5.19. Also, predicted by eq. 5.21, the entropy sum oscillates four times in one period T . When minimal, the entropy sum saturates the BBM inequality and the uncertainty product saturates the Heisenberg uncertainty relation $\Delta x \Delta p \geq 1/2$. Both boundaries are marked in fig. 5.1 as red lines.

5.1.2 Entropy of harmonic eigenstates

We now want to consider stationary states of the harmonic oscillator. The eigenstates of the harmonic oscillator are well known and, in position space, they read [79]

$$\varphi_n(x) = \sqrt{\frac{\pi}{l_0}} \sqrt{\frac{1}{2^n n!}} \exp\left(-\frac{x^2}{2l_0}\right) H_n(x/l_0), \quad (5.22)$$

where $n = 0, 1, 2, \dots$ labels the quantum number and H_n is the n -th Hermite polynomial. Due to symmetry between the momentum and position operators of the harmonic oscillator, the associated eigenstates in momentum space are of the same form, using

$k_0 = m\omega l_0$:

$$\tilde{\varphi}_n(p) = \sqrt[4]{\frac{\pi}{k_0}} \sqrt{\frac{1}{2^n n!}} \exp\left(-\frac{p^2}{2k_0}\right) H_n(p/k_0). \quad (5.23)$$

The probability space densities are the absolute squares of these functions,

$$\rho_n^{EF}(x) = |\varphi_n(x)|^2 = \sqrt{\frac{\pi}{l_0}} \frac{1}{2^n n!} \exp\left(-\frac{x^2}{l_0}\right) (H_n(x/l_0))^2, \quad (5.24)$$

$$\rho_n^{EF}(p) = |\tilde{\varphi}_n(p)|^2 = \sqrt{\frac{\pi}{k_0}} \frac{1}{2^n n!} \exp\left(-\frac{p^2}{k_0}\right) (H_n(p/k_0))^2. \quad (5.25)$$

We want to study the entropies

$$S_{x,n}^{EF} = - \int dx \rho_n^{EF}(x) \ln [\rho_n^{EF}(x)] \quad \text{and} \quad S_{p,n}^{EF} = - \int dp \rho_n^{EF}(p) \ln [\rho_n^{EF}(p)], \quad (5.26)$$

as well as the sum of both, $S_{sum,n}^{EF} = S_{x,n}^{EF} + S_{p,n}^{EF}$. These entropies can be treated analytically, however, their calculation are quite technical due to integrations over Hermite polynomials occurring in the logarithm. We present the result as given in [80]:

$$S_{x,n}^{EF} = \ln [\sqrt{\pi} 2^n n! l_0] + n + \frac{1}{2} - \frac{1}{\sqrt{\pi} 2^n n!} I_n, \quad (5.27)$$

$$S_{p,n}^{EF} = \ln [\sqrt{\pi} 2^n n! k_0] + n + \frac{1}{2} - \frac{1}{\sqrt{\pi} 2^n n!} I_n. \quad (5.28)$$

Since $l_0 k_0 = \hbar$, the entropy sum of all eigenstates of the harmonic oscillator is independent of the parameters of the harmonic potential for any n :

$$S_{sum,n}^{EF} = \ln [2\pi 2^n n! \hbar] + 2n + 1 - \frac{2}{\sqrt{\pi} 2^n n!} I_n, \quad (5.29)$$

where we defined

$$I_n = \int e^{-t^2} H_n(t)^2 \ln [H_n(t)^2] dt, \quad (5.30)$$

which can not be simplified further for arbitrary n . For the ground state one obtains:

$$S_{x,n=0}^{EF} = \frac{1}{2} \ln [e\pi l_0] \quad \text{and} \quad S_{p,n=0}^{EF} = \frac{1}{2} \ln [e\pi k_0^2]. \quad (5.31)$$

Therefore, the entropy sum

$$S_{sum,n=0}^{EF} = \ln [e\pi \hbar] \approx 2.144 + \ln \hbar \quad (5.32)$$

saturates the BBM inequality.

The entropies of the first 1400 eigenstates were calculated numerically for the case of $\hbar = \omega = m = 1$ a.u.. Representative values are given in tab. 5.2. Note that only S_x and S_p depend on the choice of parameters.

Table 5.2: Entropies derived from harmonic oscillator eigenfunctions. Numerically exact values are compared to approximations given in eq. (5.35),(5.38) and (5.50).

E/ϵ_0	$S_{x,n}^{EF}$	$S_{p,n}^{EF}$	$S_{sum,n}^{EF}$	S_{sum}^{MC}	$S_{sum,n}^{EF,asympt}$	$S_{sum,n}^{EF,approx}$
0.5	1.07236	1.07236	2.14473	0.90317	0.28946	2.18311
1.5	1.34273	1.34273	2.68546	2.00178	1.38807	2.70229
2.5	1.49861	1.49861	2.99722	2.51260	1.89890	3.00783
3.5	1.60972	1.60971	3.21943	2.84908	2.23537	3.22693
4.5	1.69655	1.69655	3.39310	3.10039	2.48668	3.39876
5.5	1.76807	1.76806	3.53613	3.30106	2.68736	3.54057
6.5	1.82897	1.82897	3.65794	3.46811	2.85441	3.66152
7.5	1.88210	1.88208	3.76417	3.61122	2.99751	3.76712
8.5	1.92922	1.92922	3.85844	3.73638	3.12267	3.86092
9.5	1.97164	1.97163	3.94327	3.84760	3.23390	3.94534
10.5	2.01016	2.01018	4.02034	3.94769	3.33398	4.02214
20.5	2.27679	2.27674	4.55353	4.61674	4.00303	4.55394
30.5	2.44150	2.44149	4.88299	5.01404	4.40033	4.88307
40.5	2.56185	2.56169	5.12354	5.29761	4.68391	5.12321
50.5	2.65656	2.65654	5.31310	5.51829	4.90458	5.31281
100.5	2.95908	2.95891	5.91800	6.20647	5.59276	5.91750
200.5	3.27132	3.27078	6.54210	6.89713	6.28342	6.54153
300.5	3.45661	3.45707	6.91369	7.30176	6.68805	6.91368
400.5	3.58870	3.59015	7.17885	7.58903	6.97532	7.18039
500.5	3.69504	3.69409	7.38913	7.81192	7.19821	7.38864
600.5	3.78010	3.77963	7.55973	7.99408	7.38037	7.55960
700.5	3.85105	3.85228	7.70334	8.14811	7.53440	7.70468
800.5	3.91581	3.91582	7.83163	8.28155	7.66784	7.83074
900.5	3.96882	3.97081	7.93964	8.39926	7.78556	7.94220
1000.5	4.02117	4.02033	8.04150	8.50457	7.89086	8.04211

It was found in [81] and [82] that in the limit of large quantum numbers the entropies behave as

$$S_{x,n}^{EF,asympt} = \frac{1}{2} \ln [\pi^2 l_0^2 (2n + 1)] - 1, \quad (5.33)$$

$$S_{p,n}^{EF,asympt} = \frac{1}{2} \ln [\pi^2 k_0^2 (2n + 1)] - 1, \quad (5.34)$$

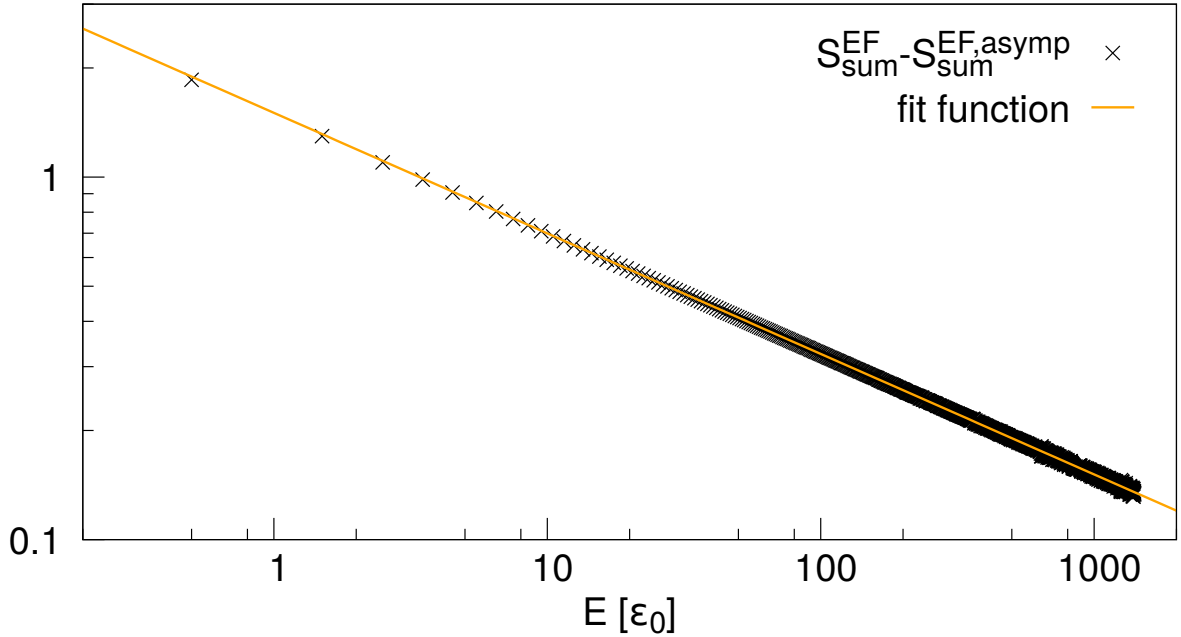


Figure 5.2: Difference of $S_{sum,n}^{EF}$ (eq. (5.29)) and $S_{sum,n}^{EF,asympt}$ (eq. (5.35)) as well as the logarithmic regression (eq. (5.37) and eq. (5.38)).

and therefore, the entropy sum is

$$S_{sum,n}^{EF,asympt} = \ln [\pi^2 \hbar (2n + 1)] - 2. \quad (5.35)$$

We test this claim by numerically calculating values for the entropy sum eq. (5.29) and comparing them to those obtained from eq. (5.35). Therefore the deviations of the numerical values from the asymptotic form are computed, and they are shown in fig. 5.2. We find that the difference behaves nearly linear in a log-log plot, which indicates a power law:

$$S_{sum,n}^{EF} - S_{sum,n}^{EF,asympt} \sim a(E/\epsilon_0)^b. \quad (5.36)$$

Note that a and b are unitless and therefore scale invariant, since, including the units, eq. (5.36) is formally $S_{sum,n}^{EF} + \ln \hbar - (S_{sum,n}^{EF,asympt} + \ln \hbar)$ and the $\ln \hbar$ cancel. By applying logarithmic regression to the entropy of the first 1400 harmonic eigenstates, we find a and b appearing in eq. (5.36),

$$a = 1.5039 \text{ and } b = -0.3325, \quad (5.37)$$

where the coefficient of determination $R^2 = 0.9992$ and the standard deviation $\sigma^2 = 0.0091$ indicate an excellent fit. Since the exponent b is negative, it validates the assumption that

the asymptotic form is indeed correct and the entropy sum converges to $S_{sum,n}^{EF,asympt}$ for large energies. This also means that the entropy sum can be approximated reasonably well by

$$S_{sum,n}^{EF,approx} \approx S_{sum,n}^{EF,asympt} + a(E/\epsilon_0)^b, \quad (5.38)$$

with a and b given in eq. (5.37). The approximation is compared to the numerically exact data in tab. 5.2 for selected states. It can be seen that $S_{sum,n}^{EF,approx}$ is closer to the exact $S_{sum,n}^{EF}$ than $S_{sum,n}^{EF,asympt}$ for all energies, thus the fit improves the approximation significantly. In particular, $S_{sum,n}^{EF,approx}$ represents $S_{sum,n}^{EF}$ more accurately for low energies. Nevertheless, the deviations of $S_{sum,n}^{EF,approx}$ from the numerically exact values are larger for lower energies than for higher ones: The ground state has the biggest deviation of ≈ 0.04 , while in higher states the error is in the third decimal place.

5.1.3 Entropy of the classical HO in a microcanonical ensemble

We now consider the harmonic oscillator in the classical microcanonical ensemble. The latter considers an isolated system where the particle number, volume and total energy E are conserved. Its distribution is obtained by equally assigning all microstates with energy E the same probability [83] and it reads:

$$\rho^{MC}(x, p) = \frac{\omega}{2\pi} \delta(H - E), \quad (5.39)$$

where H is the classical Hamiltonian $H = p^2/2m + x^2m\omega^2/2$ and E is the total energy. The position density is obtained by integration as

$$\rho^{MC}(x) = \int dp \rho_c(x, p) = \frac{\omega}{2\pi} \int dp \delta(H - E) = \frac{\omega}{2\pi} \int dp \delta(p^2/2m + x^2m\omega^2/2 - E). \quad (5.40)$$

Since for the delta distribution $\delta(g(p)) = \sum_i \delta(p - p_i)/|g'(p_i)|$ with $g(p_i) = 0$, we have

$$\rho^{MC}(x) = \frac{\omega}{2\pi} \int dp \sum_i \frac{\delta(p - p_i)}{|p_i/m|}, \quad (5.41)$$

where p_i are the roots of the original argument of the delta distribution. The roots are determined to be $p_{1/2} = \pm \sqrt{2m(E - x^2m\omega^2/2)}$, thus the position density is

$$\rho^{MC}(x) = \frac{\omega}{2\pi} \int dp \frac{2\delta(p - p_i)}{\sqrt{2m(E - x^2m\omega^2/2)/m}} = \frac{\omega}{2\pi} \frac{2m}{\sqrt{2m(E - x^2m\omega^2/2)}}. \quad (5.42)$$

Altogether this is, with the scales $l_0 = \sqrt{\hbar/m\omega}$ and $\epsilon_0 = \hbar\omega$,

$$\rho^{MC}(x) = \frac{1}{\pi l_0 \sqrt{\frac{2E}{\epsilon_0} - \frac{x^2}{l_0^2}}}. \quad (5.43)$$

By integration over space it can be confirmed that the normalization is correct.

The momentum density is determined analogously as

$$\rho^{MC}(p) = \int dx \rho^{MC}(x, p) = \frac{\omega}{2\pi} \int dx \delta(H - E) = \frac{\omega}{2\pi} \int dx \sum_i \frac{\delta(x - x_i)}{|x_i m \omega|}, \quad (5.44)$$

and the roots are $x_{1/2} = \pm \sqrt{2/m\omega(E - p^2/2m)}$. This leads to

$$\rho^{MC}(p) = \frac{\omega}{2\pi} \frac{2}{m\omega \sqrt{2/m\omega(E - p^2/2m)}} = \frac{1}{\pi k_0 \sqrt{\frac{2E}{\epsilon_0} - \frac{p^2}{k_0^2}}}. \quad (5.45)$$

All integral limits are determined by the total energy, $x_{a,e} = \pm \sqrt{\frac{2E}{\epsilon_0}} l_0$ and $p_{a,e} = \pm \sqrt{\frac{2E}{\epsilon_0}} k_0$. To calculate entropies from these densities, we use the integrals

$$\int_0^{\sqrt{a}} \frac{\ln(\sqrt{a-x^2})}{\sqrt{a-x^2}} dx = \frac{1}{4} \pi \ln \left[\frac{a}{4} \right] \quad \text{and} \quad \int_0^{\sqrt{a}} \frac{1}{\sqrt{a-x^2}} dx = \pi/2. \quad (5.46)$$

These integrals are modified by introducing the parameters b and N to transform it in form of the entropies, i.e. $S_x^{MC} = - \int dx \rho^{MC}(x) \ln[\rho^{MC}(x)]$, we want to calculate:

$$\begin{aligned} \int_{-\sqrt{a/b}}^{\sqrt{a/b}} \frac{\ln(N\sqrt{a-bx^2})}{N\sqrt{a-bx^2}} dx &= \frac{\ln N}{N} \int_{-\sqrt{a/b}}^{\sqrt{a/b}} \frac{1}{\sqrt{a-bx^2}} dx + \int_{-\sqrt{a/b}}^{\sqrt{a/b}} \frac{\ln(\sqrt{a-bx^2})}{N\sqrt{a-bx^2}} dx \\ &= \frac{\pi \ln N}{N\sqrt{b}} + \frac{\pi}{2N\sqrt{b}} \ln \left[\frac{a}{4} \right]. \end{aligned} \quad (5.47)$$

Position and momentum entropy can be calculated easily from this and we have

$$S_x^{MC} = \ln \left[\pi l_0 \sqrt{\frac{E}{2\epsilon_0}} \right] \quad (5.48)$$

and

$$S_p^{MC} = \ln \left[\pi k_0 \sqrt{\frac{E}{2\epsilon_0}} \right]. \quad (5.49)$$

The classical entropy sum of the harmonic oscillator in the microcanonical ensemble is

therefore

$$S_{sum}^{MC} = \ln \left[\pi^2 \frac{E}{2\epsilon_0} \right] + \ln \hbar. \quad (5.50)$$

The entropies eq. (5.50) are calculated for different energies in tab. 5.2. Note that in atomic units $\hbar = 1$. The Planck constant occurs in eq. (5.50) since we identified ϵ_0 with the quantum mechanical energy $\omega\hbar$ and we used the quantum relation $k_0 l_0 = \hbar$.

5.1.4 Discussion and classical limit

We have found an approximate form for the entropies of the harmonic eigenfunctions and calculated the densities and the entropies for the classical HO in the microcanonical ensemble. Fig. 5.3 compares the exact values of the entropy sum of the harmonic eigenfunctions $S_{sum,n}^{EF}$ with $S_{sum,n}^{EF,asympt}$, $S_{sum,n}^{EF,approx}$ and S_{sum}^{MC} . The numerically exact calculated entropies S_{sum}^{EF} align very well with the fit-function given in (5.38), $S_{sum}^{EF,approx}$. In particular, the fit-function is above the lower bound given by the BBM inequality (indicated by the red line in fig. 5.3) and violates it only for quantum mechanically not accessible energies lower than $E = 1/2\epsilon_0$. For very large values $E > 1000\epsilon_0$, the convergence to the asymptotic form (dark-blue line in fig. 5.3) is approached.

The line drawn in light blue in fig. 5.3 is the entropy of the HO in the microcanonical ensemble with energy E . For low values, this entropy violates the BBM inequality, since there is no Fourier relation between the classical position and momentum, and thus no minimal uncertainty which prohibits the simultaneous localization of both. Therefore, classical mechanics allows the entropy to be lower than what is derived from quantum mechanics. For $E \approx 11.5\epsilon_0$, both entropies cross, which means that their information content is similar. At larger energies, the entropy of the eigenfunctions is lower than the classical entropy.

Let us now discuss the high energy limit $E \gg \epsilon_0$, which is associated with the classical limit. Naively, one expects that the quantum density converges to the density of the classical HO in the limit of large n ,

$$\lim_{E \gg \epsilon_0} |\varphi_n|^2 \rightarrow \rho^{cl}. \quad (5.51)$$

Nevertheless, when calculating entropies from both, we find that they are of a different character from an informational theoretic point of view. In particular, we find that for

high energies there is a shift of $\sim 1 - \ln(2)$ between both entropies,

$$\begin{aligned} \lim_{E \gg \epsilon_0} (S_{sum}^{MC} - S_{sum,n}^{EF,approx}) &= S_{sum}^{MC} - S_{sum,n}^{EF,asympt} \\ &= \ln\left(\pi^2 \hbar \frac{E}{2\epsilon_0}\right) - \ln(\pi^2 \hbar (2n+1)) - 2 = 1 - \ln(2), \end{aligned} \quad (5.52)$$

where we set the classical energy to the quantum energy, $E = (n + \frac{1}{2})\epsilon_0$. Hence the quantum eigenfunction densities contain more information and are more localized than the classical counterpart. This results from the nodes in the eigenfunctions, which increases the localization of the quantum density.

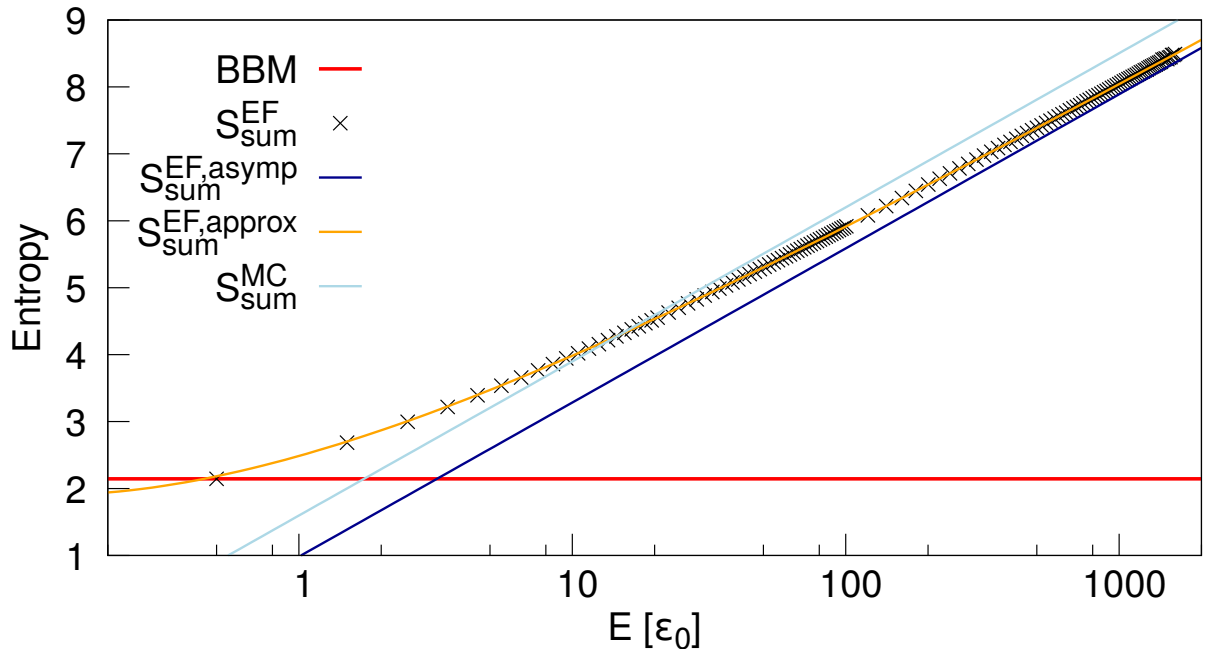


Figure 5.3: Entropy sum of the eigenstates of the harmonic oscillator plotted vs the energy (crosses), together with various approximations described in the text (lines). The red line marks the BBM inequality. Note that not all calculated data points are shown to guarantee better visibility.

5.2 Harmonic oscillator with disorder

5.2.1 Model and methods

Now the harmonic oscillator Hamiltonian is extended by including a disorder potential $V_{dis}(x)$ [13]

$$\hat{H} = \left[-\frac{\hbar^2}{2m} \frac{d^2}{dx^2} + V_0(x) + V_{dis}(x) \right], \quad (5.53)$$

where the harmonic potential $V_0(x)$ is given as before by

$$V_0(x) = \frac{1}{2}m\omega^2x^2. \quad (5.54)$$

The disorder potential is also known as the Gaussian impurity model [84] and consists of N_D Gaussians, that are spread evenly over the domain $[-x_D, x_D]$,

$$V_{\text{dis}}(x) = V_D f(x) = V_D \sum_{i=1}^{N_D} A_i \exp \left[\frac{-4(x - x_i)^2}{\sigma_D^2} \right], \quad (5.55)$$

where A_i are random numbers that fulfill $\langle A_i \rangle = 0$ and $\langle A_i^2 \rangle = 1$. The ensemble $\{A_i, i = 1, \dots, N_D\}$ is generated by using the intrinsic Fortran subroutine *random_number* and transforming the obtained unitary distribution by the Box-Muller transformation to a normal distribution. The width of the Gaussians is determined by σ_D and V_D governs the total strength of the disorder.

Three parametrizations of the potential (tab. 5.3) were chosen and are presented in fig. 5.4.

Table 5.3: Parameters of the disorder potentials (a), (b) and (c).

	V_D/ϵ_0	σ_D/l_0	N_D	x_D/l_0	$\langle A_i \rangle$	$\langle A_i^2 \rangle$
(a)	1.00	1.00	300	100.53	0.01	0.93
(b)	1.00	1.00	400	100.53	0.01	1.10
(c)	1.00	1.00	500	100.53	-0.04	0.95

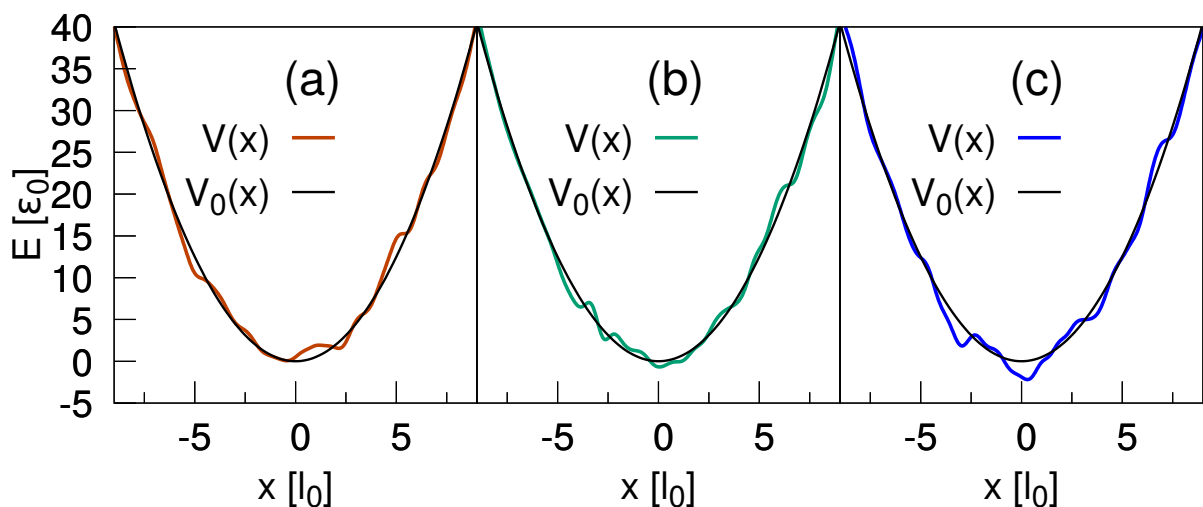


Figure 5.4: Different realizations of the disorder potential. The harmonic potential $V_0(x)$ is shown as well.

Before we consider the wave packet motion, the energy spectra are analyzed, since the spectral properties determine the dynamics. Imaginary time propagation is applied (sec. 4.3) on the domain $[-50 l_0, 50 l_0]$ with 4096 grid points and time step $dt = 0.023 T$. In the upper panel of fig. 5.5 the first 120 eigenenergies E_n are shown for all three potentials in terms of the difference

$$\delta E_n = E_n^{HO} - E_n, \quad (5.56)$$

where E_n^{HO} are the harmonic oscillator energies. In all cases, the eigenenergies of the disorder potential are very close to the harmonic ones and the deviations are of order $10^{-1}\epsilon_0$. However, the deviations for low energy eigenstates are higher for parametrization (c) than for (a) and (b). Nevertheless, neighboring energy levels of all parametrizations have a similar deviation from the harmonic ones. For increasing n the deviations are smaller but do not approach zero. However, the frequency of minima and maxima decreases as n increases. This is since the disorder positions are placed evenly with spacing d , but the width σ_n of the harmonic eigenfunctions increases only with $\sim \sqrt{n}$. Thus for larger n the number of disorder positions is $\sigma_n/d \sim \sqrt{n}/d$ and increases only slowly with n . Hence, for large n two consecutive eigenfunctions sample nearly the same disorder positions. As a result of the decreasing frequency the energy spacing between two consecutive energy levels approaches the harmonic spacing for high n , as can be seen in the lower panel of fig. 5.5. There, the difference

$$\Delta E_n - \epsilon_0 = E_{n+1} - E_n - \epsilon_0 \quad (5.57)$$

is shown. Here, the parametrizations exhibit similar behavior. In what follows we will only consider dynamics in potential (b), since the qualitative results of the dynamics in all potentials are similar and are only distinct quantitatively.

For the quantum mechanical propagation, we choose a squeezed state as initial wave function:

$$\psi(x, 0) = [2\beta/\pi]^{1/4} \exp(-\beta(x - x_0)^2), \quad (5.58)$$

with $x_0 = 5 l_0 = 5$ a.u. and $\beta = 5$ a.u.. The position- and momentum-space probability densities are

$$\rho(x, t) = |\psi(x, t)|^2 \quad \text{and} \quad \rho(p, t) = |\psi(p, t)|^2, \quad (5.59)$$

where $\psi(p, t)$ is obtained from $\psi(x, t)$ by a Fourier transformation. The wave packet is propagated on a grid using N_{grid} grid points in the domain $[-x_{max}, x_{max}]$ (tab. 5.4) using the split-operator method (sec. 4.2) with time step dt . As in the harmonic case, ω and

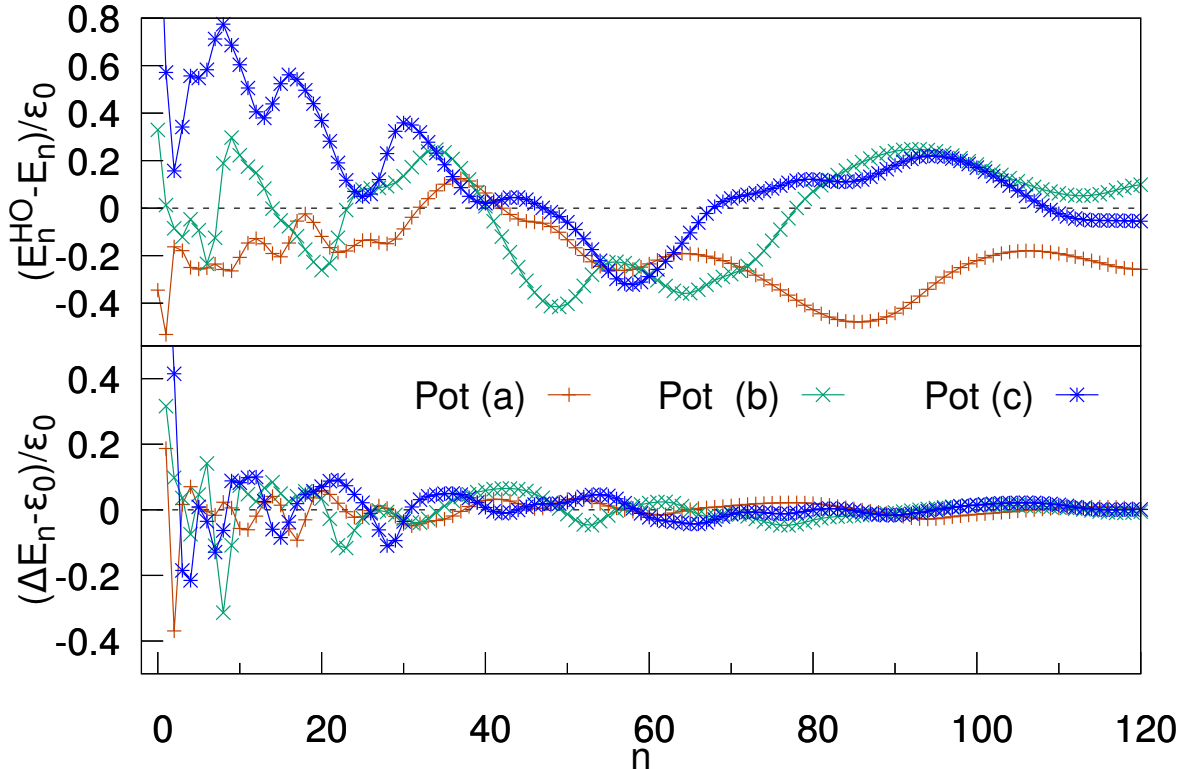


Figure 5.5: Upper panel: Energy eigenvalues derived from potentials (a), (b) and (c), respectively, plotted as deviations from the eigenvalues of the harmonic oscillator. Lower panel: Spacing between the energy eigenvalues as deviations from to the harmonic spacing. In both panels the first value obtained for potential (c) was suppressed for clarity.

m are set to 1 a.u.

Table 5.4: Parameters of the numerical simulation.

Pot	ω	m	dt	x_{max}	N_{grid}	x_0	β	N_{cl}
(b)	1 a.u.	1 a.u.	2.5 a.u.	20 a.u.	4096	5 a.u..	5 a.u.	8192

To simulate the propagation classically, we generate an ensemble of trajectories with weighting sampled from the initial quantum Wigner function. Since we are considering a Gaussian initial state, the distribution is a product of the initial position density $\rho(x_s, 0)$ and momentum density $\rho(p_s, 0)$,

$$W(x_s, p_s) = \rho(x_s, 0)\rho(p_s, 0). \quad (5.60)$$

The density is sampled by N_{cl} grid points in momentum and position, respectively. To limit the computational effort, only trajectories are considered for which position and momentum density take values larger than 1% of their respective maximum. This results

in 111 sample points in position and 433 in momentum space, which totals to 48063 propagated trajectories. The trajectories are obtained by solving the canonical equations of motion [85]

$$\frac{\partial H}{\partial p_t} = \frac{dx_t}{dt}, \quad \frac{\partial H}{\partial x_t} = -\frac{dp_t}{dt}, \quad (5.61)$$

using the velocity-Verlet algorithm (sec. 4.4). The time-dependent classical phase-space density is then the weighted sum over all orbits (x_t, p_t) :

$$\rho^{cl}(x, p, t) = \int dx_s \int dp_s W(x_s, p_s) \delta(x - x_t(x_s, p_s)) \delta(p - p_t(x_s, p_s)). \quad (5.62)$$

Numerically, $\rho^{cl}(x, p, t)$ is approximated by calculating the density at a grid point by summing the weights of all trajectories, for which this grid point is the closest. This is done for all grid points. From the classical phase-space density, the classical position- and momentum-densities are obtained as

$$\rho^{cl}(x, t) = \int dp \rho^{cl}(x, p, t) \quad \text{and} \quad \rho^{cl}(p, t) = \int dx \rho^{cl}(x, p, t). \quad (5.63)$$

From the quantum and classical densities, time-dependent entropies are calculated in position and momentum space:

$$S_x^{qm/cl}(t) = - \int dx \rho^{qm/cl}(x) \ln [\rho^{qm/cl}(x)], \quad (5.64)$$

$$S_p^{qm/cl}(t) = - \int dp \rho^{qm/cl}(p) \ln [\rho^{qm/cl}(p)], \quad (5.65)$$

as well as their sum:

$$S_{sum}^{qm/cl}(t) = S_x^{qm/cl} + S_p^{qm/cl}(t). \quad (5.66)$$

In what follows, the superscript qm is dropped for simplicity, so that i.e. $S_x(t), S_p(t)$ and $S(t)$ label the quantum entropies.

To analyze the wave packet, the initial wave function is decomposed into energy eigenstates $\varphi_n(x)$,

$$c_n = \int dx \varphi_n^*(x) \psi(x, 0). \quad (5.67)$$

The such obtained populations are shown in fig. 5.6. It is seen that the distribution is

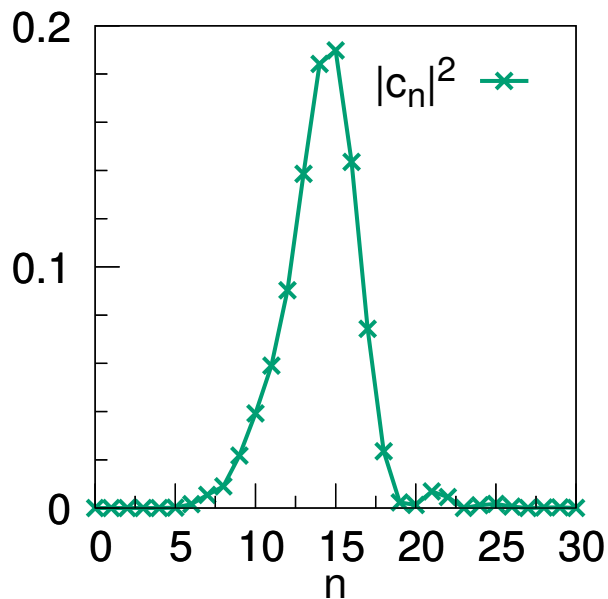


Figure 5.6: Decomposition of the initial wave function in energy eigenstates of potential (b): Shown is the occupation of different states.

sharply localized around the quantum numbers $n = 14, 15$. Note that the c_n are real since $\varphi_n(x)$ and $\psi(x, 0)$ are real valued.

5.2.2 Short-time behavior

The dynamics are shown in fig. 5.7 for times up to $10 T$. The upper panel contains the quantum mechanical density. It is seen that, up to $4 T$, the dynamics resemble that of a squeezed state in an harmonic potential where the density refocuses at the classical turning points at times that are multiples of $T/2$ and nearly no interference structures are visible. For times between $4 T - 8 T$, nodal patterns arise due to the dispersion of the wave packet.

For times $t > 8 T$, the density dephases, which is manifested by additional density fragments at the turning points. The lower panel contains the classical density. Here, the dynamics are, in particular for early times, very similar to the quantum case. For times $t > 4 T$, differences arise since the classical dynamics cannot replicate the nodal structure. The width of the classical density increases more than in the quantum case as time evolves. At the turning points, the densities start to differ as well. There, the trajectories have low kinetic energy and are very sensitive to the exact form of the disorder potential, while the quantum density is, due to tunneling, less influenced by the disorder.

In fig. 5.8, the entropies and the uncertainty product are shown up to $20 T$. For times $t < 4 T$, the quantum entropies exhibit oscillations quantitatively very close to those of the

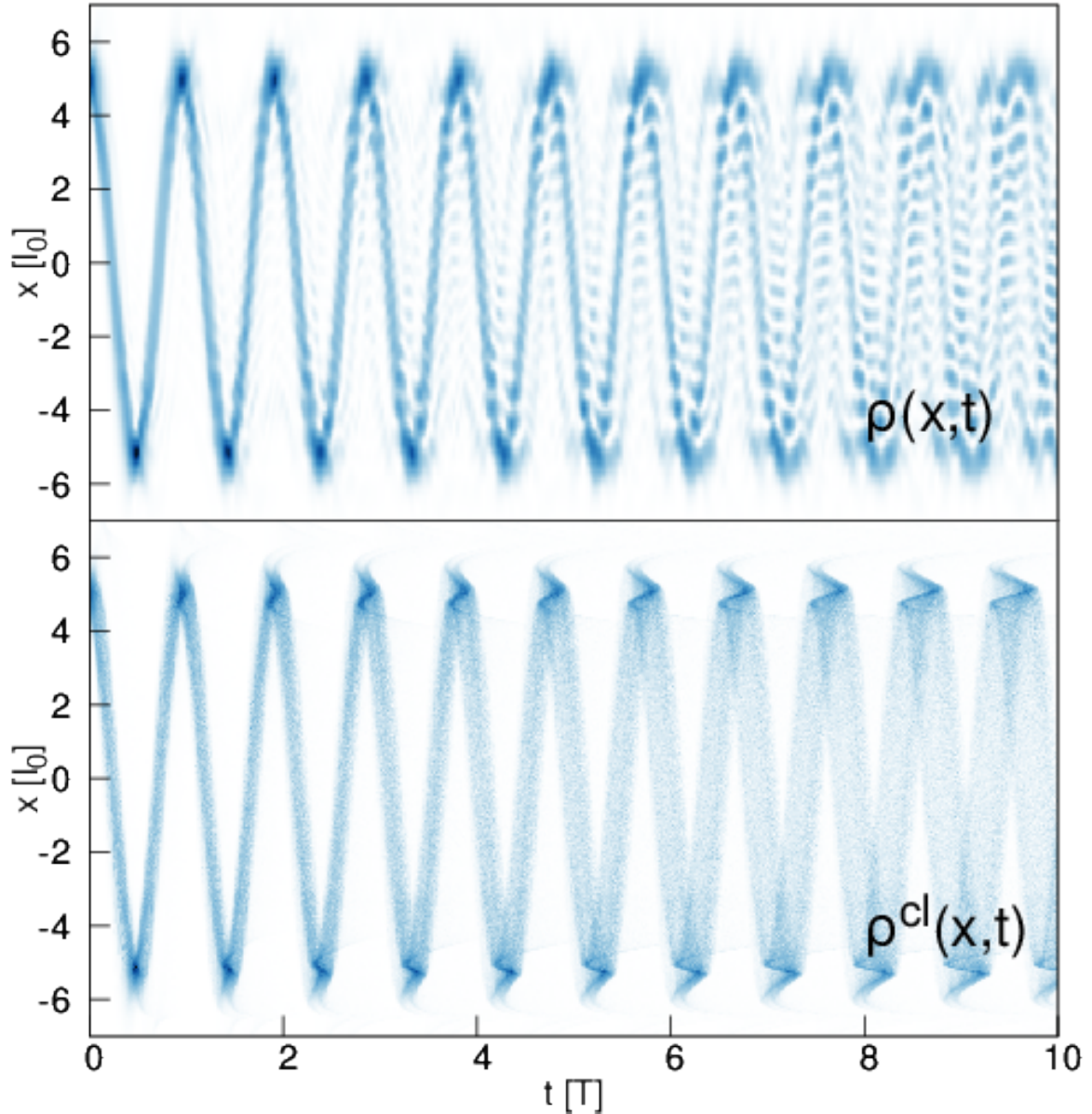


Figure 5.7: Quantum mechanical and classical position density for early times $0-10 T$.

undisturbed harmonic oscillator, see fig. 5.1. Then, the entropies increase until $10 T$ while oscillating and approach a value of $S_x(t) \approx S_p(t) \approx 2$ and $S_{sum}(t) \approx 4$. After that, they show irregular oscillations around these values but do not increase further. The entropies $S_x^{cl}(t)$ and $S_p^{cl}(t)$ agree very well with the quantum counterparts for times up to $10 T$ with only small deviations in the minima, the latter being less present in the quantum case. A possible reason for this behavior is the existence of additional density fragments in the quantum case. The deviations in $S_x(t)$ and $S_p(t)$ add up in the entropy sum so that between $7 T-10 T$ the quantum-classical differences are significant in $S_{sum}(t)$. This trend continues for times later than $10 T$. While the quantum entropies only increase until $10 T$, the classical entropies grow to values larger than their quantum counterpart

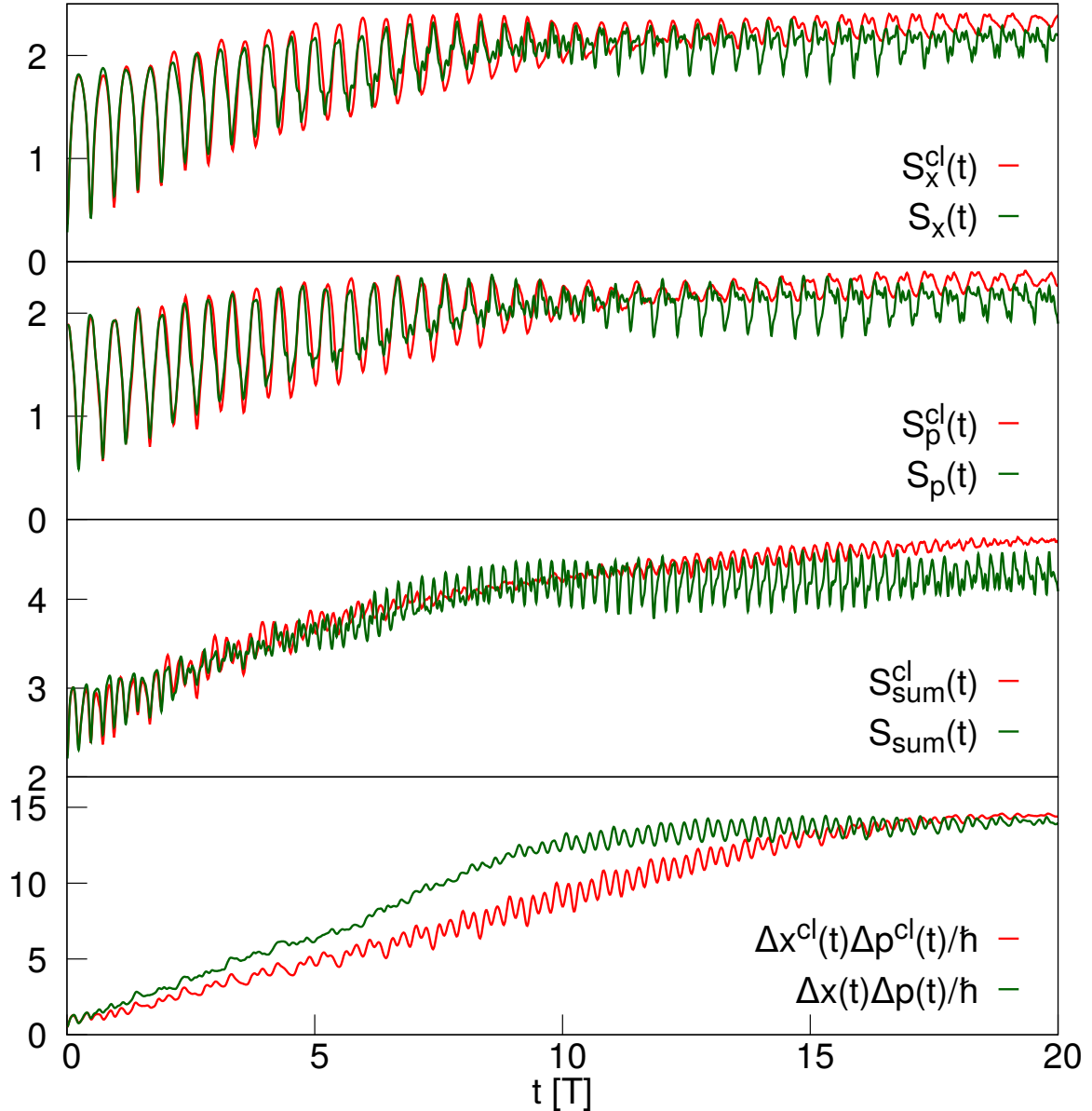


Figure 5.8: Quantum mechanical and classical entropies and uncertainty product for times 0-20 T .

until $15T$. Thus, the dispersion mechanics work slower within the classical framework. Additionally, the oscillation amplitude of the classical entropies decrease more than in the quantum curves.

In the lowest panel of fig. 5.8, the uncertainty product $\Delta x(t)\Delta p(t)$ is shown. Here, the classical and the quantum propagation only yield the same results up to $\approx 1T$. Afterwards they increase linearly to $\approx 14\hbar$ which is reached around $10T$ in the quantum and at $15T$ in the classical case. This is also seen in the entropy sum, which is plausible since for the Gaussian case they are connected by eq. (5.19). That this equation does not hold exactly can be taken from the fact that even though, at times between $15T - 20T$, the

uncertainty behaves similarly in the quantum and classical case, the entropy sums are different. Therefore, the entropy sum measures features of the dynamics that are not accounted for by the uncertainty product and width of the density.

5.2.3 Long-time behavior

We now discuss the dynamics at long times. The entropies and the uncertainty product are shown for the time interval $80 T$ - $130 T$ in fig. 5.9. Up to $115 T$, the quantum entropies oscillate irregularly about the values $S_x(t) \approx S_p(t) \approx 2$ and $S_{sum}(t) \approx 4$, while the classical values are slightly larger and exhibit much smaller amplitudes in the oscillations. The loss of information due to the disorder is therefore larger in the classical case. This could be due to interference patterns being present in the wave functions. These structures are visible in the top and middle panel of fig. 5.10, where densities are shown for a selected time of $t = 103.73 T$. There, the density gathers at the turning points so that the overall shape appears similar, and both resemble the density of the classical HO in the microcanonical ensemble. However, while the quantum dynamics yield distinct minima and maxima due to the interference patterns, the classical density follows $\rho^{MC}(x)$ much closer. Comparing the entropy sum of both densities to that of the classical HO with the same total energy ($\bar{E} = 15.82 \epsilon_0$) yields $S_{sum}^{MC} = 4.35$, which agrees well with S_{sum} in this time interval, but it is significantly lower than S_{sum}^{cl} . It is likely that this stems from the fact that since the classical density falls off smoothly for positions beyond the classical turning point, which restricts the density and decreases localization. The quantum density behaves similarly, but due to the interference structure the localization is increased, so that these effects may cancel each other here.

For times between $115 T$ and $125 T$, the oscillation amplitudes of the quantum entropies $S_x(t)$ and $S_p(t)$ increase and become more regular. This results in an overall minimum in the entropy sum, having a value comparable what is found at $t > 10 T$. The information in the quantum wave packet is therefore partially recovered. On the other hand the classical entropies show no change of behavior.

Similar dynamics are seen in the uncertainty product: The classical values remain constant at $\approx 14 T$, while the quantum values show slight deviations for times before $115 T$ and a distinct minimum between $115 T$ and $125 T$. Thus the information recovery is connected to a localization of the wave packet.

The quantum and classical density in the interval $100 T$ to $130 T$ are compared in fig. 5.11. There, it is obvious that the quantum density becomes more localized in the times

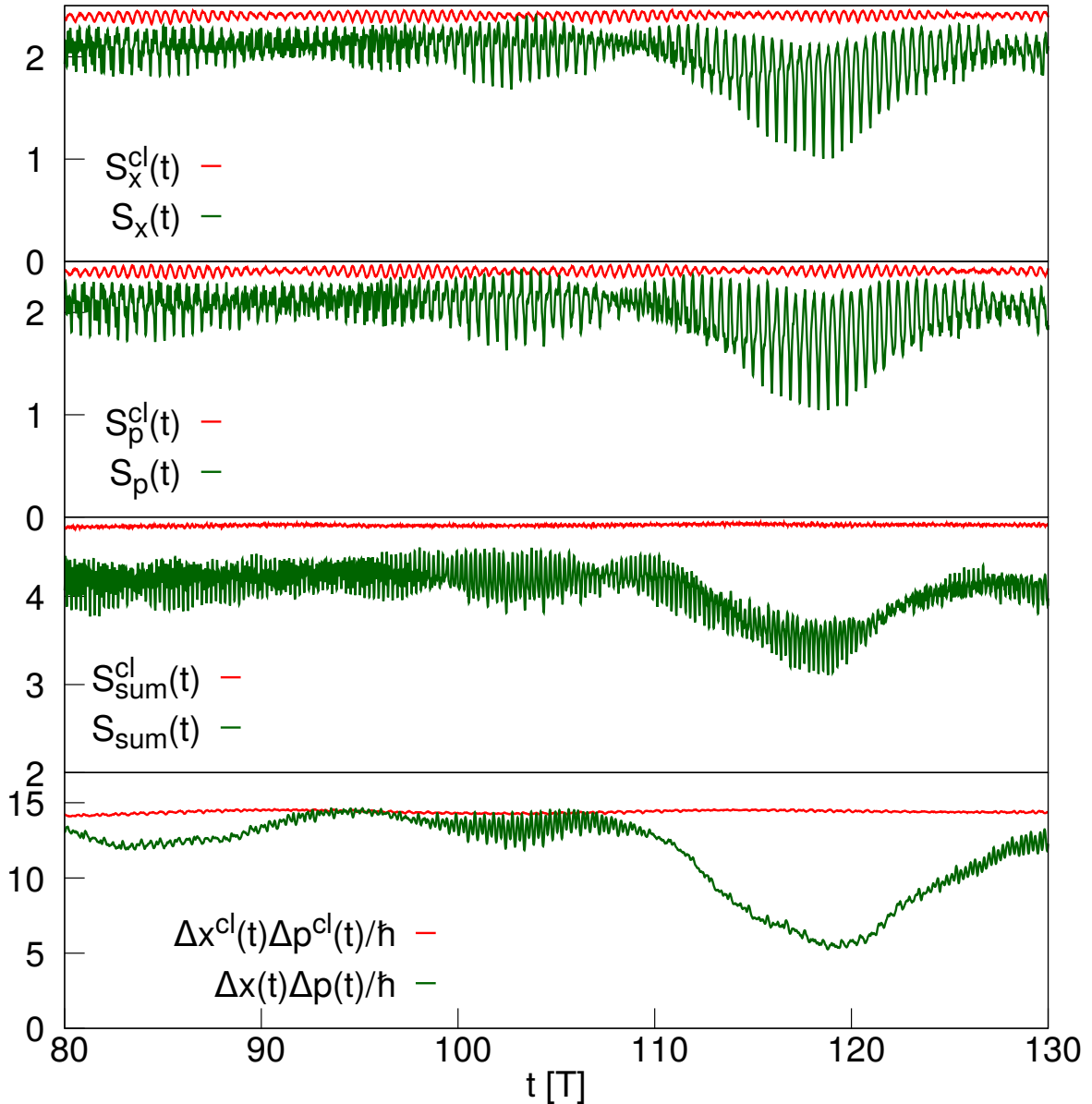


Figure 5.9: Quantum mechanical (green) and classical entropies and uncertainties (red) for $t = 100T - 130T$. The minima at $118T$, found in the quantum mechanical quantities is interpreted as a vibrational revival.

$115T - 120T$ than the classical density, and its shape resembles the initial dynamics for a short time, see fig. 5.7. We thus find an approximate revival of the initial wave function. This is also documented in the bottom panel of fig. 5.10. There, the initial density (red) is compared to the quantum density at the approximate revival time. It can be seen that the density resembles a Gaussian with a maximum of 80% if compared to the height of the maximum of the initial density. Also, these densities possess a similar width and are centered at the same position. At smaller distances, small fluctuations occur due to the not-perfect nature of the revival.

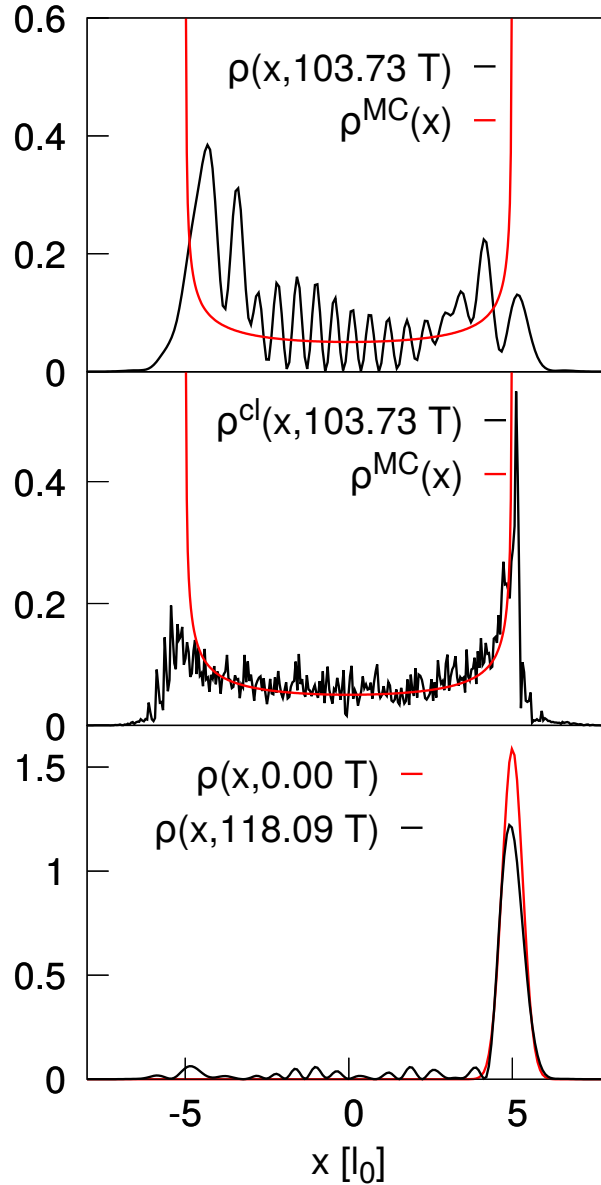


Figure 5.10: Quantum and classical density for different times. In the top and middle panel the microcanonical density eq. (5.43) is shown as well. In the bottom panel the initial density is compared to the density at the approximate revival time $t = 118T$.

A revival occurs since we are considering a pure state in an isolated quantum system. There, the time evolution of the state written in the basis of energy eigenstates $\varphi_n(x)$ with energies E_n is:

$$\psi(x, t) = \sum_n c_n e^{-iE_n t} \varphi_n(x). \quad (5.68)$$

The coefficients c_n remain constant and the dynamics is determined by the phases of the

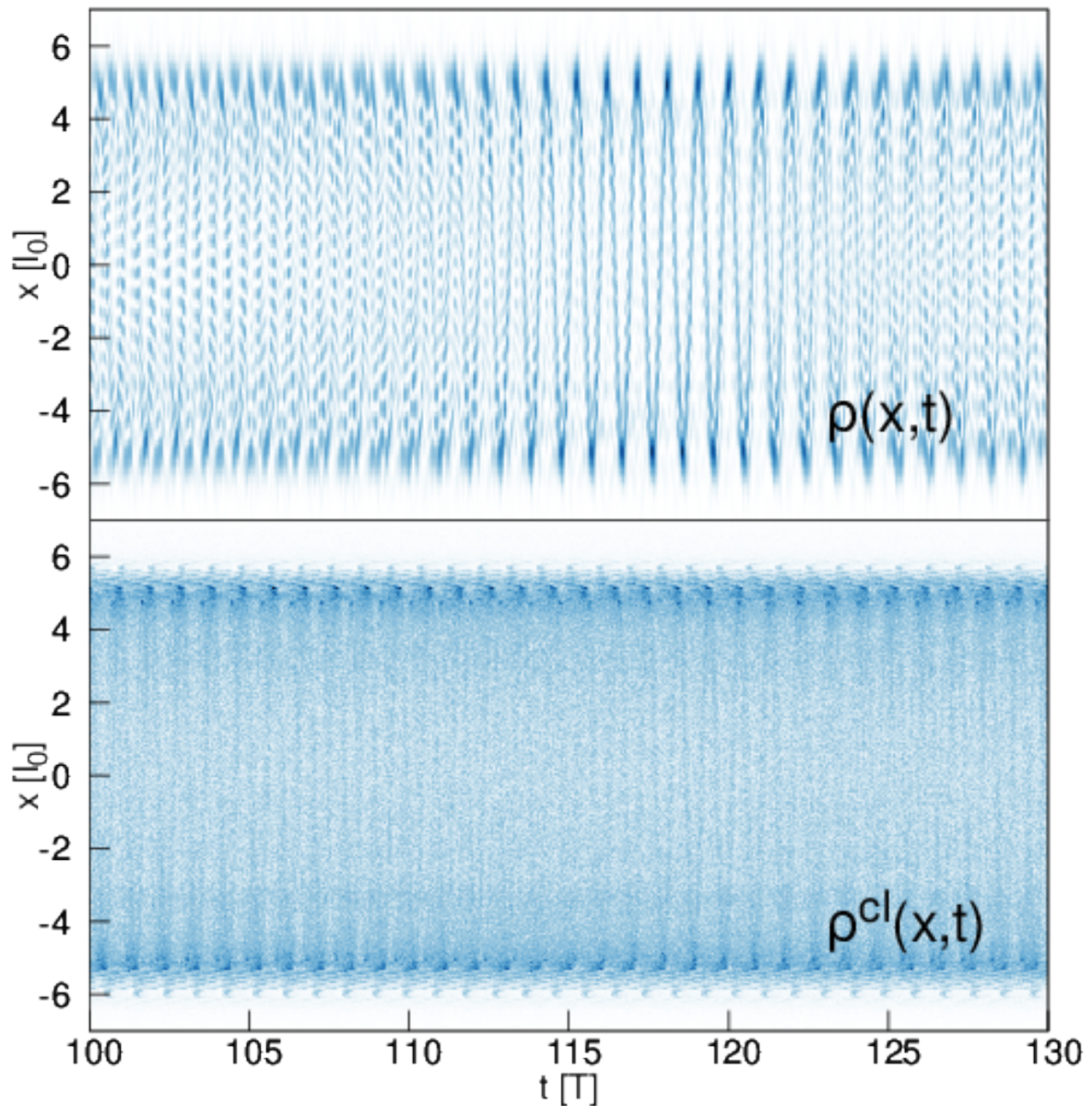


Figure 5.11: Quantum (top) and classical density (bottom) for $t = 100T - 130T$. The approximate revival is at $\approx 118T$.

eigenfunctions which built the wave packet. The dynamics of the quantum mechanical probability density is then

$$\rho(x, t) = |\psi(x, t)|^2 = \sum_{n,m} c_n c_m^* e^{-i(E_n - E_m)t} \varphi_n(x) \varphi_m^*(x), \quad (5.69)$$

and the dynamics of the density is determined by differences of the eigenenergies $\Delta E_{nm} = E_n - E_m$. A perfect revival of the density to the initial configuration occurs at times when

$$e^{-i\Delta E_{nm}(t+T_{rev})} = e^{-i\Delta E_{nm}t} \quad \forall n, m. \quad (5.70)$$

with the revival time T_{rev} .

In the sum in eq. (5.69) n and m occur pairwise so that the condition for a revival to take place can be written as

$$\cos(\omega_{mn}t) = \cos(\omega_{mn}(t + T_{rev})) \quad \forall n, m., \quad (5.71)$$

where we have replaced the energy difference by the frequency $\omega_{mn} = (E_m - E_n)$. In the harmonic oscillator the revival time equals one period due to the homogeneous eigenenergy spacing. In the considered disordered potential the situation is more complicated because of the random variation of each energy eigenvalue. Accordingly, not perfect revivals are found, where this relation holds approximately.

To arrive at an understanding of the revival patterns in the considered system, we assume that energy differences of neighboring eigenstates contribute. A revival is then determined by terms of the form

$$\sim \frac{1}{2} \text{Re}(c_n^* c_m) \cos(\omega_{mn}t), \quad (5.72)$$

where $n = m + 1$. If $\text{Re}(c_n^* c_m)$ of two of these terms are approximately equal, the following theorem can be used:

$$\cos(\omega_a t) + \cos(\omega_b t) = \cos(\omega_+ t) \cos(\omega_- t), \quad \omega_{\pm} = \frac{\omega_a \pm \omega_b}{2}. \quad (5.73)$$

This introduces two new time scales as

$$T_{\pm} = \frac{4\pi}{|\omega_{mn} \pm \omega_{op}|} = \frac{2\epsilon_0}{|\Delta E_{mn} \pm \Delta E_{op}|} T, \quad (5.74)$$

where $n = m + 1$ and $p = o + 1$, and we used the identity $2\pi\hbar = \epsilon_0 T$ to write the expression in terms of T . In the considered system the energy differences are similar $\Delta E_{mn} \approx \Delta E_{op}$ so that $T_+ \ll T_-$. In order to understand the dynamics for long times the small fluctuations with period T_+ are neglected, which are typically of order $T_+ \sim T$. But before doing so, we need to reconsider equation (5.73). There, we see that at $t + T_-/2 + nT_-$, $n = 1, 2, 3, \dots$ the cosine including ω_- assumes the negative value of its starting value. Since $T_+ \ll T_-$, the cosine $\cos(\omega_-(t + T_-/2 + nT_-)) \approx \cos(\omega_-(t + T_-/2 + nT_- \pm T_+))$. The cosine including ω_+ is equal to (-1) at least once in the time interval $t + T_-/2 + nT_- - T_+$ to $t + T_-/2 + nT_- + T_+$, so that the negative sign of the first cosine gets canceled out. Thus, the initial conditions are recovered approximately. This means that the effective time scale $T_4 = T_-/2$ needs

to be considered:

$$T_4 = \frac{\epsilon_0}{|\Delta E_{mn} - \Delta E_{op}|} T. \quad (5.75)$$

The index of T_4 refers to the property that four eigenstates (m, n, o, p) contribute to the time scale.

Table 5.5: Energy eigenvalues and expansion coefficients of the states with the largest expansion coefficients c_n in potential (b) using the initial wave packet (5.58).

n	E_n/ϵ_0	c_n
13	13.41	0.37
14	14.50	0.43
15	15.55	0.44
16	16.57	0.38

In fig. 5.6, the decomposition of the initial wave function (5.58) is shown. We find that the states with the quantum numbers 13-16 contribute most to the wave packet. The energies of these states are shown in tab. 5.5, and the energy differences ΔE_{nm} , $n = m + 1$ are

$$\Delta E_{13,14} = 1.08 \epsilon_0, \quad (5.76)$$

$$\Delta E_{15,16} = 1.02 \epsilon_0. \quad (5.77)$$

Since $c_{13}c_{14} \approx c_{15}c_{16}$ (see tab. 5.5), we can calculate T_{\pm} according to eq. (5.74) to obtain $T_- = 33.69 T$ and $T_+ = 0.95 T$. The time scale T_4 is, using eq. (5.75),

$$T_4 = 16.85 T. \quad (5.78)$$

If only the four eigenstates from tab. 5.5 contribute to the wave packet, the revival is exact, and it would occur a revival at integer multiples of T_4 . However, since further states are contributing, the revivals are only approximate. Nevertheless, observed minima in the entropy sum in fig. 5.9 agree very well with the result. The minimum is at $\approx 118 T$, which is indeed an integer multiple of T_4 : $118T/T_4 = 7.00$.

To validate this for more than one approximate revival, we calculate the entropy sum of the wave packet for very long times $0 T$ - $10000 T$. The result is shown in the top panel of fig. 5.12. There, seemingly random minima occur, indicating the refocusing of the wave packet. To connect the minima to the time scale T_4 , the data points of the entropy sum for $t=50 T$ - $10000 T$ are plotted versus the modulo $\text{mod}(t, T_4)$ scaled by T_4 . The values $< 50 T$ were suppressed to exclude the short time dynamics. Considering maximal values

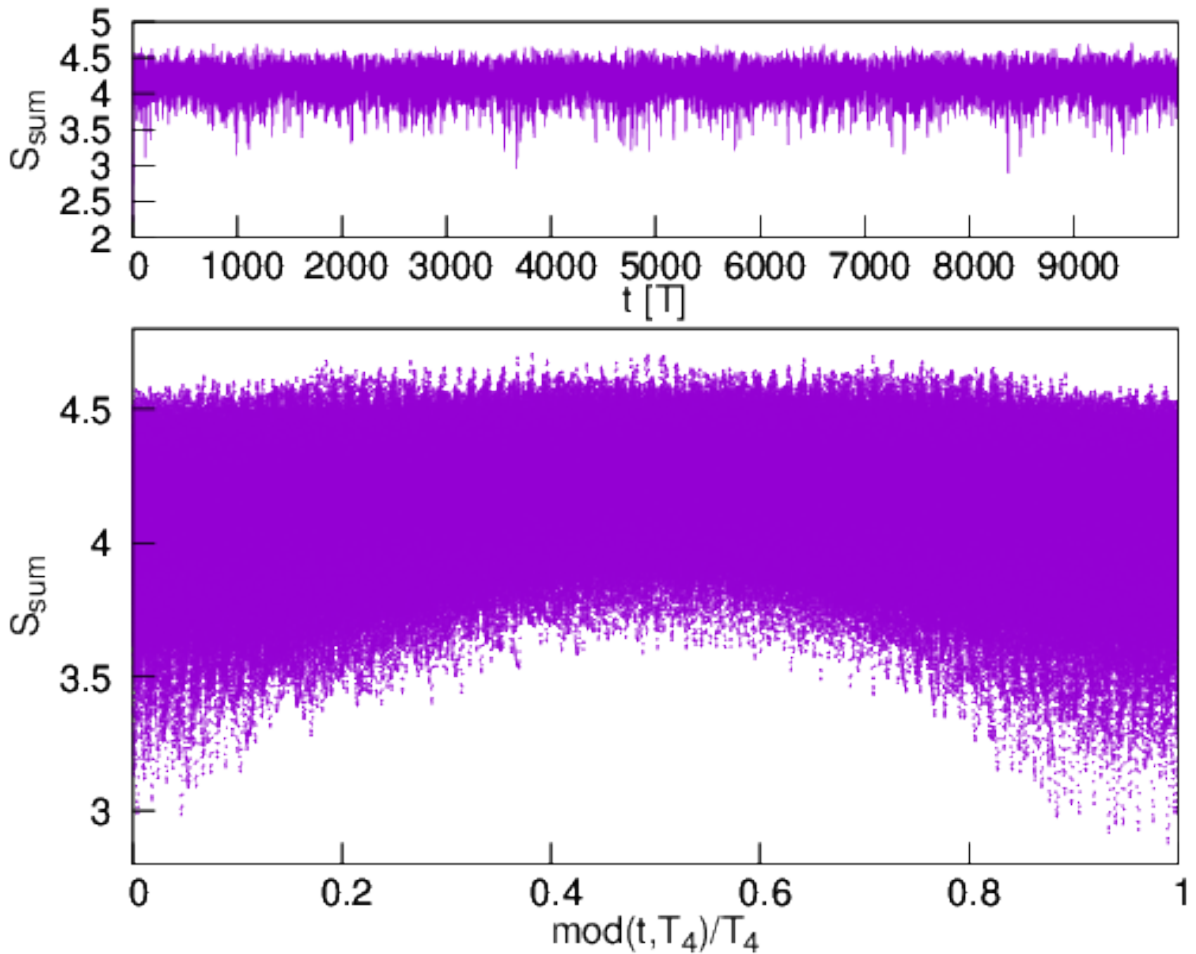


Figure 5.12: Top panel: Entropy sum in potential (b) with the initial conditions from tab. 5.4 for $t=0$ T -10000 T . Bottom panel: Entropy sum plotted against the modulo of time. The basis of the modulo is the time scale T_4 .

of the entropy sum, this representation does not show any dependencies. However, the lowest values are bound from below by an inverting parabola, where the center of the parabola is at the middle. Thus, the closer the time t is to a integer multiple of T_4 , the lower is the entropy sum, which is associated with localization and thus an approximate revival. It is important to note that time being a multiple of T_4 is only a necessary but not sufficient condition for a revival to occur.

5.3 Energy dependence of entropy for long times

As we have seen in sec. 5.2.3, for long times the entropy sum approaches a plateau value, where it fluctuates around an average number. Since this behavior is associated with reaching an equilibrium state, in [13] this process is referred to as "thermalization". However, it is important to stress, that the system is isolated, evolves with a unitary time

propagation and revivals occur inevitably. If such systems can thermalize, is to some point subjective and depends on the requirements one proposes for an isolated system to be "thermalized". There is an ongoing debate on this topic, see, e.g. [14, 86–89].

Nevertheless, depending on the structure of the energy eigenvalues, the time to reach a revival may be arbitrarily long, and hence the entropy of the system may oscillate around the plateau value for most times. It is therefore interesting to examine this plateau value more closely. Since this feature occurs in the classical dynamics as well, we compare both in the following section.

To simplify the model, we restrict our analysis to initial coherent states in the harmonic oscillator, since their symmetry in Wigner space and phase-space allows us to treat them analytically. The initial state in classical phase-space/Wigner space and $\hbar = 1$ is

$$W(x, p, 0) = \rho^{cl}(x, p, 0) = \frac{1}{\pi} \exp\left(-\frac{1}{a}(p - p_0)^2 - a(x - x_0)^2\right). \quad (5.79)$$

By choosing different values for the initial deflection x_0 , situations of different total energies are generated. Additionally, we assume that the disorder potential is small compared to the harmonic potential, meaning that the quantum eigenfunction and energy eigenvalues, as well as the classical trajectories deviate only weakly from the harmonic ones.

5.3.1 Dephased densities

At first, let us consider what happens for long times in classical phase-space. As noted in the above, we start with an initial classical phase-space density sampled from the Gaussian wave function, which is explicitly

$$\rho^{cl}(\tilde{x}, \tilde{p}, 0) = \tilde{N} \exp\left(-\frac{\text{Re}(a_t)}{|a_t|^2 \hbar^2} (\tilde{p} - \tilde{p}_0)^2 - 2\text{Re}(a_t) (\tilde{x} - \tilde{x}_0)^2\right). \quad (5.80)$$

We simplify the problem by choosing a coherent state with $a_t = a_0 = \frac{m\omega}{\hbar}$ and switching to coordinates in which the trajectories of the harmonic oscillator in the phase-space are cyclic

$$\tilde{x} = (\sqrt{2}/\omega m)x, \quad \tilde{p} = \sqrt{2}mp, \quad (5.81)$$

so that the root of the energy may be interpreted as the radius of a trajectory with energy $E = x^2 + p^2$. Specifying initial conditions for $E_0 = x_0^2 + p_0^2$ by choosing x_0 and p_0 determines the center of the two-dimensional Gaussian density. Due to symmetry, the density can always be transformed back to the case $E_0 = x_0^2, p_0 = 0$ by rotation in

phase-space without loss of generality. Using this initial condition the classical density is, in atomic units,

$$\rho^{cl}(x, p, 0) = N \exp\left(-\frac{2}{\epsilon_0} p^2 - \frac{2}{\epsilon_0} (x - x_0)^2\right), \quad (5.82)$$

where ϵ_0 is an energy scale that is associated with the quantum energy scale $\epsilon_0 = \omega \hbar$.

In the case of a purely harmonic potential $V_D = 0$, this density rotates with constant angular velocity and radius around the center of the phase-space. This is, since each sampled point of the density behaves like a classical harmonic oscillator and follows a trajectory, that itself has constant angular velocity and radius and, in particular, all trajectories have the same period T to circle the origin. Integrating out momentum or position, respectively, yields position and momentum densities that are equivalent to that of propagating the density quantum mechanically.

Let us analyze what happens when a finite disorder potential is considered at the level of a single trajectory: Now, the previously cyclic trajectory is deformed to an irregular path. However, when the disorder is small, the deformed path is still close to the undisturbed one. Also, since the energy of each trajectory is conserved, the trajectory is still a closed path but with slightly different period as in the undisturbed case. Groups of trajectories with the same energy E therefore follow the same path in phase-space. This means that the energy distribution of the system does not change. The energy distribution can be calculated by assuming that the disturbed paths are approximately cyclic, which means that we need to calculate the path integral over the initial density using a circle with radius \sqrt{E} , $C(E)$. This reads

$$\rho(E) = \int_{C(E)} \rho^{cl}(x, p, 0) ds = \int_0^{2\pi} d\phi \sqrt{E} \rho^{cl}(x, p, 0). \quad (5.83)$$

Using the parametrization $x = \sqrt{E} \cos(\phi)$ and $p = \sqrt{E} \sin(\phi)$, the integral is calculated to

$$\begin{aligned} \rho(E) &= N \sqrt{E} \exp\left(-\frac{2}{\epsilon_0} (E + E_0)\right) \int_0^{2\pi} d\phi \exp\left(4 \frac{\sqrt{E E_0}}{\epsilon_0} \cos(\phi)\right) \\ &= 2\pi N \sqrt{E} \exp\left(-\frac{2}{\epsilon_0} (E + E_0)\right) I_0\left(4 \frac{\sqrt{E E_0}}{\epsilon_0}\right), \end{aligned} \quad (5.84)$$

where $I_0(x)$ is the modified Bessel function. Now we consider groups of trajectories, moving on paths next to each other. Since their period differ, they dephase with time. But because neighboring paths are arbitrarily close, this dephasing is equal to spreading the density on a path $\rho(E)$ evenly along the path itself.

Thus, the density at a point (x, p) is the energy distribution divided by the length of the trajectory with energy E :

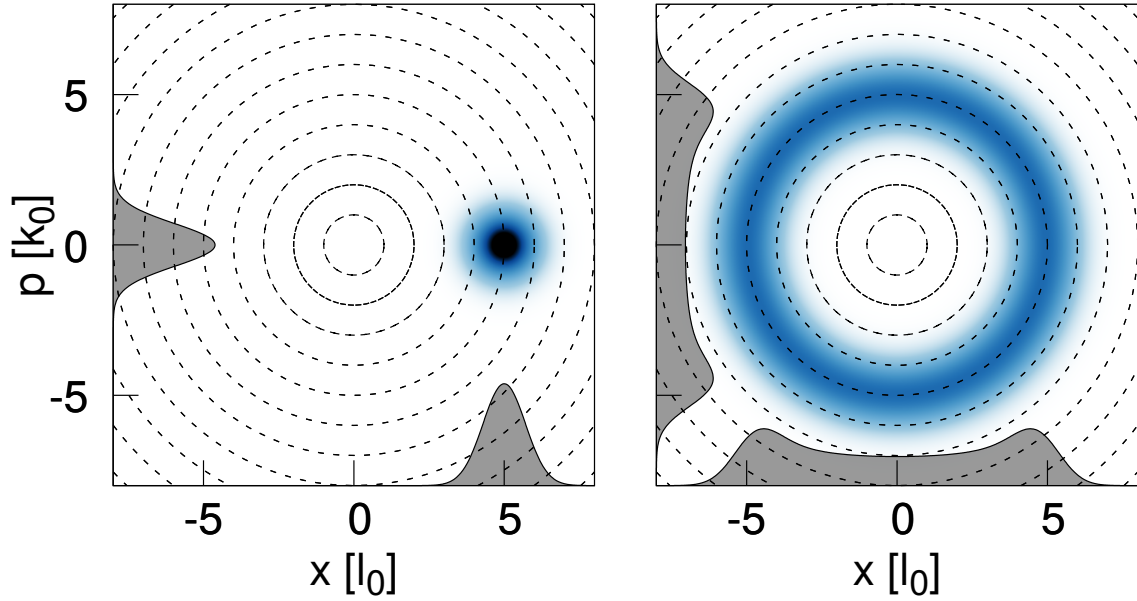


Figure 5.13: Classical dephasing in phase-space. Left: Initial density, sampled from the quantum coherent state. The initial conditions are $x_0 = 5l_0$. Right: Dephased density. On the axes the respective position/momentum density is shown. The dashed lines indicate lines of equal energy.

$$\rho^{cl,deph}(x, p) = \frac{\int_{C(E)} \rho^{cl}(x, p, 0) ds}{\int_{C(E)} ds}. \quad (5.85)$$

Note that this equation fulfills a similar role than the constant distribution of $|c_n|^2$ in the quantum dynamics, since it conserves the distribution of microstates, but in contrast to the quantum case, $\rho^{cl,deph}(E)$ is continuous. Plugging in the result of the integral in the numerator and using $\int_{C(E)} ds = 2\pi\sqrt{E}$, the asymptotic classical density reads

$$\rho^{cl,deph}(E) = N \exp\left(-\frac{2}{\epsilon_0}(E + E_0)\right) I_0\left(4\frac{\sqrt{EE_0}}{\epsilon_0}\right). \quad (5.86)$$

Note that this result is independent of the parametrization of x and p . Finally, we obtain,

$$\rho^{cl,deph}(x, p) = \frac{1}{\pi} \exp(-x^2 - p^2 - x_0^2) I_0(2\sqrt{x^2 + p^2} x_0), \quad (5.87)$$

where x and p are in terms of l_0 and k_0 , respectively, so that $E = \frac{1}{2}x^2 + \frac{1}{2}p^2$.

Let us now come back to the quantum dynamics. We compare the result eq. (5.87) with the quantum system under what is called "pure dephasing". This refers to the

thermalization behavior of a pure state in a non-isolated quantum system, without energy loss [12, 90]. Therefore, for the sake of argument, we consider the system to be non-isolated for the moment. Dephasing in this context means that off-diagonal elements in the energy representation vanish as time evolves and the density approaches

$$\rho^{deph}(t) = \sum_n |c_n|^2 |\varphi_n|^2 + \underbrace{\sum_{n>m} 2 \cos((E_n - E_m)t/\hbar) c_n c_m^* \varphi_n \varphi_m^*}_{\rightarrow 0}. \quad (5.88)$$

Let us look at the same situation in the Wigner transformation of the coherent state. The Wigner transform of $\phi(s, t)$ is

$$\begin{aligned} W(x, p, t) &= \frac{1}{2\pi\hbar} \int ds e^{ips/\hbar} \langle x - \frac{1}{2}s | \phi(t) \rangle \langle \phi(t) | x - \frac{1}{2}s \rangle \\ &= \sum_{n,m} e^{-i(E_n - E_m)/\hbar t} c_n c_m^* \frac{1}{2\pi\hbar} \int ds e^{ips/\hbar} \langle x - \frac{1}{2}s | \varphi_n \rangle \langle \varphi_m | x - \frac{1}{2}s \rangle, \end{aligned} \quad (5.89)$$

and using the same approximation as before we have

$$\begin{aligned} W(x, p, t) &= \sum_n |c_n|^2 \frac{1}{2\pi\hbar} \int ds e^{ips/\hbar} \langle x - \frac{1}{2}s | \varphi_n \rangle \langle \varphi_n | x - \frac{1}{2}s \rangle \\ &+ \sum_{n>m} 2 \cos((E_n - E_m)/\hbar t) c_n c_m^* \frac{1}{2\pi\hbar} \int ds e^{ips/\hbar} \langle x - \frac{1}{2}s | \varphi_n \rangle \langle \varphi_m | x - \frac{1}{2}s \rangle \\ &\approx \sum_n |c_n|^2 \frac{1}{2\pi\hbar} \int ds e^{ips/\hbar} \langle x - \frac{1}{2}s | \varphi_n \rangle \langle \varphi_n | x - \frac{1}{2}s \rangle. \end{aligned} \quad (5.90)$$

This procedure was illustrated for a Gaussian state in the harmonic oscillator in [12] and [90], but was not calculated analytically. The remaining term in the equation (5.90) is the Wigner transform of an harmonic eigenstate, which is known to be [46, 91, 92], in atomic units:

$$W_n(x, p) = \frac{(-1)^n}{\pi} \exp(-x^2 - y^2) L_n(2x^2 + y^2), \quad (5.91)$$

where L_n is the Laguerre polynomial given by

$$L_n(y) = \sum_{k=0}^n \binom{n}{k} \frac{(-1)^k}{k!} y^k. \quad (5.92)$$

Here, x and p are again given in terms of l_0 and k_0 , respectively. Note that the eigenstates in Wigner space are not positive semidefinite but have areas, where the function value might be negative. Thus, an interpretation as phase-space density is, in general, not

possible. Coherent states are the linear combination of eigenfunctions and the coefficients are well known. They are [91]:

$$c_n = e^{-x_0^2/4} \frac{(x_0/\sqrt{2})^n}{\sqrt{n!}}. \quad (5.93)$$

Together with eq. (5.90) this yields

$$\begin{aligned} W^{deph}(x, p) &= \sum_n |c_n|^2 \frac{(-1)^n}{\pi} \exp(-x^2 - p^2) L_n(2x^2 + 2p^2) \\ &= \sum_n \left| e^{-x_0^2/4} \frac{(x_0/\sqrt{2})^n}{\sqrt{n!}} \right|^2 \frac{(-1)^n}{\pi} \exp(-x^2 - p^2) L_n(2x^2 + 2p^2). \end{aligned} \quad (5.94)$$

By inserting the series expression of the Laguerre polynomial eq. (5.92), we have

$$W^{deph}(x, p) = \sum_n \sum_{k=0}^n \left| e^{-x_0^2/4} \frac{(x_0/\sqrt{2})^n}{\sqrt{n!}} \right|^2 \frac{(-1)^n}{\pi} e^{-x^2 - p^2} \binom{n}{k} \frac{(-1)^k}{k!} (2x^2 + 2p^2)^k. \quad (5.95)$$

The ordering of the sums can be changed by using the identity

$$\sum_n \sum_{k=0}^n f(n, k) \rightarrow \sum_{k=0}^{\infty} \sum_{n=k}^{\infty} f(n, k), \quad (5.96)$$

which leads to

$$\begin{aligned} W^{deph}(x, p) &= e^{-x^2 - p^2 - x_0^2/2} \sum_{k=0}^{\infty} \sum_{n=k}^{\infty} \frac{(x_0^2/2)^n}{n!} \frac{(-1)^n}{\pi} \binom{n}{k} \frac{(-1)^k}{k!} (2x^2 + 2p^2)^k \\ &\stackrel{n \rightarrow a+k}{=} e^{-x^2 - p^2 - x_0^2/2} \sum_{k=0}^{\infty} \sum_{a=0}^{\infty} \frac{(x_0^2/2)^{a+k}}{(a+k)!} \frac{(-1)^{a+k}}{\pi} \binom{n}{k} \frac{(-1)^k}{k!} (2x^2 + 2p^2)^k \\ &= \frac{1}{\pi} e^{-x^2 - p^2 - x_0^2/2} \sum_{k=0}^{\infty} \frac{(x_0/2)^{2k}}{k!k!} (2x^2 + 2p^2)^k \sum_{a=0}^{\infty} \frac{(x_0^2/2)^a}{a!} \\ &= \frac{1}{\pi} e^{-x^2 - p^2 - x_0^2} \sum_{k=0}^{\infty} \frac{x_0^{2k} (x^2 + p^2)^k}{k!^2} \\ &= \frac{1}{\pi} e^{-x^2 - p^2 - x_0^2} I_0(2\sqrt{x^2 + p^2} x_0), \end{aligned} \quad (5.97)$$

where we used power series expansion of the e -function and the modified Bessel function.

This is of the same form as the classical dephased phase-space density (eq. (5.87)),

$$\rho^{cl,deph}(x, p) = W^{deph}(x, p). \quad (5.98)$$

The difference is that, to obtain the quantum one, we had to assume the system is not isolated, while the classical system was considered isolated. The question arises, if a similar mechanism as the dephasing presented in eq. (5.88) could occur in the quantum isolated system. It is thinkable, that for long times and a large number of contributing states the second term in eq. (5.88) averages out due to multiple contributing cosine-terms of different sign. We address this in the next section.

From eq. (5.98), position and momentum densities are obtained by integration:

$$\rho^{deph}(x) = \int dp \rho^{cl,deph}(x, p) = \int dp W^{deph}(x, p), \quad (5.99)$$

$$\rho^{deph}(p) = \int dx \rho^{cl,deph}(x, p) = \int dx W^{deph}(x, p). \quad (5.100)$$

The latter functions are shown for an exemplary case on the axes of the right panel of fig. 5.13. The position density resembles the density shown in the middle panel of fig. 5.10 very closely. From the densities the entropy sum is derived as:

$$S_{sum}^{deph} = - \int dx \rho^{deph}(x) \ln \rho^{deph}(x) - \int dp \rho^{deph}(p) \ln \rho^{deph}(p). \quad (5.101)$$

5.3.2 Numerical simulation and high energy limit

The quantum and classical dynamics were simulated using the disorder potential (b) (fig. 5.4) for different coherent states. From these, the entropy sums $S_{sum}^{cl/qm}(t)$ was calculated. Since we are not interested in the early dynamics and concentrate on the plateau values occurring at longer times, the entropy sums were averaged for times $t_{start} \gg T_{th}$ to t_{end} , where T_{th} is the time for the system to reach the plateau value:

$$\bar{S}_{sum}^{qm/cl}(E) = \frac{\int_{t_{end}}^{t_{start}} S_{sum}^{cl/qm}(t) dt}{t_{end} - t_{start}}, \quad (5.102)$$

where E is the quantum energy expectation value. Also, the variance of the entropy

$$\sigma_S(E) = \sqrt{\bar{S}_{sum}^{qm/cl}(E)^2 - \frac{\int_{t_{end}}^{t_{start}} (S_{sum}^{cl/qm})^2(t) dt}{t_{end} - t_{start}}} \quad (5.103)$$

is computed.

As before, the parameters are $\omega = m = 1$ a.u.. In the quantum case the propagation was realized using a time step of $dt = 2.5$ a.u.. For energies $< 10 \epsilon_0$, a spatial grid in the interval $[-20l_0, 20l_0]$ with 4096 grid points was employed. For the averaging according to eq. (5.102), $t_{start} = 100 T$ and $t_{end} = 300 T$ were chosen. For energies larger than $10 \epsilon_0$, the domain was increased to $[-100l_0, 100l_0]$ with 8192 grid points. Due to the higher energy, T_{th} is longer and the entropy reaches a plateau at later times. Thus, the time interval was taken to be $t_{start} = 1800 T$ and $t_{end} = 2000 T$.

For the classical dynamics, the domain $[-100l_0, 100l_0]$ was sampled by 8192 points and trajectories were generated as described in sec. 5.2.1. Since the classical entropy shows much less oscillations and for computational efficiency, we use $t_{start} = 90 T$ and $t_{end} = 100 T$ for energies $< 8 \epsilon_0$ and $t_{start} = 490 T$ and $t_{end} = 500 T$ for higher energies. In all classical propagations there were no signs found for exact or approximate revivals. This is due to the theoretically continuous distributions of trajectories in phase-space.

The initial states were prepared by shifting the coherent Gaussians in position space by x_0 . Then, the energy expectation value E was calculated. Cases with lower energy than $\epsilon_0/2$ are possible, since the disorder potential can locally lower the potential energy to negative values. For the classical dynamics, fewer initial states were calculated, since the computational effort is significantly higher compared to the quantum propagation. Additionally, the entropy sum eq. (5.101) was computed, where numerically the modified Bessel function was implemented following the prescriptions in [93].

The results are shown in fig 5.14. There, the red crosses are the classical entropy averages $\bar{S}_{sum}^{cl}(E)$. They agree well with the numerically determined entropy of the dephased density eq. (5.101) (gray line). The black crosses representing the quantum averages $\bar{S}_{sum}^{qm}(E)$ are following the approximated entropy of the eigenfunctions (yellow line) from eq. (5.38). There seems to be no trivial mathematical reason for this. The interpretation is that, in the mean, the information is similar to that deduced from an harmonic eigenfunction of the same energy. This could be related to the number of occurring maxima (minima): It is plausible that at long times the number of maxima (minima) in the simulated wave function fluctuates around that of the most contributing harmonic eigenfunction.

For higher energies, the plateau entropies are slightly lower than the analytically determined ones. This is because the time T_{th} increases as the degree of disorder is small compared to the energy of the wave packet, and t_{start} becomes of order of T_{th} . Then,

the averaging includes times where the entropy is still growing. It is expected that the plateau entropies agree to S_{sum}^{approx} (S_{sum}^{deph} in the classical case) for higher energies than shown. Finally we note that all classical and quantum data points are in agreement with the BBM-inequality.

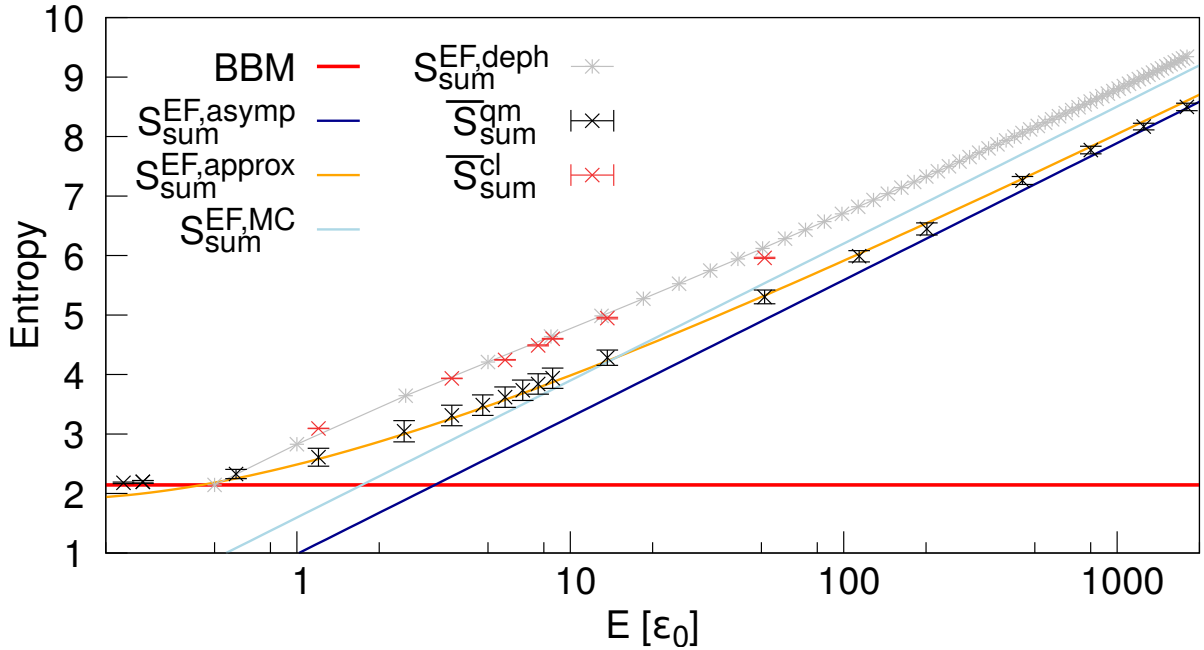


Figure 5.14: Long time behavior: Averaged entropy sum for late times $t \gg T_{th}$ obtained by classical and quantum dynamics. In gray, the entropy eq. (5.101) is shown. For orientation the lines from figure 5.3 were adopted.

Let us now consider very high energies. We start with the classical dynamics. For high energies $\epsilon_0 \ll E$ the exponential function in eq. (5.86) becomes

$$\lim_{\epsilon_0 \ll E} \exp\left(-\frac{2}{\epsilon_0}(E + E_0)\right) \rightarrow \sim \delta(E - E_0), \quad (5.104)$$

since the argument of the exponential is $\sim E/\epsilon_0 \rightarrow \infty$ in this limit. Therefore, the limit of the classical asymptotic densities at high energies approaches the classical microcanonical density,

$$\lim_{\epsilon_0 \ll E} \rho^{deph}(x, p) \rightarrow \rho^{MC}(x, p), \quad (5.105)$$

and thus we expect the entropies to converge as well. This is also reflected in the numerically calculated entropies: the gray line representing the entropy of the classical asymptotic entropy in fig 5.14 approaches that of the microcanonical density, represented by the light

blue line. This limit is not reached in the shown regime, nevertheless we can note a slow convergence behavior.

Thus, in total, the entropy takes a maximal value defined by S_{sum}^{deph} and, because revivals are not possible due to the continuous nature of classical phase-space, one may argue that the system reaches a form of thermal equilibrium. The high energy limit is an interesting limiting case. There, the system starts localized and reaches the density of the microcanonical ensemble. This process takes infinite time, since the thermalization time scales with energy. Thus formally, the density thermalizes in a strict sense in this limit.

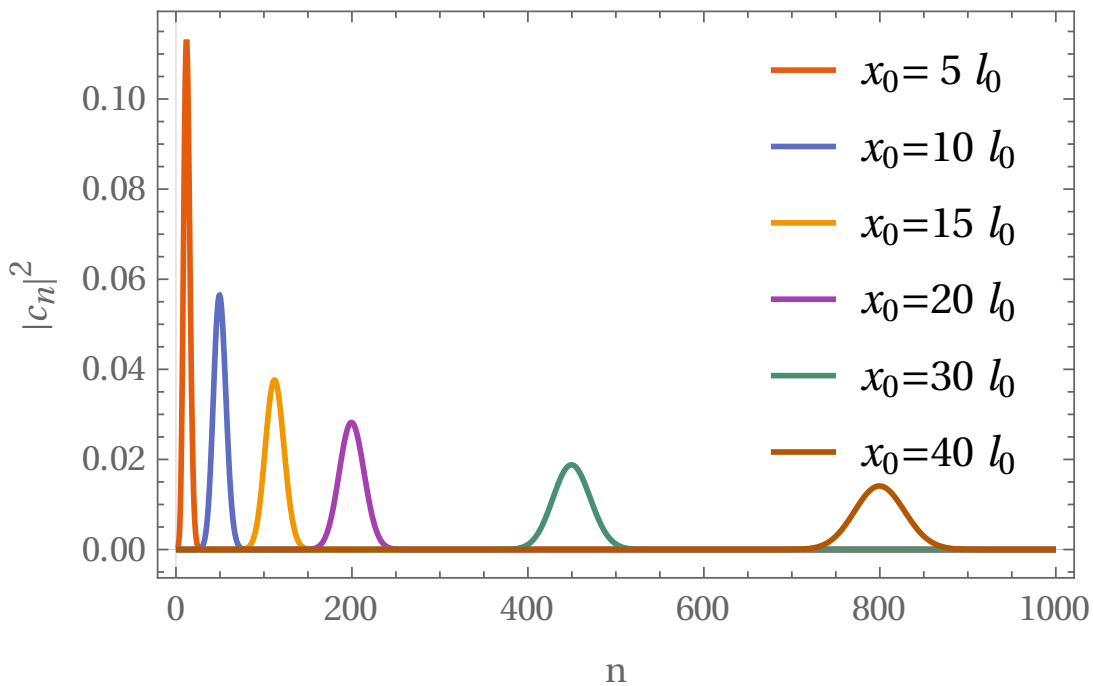


Figure 5.15: Distribution of coefficients $|c_n|^2$ from equation (5.106) for different excitations x_0 . The distributions become broader for higher excited states.

Now let us consider the quantum case again. The distribution of eigenfunctions determined by the absolute square of the c_n from eq. (5.93)

$$|c_n|^2 = e^{-x_0^2/2} \frac{(x_0^2/2)^n}{n!} \quad (5.106)$$

has the width

$$\sigma_{c_n} = \sqrt{\sum_n n^2 |c_n|^2 - \left(\sum_n n |c_n|^2\right)^2} = \frac{x_0}{\sqrt{2}}. \quad (5.107)$$

where Mathematica [94] was used to simplify the equation. Thus, the width of the dis-

tribution of the coefficients c_n increases as the excitation determined by the displacement x_0 increases. This is illustrated in fig. 5.15, where the distributions of the coefficients (eq. (5.106)) is shown for different values of x_0 . While low excited states are localized around a few eigenstates, the distribution for $x_0 = 40 l_0$ includes about one hundred significantly contributing eigenstates. In total, this means that an increasing number of eigenstates contribute to high-energy coherent states, which is associated with a decreased probability of revivals and weaker fluctuations in the disordered HO. This can be seen in the in fig. 5.14, since the entropy sum variance (eq. (5.103)) of high energy entropies is indeed smaller than for low energies, and we expect that this trend holds for higher energies than shown. However, the increasing number of eigenstates does not lead to a cancellation of the off diagonal terms in eq. (5.88) and therefore no comparable effect to pure dephasing occurs. As a results, S_{sum}^{MC} and $S_{sum}^{EF,approx}$ do not converge for high energies, which means that classical and quantum dynamics lead to different localization behavior, and we find a gap between both entropies which converges to $1 - \ln(2)$ for high energies. This is the same gap as found between S_{sum}^{MC} and $S_{sum}^{EF,asympt}$. If one would change the system to have pure dephasing, the classical and quantum system would have the same plateau entropy sum S_{sum}^{deph} .

Note that the entropy sums S_{sum}^{deph} and $S_{sum}^{EF,asympt}$, and therefore the plateau values, are only dependent on the energy in terms of the energy scale, E/ϵ_0 and no other system parameters. Due to the symmetry of the problem, the initial conditions for x_0 and p_0 are not relevant, as long as $mx_0^2/2 + p_0^2/2m = E$. Since we only considered coherent states in the harmonic oscillators it would be interesting to generalize the analysis to initially squeezed states and to study the impact of different initial widths. However, this is not within the scope of this thesis, since this breaks the symmetry in phase-space/Wigner-space and is therefore very difficult to handle analytically.

5.4 Conclusion

We investigated differential Shannon entropies from position and momentum densities in an harmonic oscillator with and without disorder. First, the entropy for coherent and squeezed states in an undisturbed harmonic oscillator were considered analytically. Time-dependent expressions were derived for the entropies that depend on the width in the respective space. This demonstrates the relation between entropy and localization of the wave function.

The entropies of harmonic eigenstates in position- and momentum-space were examined. The complicated structure of the expressions for the entropies prohibits an exact cal-

ulation. Therefore, a fit-equation for the entropy sum was presented to increase the accuracy of the existing approximation. Entropies have also been calculated for the classical harmonic oscillator in the microcanonical ensemble. We compared the entropy of the quantum eigenstates and the microcanonical ensemble in the classical limit and found that both do not converge and differ by a shift of $1 - \ln(2)$.

The model was extended by adding a static disorder to the harmonic potential. In an exemplary study, the short-time and long-time behavior of the entropy was investigated by considering quantum and classical dynamics in this system. Initially, the quantum dynamics are similar to that of the undisturbed oscillator but due to dispersion, the wave packet breaks up and spreads over the entire classical accessible region. The classical dynamics are similar, but the dispersion takes more time and higher values of the entropy are reached. After the initial dynamics, the classical entropies remain fairly constant, while the quantum ones show strong irregular oscillations around a plateau value. Minima in the quantum entropy sum have been attributed to the revival behavior of the wave function. The timescale of the revivals is related to the four most contributing energy eigenstates of the wave packet. Finally, the energy dependence of the entropy plateau values was studied.

For long times, the classical dynamics lead to a defined energy-dependent maximal entropy sum, which can be predicted by computing a dephased density in phase-space. The maximal entropy sum is subject to only very small fluctuations and there is no reason to expect revivals in the dynamics. Thus, the information in the system is irreversibly lost and can not be recovered, and the system reaches a form of thermal equilibrium. At very high energies, the entropy plateau values converge to that of an harmonic oscillator in the microcanonical ensemble.

6 Information-Theoretical Approach to Coupled Electron-Nuclear Dynamics

Particle correlation is of great interest in quantum chemistry. To illustrate this, consider a particle A with wave function $\Psi_A(x_A, t)$ and a particle B with wave function $\Psi_B(x_B, t)$, where x_A and x_B are the respective positions. Assuming that the particles do not interact until $t > 0$, the total wave function describing both particles $\Psi_{AB}(x_A, x_B, t)$ can be written in a product form:

$$\Psi_{AB}(x_A, x_B, t) = \Psi_A(x_A, t)\Psi_B(x_B, t) \text{ for } t \leq 0. \quad (6.1)$$

In general, factorizing wave functions like this are easier to find analytically as well as computationally, since no coupling terms are present. If now the interaction, e.g. a Coulomb interaction, is switched on at $t > 0$, particle A is influenced by particle B and vice versa. Consequently, factorizing the wave function is no longer possible.

As an example for correlated particles, consider particle A and B to be electrons of equal spins. Then, $\Psi_{AB}(x_A, x_B, t) = 0$ for $x_A = x_B$ due to the Pauli principle. Trying to write this in product form as eq. (6.1) implies, that for the total wave function to vanish at those points, $\Psi_A(x_B, t) = 0$ or $\Psi_B(x_A, t) = 0$. This means that Ψ_A depends on x_B (or, Ψ_B depends on x_A , respectively), which contradicts the product form. This gets even more complicated, if we consider the Coulomb interactions between the electrons as well. In electron structure theory, where multiple electrons interact with each other, it is, in general, not possible to find the total wave function [10]. To tackle this problem, approaches like DFT (density functional theory) are applied. DFT relies on the Hohenberg Kohn Theorem, which states that there is a functional of the electron density, $E[\rho^{el}]$, which yields the accurate ground state electron density of the molecule at its global minimum [10]. However, this functional is yet to be found and in particular contributions due to electron-electron correlation are yet to be understood.

Particle correlation is not only relevant between electrons but also between electrons and nuclei, since the nuclear geometry determines the electron densities, which, in turn, give rise to chemical bonding. As an example, vibrational modes of molecules, observed in techniques like infrared spectroscopy, are influenced by electron-nuclear coupling: Changes in the electron distribution due to oscillating nuclei change the vibrational frequencies [95]. Also in non-equilibrium dynamics, the electron-nuclear correlation is important: In [96] it was shown that nuclear movement leaves an imprint on the photoelectron spectrum

after XUV-ionization. In [97] the significance of electron-nuclear correlation was shown for hydrogen tunneling. The connection of localization of the nuclei and electron-nuclear correlation is highlighted in [98]. Other notable studies on electron-nuclear correlation can be found in, e.g., refs. [99, 100].

Here, we use an information-theoretical approach to coupled electron-nuclear dynamics. Various groups applied information-theoretical measures to access correlated systems before [34–40]. However, these studies consider systems in stationary states and are to be seen in context with electron structure theory and electron-electron correlation. In contrast to that, information-theoretical approaches have not been applied to electron-nuclear correlation in the literature, to the best of our knowledge. Although formally, there are similarities to electron-electron correlation, electron-nuclear correlation is distinct, e.g., because of the mass difference, the distinguishability and the opposite charge of both sorts of particles. Also, comparable studies for explicitly time-dependent motions have not been performed.

The following chapter presents four thematically consecutive publications on the application of information-theoretical measures to a system of coupled electron-nuclear dynamics [3–6]. These works are the result of the collaboration with my supervisor, Prof. Dr. Volker Engel. In all papers, the implementation of the investigated model, the numerical calculations and data curation were done by me. Analytic results were mainly elaborated by myself. The ideas, conceptualization and findings are the result of discussions with equal parts from both authors. The individual contributions are listed in more detail for each paper in sec. 10.

The chapter is structured as follows. First, the considered model and setup is explained. Then, the papers are summarized and the key findings are presented. Finally, the publications are reprinted.

6.1 Model and setup

The model that we investigate is based on the works of Shin and Metiu [101, 102]. It was originally used to study the transfer of an electron and a sodium ion between two zeolite cages. It allows to access different coupling regimes between electronic and nuclear degrees of freedom and presents a case where the dynamics are solvable numerically exactly. Several applications, including extensions of the original model have been presented in the literature [96, 103–108]. The particle configuration is schematically shown in fig 6.1.

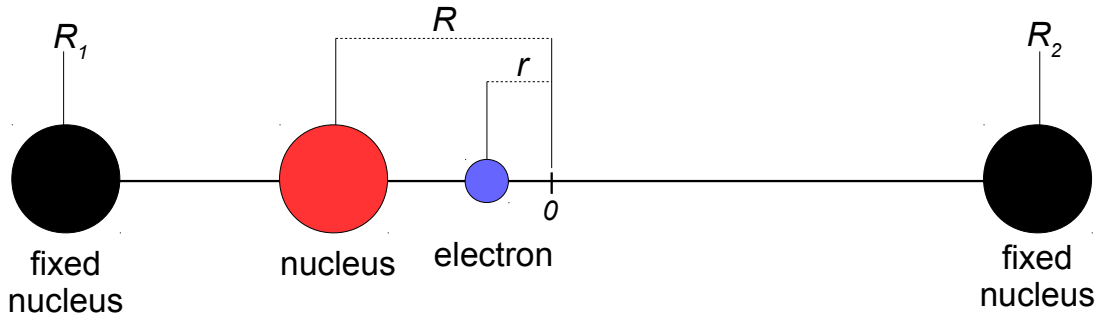


Figure 6.1: The Shin-Metiu model: A mobile electron and a mobile nucleus interact with two fixed nuclei.

The model consists of one mobile electron and one mobile nucleus that interact with each other and with two fixed nuclei at position $R_1 = -5 \text{ \AA}$ and $R_2 = 5 \text{ \AA}$ in one dimension. Here, the charge of all nuclei is taken to be equal, $Q = Q_1 = Q_2 = |e|$. The electron interacts with the nuclei by soft Coulomb interactions which are realized by error-functions with parameters R_f and R_c , so that the potential is given by (in atomic units) [101, 102]:

$$\begin{aligned}
 V(r, R) = & \frac{1}{|R_1 - R|} + \frac{1}{|R_2 - R|} - \frac{\text{erf}[|R_1 - r|/R_f]}{|R_1 - r|} \\
 & - \frac{\text{erf}[|R - r|/R_c]}{|R - r|} - \frac{\text{erf}[|R_2 - r|/R_f]}{|R_2 - r|} + \Delta,
 \end{aligned} \tag{6.2}$$

where r and R are the electronic and nuclear coordinates, respectively. The parameter R_c governs the interaction strength between electron and mobile nucleus, while R_f governs the interactions between the fixed nuclei and both mobile particles. By tuning R_f and R_c , different non-adiabatic coupling strengths can be realized. This involves cases where the Born-Oppenheimer approximation holds with high accuracy and also cases where large population transfer occurs between different adiabatic electronic states. The energy shift Δ is added to ensure that the potential assumes positive values in the considered spatial domain.

The dynamics is described by the time-dependent Schrödinger equation

$$i \frac{\partial}{\partial t} \Psi(r, R, t) = \hat{H} \Psi(r, R, t). \tag{6.3}$$

where the Hamiltonian is

$$\hat{H} = \frac{\hat{P}^2}{2M} + \frac{\hat{p}^2}{2} + V(r, R), \tag{6.4}$$

with nuclear momentum operator \hat{P} , electron momentum operator \hat{p} and nuclear mass M . The time-dependent Schrödinger equation is solved numerically exactly by using the split-operator method (sec. 4.2). As initial function we employ

$$\Psi(r, R, 0) = N_0 e^{-\beta_0(R-R_0)^2} \varphi_n(r; R), \quad (6.5)$$

where β_0 determines the initial width, R_0 is the center of the Gaussian nuclear wave packet, and $\varphi_n(r; R)$ is the n -th eigenfunction of the electronic Hamiltonian

$$\left[\frac{\hat{p}^2}{2} + V(r, R) \right] \varphi_n(r; R) = V_n(R) \varphi_n(r; R). \quad (6.6)$$

Here, $V_n(R)$ is the n -th adiabatic potential curve at nuclear geometry R . Numerically $V_n(R)$ and $\varphi_n(r; R)$ are obtained by using the relaxation method (sec. 4.3) involving the electronic Hamiltonian eq. (6.6) for every considered nuclear geometry R . In the wave packet eq. (6.5), the value of R_0 is chosen to be close to one of the fixed nuclei.

The total position density is defined as

$$\rho(r, R, t) = |\Psi(r, R, t)|^2. \quad (6.7)$$

The marginal densities are obtained by integrating out one or the other degree of freedom. This yields electron position density

$$\rho^{el}(r, t) = \int dR \rho(r, R, t), \quad (6.8)$$

and the nuclear position density

$$\rho^{nuc}(R, t) = \int dr \rho(r, R, t). \quad (6.9)$$

The momentum density is obtained from the momentum-space representation of the wave function,

$$\rho(p, P, t) = |\Psi(p, P, t)|^2, \quad (6.10)$$

where $\Psi(p, P, t)$ is the Fourier transform of $\Psi(r, R, t)$. The electron momentum density

and the nuclear momentum density are calculated in analog to the position-space as

$$\rho^{el}(p, t) = \int dP \rho(p, P, t), \quad (6.11)$$

$$\rho^{nuc}(P, t) = \int dp \rho(p, P, t). \quad (6.12)$$

6.2 Overview over the information-theoretical approach to coupled electron-nuclear dynamics

Our first study on this system using an information-theoretical ansatz was published in the letter [3]. This publication is reprinted in sec. 6.3.1. The objective of this study was to benchmark information-theoretical quantities and investigate how they relate to the general dynamics of a coupled non-trivial system. For this, the time-dependent electron and nuclear average position

$$\langle r \rangle_t = \int dr \rho^{el}(r, t) r, \quad (6.13)$$

$$\langle R \rangle_t = \int dR \rho^{nuc}(R, t) R, \quad (6.14)$$

and electron and nuclear width

$$\sigma_r^2(t) = \int dr \rho^{el}(r, t) (r - \langle r \rangle_t)^2, \quad (6.15)$$

$$\sigma_R^2(t) = \int dR \rho^{nuc}(R, t) (R - \langle R \rangle_t)^2 \quad (6.16)$$

were calculated and compared with the position-space differential Shannon entropies from the total density

$$S_x(t) = - \int dr \int dR \rho(r, R, t) \ln [\rho(r, R, t)], \quad (6.17)$$

as well as those derived from the electron and nuclear densities, respectively:

$$S_r^{el}(t) = - \int dr \rho^{el}(r, t) \ln [\rho^{el}(r, t)], \quad (6.18)$$

$$S_R^{nuc}(t) = - \int dR \rho^{nuc}(R, t) \ln [\rho^{nuc}(R, t)]. \quad (6.19)$$

From the Shannon entropies, the mutual information was computed:

$$I_x(t) = S_r^{el}(t) + S_R^{nuc}(t) - S_x(t). \quad (6.20)$$

The definitions of all information-theoretical quantities are summarized in tab. 6.1 at the end of this chapter.

By choosing different values for the parameter R_c in the interaction potential, two different situations are created: In the first one (weak adiabatic coupling), the dynamics of the wave packet take place nearly exclusively in the electronic ground state, in the other one (strong adiabatic coupling) the ground state adiabatic potential and the first excited adiabatic potential exhibit a sharp avoided crossing so that nearly a complete population transfer occurs.

In the first case, where the BO approximation applies, the electron follows the mobile nucleus very closely and reverses its direction together with the nucleus at the classical turning points, which is caused by the repulsion of the mobile and the fixed nucleus. The entropies show a similar oscillating structure as found in the entropy of a wave packet in a harmonic oscillator. Here, we observe a key finding regarding the dynamics and entropy in our system: Entropy values for both, nucleus and electron, correlate with the width of their respective densities. This indicates the connection between the localization of the density and entropy. In particular, this occurs at the turning points, since the density refocuses, comparable to a squeezed state in a harmonic oscillator. This results in minima at the widths as well as the entropies.

Nevertheless, we find that the time-dependence of the total entropy is primarily related to the nuclear density dynamics, while the electron influence on the total entropy is less. The mutual information increases over time, exhibiting minima and maxima, up to a maximal value. This can be traced back to the dispersion of the wave packet. The minima coincide with the classical turning points of the density as well. We show in [3], that this is related to the refocusing of $\rho(r, R, t)$ at these points.

The same analysis was conducted for the case of a strong adiabatic coupling. There, the electron width and entropy is nearly constant, since the electron is bound to one of the fixed nuclei. The dynamics of the total entropy is thus completely determined by that of the nuclear entropy. In contrast to the case of weak adiabatic couplings, the mutual information vanishes in this setup, which means that the electron and the mobile nucleus do not share information. This difference illustrates the relation of mutual information to the degree of coupling in the system: It does not relate to the coupling of the adiabatic potentials but the relative mobility of the electron and the nucleus. Therefore the mutual information serves as a metric for the composition of the total density in the $R - r$ space. We argue that this reveals details about the adiabaticity of the dynamics and the

correlation between electrons and nuclei within the system.

For strong adiabatic coupling, state dependent entropies were defined as well. For this the total density was decomposed into adiabatic matrix elements:

$$\rho(r, R, t) = \left| \sum_{n=0}^{\infty} \psi_n(R, t) \varphi_n(r, R, t) \right|^2 = \sum_{n,m=0}^{\infty} \rho_{nm}(r, R, t), \quad (6.21)$$

$$\rho_{nm}(r, R, t) = \psi_n(R, t)^* \psi_m(R, t) \varphi_n(r, R, t) \varphi_m(r, R, t), \quad (6.22)$$

where the population of the n -th state is $P_n(t) = \int dR dr \rho_{nn}(r, R, t)$. By integration, the adiabatic matrix elements of the electron and nuclear density are obtained, respectively:

$$\rho_{nm}(r, t) = \int dR \rho_{nm}(r, R, t) \quad \text{and} \quad \rho_{nm}(R, t) = \int dr \rho_{nm}(r, R, t). \quad (6.23)$$

We use that the diagonal elements are positive semidefinite and define the state dependent entropies

$$S_n(t) = - \int dR \int dr \rho_{nn}(r, R, t) \ln [\rho_{nn}(r, R, t)], \quad (6.24)$$

$$S_n^{el}(t) = - \int dr \rho_{nn}(r, t) \ln [\rho_{nn}(r, t)], \quad (6.25)$$

$$S_n^{nuc}(t) = - \int dR \rho_{nn}(R, t) \ln [\rho_{nn}(R, t)]. \quad (6.26)$$

We find that the state specific entropies carry information about the population as well as the form of the density in the respective adiabatic state. Comparing the sums $\sum_n S_n(t)$, $\sum_n S_n^{el}(t)$ and $\sum_n S_n^{nuc}(t)$ to the respective not decomposed entropies, gives insight how the respective density transfers to a different adiabatic state at the avoided crossing.

Motivated by the established strong relationship between the width and the entropy, an analytical ansatz was applied to the model with weak adiabatic coupling in the paper [5]. This paper is reprinted in sec. 6.3.2. Since for weak adiabatic coupling, the dynamics are restricted predominantly to the electronic groundstate, the Born-Oppenheimer approximation can be applied. Thus the ansatz

$$\Psi(r, R, t) = \left[\frac{\sqrt{\gamma\beta_t}}{\pi} \right]^{\frac{1}{2}} e^{-\frac{\beta_t}{2}(R-R_t)^2} e^{-\frac{\gamma}{2}(r-R)^2} \quad (6.27)$$

was used. Here, R_t determines the time-dependent center of the wave function and β_t and γ are related to the width of the nuclear and electron density. The electronic eigenfunction

was taken to be of form

$$\varphi_0(r; R) = \left[\frac{\gamma}{\pi} \right]^{\frac{1}{4}} e^{-\frac{\gamma}{2}(r-R)^2}. \quad (6.28)$$

This is a good approximation, since the error-function which governs the particle interaction can be expanded as a power series:

$$\text{erf}(x) = \frac{2}{\sqrt{\pi}} \left(x - \frac{x^3}{3} + \frac{x^5}{10} - \frac{x^7}{42} + \frac{x^9}{216} + \mathcal{O}(x^{11}) \right). \quad (6.29)$$

This means that the soft-coulomb interaction for small $x = (R - r)$ behaves harmonic:

$$-\frac{\text{erf}(x)}{x} = -\frac{2}{\sqrt{\pi}} \left(1 - \frac{x^2}{3} + \mathcal{O}(x^4) \right) \sim x^2. \quad (6.30)$$

This is fulfilled as long as the interaction between the fixed nuclei is negligible. The electronic groundstate wave function is therefore Gaussian-like, as is illustrated in fig. 6.2.

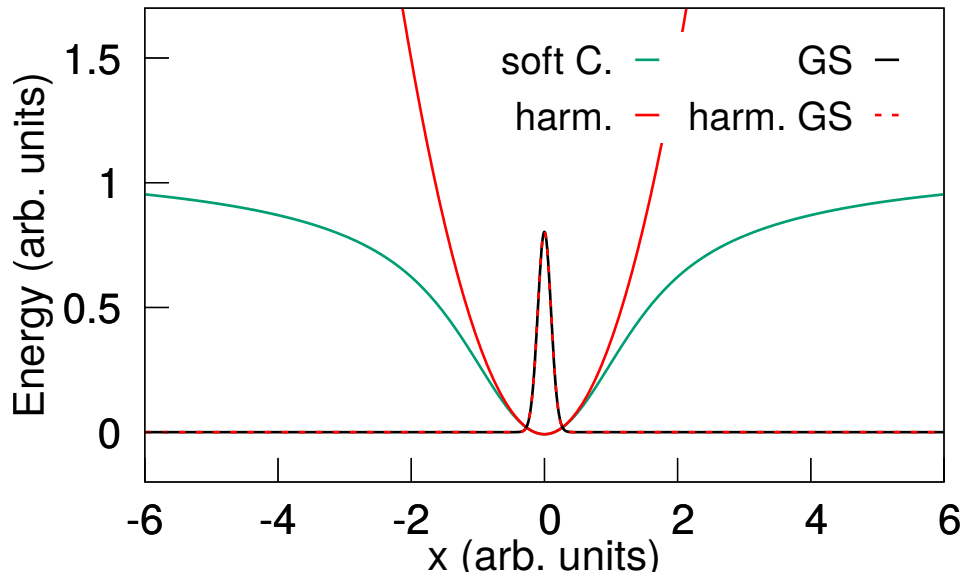


Figure 6.2: Schematic comparison: The soft Coulomb potential (soft C., green) is approximately harmonic (harm-, red) for small values of x . This results into the groundstate of the soft Coulomb- (GS, black) and the harmonic potential (harm. GS, red dashed line) being nearly identical.

By Gaussian integration, the width of the wave function eq. (6.28) is determined:

$$\sigma_\gamma^2 = \int dr |\varphi_0(r; R)|^2 (r - R)^2 = \frac{1}{2\gamma}. \quad (6.31)$$

This equation is used to gauge the analytical ansatz to the system: After numerically finding the eigenfunctions, their average width $\bar{\sigma}_\gamma$ in the regime between the fixed nuclei $[-5 \text{ \AA}, 5 \text{ \AA}]$ is calculated. The parameter γ is then taken as $\gamma = \frac{1}{2\bar{\sigma}_\gamma^2}$. The nuclear width of eq. (6.27) is

$$\sigma_R^2(t) = \int dr \int dR |\Psi(r, R, t)|^2 (R - R_t)^2 = \frac{1}{2\beta_t}. \quad (6.32)$$

The parameter β_t introduces the time-dependence into the analytical ansatz by relating the numerically determined, time-dependent nuclear width to the analytical nuclear width, so that we have $\beta_t = \frac{1}{2\sigma_R^2(t)}$. Through the comparable easy form of eq. (6.27) we can calculate approximate relations between the nuclear width and the investigated quantities analytically. These are summarized in the left column of tab. 6.2.

In [5] we found that the described Born-Oppenheimer ansatz yields good results in predicting the considered entropies. We also compared the analytical ansatz with numerical results for the mutual information (eq. (6.20)), as well as the covariance

$$cov_x(t) = \int dr \int dR \rho(r, R, t) (r - \langle r \rangle_t)(R - \langle R \rangle_t), \quad (6.33)$$

and the linear correlation coefficient

$$corr_x(t) = \frac{cov_x(t)}{\sigma_r(t)\sigma_R(t)}. \quad (6.34)$$

The two latter functions are a measure of linear correlation effects, whereas the mutual information also includes higher correlation effects. Here, very good agreement was found. This implies that in position-space, the information dynamics, even for the electronic degrees of freedom, as well as the correlation is nearly completely determined by the nuclear width, since this is the only time-dependent parameter.

We expanded the position-space analysis method to the momentum-space in the thematically following paper [4]. This publication is reprinted in sec. 6.3.3. The Fourier transform of the wave function given in eq. (6.27) was calculated, which allows us to

derive analytic expressions for the total, electron and nuclear entropy:

$$S_\pi(t) = - \int dp \int dP \rho(p, P, t) \ln[\rho(p, P, t)], \quad (6.35)$$

$$S_p^{el}(t) = - \int dp \rho^{el}(p, t) \ln[\rho^{el}(p, t)], \quad (6.36)$$

$$S_P^{nuc}(t) = - \int dP \rho^{nuc}(P, t) \ln[\rho^{nuc}(P, t)]. \quad (6.37)$$

Additionally, the correlation measures

$$cov_\pi(t) = \int dp \int dP \rho(p, P, t) (p - \langle p \rangle_t)(P - \langle P \rangle_t), \quad (6.38)$$

$$corr_\pi(t) = \frac{cov_\pi(t)}{\sigma_p(t)\sigma_P(t)}, \quad (6.39)$$

$$I_\pi(t) = S_p^{el}(t) + S_P^{nuc}(t) - S_\pi(t), \quad (6.40)$$

are calculated. The analytic results are summarized in the right column of tab. 6.2. The electron and nuclear momentum width are

$$\sigma_p^2(t) = \int dp \rho^{el}(p, t)(p - \langle p \rangle_t)^2, \quad (6.41)$$

$$\sigma_P^2(t) = \int dP \rho^{nuc}(P, t)(P - \langle P \rangle_t)^2, \quad (6.42)$$

where $\langle p \rangle_t$ and $\langle P \rangle_t$ are the electron and nuclear momentum expectation values, respectively. Analogous to the analysis in position-space, we determined the parameter β_t from the nuclear momentum width. The main dynamical features of the numerical simulation can be reproduced by the analytic ansatz, but the structure of the density is more complex in momentum- than in position-space, so that good agreement is only found for early times. This is even more apparent in the correlation measures: There, only the linear correlation coefficient eq. (6.39) is predicted with good accuracy. Finally, we found that the numerical mutual information in momentum space eq. (6.40) increases with the number of nodes in the momentum density. This behavior cannot be modeled within the analytic ansatz, which does not incorporate nodes in the wave functions.

Finally, in [4] a situation with strong adiabatic coupling was considered, where the electron remains nearly completely at one of the fixed nuclei. We expanded the ansatz eq. (6.27) to diabatic dynamics by modifying it to

$$\Psi(r, R, t) = \left[\frac{\sqrt{\gamma\beta_t}}{\pi} \right]^{\frac{1}{2}} e^{-\frac{\beta_t}{2}(R-R_t)^2} e^{-\frac{\gamma}{2}(r-R_d)^2}. \quad (6.43)$$

The electronic wave function is therefore a Gaussian that is fixed at nuclear geometry R_d . The analytic results for this ansatz are summarized in tab. 6.3. To apply the analytic expressions, γ was determined from the electron width at R_d . As in the weakly coupled situation, β_t was computed from the position-space nuclear width for quantities determined in position-space, and the momentum-space nuclear width for those in momentum space, respectively. The analytic ansatz showed very good agreement due to the comparable simple dynamics.

The last part of the puzzle, namely the increase of mutual information in momentum-space, led to an in-depth study on the influence of nodes on correlation measures. This was published in the paper [6], which is reprinted in sec. 6.3.4. There, we firstly considered an example density, where we observed that the linear correlation remained largely unaffected by the presence of nodes, while the mutual information showed sensitivity to the alignment and the number of nodes.

Building upon these findings, we applied the insights gained from the example density to our model: By adjusting the numerical ansatz eq. (6.27) to include nodes, we managed to reproduce the increase of mutual information, while the linear correlation remained unchanged. Thus, it is not only necessary to know the nuclear width in position- and momentum-space, but nodal patterns are also relevant to predict the particle correlation.

Table 6.1: Overview of the definitions of the investigated quantities.

	Position space	Momentum space
Total entropy	$S_x(t) = - \int dr \int dR \rho(r, R, t) \ln [\rho(r, R, t)]$	$S_\pi(t) = - \int dp \int dP \rho(p, P, t) \ln [\rho(p, P, t)]$
Electron entropy	$S_r^{el}(t) = - \int dr \rho(r, t) \ln [\rho(r, t)]$	$S_p^{el}(t) = - \int dp \rho(p, t) \ln [\rho(p, t)]$
Nuclear entropy	$S_R^{nuc}(t) = - \int dR \rho(R, t) \ln [\rho(R, t)]$	$S_P^{nuc}(t) = - \int dP \rho(P, t) \ln [\rho(P, t)]$
MI	$I_x(t) = S_r^{el}(t) + S_R^{nuc}(t) - S_x(t)$	$I_\pi(t) = S_p^{el}(t) + S_P^{nuc}(t) - S_\pi(t)$
Electron width	$\sigma_r^2(t) = \int dr \rho^{el}(r, t) (r - \langle r \rangle_t)^2$	$\sigma_p^2(t) = \int dp \rho^{el}(p, t) (p - \langle p \rangle_t)^2$
Nuclear width	$\sigma_R^2(t) = \int dR \rho^{nuc}(R, t) (R - \langle R \rangle_t)^2$	$\sigma_P^2(t) = \int dP \rho^{nuc}(P, t) (P - \langle P \rangle_t)^2$
Covariance	$cov_x(t) = \int dr \int dR \rho(r, R, t) (r - \langle r \rangle_t)(R - \langle R \rangle_t)$	$cov_\pi(t) = \int dp \int dP \rho(p, P, t) (p - \langle p \rangle_t)(P - \langle P \rangle_t)$
Correlation	$corr_x(t) = \frac{cov_x(t)}{\sigma_r(t)\sigma_R(t)}$	$corr_\pi(t) = \frac{cov_\pi(t)}{\sigma_p(t)\sigma_P(t)}$

Table 6.2: Overview of the analytic results derived within the Born-Oppenheimer adiabatic ansatz for the wave function.

	Position space	Momentum space
Total entropy	$S_x(t) = \ln \left[\frac{\pi}{\sqrt{\gamma\beta_t}} \right] + 1$	$S_\pi(t) = \ln \left[\sqrt{\gamma\beta_t\pi} \right] + 1$
Electron entropy	$S_r^{el}(t) = \ln \left[\sqrt{\frac{(\beta_t+\gamma)\pi}{\beta_t\gamma}} \right] + \frac{1}{2}$	$S_p^{el}(t) = \ln \left[\sqrt{\pi\gamma} \right] + \frac{1}{2}$
Nuclear entropy	$S_R^{nuc}(t) = \ln \left[\sqrt{\frac{\pi}{\beta_t}} \right] + \frac{1}{2}$	$S_P^{nuc}(t) = \ln \left[\sqrt{\pi(\beta_t + \gamma)} \right] + \frac{1}{2}$
MI	$I_x(t) = \frac{1}{2} \ln \left[1 + \frac{\gamma}{\beta_t} \right]$	$I_\pi(t) = \frac{1}{2} \ln \left[1 + \frac{\gamma}{\beta_t} \right]$
Electron width	$\sigma_r^2(t) = \frac{1}{2} \frac{\gamma+\beta_t}{\gamma\beta_t}$	$\sigma_p^2(t) = \frac{\gamma}{2}$
Nuclear width	$\sigma_R^2(t) = \frac{1}{2\beta_t}$	$\sigma_P^2(t) = \frac{1}{2}(\beta_t + \gamma)$
Covariance	$cov_x(t) = \frac{1}{2\beta_t}$	$cov_\pi(t) = -\frac{1}{2}\gamma$
Correlation	$corr_x(t) = \frac{1}{\sqrt{1+\beta_t/\gamma}}$	$corr_\pi(t) = -\frac{1}{\sqrt{1+\beta_t/\gamma}}$

Table 6.3: Overview of the analytic results derived from the diabatic ansatz. This table includes results that are not explicitly shown in [4] but were added for completeness.

	Position space	Momentum space
Total entropy	$S_x(t) = \ln \left[\frac{\pi}{\sqrt{\beta_t\gamma}} \right] + 1$	$S_\pi(t) = \ln \left[\sqrt{\gamma\beta_t\pi} \right] + 1$
Electron entropy	$S_r^{el}(t) = \ln \left[\sqrt{\frac{\pi}{\gamma}} \right] + \frac{1}{2}$	$S_p^{el}(t) = \ln \left[\sqrt{\pi\gamma} \right] + \frac{1}{2}$
Nuclear entropy	$S_R^{nuc}(t) = \ln \left[\sqrt{\frac{\pi}{\beta_t}} \right] + \frac{1}{2}$	$S_P^{nuc}(t) = \ln \left[\sqrt{\pi\beta_t} \right] + \frac{1}{2}$
MI	$I_x(t) = 0$	$I_\pi(t) = 0$
Electron width	$\sigma_r^2(t) = \frac{1}{2\gamma}$	$\sigma_p^2(t) = \frac{\gamma}{2}$
Nuclear width	$\sigma_R^2(t) = \frac{1}{2\beta_t}$	$\sigma_P^2(t) = \frac{\beta_t}{2}$
Covariance	$cov_x(t) = 0$	$cov_\pi(t) = 0$
Correlation	$corr_x(t) = 0$	$corr_\pi(t) = 0$

6.3 Reprinted publications

In this section, the papers [3–6] are reprinted. The respective copyright statements can be found in tab. 6.4.

Table 6.4: Copyright statements of the respective papers. The Creative Commons Attribution license (CC BY 4.0) can be found under the link <https://creativecommons.org/licenses/by/4.0> (accessed 28.01.2024).

Section	Copyright declaration	Ref.
6.3.1	Reprinted with permission from "P. Schürger, V. Engel, J. Phys. Chem. Lett. 2023, 14, 334–339". Copyright 2023 American Chemical Society.	[3]
6.3.2	Reproduced from "P. Schürger, V. Engel, Phys. Chem. Chem. Phys. 2023, 25, 28373-28381" with permission from the PCCP Owner Societies.	[5]
6.3.3	Reprinted from "P. Schürger, V. Engel, Entropy 2023, 25(7), 970"; licensed under a Creative Commons Attribution (CC BY) license (CC BY 4.0).	[4]
6.3.4	Reprinted from "P. Schürger, V. Engel, AIP Advances 2023, 13, 125307"; licensed under a Creative Commons Attribution (CC BY) license (CC BY 4.0).	[6]

6.3.1 Information Theoretical Approach to Coupled Electron-Nuclear Wave Packet Dynamics: Time-Dependent Differential Shannon Entropies [3]

Reprinted with permission from "P. Schürger, V. Engel, *J. Phys. Chem. Lett.* 2023, 14, 334–339". Copyright 2023 American Chemical Society.

THE JOURNAL OF
PHYSICAL CHEMISTRY
LETTERS
A JOURNAL OF THE AMERICAN CHEMICAL SOCIETY

pubs.acs.org/JPCLETT

Letter

Information Theoretical Approach to Coupled Electron–Nuclear Wave Packet Dynamics: Time-Dependent Differential Shannon Entropies

Peter Schürger and Volker Engel*

Cite This: *J. Phys. Chem. Lett.* 2023, 14, 334–339

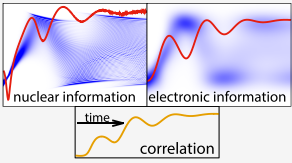
Read Online

[ACCESS |](#)

Metrics & More

Article Recommendations

ABSTRACT: We study differential Shannon entropies determined from position-space quantum probability densities in a coupled electron–nuclear system. In calculating electronic and nuclear entropies, one gains information about the localization of the respective particles and also about the correlation between them. For Born–Oppenheimer dynamics, the correlation decreases at times when the wave packet reaches the classical turning points of its motion. If a strong non-adiabatic coupling is present, leading to a large population transfer between different electronic states, the electronic entropy is approximately constant. Then the time dependence of the entropy reflects the information on the nucleus alone, and the correlation is absent. A decomposition of the entropy into contributions from the participating electronic states reveals insight into the state-specific population and nuclear wave packet localization.



As a driving force, entropy is of major importance to understand the course of chemical reactions. Besides its role in thermodynamics, meaningful definitions of entropy for systems in pure quantum states can be found. One such definition is based on information theory and is due to Shannon,^{1–4} for some chemical applications see, e.g., refs 5–9. Starting from a time-dependent wave packet $\psi(x, t)$ describing a system as a function of coordinates x and time t , the “differential Shannon entropy”^{10,11} is defined via the probability density $\rho(x, t) = |\psi(x, t)|^2$ as (in multiples of the Boltzmann constant):

$$S(t) = - \int dx \rho(x, t) \ln[\rho(x, t)] \quad (1)$$

Note that $S(t)$ depends on the units of the density $\rho(x)$. In the present work we use atomic length units. That the entropy is related to the width of the wave packet is seen, e.g., for a Gaussian wave packet moving in a harmonic potential, where one can show analytically that the entropy increases with increasing width.^{12–14} Thus, the less we know about the position of a particle, the larger is the entropy, and the relation to the information available on the system (or the lack of it) is obvious. There also exists a close relationship between the entropy and the coordinate–momentum uncertainty.^{11,15–17}

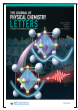
Regarding the combined motion of electrons and nuclei in molecules, the total entropy is a measure of the information on the entire system. One may, however, calculate electronic and nuclear probability densities and derive entropies associated with one or the other kind of particles. In the simplest case, where there is no correlation between electrons and nuclei, the overall entropy is the sum of the two particle entropies, and deviations from this sum are a measure of correlation. In this paper we address the question of the extent to which the Shannon differential entropy yields information on the combined electronic and nuclear motion and on the correlation between these particles.

To determine entropies evolving from a coupled electron–nuclear motion, we employ a model^{18,19} consisting of an electron and a proton which move in a single dimension and interact with two protons at fixed positions $R_1 = -5 \text{ \AA}$ and $R_2 = +5 \text{ \AA}$, respectively. The potential is parametrized as (in atomic units)

$$V(r, R) = \frac{1}{|R_1 - R|} + \frac{1}{|R_2 - R|} - \frac{\text{erf}(|R_1 - r|/R_T)}{|R_1 - r|} - \frac{\text{erf}(|R_2 - r|/R_T)}{|R_2 - r|} + \Delta E \quad (2)$$

where r and R are the coordinates of the electron and proton, respectively. The interactions between the protons are described by bare Coulomb potentials, whereas the electron–nuclear interactions are screened using error functions.

Received: November 29, 2022
Accepted: December 28, 2022
Published: January 6, 2023



© 2023 The Authors. Published by American Chemical Society

334

<https://doi.org/10.1021/acs.jpclett.2c03635>
J. Phys. Chem. Lett. 2023, 14, 334–339

Downloaded via UNIV LIBRARY OF WUERZBURG on November 13, 2023 at 12:04:07 (UTC).
See <https://pubs.acs.org/sharingguidelines> for options on how to legitimately share published articles.

6. INFORMATION-THEORETICAL APPROACH TO COUPLED ELECTRON-NUCLEAR DYNAMICS

The potential is shifted by ΔE so that the minimum of $V(r, R)$ is at zero energy in the region of our numerical grid. The parameter R_c is chosen as 1.5 Å. We regard two values of the screening parameter R_c appearing in the electron–nuclear interaction term (see below). The Hamiltonian of the system is

$$\hat{H} = \frac{\hat{p}^2}{2} + \frac{\hat{P}^2}{2M} + V(r, R) \quad (3)$$

in which \hat{p} and \hat{P} are the momentum operators for the electronic and nuclear motion, respectively, and M is the proton mass. We numerically solve the time-dependent Schrödinger equation for the coupled electron–nuclear motion with help of the split operator method.²⁰ The spatial grid on which the wave functions $\Psi(r, R, t)$ are represented ranges from -12 Å to $+12$ Å for the electronic coordinate r and extends from -6 Å to $+6$ Å for the nuclear coordinate R . The number of grid points is 512 in each direction, and the time step of the propagations is set to 0.0024 fs.

Different initial wave functions are incorporated. They are defined as

$$\Psi(r, R, 0) = N e^{-\beta(R-R_0)^2} \phi_n(r; R) \quad (4)$$

where N is a normalization constant and β is set to 3.57 Å^{-2} in all of our numerical examples. In eq 4 appear the adiabatic (real-valued) electronic wave functions, which are determined by solution of the electronic Schrödinger equation. This also yields the adiabatic potential curves $V_n(R)$ in the electronic states with quantum number n . We solve the electronic problem using imaginary time propagation²¹ on the electronic grid.

Figure 1 shows the potential curves of the first two electronic states, obtained for different values of the screening parameter R_c as indicated. In the case of $R_c = 1.5$ Å (upper left panel), the electronic ground state potential $V_0(R)$ is energetically well separated from the curves of the excited states. This suggests that a ground-state wave packet motion can accurately be described using the Born–Oppenheimer (BO) approximation. The larger value $R_c = 5.0$ Å leads to the potentials displayed in upper right panel of the figure. This is a case of strong coupling, where the energy gap at the avoided crossing of the potentials at $R = 0$ is only 0.0076 eV.

Inserting the probability density $\rho(r, R, t) = |\Psi(r, R, t)|^2$ into eq 1 yields the total entropy $S^{\text{tot}}(t)$. The nuclear ($\rho^{\text{nuc}}(R, t)$) and electronic ($\rho^{\text{el}}(r, t)$) particle densities are obtained by integration over the coordinates r and R , respectively. We may then, via eq 1, determine the single-particle entropies $S^{\text{nuc}}(t)$ and $S^{\text{el}}(t)$. An important quantity is the “mutual information” $I(t)$, which provides information on the correlation between the single particles¹ (for an illustrative example, see the work on quantum oscillator systems²²). In our case $I(t)$ is defined as

$$I(t) = S^{\text{el}}(t) + S^{\text{nuc}}(t) - S^{\text{tot}}(t) \quad (5)$$

The expansion of the total wave function in terms of the adiabatic basis of electronic functions reads

$$\Psi(R, r, t) = \sum_{n=0}^{\infty} \psi_n(R, t) \phi_n(r; R) \quad (6)$$

and the state-specific populations are calculated by projection as $P_n(t) = |\langle \phi_n | \Psi(t) \rangle|^2$. In what follows, we refer to the BO case if we use the $n = 0$ term of the expansion to arrive at the numerical results. We have checked that (for the case with $R_c =$

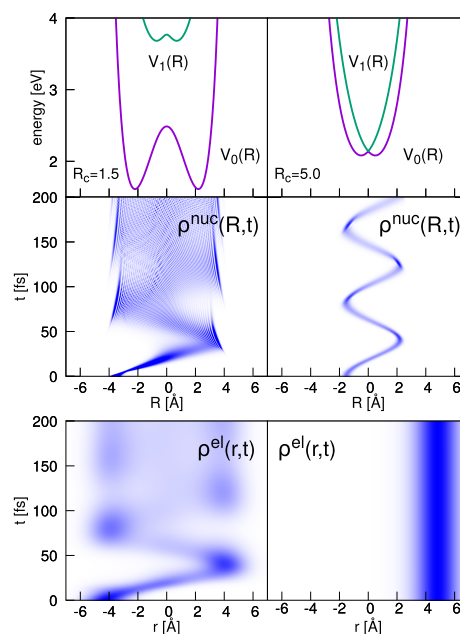


Figure 1. Upper panels: Adiabatic potential curves obtained for screening parameters $R_c = 1.5$ Å (left) and $R_c = 5.0$ Å (right). The nuclear and electronic probability densities for the two cases are displayed in the middle and lower panels, respectively. In the first case ($R_c = 1.5$ Å), the initial Gaussian wave function is centered at $R_0 = -3.5$ Å (middle left), whereas for $R_c = 5.0$ Å its center is at $R_0 = -1.5$ Å (middle right).

1.5 Å) this yields the same results as when the usual BO wave function $\Psi^{\text{BO}}(r, R, t) = \psi_0^{\text{BO}}(R, t) \phi_0(r; R)$ is employed, where $\psi_0^{\text{BO}}(R, t)$ is determined from the nuclear Schrödinger equation which contains the ground-state potential $V_0(R)$.

In the first numerical example, the screening parameter is set to $R_c = 1.5$ Å, and the initial wave function (eq 4) contains the ground-state electronic wave function $\phi_0(r; R)$. The center of the Gaussian is at $R_0 = -3.5$ Å. For this initial condition, the dynamics takes place exclusively in the ground electronic state. In other words, the ground-state population $P_0(t)$ remains equal to 1 at all times regarded, where numerical deviations are in the order of 0.1%. Thus, we deal with a situation where the BO approximation is accurate.

The nuclear and electronic density dynamics are illustrated in the middle and lower left panels of Figure 1. It is seen that the densities perform an in-phase oscillation which is in accord with the picture of an adiabatic motion, where electrons instantaneously adapt to changes in the nuclear geometry. As time goes along, dispersion occurs, so that at 200 fs the densities are spread throughout the classically accessible region.

To characterize the motion of the electron–nuclear wave packet, we also calculate the expectation values $\langle x \rangle_t$ and the variances $\Delta x_t = \sqrt{\langle (x - \langle x \rangle_t)^2 \rangle}$ associated with the nuclear ($x = R$) and electronic ($x = r$) degrees of freedom. As can be seen in the middle left panel of Figure 2, the proton starts at the center of the initial Gaussian wave function, and as can be illustrated in the density dynamics shown in Figure 1, it

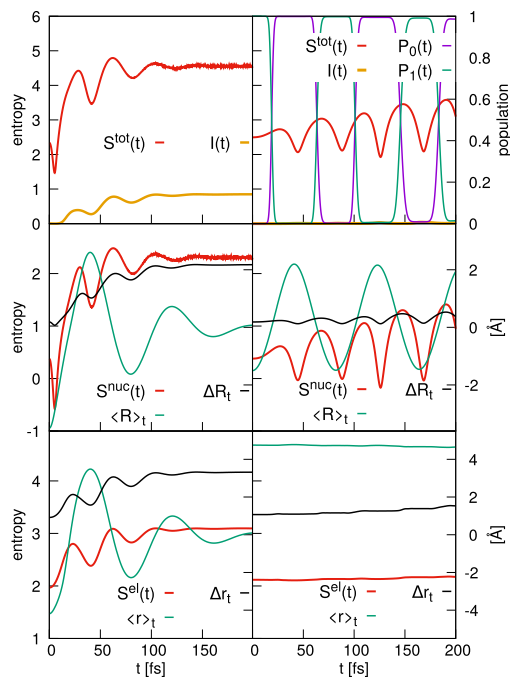


Figure 2. BO dynamics (left) versus non-adiabatic dynamics (right). The upper panels contain the total entropy $S^{\text{tot}}(t)$, the populations $P_n(t)$, and the mutual information $I(t)$. The middle and lower panels show the nuclear and electronic entropies, respectively. Also shown are the coordinate expectation values and the widths, as indicated.

performs oscillations with a period of ~ 80 fs. Due to dispersion, the oscillation amplitude decreases as a function of time. Simultaneously, the width of the density (ΔR_t) increases, in the average, thereby exhibiting local minima and maxima. The minima occur at times when the wave packet reverses its direction of motion at the classical turning points, where the probability density is focused. An additional minimum can be seen at around 5 fs, which is related to a localization of the nuclear density behaving, for short times, like a squeezed Gaussian state in a harmonic potential.²³

The time behavior of the nuclear entropy (middle left panel of Figure 2) is directly related to the nuclear density dynamics. Comparing the width ΔR_t with the nuclear entropy shows that the two functions exhibit extrema at the same times. The smaller the width, the more we know about the location of the nucleus, independently of the position of the electron. This goes in hand with a smaller entropy, i.e., a larger amount of information. For longer times, the nuclear entropy approaches a value of 2.3. We note that if one assumes a uniform nuclear density between the classical turning points at $R_{\pm} \approx \pm 3.5$ Å, a value of 2.58 is found for the entropy. It is important to realize that the sign change of the entropy has no meaning because the entropy may be shifted by a coordinate transformation to positive values.¹¹

The expectation value of the electronic coordinate oscillates with the same period as the one for the nuclear coordinate (Figure 2, lower left). Also, the electronic width follows the

respective curve for the nucleus. They are a little out of phase at early times (because of the squeezing of the nuclear density) but then are in phase after the first reflection of the wave packet takes place. The temporal variation of the electronic entropy is determined by the width of the electronic density. In particular, the minima and maxima of the two curves show a clear correlation. Thus, the entropies associated with the two particles are similar, and what is different is their magnitude. This is related to the fact that the electronic density is more delocalized than the nuclear density.

The total entropy $S^{\text{tot}}(t)$ is displayed in the upper left panel of Figure 2. Its time dependence is similar to those of the particle entropies. The mutual information $I(t)$ (see eq 5) is also shown in the figure. Its extrema directly correlate with those of the widths calculated for the electronic and nuclear degrees of freedom. In particular, at the turning points, where a focusing of the wave packet takes place, $I(t)$ shows minima, which implies that the electron–nuclear correlation decreases. This is an interesting observation which can be explained in regard to the wave function $\psi_0(R, t)\phi_0(r; R)$ describing the BO dynamics. For the nuclear wave function $\psi_0(R, t)$ being localized sharply around $\langle R \rangle_t$ at time t , the dependence of the electronic wave function $\phi_0(r; R)$ on R may be approximated by setting $R = \langle R \rangle_t$, so that the electronic wave function is $\phi_0(r, \langle R \rangle_t)$ and the particle densities are $\rho^{\text{nuc}}(R, t) = |\psi_0(R, t)|^2$ and $\rho^{\text{el}}(r, t) = |\phi_0(r; \langle R \rangle_t)|^2$. The total entropy then is

$$\begin{aligned} S^{\text{tot}} &= - \int dr \int dR \rho^{\text{nuc}}(R, t) \rho^{\text{el}}(r, t) \ln[\rho^{\text{nuc}}(R, t) \rho^{\text{el}}(r, t)] \\ &= S^{\text{nuc}}(t) + S^{\text{el}}(t) \end{aligned} \quad (7)$$

where we have used the fact that the ground-state population $P_0(t)$ is equal to 1 and the electronic wave function is normalized. Then, according to eq 5, the mutual information vanishes. In the numerical example, the involved approximations are only partly fulfilled, so that $I(t)$ is not zero at the reflection points but exhibits minima. With increasing spreading of the nuclear wave function, the R dependence of the electronic wave function becomes more significant, which goes in hand with an increasing amount of correlation, i.e., a larger value of the mutual information.

After studying the BO case, we now turn to a motion with strong non-adiabatic transitions. This can be realized in setting the screening parameter R_c appearing in the potential $V(r, R)$ to a value of 5.0 Å. We start the wave packet motion with the initial function of eq 4, where the electronic wave function is that of the first excited electronic state ($\phi_1(r; R)$) and the nuclear Gaussian function is centered at $R_0 = -1.5$ Å. The nuclear and electronic density dynamics are illustrated in the middle and lower right panels of Figure 1. It is seen that the nuclear density remains rather localized and oscillates almost harmonically. This can be interpreted as a nuclear motion in the diabatic potential which is obtained by connecting the branch of the adiabatic potential $V_1(R)$ at negative distances R with that of the adiabatic potential $V_0(R)$ at positive distances (see the upper right panel of the figure). On the other hand, the electronic density remains located around the position of the fixed proton at 5 Å during the large-amplitude motion of the nucleus, i.e., it is independent of the nuclear coordinate R . Thus, we encounter the case of a diabatic motion.²⁴

What can be taken from the densities is also apparent in the coordinate expectation values for the two particles. They are displayed, together with the associated variances and entropies, in the middle and lower right panels of Figure 2. Whereas in

the nuclear case a quasi-harmonic curve is found, the mean electronic position is nearly constant. During the motion, the nuclear variance exhibits an overall small increase, thereby showing local minima and maxima. As already discussed in connection with the BO motion, at the turning points, where the density is focused and thus its width is reduced, the entropy $S^{\text{nuc}}(t)$ exhibits minima, which means that at these times we acquire more information about the proton's position. In contrast to the nuclear case, the electronic variance is almost time-independent, and as a consequence, the electronic entropy is nearly constant. Because the electronic wave function does not carry a significant dependence on the nuclear coordinate, eq 7 applies, i.e., the total entropy is just the sum of the electronic and nuclear entropies. Accordingly, the mutual information is zero, and thus, for this example of a diabatic motion, no correlation between the electron and nucleus exists.

The fact that in the just discussed example we do not find a correlation between the two particles does not come as a surprise because the electronic eigenfunction does not depend on the nuclear position. This somehow contradicts what is suggested by the picture evolving from the adiabatic expansion of the wave function (eq 6): The populations $P_n(t)$ in the first two electronic states show a clear reminiscence of a strong non-adiabatic coupling (see Figure 2, upper right). Starting with a population $P_1(t) = 1$, a transition to the ground state takes place at around 18.7 fs with an efficiency of 100%. The population exchange between the two states then occurs periodically. One would expect that at the times when the transitions occur, a strong electron–nuclear correlation is present, but this should not be confused with a strong non-adiabatic coupling. To discuss this point in more detail, we regard the decomposition of the entropy in terms of the adiabatic expansion of the total wave function, which yields the following expression for the probability density:

$$\rho(r, R, t) = |\Psi(r, R, t)|^2 = \sum_{n,m=0}^{\infty} \rho_{nm}(r, R, t) \quad (8)$$

with the matrix elements

$$\rho_{nm}(r, R, t) = \psi_n^*(R, t) \psi_m(R, t) \phi_n^{\text{el}}(r; R) \phi_m^{\text{nuc}}(r; R) \quad (9)$$

From these matrix elements we calculate adiabatic nuclear ($\rho_{nm}^{\text{nuc}}(R, t)$) and electronic matrix elements ($\rho_{nm}^{\text{el}}(r, t)$) by integration. Whereas the off-diagonal elements of $\rho_{nm}^{\text{nuc}}(R, t)$ are equal due to the orthogonality of the electronic eigenfunctions, the respective elements of $\rho_{nm}^{\text{el}}(r, t)$ are not. However, in our example they are negligible. The diagonal terms are positive-semidefinite and can thus be interpreted as densities (which are not normalized to unity). Using the diagonal elements of the total, nuclear, and electronic densities in the definition for the entropy (eq 1), one arrives at the respective state-specific entropies $S_n(t)$, $S_n^{\text{nuc}}(t)$, and $S_n^{\text{el}}(t)$. The total entropy and the components $S_n(t)$ are displayed in the upper panel of Figure 3. Also shown is the sum over the components. It is seen that the sum is a very good approximation to the total entropy, with only minor deviations found at the times when the non-adiabatic transitions take place. The reason is that in our case where only two states participate, the two nuclear wave packets $\psi_0(R, t)$ and $\psi_1(R, t)$ do not have a significant spatial overlap, even at the times of the transitions. The single components $S_n(t)$ are directly related to the populations in the two states. If only one state m is populated, then we have $S^{\text{tot}}(t) = S_n(t)$, and

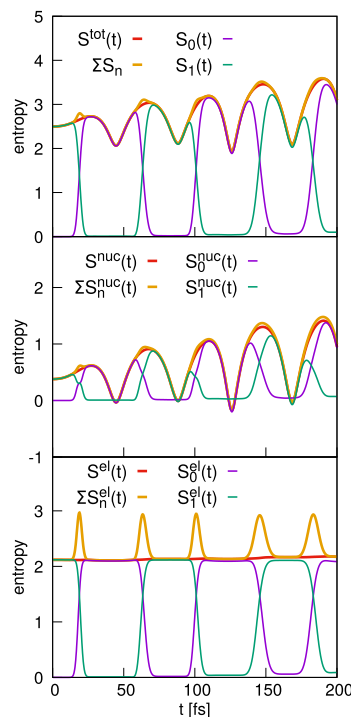


Figure 3. Decomposition of the total entropy $S^{\text{tot}}(t)$ (upper panel) and the particle entropies $S^{\text{nuc}}(t)$ and $S^{\text{el}}(t)$ (middle and lower panels, respectively) in terms of the single-state entropies $S_n(t)$, $S_n^{\text{nuc}}(t)$, and $S_n^{\text{el}}(t)$. Also shown are the sums over the respective components.

during the transitions one component decreases in the same way as the other increases. Thus, the first kind of information encoded in the state-specific entropies is the occupation of the states. Second, we learn about the focusing and broadening of the probability density in the different states, which is reflected in additional extrema.

The entropy of the proton density and its decomposition are illustrated in the middle panel of Figure 3. For the same reasons as mentioned in the case of the total entropy, the sum over the components $S_n^{\text{nuc}}(t)$ reproduces the nuclear entropy excellently. The nuclear components carry information about the populations in the adiabatic states and the degree of localization of the nucleus.

A different situation is encountered in the electronic case, as can be seen in the lower panel of Figure 3. There, the components exclusively reflect the populations in the two states. Also, their summation yields a curve which shows considerable deviations from the constant electronic entropy at the times of the non-adiabatic transitions. Because the off-diagonal elements appearing in the electronic density expansion can be neglected, we have

$$S^{\text{el}}(t) = -\int dr \sum_{n=0}^1 \left(\int dR |\psi_n(R, t)|^2 |\phi_n(r; R)|^2 \right) \times \ln \left[\sum_{m=0}^1 \left(\int dR |\psi_m(R, t)|^2 |\phi_m(r; R)|^2 \right) \right] \quad (10)$$

We have checked numerically that at the time of the first transition ($t_{\text{tr}} = 18.7$ fs), where one has $P_0(t_{\text{tr}}) = P_1(t_{\text{tr}})$, the integrals $\int dR |\psi_n(R, t_{\text{tr}})|^2 |\phi_n(r; R)|^2$ ($n = 0, 1$) are approximately equal. This has the consequence that the electronic entropy can be written as

$$S^{\text{el}}(t_{\text{tr}}) \approx -\ln[2] + S_0^{\text{el}}(t_{\text{tr}}) + S_1^{\text{el}}(t_{\text{tr}}) \quad (11)$$

so that the sum of the diagonal contributions differs by an additive constant of $\ln[2]$ from $S^{\text{el}}(t_{\text{tr}})$. This is confirmed by the curve shown in the lower panel of Figure 3.

To summarize, we have determined coordinate-space differential Shannon entropies for coupled electronic–nuclear wave packet motion. Two limiting cases have been considered. One is BO dynamics taking place exclusively in the electronic ground state. Here, the nuclear and electronic entropies vary in phase as a function of time. Entropic minima correlate with a focusing of the electronic and nuclear probability densities, which is accompanied by an increased knowledge of one or the other particle's position. At the times when the localizations take place, the mutual information exhibits minima indicating a loss of electron–nuclear correlation.

Another situation is the case of diabatic motion, where the electron density changes only marginally during the nuclear dynamics. As a consequence, the electronic entropy is constant, and the total entropy is the sum of the single-particle entropies. This means that the mutual information is zero, and thus, nuclear–electron correlation is absent. This also holds at the times when the avoided crossing is passed. Although there is a strong non-adiabatic coupling, this does not influence the lack of particle correlation. A decomposition of the entropies into components relating to the different electronic states shows that the total and nuclear entropies are well-approximated by summing the diagonal contributions from the participating states, which is not true for the electronic entropy. In the latter case, the state-specific entropies contain only information about the state populations, whereas for the nuclear motion they reveal entangled information about the occupation of the states and, separately, the nuclear localization in these states.

We have demonstrated that the Shannon differential entropies reveal information on the electronic and nuclear localization and thus are closely related to the widths of the respective densities. The mutual information (MI) contains correlation effects of all orders, whereas other measures, like the covariance, are restricted to describing linear effects (for a comparison and extended discussion, see, e.g., ref 22). We have calculated the covariance for the case of the coordinates r and R and the BO dynamics. It is found that this function behaves similar to the MI. Thus, in our study of coupled electron–nuclear dynamics, linear correlations seem to dominate. However, when the MI is determined in momentum space (using the momentum-space densities) and compared to the covariance for the electronic and nuclear momenta, larger deviations are found, in particular when the BO approximation is applied. This important point will be investigated in more detail in the future.

■ AUTHOR INFORMATION

Corresponding Author

Volker Engel – Institut für Physikalische und Theoretische Chemie, Universität Würzburg, 97074 Würzburg, Germany; orcid.org/0000-0003-1429-1833; Phone: +499313186376; Email: volker.engel@uni-wuerzburg.de

Author

Peter Schürger – Institut für Physikalische und Theoretische Chemie, Universität Würzburg, 97074 Würzburg, Germany

Complete contact information is available at:

<https://pubs.acs.org/10.1021/acs.jpclett.2c03635>

Notes

The authors declare no competing financial interest.

■ REFERENCES

- (1) Shannon, C. E. A mathematical theory of communication. *Bell Syst. Tech. J.* **1948**, *27*, 379–423.
- (2) Jaynes, E. T. Information theory and statistical mechanics. *Phys. Rev.* **1957**, *106*, 620–630.
- (3) Jaynes, E. T. Information theory and statistical mechanics. II. *Phys. Rev.* **1957**, *108*, 171–190.
- (4) Ben-Naim, A. *A Farewell to Entropy*; World Scientific, 2008.
- (5) Levine, R. D. The information theoretic approach to intramolecular dynamics. *Ad. Chem. Phys.* **2007**, *47*, 239–292.
- (6) Quack, M. In *Femtosecond Chemistry: A Handbook in Two Volumes*; Manz, J., Wöste, L., Eds.; VCH: Weinheim, Germany, 1995; Vol. II, pp 781–818.
- (7) Quack, M. On the emergence of simple structures in complex phenomena: Concepts and some numerical examples. *Adv. Chem. Phys.* **2014**, *157*, 97.
- (8) Jia, D.; Manz, J.; Yang, Y. From coherent quasi-irreversible quantum dynamics towards the second law of thermodynamics: The model boron rotor B_{13}^+ . *AIP Adv.* **2018**, *8*, 045222.
- (9) Ludeña, E. V.; Torres, F. J.; Becerra, M.; Rincón, L.; Liu, S. Shannon entropy and Fisher information from a non-Born-Oppenheimer perspective. *J. Phys. Chem. A* **2020**, *124*, 386–394.
- (10) Cover, T. M.; Thomas, J. A. *Elements of Information Theory*, 2nd ed.; Wiley Series in Telecommunications and Signal Processing; Wiley-Interscience, 2006.
- (11) Hertz, A.; Cerf, N. J. Continuous-variable entropic uncertainty relations. *J. Phys. A* **2019**, *S2*, 173001.
- (12) Majerník, V.; Opatrný, T. Entropic uncertainty relations for a quantum oscillator. *J. Phys. A* **1996**, *29*, 2187–2197.
- (13) Garbaczewski, P. Differential entropy and time. *Entropy* **2005**, *7*, 253–299.
- (14) Schürger, P.; Schaupp, T.; Kaiser, D.; Engels, B.; Engel, V. Wave packet dynamics in an harmonic potential disturbed by disorder: Entropy, uncertainty, and vibrational revivals. *J. Chem. Phys.* **2022**, *156*, 054303.
- (15) Hirschman, I. I. A Note on Entropy. *Am. J. Math.* **1957**, *79*, 152.
- (16) Beckner, W. Inequalities in Fourier Analysis. *Ann. Math.* **1975**, *102*, 159.
- (17) Białynicki-Birula, I.; Mycielski, J. Uncertainty relations for information entropy in wave mechanics. *Commun. Math. Phys.* **1975**, *44*, 129–132.
- (18) Shin, S.; Metiu, H. Multiple time scale quantum wavepacket propagation: Electron-nuclear Dynamics. *J. Phys. Chem.* **1996**, *100*, 7867–7872.
- (19) Shin, S.; Metiu, H. Nonadiabatic effects on the charge transfer rate constant: A numerical study of a simple model system. *J. Chem. Phys.* **1995**, *102*, 9285–9295.
- (20) Feit, M. D.; Fleck, J. A.; Steiger, A. Solution of the Schrödinger equation by a spectral method. *J. Comput. Phys.* **1982**, *47*, 412–433.

- (21) Kosloff, R.; Tal-Ezer, H. A direct relaxation method for calculating eigenfunctions and eigenvalues of the Schrödinger equation on a grid. *Chem. Phys. Lett.* **1986**, *127*, 223–230.
- (22) Salazar, S. J. C.; Laguna, H. G.; Sagar, R. P. Pairwise and higher-order statistical correlations in excited states of quantum oscillator systems. *Eur. Phys. J. Plus* **2022**, *137*, 19.
- (23) Tannor, D. J. *Introduction to Quantum Mechanics: A Time-Dependent Perspective*; University Science Books: Sausalito, CA, 2007.
- (24) Baer, M. *Beyond Born-Oppenheimer: Electronic Nonadiabatic Coupling Terms and Conical Intersections*; Wiley: Hoboken, NJ, 2006.

Recommended by ACS

Density Matrix via Few Dominant Observables for the Ultrafast Non-Radiative Decay in Pyrazine

Ksenia Komarova.

JANUARY 19, 2023

JOURNAL OF CHEMICAL THEORY AND COMPUTATION

READ 

Factorized Electron–Nuclear Dynamics with an Effective Complex Potential

Sophya Garashchuk, Vitaly Rassolov, *et al.*

FEBRUARY 16, 2023

JOURNAL OF CHEMICAL THEORY AND COMPUTATION

READ 

Time-Dependent Expectation Values from Integral Equations for Quantum Flux and Probability Densities

P. Schürger, V. Engel, *et al.*

NOVEMBER 22, 2022

THE JOURNAL OF PHYSICAL CHEMISTRY A

READ 

Variational Approach for Linearly Dependent Moving Bases in Quantum Dynamics: Application to Gaussian Functions

Loïc Joubert-Doriot.

SEPTEMBER 27, 2022


JOURNAL OF CHEMICAL THEORY AND COMPUTATION

READ 


Get More Suggestions >

6.3.2 Differential Shannon entropies and correlation measures for Born–Oppenheimer electron–nuclear dynamics: numerical results and their analytical interpretation [5]


Reproduced from "P. Schürger, V. Engel, *Phys. Chem. Chem. Phys.* 2023, 25, 28373–28381" with permission from the PCCP Owner Societies.




PAPER



View Article Online
View Journal | View Issue

 Check for updates

Differential Shannon entropies and correlation measures for Born–Oppenheimer electron–nuclear dynamics: numerical results and their analytical interpretation

Peter Schürger and Volker Engel *

Cite this: *Phys. Chem. Chem. Phys.*, 2023, 25, 28373

Received 27th July 2023, Accepted 24th September 2023
DOI: 10.1039/d3cp03573e
rsc.li/pccp

1. Introduction

An isolated quantum system at a time t , having coordinates x , is completely characterized by its wave function $\psi(x, t)$. However, a wave function is a complicated object, and the stored information is often not easily extracted, in particular for systems composed of many particles moving in three-dimensional space. In statistical mechanics, entropy may be interpreted in terms of the amount of available information where, for a thermodynamical ensemble, a large entropy correlates with a low degree of information.^{1–4} For a quantum mechanical ensemble in a pure state, one may follow an analogous approach in introducing the differential Shannon entropy $S(t)$ ^{5,6} derived from the probability density $\rho(x, t) = |\psi(x, t)|^2$ as

$$S(t) = - \int dx \rho(x, t) \ln[\rho(x, t)]. \quad (1)$$

A pedagogical example to illustrate the information theoretical interpretation of differential entropy in a pure quantum system is the motion of a Gaussian in a harmonic potential.^{7–10} There, it can be shown analytically that the entropy is directly related to the width of the Gaussian. Thus, for a broad spatial wave function, where one knows less about the localization of a particle, the entropy assumes a large value. Also, one finds that the sum of entropies calculated from coordinate-space and momentum-space densities is a measure for the coordinate-momentum uncertainty, a property which also holds in general.^{6,11–13} Several authors have used the entropy in the context of chemical problems, see, e.g., ref. 14–18. Here we also mention investigations on different entropic measures used to characterize chemical reactions,¹⁹ neutral atoms and ions.^{20,21}

The above discussed example refers to a single particle harmonic oscillator motion. However, the entropy concept can easily be extended to several interacting particles. A fundamental problem in molecular systems is the combined motion of electrons and nuclei, which is characterized by the time-dependent probability density. Using the latter, one may calculate the differential Shannon entropy of the total system and also, employing the electronic and nuclear coordinate densities, the entropies associated with the different particles. These functions reveal information about the localization of one or the other kind of particles.

Of large interest is the correlation between electrons and nuclei. In a more fashionable formulation this is the “entanglement” of these particles.²² Having the Shannon entropies at hand, the “mutual information” (MI) which is a measure of correlation,^{1,23} can be determined. We use the differential Shannon entropy to extract information on the system under consideration. Even though the von Neumann entropy, which is a quantum mechanical extension to the Gibbs entropy, is a much more common entropy measure, the advantage is that, while the von Neumann entropy is per definition equal to zero in an isolated quantum system (as is treated here), we can use the differential Shannon entropy to obtain a meaningful

Universität Würzburg, Institut für Physikalische und Theoretische Chemie, Emil-Fischer-Str. 42, 97074 Würzburg, Germany. E-mail: volker.engel@uni-wuerzburg.de; Fax: +49 931 85423; Tel: +49 931 31 86376

This journal is © the Owner Societies 2023

Phys. Chem. Chem. Phys., 2023, 25, 28373–28381 | 28373

Published on 26 September 2023. Downloaded by Universitaetsbibliothek Wuerzburg on 11/13/2023 12:04:29 PM.

definition of entropy and study dynamical effects. We concentrate on the coordinate space dynamics. One also can derive the entropies from the momentum space wave functions, and these functions yield different information. Therefore, it has been noted that one should combine these two entropy functions,⁶ which is, however, out of the scope of the present paper.

In the present work we calculate the mutual information emerging from a coupled electron–nuclear dynamics and compare it to other measures of correlation, thereby extending our earlier work.²⁴ This will be done under simplifying assumptions analytically, and also using a numerical example. The focus of the present study is to give the numerical results a mathematical foundation and thus gain a deeper insight into the behavior of the quantum entropy dynamics. The motion considered is one where the Born–Oppenheimer (BO) approximation^{25,26} is valid. This means that the motion is restricted to take place in a single electronic state and thus couplings to other states are negligible.²⁷ In order to realize this situation, we pick a useful model for a one-dimensional coupled electron–nuclear dynamics which was introduced in ref. 28 and 29.

The paper is organized as follows. In Section 2, we describe the model used in the numerical calculations, and we provide the definitions of the time-dependent quantities considered. The analytical and numerical results are collected in Section 3, and concluding remarks are presented in Section 4.

2. Theory and model

2.1 Model for the coupled electronic–nuclear motion

We treat an electron and a proton which move along the coordinates r and R , respectively. They interact with two protons where one is located at $R_1 = -5 \text{ \AA}$ and the other is at $R_2 = +5 \text{ \AA}$. The potential is parameterized as^{28,29} (in atomic units):

$$V(r, R) = \frac{1}{|R_1 - R|} + \frac{1}{|R_2 - R|} - \frac{\text{erf}[|R_1 - r|/R_f]}{|R_1 - r|} - \frac{\text{erf}[|R - r|/R_c]}{|R - r|} - \frac{\text{erf}[|R_2 - r|/R_f]}{|R_2 - r|} + \Delta. \quad (2)$$

Here, the electron–proton interactions are screened using error functions, and an energy shift Δ is introduced so that the minimum of $V(r, R)$ occurs at zero energy in the spatial region covered in our numerical calculations. The parameters R_f and R_c are fixed at values of 1.5 \AA and 1.0 \AA , respectively.

Concerning the relevance of the model, we cite the original paper by Shin and Metiu²⁸ which states that “The model was inspired by a real problem, the transfer of an electron and a sodium ion from one zeolite cage to another. One can also think of the moving ion as a particle of a “medium” which is displaced *i.e.*, polarized when the electron changes its location”. Besides that, the model allows to study the electronic–nuclear motion in various coupling regimes. By tuning the interaction potential, situations ranging from a Born–Oppenheimer dynamics to those of effective non-adiabatic transitions can be realized. In this way it is possible to study many

fundamental aspects because it is feasible to solve the time-dependent Schroedinger equation numerically exactly, see *e.g.*, ref. 30–35. The potential curves evolving from the model reflect characteristics of the electronic structure of diatomic molecules. In the example studied here, we are interested in a BO dynamics and we may compare an approximate BO treatment with what evolves from the exact dynamics. Concerning a generalization of the model, we note that extensions have been presented which are able to characterize BO dynamics and also the motion at conical intersections involving several degrees of freedom.^{36,37} We believe that the results presented in Section 3 are of a more general importance than what could be anticipated by regarding the simplicity of the model.

We numerically solve the time-dependent Schroedinger equation

$$i\hbar \frac{\partial}{\partial t} \Psi(r, R, t) = \hat{H} \Psi(r, R, t) \quad (3)$$

for the coupled electron–nuclear motion with help of the split operator method.³⁸ The Hamiltonian reads

$$\hat{H} = \frac{\hat{p}^2}{2} + \frac{\hat{P}^2}{2M} + V(r, R), \quad (4)$$

where \hat{p} and \hat{P} are the electronic and nuclear momentum operators, respectively, and M is the proton mass. The wave functions $\Psi(r, R, t)$ are represented on a grid with $-12 \text{ \AA} \leq r \leq +12 \text{ \AA}$ and $-6 \text{ \AA} \leq R \leq +6 \text{ \AA}$. For each coordinate a number of 512 grid points is used, and the time step entering the propagators is $\Delta t = 0.0024 \text{ fs}$.

As initial conditions we employ a function of the form

$$\Psi(r, R, 0) = N_0 e^{-\beta_0(R-R_0)^2} \varphi_0(r; R), \quad (5)$$

with N_0 being a normalization constant. The Gaussian in the latter equation is centered at $R_0 = -3.5 \text{ \AA}$, and its width is determined by the parameter β_0 which is set to a value of 7.14 \AA^{-2} . The electronic wave function $\varphi_0(r; R)$ is obtained, employing imaginary time propagation,³⁹ in solving the electronic Schroedinger equation

$$\left[\frac{\hat{p}^2}{2} + V(r, R) \right] \phi_0(r; R) = V_0(R) \phi_0(r; R). \quad (6)$$

Here, $V_0(R)$ is the adiabatic potential curve associated with the electronic ground state. This potential is displayed in the upper panel of Fig. 1. The energy gap between $V_0(R)$ and the potential $V_1(R)$ of the first excited state is about 4 eV (at $R = 0$) which hints at the fact that, under the specified initial condition (eqn (5)), the dynamics is restricted to take place in the ground state. This is indeed the case in our numerical example which is checked in calculating the time-dependent population $P_0(t) = |\langle \varphi_0 | \Psi(t) \rangle|^2$. The latter is, within a deviation of 0.1% , equal to one.

The electronic ground state wave function $\varphi_0(r; R)$ is also displayed in Fig. 1, lower panel. It is seen that it shifts almost linearly with increasing values of the nuclear coordinate R . This is characteristic for an adiabatic motion, where the electronic properties smoothly adapt to the nuclear geometry. We note

PCCP

[View Article Online](#)

Paper

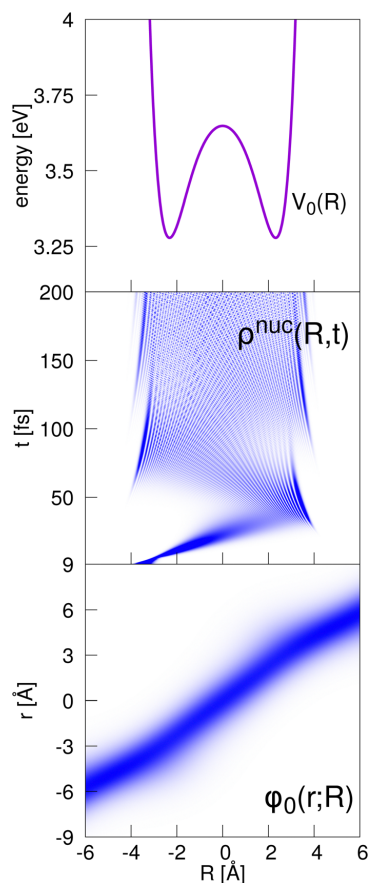


Fig. 1 Upper panel: Adiabatic potential curve of the electronic ground state. Middle panel: Time-dependent nuclear probability density for times up to 200 fs. The lower panel shows the ground state electronic wave function $\phi_0(r; R)$.

that the function approximately is of Gaussian form with a constant width.

2.2 Differential entropies and correlation measures for electronic–nuclear motion

In order to calculate entropies according to eqn (1), we need probability densities. Given the time-dependent wave function, the coordinate probability density is

$$\rho(r, R, t) = |\Psi(r, R, t)|^2. \quad (7)$$

Single particle densities are obtained by integration. This leads to the electronic (el) density

$$\rho^{\text{el}}(r, t) = \int dR |\Psi(r, R, t)|^2, \quad (8)$$

and the nuclear (nuc) density

$$\rho^{\text{nuc}}(R, t) = \int dr |\Psi(r, R, t)|^2. \quad (9)$$

From the three probability densities we determine the total differential Shannon entropy

$$S(t) = - \int dr \int dR \rho(r, R, t) \ln[\rho(r, R, t)], \quad (10)$$

and the single particle entropies are

$$S^{\text{el}}(t) = - \int dr \rho^{\text{el}}(r, t) \ln[\rho^{\text{el}}(r, t)], \quad (11)$$

$$S^{\text{nuc}}(t) = - \int dR \rho^{\text{nuc}}(R, t) \ln[\rho^{\text{nuc}}(R, t)]. \quad (12)$$

We next regard different measures for the electron–nuclear correlation, and the first one is the “mutual information” $I(t)$ which is

$$I(t) = S^{\text{el}}(t) + S^{\text{nuc}}(t) - S(t). \quad (13)$$

Another measure for correlation is the “covariance”⁴⁰ which, for our two coordinates R and r , is defined as

$$\text{cov}(t) = \langle Rr \rangle_t - \langle r \rangle_t \langle R \rangle_t, \quad (14)$$

where the brackets denote the time-dependent expectation values. Furthermore, the “correlation”⁴⁰ is defined as

$$\text{corr}(t) = \frac{\text{cov}(t)}{\sigma_R(t)\sigma_r(t)}, \quad (15)$$

with the variances

$$\sigma_R^2(t) = \langle R^2 \rangle_t - \langle R \rangle_t^2, \quad (16)$$

$$\sigma_r^2(t) = \langle r^2 \rangle_t - \langle r \rangle_t^2. \quad (17)$$

3. Results

3.1 Analytical considerations

In this section we calculate entropies and correlation measures analytically. The resulting expressions mainly derive from the evaluation of various forms of Gaussian-type integrals. Here we summarize the central equations, for more details the reader is referred to the appendix.

We treat a Born–Oppenheimer dynamics in the electronic ground state, where (suppressing, for convenience, the electronic quantum number $n = 0$) the wave function of the system reads

$$\Psi(r, R, t) = \psi(R, t) \phi(r; R). \quad (18)$$

In what follows, we assume that the nuclear wave packet, initially being a Gaussian (see eqn (5)) remains of Gaussian form in the time interval considered. The electronic wave function $\phi(r; R)$ is set to a Gaussian of constant width (*i.e.* it is independent of R) and is centered at the nuclear coordinate R . Regarding Fig. 1 (lower panel), it is seen that the latter

assumptions are not unrealistic for the present parameterization of the interaction potential. On the other hand, the nuclear density which is displayed in the middle panel of Fig. 1 exhibits a large dispersion which means that a frozen Gaussian approximation is poor, but a Gaussian with time-dependent width is potentially a good approximation for the wave function. Under the specified conditions, the BO wave function is

$$\Psi(r, R, t) = N_t e^{-\frac{\beta_t}{2}(R-R_t)^2} e^{-\frac{\gamma}{2}(r-R_t)^2}. \quad (19)$$

Here, R_t is the center of the Gaussian wave packet which shifts as a function of time. Note that the normalization factor N_t and the parameter β_t are as well time-dependent because dispersion of the wave packet occurs. On the other hand, we choose γ as a constant.

Using the ansatz for the wave (eqn (19)), the entropy can be evaluated as:

$$S(t) = -\ln \left[\frac{\sqrt{\gamma\beta_t}}{\pi} \right] + 1. \quad (20)$$

To determine the electronic entropy, the electronic density is needed, and it takes the form

$$\rho^{\text{el}}(r, t) = \sqrt{\frac{\beta_t \gamma}{(\beta_t + \gamma)\pi}} e^{-\frac{\gamma\beta_t}{\beta_t + \gamma}(r-R_t)^2}. \quad (21)$$

Note that the time-dependence of the electronic density enters through the nuclear wave packet motion, namely through the width β_t and the center of the Gaussian at R_t . For the expectation value of the electronic coordinate we then have $\langle r_t \rangle = R_t$, and the electronic entropy is

$$S^{\text{el}}(t) = -\ln \left[\sqrt{\frac{\beta_t \gamma}{(\beta_t + \gamma)\pi}} \right] + \frac{1}{2}. \quad (22)$$

The nuclear density is obtained upon integration over the electronic coordinate r :

$$\rho^{\text{nuc}}(R, t) = \sqrt{\frac{\beta_t}{\pi}} e^{-\beta_t(R-R_t)^2}, \quad (23)$$

from which it follows that $\langle R_t \rangle = R_t$, and the nuclear entropy is:

$$S^{\text{nuc}}(t) = -\ln \left[\sqrt{\frac{\beta_t}{\pi}} \right] + \frac{1}{2}. \quad (24)$$

Having equations for the total entropy and the two particle entropies, we now are in the position to give an analytical expression for the mutual information (eqn (13)). In calculating it, the constant terms cancel, and one arrives at the expression

$$I(t) = \frac{1}{2} \ln \left[1 + \frac{\gamma}{\beta_t} \right]. \quad (25)$$

To calculate the covariance, we evaluate the expectation value for the product of the two coordinates with the result:

$$\langle Rr \rangle_t = \frac{1}{2\beta_t} + R_t^2. \quad (26)$$

Taking into account that the expectation values of the two

coordinates are equal to zero, the covariance then is

$$\text{cov}(t) = \frac{1}{2\beta_t}. \quad (27)$$

To determine the correlation, we need the variances for the two degrees of freedom. Using the equation

$$\langle Rr \rangle_t = \langle R^2 \rangle_t, \quad (28)$$

it follows that

$$\sigma_R^2(t) = \text{cov}(t) = \frac{1}{2\beta_t}. \quad (29)$$

Regarding the electronic coordinate, the expectation value of r^2 is determined as:

$$\langle r^2 \rangle_t = \frac{1}{2\gamma} + \langle R^2 \rangle_t = \frac{1}{2\gamma} + \frac{1}{2\beta_t} + R_t^2. \quad (30)$$

We then have the electronic variance

$$\sigma_r^2(t) = \frac{1}{2} \frac{\gamma + \beta_t}{\gamma\beta_t}, \quad (31)$$

leading to

$$\text{corr}(t) = \frac{1}{\sqrt{1 + \beta_t/\gamma}} = \frac{\sigma_R(t)}{\sigma_r(t)}. \quad (32)$$

Let us comment on the results obtained so far. Due to the ansatz for the wave function (eqn (19)), the time dependence of all entropies is determined by the width parameter β_t . Whereas the nuclear entropy depends only on the width (*i.e.* β_t) of the nuclear density, the width of the electronic density also enters into the electronic and total entropy. Both, the mutual information $I(t)$ and the correlation $\text{corr}(t)$, depend on the ratio $f = \gamma/\beta_t$, whereas the covariance $\text{cov}(t)$ depends only on β_t .

We may discuss two different limits, where the first one is that of a fixed value of β_t and large values of γ or, alternatively, fixed γ and small values of β_t . Then, we have

$$\frac{\beta_t \gamma}{\beta_t + \gamma} \rightarrow \beta_t, \quad (33)$$

with the consequence that the electronic density becomes

$$\rho^{\text{el}}(r, t) \rightarrow \sqrt{\frac{\beta_t}{\pi}} e^{-\beta_t(r-R_t)^2} = \rho^{\text{nuc}}(R = r, t). \quad (34)$$

It then follows that the electronic entropy and the nuclear entropy are equal:

$$S^{\text{el}}(t) \rightarrow -\ln \left[\sqrt{\frac{\beta_t}{\pi}} \right] + \frac{1}{2} = S^{\text{nuc}}(t). \quad (35)$$

This means that the information stored in the electronic and nuclear degrees of freedom is equivalent which is associated with a large particle correlation. In the discussed limit, the MI and the covariance diverges, and the correlation takes its maximum value:

$$\lim_{\beta_t \rightarrow 0} \text{cov}(t) = \lim_{\beta_t \rightarrow 0} \frac{1}{2\beta_t} = \infty, \quad (36)$$

$$\lim_{f \rightarrow \infty} I(t) = \lim_{f \rightarrow \infty} \frac{1}{2} \ln[1+f] = \infty, \quad (37)$$

$$\lim_{f \rightarrow \infty} \text{corr}(t) = \lim_{f \rightarrow \infty} \frac{1}{1+f^{-1}} = 1. \quad (38)$$

Note that, because the covariance depends on β_t only, the two cases of fixed β_t and large γ and fixed γ and small β_t are not equivalent for the function $\text{cov}(t)$.

Because, in the discussed limit, the electronic density assumes exactly the form of the nuclear density, the two particles are located very close to each other and if the nucleus moves, the electron which is tacked to it, follows this motion immediately. As a consequence, the information about the electronic and nuclear dynamics is the same which results in an identical electronic and nuclear entropy. Also, the instantaneous following of the electron upon a nuclear displacement yields to a large degree of correlation (however it is measured).

Regard now the second situation where the width parameter, γ takes very small values with β_t being constant or γ being constant and β_t approaching large values. We then find

$$\frac{\beta_t \gamma}{\beta_t + \gamma} \rightarrow \gamma, \quad (39)$$

so that the electronic entropy takes the value

$$S^{\text{el}}(t) \rightarrow -\ln \left[\sqrt{\frac{\gamma}{\pi}} \right] + \frac{1}{2}. \quad (40)$$

This entropy does not depend on properties of the nucleus so that no correlation between the particles is present. This is also reflected in the MI and the correlation which, in the limit of vanishing ratio $f = \gamma/\beta_t$, approaches zero:

$$\lim_{f \rightarrow 0} I(t) = \lim_{f \rightarrow 0} \text{corr}(t) = 0. \quad (41)$$

The covariance also approaches zero with increasing values of β_t :

$$\lim_{\beta_t \rightarrow \infty} \text{cov}(t) = 0. \quad (42)$$

In the first limiting case discussed above, the electronic density responds instantaneously to changes in the width of the nuclear density, whereas in the second limit, it does not. Because the nuclear density is strongly peaked around $R = R_t$, the electronic density effectively behaves as $\rho^{\text{el}} \sim e^{-\gamma(r-R_t)^2}$ so that it takes the form of an electronic eigenfunction at the average nuclear position R_t . The electronic density is spread over a large region of space, and thus the electron is bound only very loosely to the nucleus. This results in a low degree of correlation. To summarize, the meaning of the two limits is that in the “strongly” correlated case, the electron density is forced to be identical to the nucleus density, while in the uncorrelated case, the electron does not depend on the nuclear density. Of course the above discussed limits are not realized in a real system. Rather, we have to distinguish the cases where f (or β_t) takes on a larger or a smaller number. This will be discussed in regarding the numerical example presented in Section 3.2.

3.2 Numerical example

Having the analytical results given in Section 3.1 at hand, we now turn to a numerical example. Therefore we integrate the Schrodinger equation for the coupled two particle motion subject to the initial condition of eqn (5). The time-dependent nuclear probability density is displayed in the middle panel of Fig. 1. Starting with the localized Gaussian at time $t = 0$, the wave packet moves inwards, and it reaches the region of the classical turning point at about 43 fs. Then, the motion is reversed and the starting region is revisited after one vibrational period. Afterwards, dispersion becomes more effective, leading to a nuclear wave packet which, at the end of the shown time interval, spreads over the entire classically accessible region.

The upper panel of Fig. 2 compares the numerically determined nuclear entropy to the analytical result given in eqn (24).

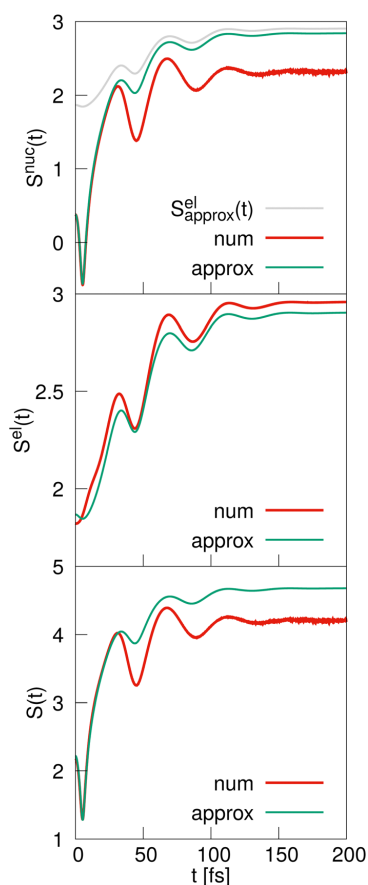


Fig. 2 Shown are the nuclear (upper panel), electronic (middle panel) and total entropies (lower panel). In each case the results from the analytical considerations (approx, eqn (20), (22) and (24)) are compared to the numerically (num) obtained result. For better comparison, the upper panel also contains the analytically derived electronic entropy ($S^{\text{el}}_{\text{approx}}(t)$).

Paper

View Article Online

PCCP

In the latter equation enters the width parameter β_t which is determined from the propagated wave function in calculating the variance $\sigma_R^2(t)$ and using eqn (29). Initially, the two curves agree perfectly. As can be taken from Fig. 1, the Gaussian approximation to the nuclear density is no longer valid around the time, the classical turning point at positive distances R is reached and also does not hold afterwards. This explains the deviations of the two entropies. In more detail, it can be proved that a Gaussian distribution maximizes the entropy over all distributions with the same variance⁵ so that our approximate treatment yields a curve which is larger than the numerically derived one. Nevertheless, the general time dependence of $S^{\text{nuc}}(t)$ is well described by the analytical result. This, in particular, applies to the existence of the extrema. A minimum is found upon the reflection of the wave packet at ≈ 42.5 fs. This is related to the focusing of the nuclear density so that the value of β_t increases, causing the entropy to decrease as it is predicted by eqn (24). The result is in accordance with the interpretation of the entropy: a more localized probability distribution allows to locate the nucleus more precisely which is associated with a larger amount of information. After leaving the turning point region, a spreading of the nuclear density occurs so that information is lost and, accordingly, the entropy increases. We note that there appears an additional minimum in the nuclear entropy at early times (around 5.4 fs). This is due to a “squeezing” of the inward moving wave packet.⁹

The numerically and analytically determined electronic entropies are displayed in the middle panel of Fig. 2, and the agreement between the two curves is excellent. In evaluating the analytical expression, we used an average value of $\gamma = 0.75 \text{ \AA}^{-2}$ which is determined from the electronic wave function $\varphi_0(r; R)$. Besides the minimum at early time which is due to the squeezing of the nuclear density, the time dependence of $S^{\text{el}}(t)$ follows that of the nuclear entropy. This is predicted by eqn (22) which contains the nuclear width parameter β_t . At longer times, the curve becomes constant and for the analytical curves we find that the limit is reached where the nuclear and electronic entropies are approximately equal (see eqn (35)). This, however, is not the case if the numerically determined entropies are compared. The total entropy follows the time dependence of the single particle entropies, and the deviations from the analytically obtained result (eqn (20)) are in the order of those seen in the nuclear entropy.

We next turn to the different functions which characterize the correlation between the electron and the nucleus. Analytical and numerical results for the covariance $\text{cov}(t)$, the correlation $\text{corr}(t)$ and the mutual information $I(t)$ are compared in Fig. 3. Regarding the numerically determined curves, it is seen that their overall appearance is similar. This applies to the location of the minima and maxima and the trend that an overall increase of the functions is found which, at longer times, results in constant values.

The approximate curves track the numerically determined ones rather well so that we may use the analytical results for interpretation. Because the electronic width parameter γ is approximately constant (see Fig. 1), we may discuss the

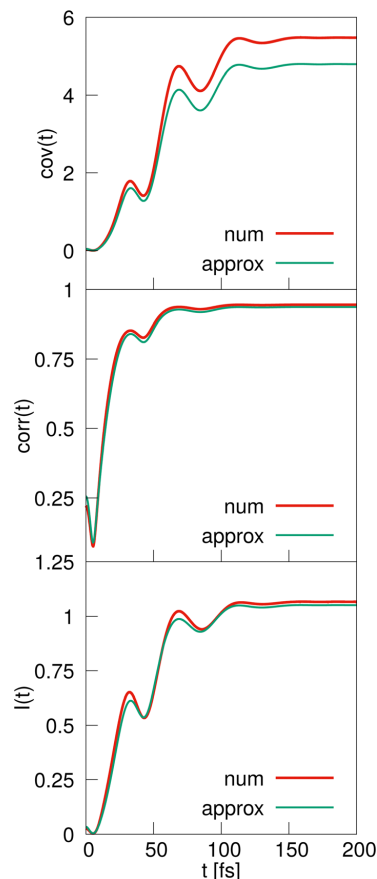


Fig. 3 Comparison of the covariance $\text{cov}(t)$, correlation $\text{corr}(t)$ and mutual information $I(t)$, as indicated. In each case the results from the analytical considerations (approx, eqn (27), (32), (A12)) are compared to the numerical (num) obtained results.

existence of the minima and maxima in terms of variations of the width parameter β_t . For all three curves, maxima in the time-dependent width parameter β_t result in minima which means that a localized nuclear density is associated with a lower degree of electron–nuclear correlation. This finding can be traced back to the BO wave function of eqn (18). If the nuclear function $\psi(R, t)$ is located in a small region around R_t , the R -dependence of the electronic function $\varphi(r; R)$ may be ignored, *i.e.* we may set $\varphi(r; R) = \varphi(r; R_t)$. As a consequence, the total wave function is separable which is equivalent with the absence of correlation. This is the limiting case with $\text{corr}(t) = \text{cov}(t) = I(t) = 0$, and in a realistic situation these functions do not vanish but exhibit minima. Naturally, if the width of the nuclear density increases, so does the correlation and all three functions take on larger values. From Fig. 3 it emerges that the analytical expressions for the mutual information and the

correlation are in excellent agreement with the numerical results, whereas for the covariance, the deviations are larger. In the case of the entropies, we found that the largest deviations between the analytical and numerical results occur in the nuclear case. Because analytically, the covariance does only depend on the nuclear width parameter β_t , it then seems consistent that the same degree of disagreement is found. On the other hand, for the correlation as well as the MI, the analytical predictions are astonishingly good. In the case of the MI this can be understood in rewriting the total entropy as

$$S(t) = S^{\text{nuc}}(t) + \int dR \rho^{\text{nuc}}(R, t) s(R), \quad (43)$$

where

$$s(R) = - \int dr |\varphi(r; R)|^2 \ln[|\varphi(r; R)|^2] \quad (44)$$

is the electronic entropy at fixed geometry R . The entropy is thus the sum of the nuclear entropy and the electronic entropy at fixed values of R , averaged over the nuclear density. Then, the mutual information takes the form:

$$I(t) = S^{\text{el}}(t) + \int dR \rho^{\text{nuc}}(R, t) s(R), \quad (45)$$

which means that the contribution of the pure nuclear entropy is no longer present and the electronic entropy determines the mutual information. Because the Gaussian approximation for the electronic density is accurate, the analytically determined electronic entropy agrees rather well with the numerical result, and so does the MI. Concerning the correlation $\text{corr}(t)$ it can be shown that the Gaussian ansatz for the nuclear and electronic part of the BO wave function is not essential. Under the assumption that the electronic wave functions fulfill $\varphi(r; R) = \varphi(r - R)$ and is symmetric in its argument, the correlation depends only on the variances and not on the particular form of the two wave functions.

4. Summary

To summarize, we investigate an electron–nuclear coupled dynamics taking place in the BO regime, where the time dependence of differential Shannon entropies is determined by properties of the nuclear wave packet. The results of a numerical calculation treating the coupled motion are explained analytically using a Gaussian ansatz for the wave function. In this way, we obtain a more detailed understanding of the complex correlated particle motion, and in particular, its information theoretical aspects evolving in time. The nuclear, electronic and total entropies reflect the combined motion of the particles. If the electron–nuclear density is focused upon reaching classical turning points, more information on the positions of the particles is available, and the total and single particle entropies exhibit minima. This supports the concept of entropy as a measure of (or the lack of) information.

During the adiabatic motion, electron and nucleus move in phase, *i.e.* they are strongly correlated. However, at the turning

points of the wave packet motion, the correlation decreases. This is seen in different quantities used to measure electron–nuclear correlation effects, *i.e.* the covariance $\text{cov}(t)$, the correlation $\text{corr}(t)$ and also the mutual information $I(t)$. Because the time dependence of these functions is similar, the question which function is more valuable to measure the entanglement is, at least in the situation treated here, not uniquely to be answered. From the analytical model it emerges that the covariance does only depend on properties of the nuclear part of the BO wave function. On the other hand, the correlation and the MI contain characteristics of the electronic wave function as well. This suggests that the latter two quantities provide a better measure of the entanglement. Interestingly, the MI is mainly determined by the electronic contribution to the entropies entering in its definition. This, however, holds only in the limit where the BO approximation is valid. Finally, we note that the numerical results change only weakly if the parametrization of the interaction potential is modified within limits such that the population remains basically in the electronic ground state.

Conflicts of interest

There are no conflicts to declare.

A. Appendix

In what follows, we outline the derivations of the analytical results given in Section 3.1. The starting point is the BO wave function

$$\Psi(r, R, t) = N_t e^{-\frac{\beta_t}{2}(R-R_t)^2} e^{-\frac{\gamma}{2}(r-R)^2}. \quad (A1)$$

In the analysis presented below, frequently appear integrals over Gaussians which, for completeness, we list explicitly:

$$\int dy e^{-ay^2+by} = \sqrt{\frac{\pi}{a}} \int dy y^2 e^{-y^2} = \frac{\sqrt{\pi}}{2}. \quad (A2)$$

The normalization factor N_t can be determined by evaluating the double Gaussian integral over the density, and one finds

$$N_t^2 = \frac{\sqrt{\gamma\beta_t}}{\pi}. \quad (A3)$$

Next we calculate the differential Shannon entropy using the particular form of the spatial wave function given in eqn (19). This leads to the expression

$$\begin{aligned} S(t) = & -N_t^2 \ln[N_t^2] \int dr \int dR e^{-\beta_t(R-R_t)^2 - \gamma(r-R)^2} \\ & + N_t^2 \beta_t \int dr \int dR e^{-\beta_t(R-R_t)^2 - \gamma(r-R)^2} (R - R_t)^2 \\ & + N_t^2 \gamma \int dr \int dR e^{-\beta_t(R-R_t)^2 - \gamma(r-R)^2} (r - R)^2. \end{aligned} \quad (A4)$$

Employing the analytical results for the Gaussian integrals

(eqn (A2)), the entropy is determined as

$$S(t) = -\ln \left[\frac{\sqrt{\gamma\beta_t}}{\pi} \right] + 1. \quad (\text{A5})$$

The electronic density is

$$\rho^{\text{el}}(r, t) = N_t^2 \int dR e^{-\beta_t(R-R_t)^2} e^{-\gamma(r-R)^2}. \quad (\text{A6})$$

Introducing the new variables $R' = R - R_t$ and $r' = r - R_t$, the density takes the form

$$\begin{aligned} \rho^{\text{el}}(r', t) &= N_t^2 \int dR' e^{-\beta_t R'^2} e^{-\gamma(r'-R')^2} \\ &= N_t^2 e^{-\gamma r'^2} \int dR' e^{-(\beta_t + \gamma)R'^2 + 2\gamma r' R'}, \end{aligned} \quad (\text{A7})$$

leading to

$$\rho^{\text{el}}(r, t) = \sqrt{\frac{\beta_t \gamma}{(\beta_t + \gamma)\pi}} e^{-\frac{\gamma \beta_t}{\beta_t + \gamma}(r-R_t)^2}. \quad (\text{A8})$$

In evaluating the electronic entropy, similar integrals as encountered in the determination of the total entropy appear, and one arrives at the expression:

$$S^{\text{el}}(t) = -\ln \left[\sqrt{\frac{\beta_t \gamma}{(\beta_t + \gamma)\pi}} \right] + \frac{1}{2}. \quad (\text{A9})$$

The nuclear density

$$\rho^{\text{nuc}}(R, t) = \sqrt{\frac{\beta_t}{\pi}} e^{-\beta_t(R-R_t)^2}, \quad (\text{A10})$$

is of the same functional form as the electronic density so that, by a proper replacement, one finds

$$S^{\text{nuc}}(t) = -\ln \left[\sqrt{\frac{\beta_t}{\pi}} \right] + \frac{1}{2}. \quad (\text{A11})$$

Inserting the equations for the total entropy and the two particle entropies, the mutual information (eqn (13)) is:

$$\begin{aligned} I(t) &= -\ln \left[\sqrt{\frac{\beta_t \gamma}{(\beta_t + \gamma)\pi}} \right] - \ln \left[\sqrt{\frac{\beta_t}{\pi}} \right] + \ln \left[\frac{\sqrt{\gamma\beta_t}}{\pi} \right] \\ &= \frac{1}{2} \ln \left[1 + \frac{\gamma}{\beta_t} \right]. \end{aligned} \quad (\text{A12})$$

To calculate the covariance we evaluate the expectation value for the product of the coordinates:

$$\begin{aligned} \langle Rr \rangle_t &= \frac{\sqrt{\gamma\beta_t}}{\pi} \int dR R e^{-\beta_t(R-R_t)^2} \int dr r e^{-\gamma(r-R)^2} \\ &= \frac{\sqrt{\gamma\beta_t}}{\pi} \int dR R e^{-\beta_t(R-R_t)^2} \int dr' (r' + R) e^{-\gamma r'^2} \\ &= \frac{\sqrt{\gamma\beta_t}}{\pi} \int dR R^2 e^{-\beta_t(R-R_t)^2} \sqrt{\frac{\pi}{\gamma}} \\ &= \sqrt{\frac{\beta_t}{\pi}} \int dR (R + R_t)^2 e^{-\beta_t R^2} = \frac{1}{2\beta_t} + R_t^2. \end{aligned} \quad (\text{A13})$$

Taking into account that $\langle r \rangle_t = \langle R \rangle_t = 0$, the covariance is

$$\text{cov}(t) = \frac{1}{2\beta_t}. \quad (\text{A14})$$

To determine the correlation, we need the variances for the two degrees of freedom. From the calculation given in eqn (A13) it follows that

$$\langle Rr \rangle_t = \langle R^2 \rangle_t \quad (\text{A15})$$

so that

$$\sigma_R^2(t) = \text{cov}(t) = \frac{1}{2\beta_t}. \quad (\text{A16})$$

The expectation value of r^2 is determined as:

$$\begin{aligned} \langle r^2 \rangle_t &= \frac{\sqrt{\gamma\beta_t}}{\pi} \int dR e^{-\beta_t(R-R_t)^2} \int dr r^2 e^{-\gamma(r-R)^2} \\ &= \frac{\sqrt{\gamma\beta_t}}{\pi} \int dR e^{-\beta_t(R-R_t)^2} \int dr' (r' + R)^2 e^{-\gamma r'^2} \\ &= \frac{\sqrt{\gamma\beta_t}}{\pi} \int dR e^{-\beta_t(R-R_t)^2} \left[\frac{\sqrt{\pi}}{2\gamma^{3/2}} + R^2 \sqrt{\frac{\pi}{\gamma}} \right] \\ &= \frac{1}{2\gamma} + \langle R^2 \rangle_t = \frac{1}{2\gamma} + \frac{1}{2\beta_t} + R_t^2. \end{aligned} \quad (\text{A17})$$

We then have the result

$$\sigma_r^2(t) = \frac{1}{2} \frac{\gamma + \beta_t}{\gamma\beta_t}. \quad (\text{A18})$$

Inserting the expressions for the variances in the definition for the correlation leads to the result

$$\text{corr}(t) = \frac{1}{\sqrt{1 + \beta_t/\gamma}}. \quad (\text{A19})$$

Notes and references

- 1 C. E. Shannon, *Bell Syst. Tech. J.*, 1948, **27**, 379–423.
- 2 E. T. Jaynes, *Phys. Rev.*, 1957, **106**, 620–630.
- 3 E. T. Jaynes, *Phys. Rev.*, 1957, **108**, 171–190.
- 4 A. Ben-Naim, *A Farewell to Entropy*, World Scientific, 2008.
- 5 T. M. Cover and J. A. Thomas, *Elements of Information Theory*, Wiley Series in Telecommunications and Signal Processing, Wiley-Interscience, 2nd edn, 2006.
- 6 A. Hertz and N. J. Cerf, *J. Phys. A*, 2019, **52**, 173001.
- 7 V. Majernik and T. Opatrný, *J. Phys. A*, 1996, **29**, 2187–2197.
- 8 P. Garbaczewski, *Entropy*, 2005, **7**, 253–299.
- 9 D. J. Tannor, *Introduction to Quantum Mechanics: A Time-dependent Perspective*, University Science Books, Sausalito, 2007.
- 10 P. Schürger, T. Schaupp, D. Kaiser, B. Engels and V. Engel, *J. Chem. Phys.*, 2022, **137**, 054303.
- 11 I. I. Hirschman, *Am. J. Math.*, 1957, **79**, 152–156.
- 12 W. Beckner, *Ann. Math.*, 1975, **102**, 159–182.

[View Article Online](#)



PCCP

Paper

- 13 I. Białyński-Birula and J. Mycielski, *Commun. Math. Phys.*, 1975, **44**, 129–132.
- 14 R. D. Levine, *Adv. Chem. Phys.*, 1981, **47**, 239–292.
- 15 M. Quack, *Femtosecond Chemistry*, VCH, Weinheim, 1995, vol. II, pp. 781–818.
- 16 M. Quack, *Adv. Chem. Phys.*, 2014, **157**, 97–118.
- 17 D. Jia, J. Manz and Y. Yang, *AIP Adv.*, 2018, **8**, 045222.
- 18 E. V. Ludeña, F. J. Torres, M. Becerra, L. Rincón and S. Liu, *J. Phys. Chem. A*, 2020, **124**, 386–394.
- 19 S. López-Rosa, R. O. Esquivel, J. C. Angulo, J. Antolín, J. S. Dehesa and N. Flores-Gallegos, *J. Chem. Theory Comput.*, 2010, **6**, 145–154.
- 20 S. López-Rosa, A. L. Martín, J. Antolín and J. C. Angulo, *Int. J. Quantum Chem.*, 2019, **119**, e25861.
- 21 J. C. Angulo and S. López-Rosa, *Entropy*, 2022, **24**, 233.
- 22 F. Agostini, E. Gross and B. F. Curchod, *Comput. Theor. Chem.*, 2019, **1151**, 99–106.
- 23 S. J. C. Salazar, H. G. Laguna and R. P. Sagar, *Eur. Phys. J. Plus*, 2022, **137**, 1–26.
- 24 P. Schürger and V. Engel, *J. Phys. Chem. Lett.*, 2023, 334–339.
- 25 M. Born and R. Oppenheimer, *Ann. Phys.*, 1927, **84**, 457–484.
- 26 M. Born and K. Huang, *Theory of Crystal Lattices*, Oxford University Press, London, 1954.
- 27 M. Baer, *Beyond Born-Oppenheimer: Electronic Nonadiabatic Coupling Terms and Conical Intersections*, Wiley, Hoboken, 2006.
- 28 S. Shin and H. Metiu, *J. Phys. Chem.*, 1996, **100**, 7867–7872.
- 29 S. Shin and H. Metiu, *J. Chem. Phys.*, 1995, **102**, 9285–9295.
- 30 M. Erdmann, P. Marquetand and V. Engel, *J. Chem. Phys.*, 2003, **119**, 672–679.
- 31 M. Falge, V. Engel and S. Gräfe, *J. Chem. Phys.*, 2011, **134**, 184307.
- 32 M. Falge, V. Engel and S. Gräfe, *J. Phys. Chem. Lett.*, 2012, **3**, 2617–2620.
- 33 J. Albert, M. Falge, S. Gomez, I. R. Sola, H. Hildenbrand and V. Engel, *J. Chem. Phys.*, 2015, **143**, 041102.
- 34 F. G. Fröbel, K. M. Ziemis, U. Peschel, S. Gräfe and A. Schubert, *J. Phys. B*, 2020, **53**, 144005.
- 35 T. Schaupp and V. Engel, *J. Chem. Phys.*, 2020, **152**, 204310.
- 36 J. Albert, K. Hader and V. Engel, *J. Chem. Phys.*, 2017, **147**, 064302.
- 37 T. Schaupp and V. Engel, *J. Chem. Phys.*, 2022, **156**, 074302.
- 38 M. D. Feit, J. A. Fleck and A. Steiger, *J. Comput. Phys.*, 1982, **47**, 412–433.
- 39 R. Kosloff and H. Tal-Ezer, *Chem. Phys. Lett.*, 1986, **127**, 223–230.
- 40 E. Mandel and E. Wolf, *Optical Coherence and Quantum Optics*, Cambridge University Press, Cambridge, 1995.

6.3.3 Differential Shannon Entropies Characterizing Electron–Nuclear Dynamics and Correlation: Momentum-Space Versus Coordinate-Space Wave Packet Motion [4]

Reprinted from "P. Schürger, V. Engel, Entropy 2023, 25(7), 970"; licensed under a Creative Commons Attribution (CC BY) license (CC BY 4.0).



Article


Differential Shannon Entropies Characterizing Electron–Nuclear Dynamics and Correlation: Momentum-Space Versus Coordinate-Space Wave Packet Motion

Peter Schürger ^{*,†} and Volker Engel [†]

Institute of Physical and Theoretical Chemistry, University of Würzburg, Emil-Fischer-Str. 42, 97074 Würzburg, Germany; volker.engel@uni-wuerzburg.de
* Correspondence: peter.schuerger@uni-wuerzburg.de
† These authors contributed equally to this work.

Abstract: We calculate differential Shannon entropies derived from time-dependent coordinate-space and momentum-space probability densities. This is performed for a prototype system of a coupled electron–nuclear motion. Two situations are considered, where one is a Born–Oppenheimer adiabatic dynamics, and the other is a diabatic motion involving strong non-adiabatic transitions. The information about coordinate- and momentum-space dynamics derived from the total and single-particle entropies is discussed and interpreted with the help of analytical models. From the entropies, we derive mutual information, which is a measure for the electron–nuclear correlation. In the adiabatic case, it is found that such correlations are manifested differently in coordinate- and momentum space. For the diabatic dynamics, we show that it is possible to decompose the entropies into state-specific contributions.

Keywords: differential Shannon entropy; correlation; electron–nuclear dynamics

 **check for updates**

Citation: Schürger, P.; Engel, V. Differential Shannon Entropies Characterizing Electron–Nuclear Dynamics and Correlation: Momentum-Space Versus Coordinate-Space Wave Packet Motion. *Entropy* **2023**, *25*, 970. <https://doi.org/10.3390/e25070970>

Academic Editors: Andrei Khrennikov and Karl Svozil

Received: 7 June 2023
Revised: 15 June 2023
Accepted: 20 June 2023
Published: 23 June 2023

1. Introduction


Given the coordinate-space wave function $\psi(x, t)$ of a quantum system, the differential Shannon entropy is obtained from the probability density $\rho(x, t) = |\psi(x, t)|^2$ as [1,2]

$$S_x(t) = - \int dx \rho(x, t) \ln [\rho(x, t)], \quad (1)$$

where x and t stand for the coordinates and time, respectively. This function is a measure for the information available on the system, and the larger its value, the less information is provided. Likewise, one may start with the momentum (π) space wave functions $\psi(\pi, t)$ being the Fourier transform of $\psi(x, t)$, yielding the density $\rho(\pi, t) = |\psi(\pi, t)|^2$, and define the entropy

$$S_\pi(t) = - \int d\pi \rho(\pi, t) \ln [\rho(\pi, t)]. \quad (2)$$

Following the information-theoretical line of thought, $S_x(t)$ and $S_\pi(t)$ provide us with knowledge about what happens in coordinate- and momentum-space, respectively. If one encounters a less localized coordinate-space probability density, the position of a particle is less precisely known so that the entropy $S_x(t)$ takes on a larger value. If we consider, for example, a Gaussian-like density, due to the Fourier relation, a broad coordinate-space distribution is associated with a more localized momentum-space density and, accordingly, $S_\pi(t)$ is smaller. This general behavior is connected to the coordinate-momentum uncertainty relation. In more detail, one finds that the sum $S_x(t) + S_\pi(t)$ is a measure for the coordinate-momentum uncertainty [2–5].



Copyright: © 2023 by the authors. Licensee MDPI, Basel, Switzerland. This article is an open access article distributed under the terms and conditions of the Creative Commons Attribution (CC BY) license (<https://creativecommons.org/licenses/by/4.0/>).

Entropy **2023**, *25*, 970. <https://doi.org/10.3390/e25070970>

<https://www.mdpi.com/journal/entropy>

Concerning chemical dynamics, differential Shannon entropies have been discussed, see Refs. [6–10]. They are also important in the connection with reactivity [11], aromaticity [12] and stereochemistry [10]. Other applications include the thermalization of isolated quantum systems caused by disorder [13,14], and in the static case, differential Shannon entropies were applied to study wavefunction behavior in various potentials [15–17], avoided crossings [18–20] and correlation effects [21,22].

Regarding now, more specifically, a molecule composed of electrons and nuclei. We then may calculate the differential Shannon entropies $S_x(t)$ and $S_\pi(t)$ from the total probability densities; additionally, using the electron (*el*) and nuclear (*nuc*) densities, the particle entropies $S_x^{el}(t)$, $S_\pi^{el}(t)$ and $S_x^{nuc}(t)$, $S_\pi^{nuc}(t)$ are accessible. It is the purpose of this paper to illustrate coordinate-space and momentum-space entropies for a coupled electron–nuclear dynamics. There, one may distinguish two opposite situations. The first one is that of a Born–Oppenheimer (BO) adiabatic motion [23,24], where the nuclear dynamics is restricted to a single electronic state, and couplings to other states are negligible. This is often realized if the motion takes place in the electronic ground state. The opposite limit is reached if strong non-adiabatic couplings are present [25]. Then, nuclear densities are transferred with large efficiency between different electronic states, as is usually the case when an avoided crossing between potential curves [26,27] or a conical intersection between potential surfaces [28–30] is passed. Differential entropies evolving from the weak and strong coupling cases are considered in this paper. Additionally, the electron–nuclear correlation, which can be characterized by the “mutual information” derived from the entropy functions [21,31], is discussed. In doing so, the interpretations evolving from coordinate-space and momentum-space are investigated, thereby extending our former work [32]. This is performed using analytical approaches and also giving numerical examples. The latter are restricted to a coupled one-dimensional motion of an electron and a nucleus [33,34]. We use parameterizations of the electronic–nuclear interaction potential, which cover the two coupling cases outlined above. The paper is organized as follows. In Section 2, we describe the model used in the numerical calculations, and we also provide the basic equations to arrive at the various entropies. The analytical and numerical results are collected in Section 3, and a summary is given in Section 4.

2. Theory and Model

2.1. Model for the Coupled Electronic–Nuclear Motion

A useful model for the one-dimensional electron–nuclear motion was established in the work of Shin and Metiu [33,34]. It has been used to describe basic properties of such dynamics [35–37], and was extended to include more than one electron [36] and also a planar motion to describe dynamics taking place at a conical intersection [38–40]. The interaction potential is taken as (in atomic units)

$$V(r, R) = \frac{1}{|R_1 - R|} + \frac{1}{|R_2 - R|} - \frac{\text{erf}[|R_1 - r|/R_f]}{|R_1 - r|} - \frac{\text{erf}[|R - r|/R_c]}{|R - r|} - \frac{\text{erf}[|R_2 - r|/R_f]}{|R_2 - r|} + \Delta, \quad (3)$$

where r and R denote the coordinate of the electron and nucleus, respectively. They interact via screened Coulomb potentials involving error functions. Additionally, there are two protons at fixed positions $R_1 = -5 \text{ \AA}$ and $R_2 = +5 \text{ \AA}$ so that further terms are present in the potential energy surface. The strength of the screening is determined by the two parameters R_f and R_c , where in our examples, R_f is fixed at a value of 1.5 \AA , and R_c takes the value of $R_c = 1 \text{ \AA}$ and $R_c = 5 \text{ \AA}$ for the cases of weak and strong non-adiabatic coupling, respectively. Finally, Δ is an energy shift which is chosen such that the potential $V(r, R)$ has its minimum at zero energy in the range of our spatial grid.

The time-dependent Schrödinger equation reads

$$i\hbar \frac{\partial}{\partial t} \Psi(r, R, t) = \hat{H} \Psi(r, R, t), \quad (4)$$

with the Hamiltonian

$$\hat{H} = \frac{\hat{p}^2}{2m_e} + \frac{\hat{P}^2}{2M} + V(r, R). \quad (5)$$

Here, the momentum operators for the electron and the nucleus are \hat{p} and \hat{P} , respectively, M denotes the proton mass, and m_e is the mass of the electron.

The time propagation is performed with the split-operator method [41] on a grid in the spatial ranges of $-12 \text{ \AA} \leq R \leq +12 \text{ \AA}$ and $-6 \text{ \AA} \leq r \leq +6 \text{ \AA}$, using 512 grid points in each direction and a time step of $\Delta t = 0.0024 \text{ fs}$.

Different initial conditions are employed in solving the time-dependent Schrödinger equation. The initial functions are of the form

$$\Psi(r, R, 0) = N_0 e^{-\beta_0(R-R_0)^2} \varphi_n(r; R). \quad (6)$$

Here, N_0 is a normalization constant, and the appearing Gaussian is characterized by its center R_0 and the width parameter β_0 , which is set to a value of 7.14 \AA^{-2} throughout, and the center of the Gaussian R_0 takes on different values. Solving the electronic Schrödinger equation

$$\left[\frac{\hat{p}^2}{2m_e} + V(r, R) \right] \varphi_n(r; R) = V_n(R) \varphi_n(r; R), \quad (7)$$

using imaginary time propagation [42] yields the electronic wave functions $\varphi_n(r; R)$ and the adiabatic potentials $V_n(R)$ corresponding to the electronic state with quantum number (n).

A variation of the screening parameter entering into the interaction potential leads to different adiabatic potentials. The ground state potential obtained for a value of $R_c = 1 \text{ \AA}$ is shown in the left upper panel of Figure 1. The energy gap to the potential $V_1(R)$ is about 4 eV (not shown) so that here, the electronic ground state is separated from the excited electronic states, and we encounter a case where the BO approximation is valid (Section 3.1). The electronic eigenfunctions $\varphi_0(r; R)$ and $\varphi_1(r; R)$ are also contained in the figure (left middle and left lower panel). The ground state function shifts almost linearly with increasing values of the nuclear coordinate, thereby approximately keeping a Gaussian-like shape of constant width. This is not true for $\varphi_1(r; R)$, which varies considerably in its width.

The situation of a strong coupling is illustrated in the right-hand column of Figure 1, and it is obtained in setting $R_c = 5 \text{ \AA}$. The potentials of the two lowest states show a very small energy gap of $[V_1(0) - V_0(0)] < 0.01 \text{ eV}$ at the avoided crossing. The respective electronic eigenfunctions, displayed in the lower right two panels of the figure, do not change their form in varying R at negative distances. Reaching the avoided crossing at $R = 0$, a sudden jump of the probability density occurs, and then, at positive values of R , the shape again remains invariant upon a change in geometry. This is characteristic for the diabatic dynamics, see Section 3.2.

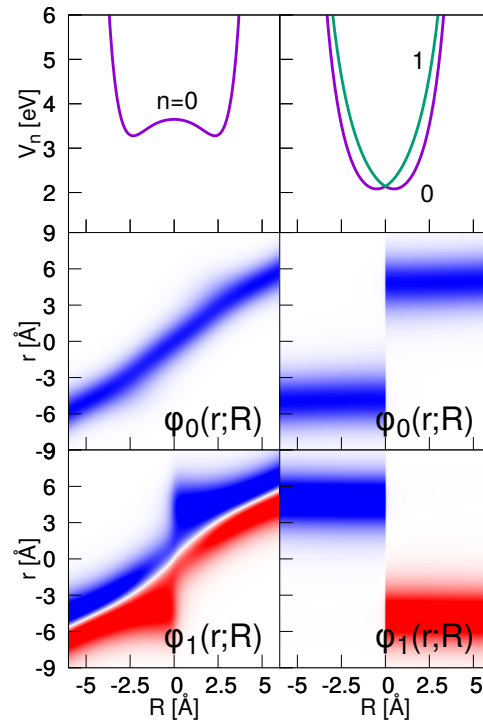


Figure 1. Upper panels: Adiabatic potential curves $V_n(R)$ obtained for two choices of the screening parameter R_c . The left- and right-hand columns are associated with the cases of a BO motion ($R_c = 1 \text{ \AA}$) and a diabatic motion ($R_c = 5 \text{ \AA}$), respectively. The two lower rows show the electronic eigenfunctions $\phi_0(r;R)$ and $\phi_1(r;R)$ as indicated.

2.2. Differential Entropies for Electronic–Nuclear Motion

In order to calculate entropies, according to Equations (1) and (2), probability densities are needed. From the time-dependent wave function, the coordinate probability density is calculated as

$$\rho(r, R, t) = |\Psi(r, R, t)|^2. \quad (8)$$

Single-particle densities are obtained by integration. This leads to the electronic density

$$\rho^{el}(r, t) = \int dR \rho(r, R, t), \quad (9)$$

and for the nucleus, one has

$$\rho^{nuc}(R, t) = \int dr \rho(r, R, t). \quad (10)$$

A two-dimensional Fourier transform of $\Psi(r, R, t)$ yields the momentum-space wave function $\Psi(p, P, t)$ and the density

$$\rho(p, P, t) = |\Psi(p, P, t)|^2, \quad (11)$$

with p and P being the electronic and nuclear momenta, respectively. We then have

$$\rho^{el}(p, t) = \int dP \rho(p, P, t), \tag{12}$$

$$\rho^{nuc}(P, t) = \int dp \rho(p, P, t). \tag{13}$$

Using the coordinate- and momentum-space densities, the total differential Shannon entropies can be calculated as follows:

$$S_x(t) = - \int dr \int dR \rho(r, R, t) \ln[\rho(r, R, t)], \tag{14}$$

$$S_\pi(t) = - \int dp \int dP \rho(p, P, t) \ln[\rho(p, P, t)]. \tag{15}$$

For the single particles, one obtains the following entropies:

$$S_r^{el}(t) = - \int dr \rho^{el}(r, t) \ln[\rho^{el}(r, t)], \tag{16}$$

$$S_p^{el}(t) = - \int dp \rho^{el}(p, t) \ln[\rho^{el}(p, t)], \tag{17}$$

$$S_R^{nuc}(t) = - \int dR \rho^{nuc}(R, t) \ln[\rho^{nuc}(R, t)], \tag{18}$$

$$S_P^{nuc}(t) = - \int dP \rho^{nuc}(P, t) \ln[\rho^{nuc}(P, t)]. \tag{19}$$

Another quantity is the “mutual information” (MI). This function contains information on the correlation between different particles [21,31]. In the present situation of a coupled electron–nuclear motion, we derive from the densities the coordinate-space and momentum-space MI:

$$I_x(t) = S_r^{el}(t) + S_R^{nuc}(t) - S_x(t), \tag{20}$$

$$I_\pi(t) = S_p^{el}(t) + S_P^{nuc}(t) - S_\pi(t). \tag{21}$$

We also regard two additional measures for correlation. The first one is the “covariance” [43], which is defined in terms of expectation values of the coordinates r and R or the momenta p and P as

$$cov_x(t) = \langle rR \rangle_t - \langle r \rangle_t \langle R \rangle_t, \tag{22}$$

$$cov_\pi(t) = \langle pP \rangle_t - \langle p \rangle_t \langle P \rangle_t. \tag{23}$$

Using the variances for the variables $y = r, R, p, P$

$$\sigma_y^2(t) = \langle y^2 \rangle_t - \langle y \rangle_t^2, \tag{24}$$

one defines the “correlations” as

$$corr_x(t) = \frac{cov_x(t)}{\sigma_R(t)\sigma_r(t)}, \tag{25}$$

$$corr_\pi(t) = \frac{cov_\pi(t)}{\sigma_P(t)\sigma_p(t)}. \tag{26}$$

3. Results

3.1. Weak Coupling: Born–Oppenheimer Dynamics

Setting the screening parameter to a value of $R_c = 1 \text{ \AA}$ and imposing the initial condition given in Equation (6) with $R_0 = -3.5 \text{ \AA}$ and with the electronic wave function $\varphi_0(r; R)$ yields the dynamics which exclusively takes place in the electronic ground state. This means that the population $\tilde{P}_0(t) = |\langle \varphi_0 | \Psi(t) \rangle|^2$ remains equal to one at all times regarded (where the numerical deviations are in the order of 0.2%).

In a former paper, we used a Gaussian ansatz for the BO wave function to analyze the numerically determined entropies and correlation measures [32]. This function reads

$$\Psi(r, R, t) = N_t e^{-\frac{\beta_t}{2}(R-R_t)^2} e^{-\frac{\gamma}{2}(r-R)^2}, \quad (27)$$

where the normalization factor is

$$N_t = \left[\frac{\sqrt{\gamma\beta_t}}{\pi} \right]^{\frac{1}{2}}. \quad (28)$$

The time dependence of the wave function is contained in the center of the nuclear Gaussian at $R = R_t$ and also its width, which is determined by the parameter β_t . Phase factors are thus not included in the ansatz. On the other hand, the electronic wave function is assumed to have a constant width (i.e., $\gamma = \text{const.}$), and its center shifts linearly with the nuclear coordinate R . These assumptions are approximately fulfilled for $\varphi_0(r; R)$, as it can be taken from Figure 1, middle left panel. The ansatz of Equation (27) allows to calculate the various quantities derived from the coordinate-space densities. The details of these calculations can be found in Ref. [44]. Here, we additionally need the respective equations evolving from a momentum-space analysis. The latter is presented in Appendix A. The results for the entropies, variances and correlation measurements are as follows:

$$S_x(t) = \ln \left[\frac{\pi}{\sqrt{\gamma\beta_t}} \right] + 1, \quad (29)$$

$$S_\pi(t) = \ln \left[\sqrt{\gamma\beta_t\pi} \right] + 1, \quad (30)$$

$$S_r^{el}(t) = \ln \left[\sqrt{\frac{(\beta_t + \gamma)\pi}{\beta_t\gamma}} \right] + \frac{1}{2}, \quad (31)$$

$$S_p^{el}(t) = \ln \left[\sqrt{\pi\gamma} \right] + \frac{1}{2}, \quad (32)$$

$$S_R^{nuc}(t) = \ln \left[\sqrt{\frac{\pi}{\beta_t}} \right] + \frac{1}{2}, \quad (33)$$

$$S_P^{nuc}(t) = \ln \left[\sqrt{\pi(\beta_t + \gamma)} \right] + \frac{1}{2}, \quad (34)$$

$$I_x(t) = \frac{1}{2} \ln \left[1 + \frac{\gamma}{\beta_t} \right], \quad (35)$$

$$I_\pi(t) = \frac{1}{2} \ln \left[1 + \frac{\gamma}{\beta_t} \right], \quad (36)$$

$$\sigma_r^2(t) = \frac{1}{2} \frac{\gamma + \beta_t}{\gamma\beta_t}, \quad (37)$$

$$\sigma_p^2(t) = \frac{\gamma}{2}, \quad (38)$$

$$\sigma_R^2(t) = \frac{1}{2\beta_t}, \quad (39)$$

$$\sigma_P^2(t) = \frac{1}{2}(\beta_t + \gamma), \quad (40)$$

$$\text{cov}_x(t) = \frac{1}{2\beta_t}, \quad (41)$$

$$\text{cov}_\pi(t) = -\frac{1}{2}\gamma, \quad (42)$$

$$\text{corr}_x(t) = \frac{1}{\sqrt{1 + \beta_t/\gamma}}, \quad (43)$$

$$\text{corr}_\pi(t) = -\frac{1}{\sqrt{1 + \beta_t/\gamma}}. \quad (44)$$

6. INFORMATION-THEORETICAL APPROACH TO COUPLED ELECTRON-NUCLEAR DYNAMICS

In this section, the latter equations are used—as far as possible—for the interpretation of the numerical results.

The nuclear dynamics is illustrated in Figure 2, left upper panel. It is seen that the probability density performs a vibrational motion, but at the end of the displayed time interval, dispersion causes the density to be distributed over the entire classically allowed region. The corresponding momentum density is shown below the coordinate density. It reveals a complex structure which includes, as is also seen in the coordinate-space density, interference fringes. The latter arise when $\rho^{nuc}(R, t)$ reverses its direction of motion so that $\rho^{nuc}(P, t)$ changes from a positive to a negative momentum distribution. It is obvious that the ansatz for the nuclear momentum density given in Equation (A15) cannot accurately describe the numerical result shown in the figure. This, in particular, applies to the seen fringes and also to the rapid change from positive to negative momenta. Nevertheless, the derived analytical entropies still prove to be valuable because they are quantities derived from an integration over all momenta.

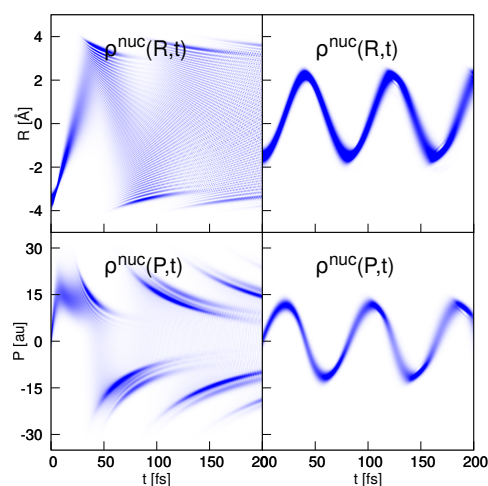


Figure 2. Nuclear density dynamics in the presence of weak (BO dynamics, left-hand column) and strong non-adiabatic coupling (diabatic dynamics, right-hand column). The upper panels show the nuclear densities in coordinate space and the lower panels in momentum space. While in the weakly coupled case the densities disperse quickly, the strongly coupled case shows quasi-harmonic dynamics.

The coordinate space nuclear entropy is displayed in the upper left panel of Figure 3. It was checked upon numerically (not shown) that exactly the same curve is obtained if the BO wave function is employed in the calculation. This function is the product of $\varphi_0(r; R)$ and a component $\psi_0^{BO}(R, t)$, which is obtained in solving the nuclear time-dependent Schrödinger equation involving the adiabatic potential $V_0(R)$. We found that the BO approximation is excellent for all entropies presented in the figure. The approximate curve for $S_R^{nuc}(t)$ (Equation (33)) is determined for a value of $\gamma = 0.733 \text{ \AA}$, which is calculated in taking an average of the variance $\sigma_r^2(R)$ of the electronic eigenfunction in the interval $|R| \leq 5 \text{ \AA}$. The time-dependent parameter β_t is obtained from the numerically calculated variance $\sigma_R(t)$ using Equation (39). The analytical expression initially tracks the numerical obtained entropy excellently. Deviations occur when the classical turning point of the wave packet motion is approached for the first time. At this time, the Gaussian approximation to the nuclear density is no longer accurate, see Figure 2. Nevertheless, the analytical curve predicts the time dependence of the nuclear entropy rather well. The minima in the entropy occur at times when the wave packet is focused (large value of β_t) as can be understood from Equation (33).

This is the case at the classical turning points of the motion, and it is in accord with the notion that a more localized coordinate space probability density is associated with a larger information on a particle's position and, in turn, with a smaller entropy. Note that a focusing also takes place around 5 fs, which is due to a squeezing [45] of the wave packet.

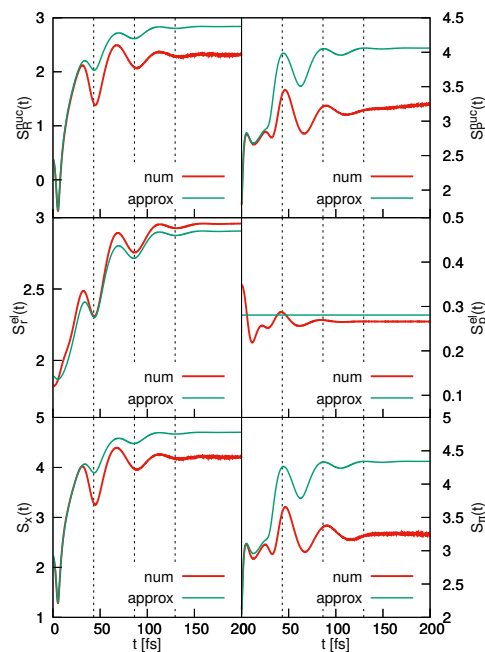


Figure 3. BO dynamics. The left-hand panels show the coordinate-space entropies for the nuclear (**upper panel**) and electronic (**middle panel**) degrees of freedom. Also displayed is the entropy of the coupled system (**lower panel**). The right-hand column contains the same functions derived from the momentum-space densities. In each case, the numerically determined functions are compared to the analytically ones. The dashed lines mark the times when the wave packet reaches the classical turning points of its motion.

The momentum-space nuclear entropy is shown in the right upper panel of Figure 3. To arrive at the approximate entropy, we again use the value of $\gamma = 0.733 \text{ \AA}$, and the parameter β_t is then calculated from the numerically determined variance using Equation (40). The deviations between the numerical and analytical entropies are larger than those found in coordinate space, for the reasons discussed above. Nevertheless, the positions of the extrema are well predicted. From Equation (34), it can be inferred that a minimum is found at times when β_t assumes a minimum, which correlates with a more localized momentum-space density. Thus, at times when a maximum is found in the coordinate-space entropy, the momentum-space entropy assumes a minimum and vice versa. This illustrates the Fourier relation between the two nuclear densities.

The comparison of Equations (31) and (33) shows that the nuclear and electronic coordinate entropies exhibit minima and maxima at the same times. This indeed is seen if these curves are compared (upper and middle left panel of Figure 3). The agreement between the numerically and analytically determined electronic entropies is astonishingly good. Not unsurprisingly, we find that at the turning points where the electron–nuclear wave packet reverses its motion, we know more precisely where the electron is located as is the case for the nucleus. This is also reflected in the total spatial entropy (lower left panel of the figure). The

approximate function $S_x(t)$ is, at all times, larger than the numerical one, which is a property of the normal probability distribution [1].

The electronic momentum-space entropy is contained in the middle right panel of Figure 3. Whereas the analytical solution predicts a time-independent entropy, the numerical results show that there are smaller time variations, where, as for the coordinate-space entropies, the minima and maxima correlate with those found for the nuclear degree of freedom. The time dependence of the total momentum entropy is determined by that of the nuclear entropy because the latter has a more pronounced time dependence as $S_x^{el}(t)$. Note, however, that it is not the sum of the two particle entropies; see the discussion below.

The results presented so far show that the time dependence of the entropies is determined by the nuclear component of the wave function. This, of course, does not come as a surprise because in the present case, the BO approximation is valid, and thus the electronic part of the wave functions does not include time as a parameter. The predictions derived from our Gaussian ansatz for the wave function, namely that the minima in the entropies correlate with a more localized nuclear coordinate-space density, are confirmed by the numerical calculation. Concerning the information available, it is seen that the coordinate-space and momentum-space entropies reflect the Fourier relation between the two spaces. In particular, if we know more about the localization of one or the other particle, less is known about its momentum and vice versa.

Let us, in what follows, discuss the three measures of particle entanglement, namely the covariance, correlation and mutual information as defined in Section 2.2. The covariance functions $cov_x(t)$ are shown in the upper left panel of Figure 4, and it is seen that the analytically derived curve again provides a very good approximation of the numerically exact one. Thus, using Equation (41) for interpretation, a localized nuclear density, corresponding to a large value of β_t , goes in hand with a low degree of particle correlation. The reason is that in this case, the R -dependence of the electronic wave function entering into the BO wave function is of minor importance so that the wave function is approximately separable. This shows that at times when the classical turning points (which are indicated as dashed vertical lines in Figure 4) are reached, the covariance takes on minimal values. The same applies to the correlation (middle left panel of Figure 4) and also to the MI (lower left panel). All three functions exhibit a comparable time dependence so that we conclude that they measure the correlation in a very similar way.

A different picture evolves from the momentum-space functions displayed in the right-hand column of Figure 4. The nuclear momentum covariance and correlation behave rather similarly as a function of time. They exhibit an overall decrease, which is modulated with the vibrational period, and for longer times, they level to a value of about zero. Both numerically determined functions are negative initially, and they switch sign for later times, whereas the analytical predictions stay negative throughout. This deviation is a non-BO effect, which was checked upon in performing a BO propagation.

It is seen that at times when the turning points are reached, the momentum correlation approaches zero, which agrees with the behavior in configuration space. Whereas no time dependence appears in the analytical covariance expression, the change of the nuclear variance causes the correlation $corr_\pi(t)$ to vary, similar to the numerical curve.

The momentum-space MI, displayed in the lower right panel of Figure 4, exhibits an unusual behavior. The overall rise of the function is modulated by the vibrational period of the quantum motion. The analytically determined MI does only give reasonable results at very early times. It is interesting to observe that around the times when $corr_x(t)$ and $cov_x(t)$ predict a low degree of particle correlation, the MI does not, i.e., the MI is phase shifted with respect to the other two functions. We also note that the fast oscillations seen in the MI are neither of numerical origin nor are they due to non-BO effects as seen, for example, in time-dependent electron momentum expectation values [46].

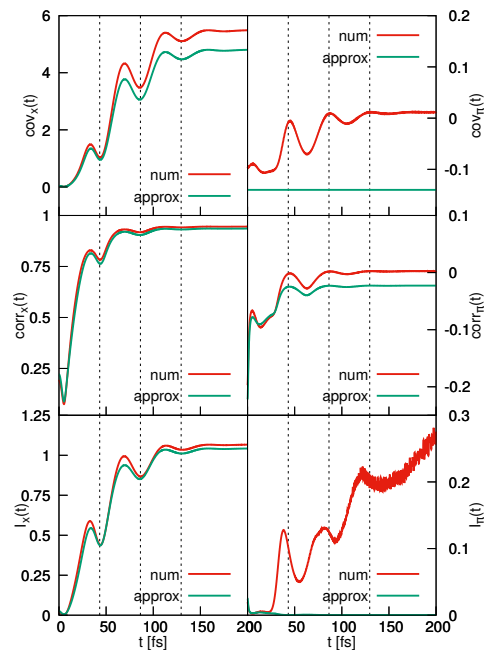


Figure 4. BO-dynamics. The left-hand column shows the coordinate-space covariance, correlation and mutual information, as indicated. The respective curves obtained from the momentum-space densities are depicted in the right-hand column. In each case, numerically and analytically derived results are compared. The times when the turning points are reached are marked by the vertical lines.

To gain more insight into the behavior of $I_\pi(t)$, we show in Figure 5a snapshots of the momentum-space density at times when maxima and minima in the MI occur. It is seen that initially, when $I_\pi(t)$ is small, the density is a nodeless Gaussian-like distribution. At a time of $t = 38$ fs, there appears a clear nodal structure, and the MI takes on a maximum. Then, at 54 fs, the density in the region of its largest amplitude has lost the nodal pattern (although, at larger nuclear momenta there is a region where the density shows nodes, but the overall amplitude is small). Nodes appear another time at the location of the next maximum (82 fs). A similar trend is seen at later times. The conclusion is that an increase in the MI goes in hand with the appearance of nodal patterns in the momentum-space density found in the direction of the nuclear momentum, and that with an increasing number of nodes, the MI grows. To observe this behavior, it is important that the nodes are not oriented parallel to the axes because otherwise they do not give a contribution to wave packet entanglement. This is the case for the coordinate-space density. The latter is depicted, for selected times, in Figure 5b. Starting with a Gaussian-like function at time zero, the density moves along the line $r = R$. There also appears a nodal structure but here, all nodal lines are oriented perpendicular to the nuclear coordinate axis. This does not change as a function of time as is illustrated for the times $t = 69$ fs and 113 fs, where the coordinate-space MI assumes maxima. At later times (250 fs and 300 fs), the densities are quite similar, which leads to a constant value of $I_x(t)$. A clearer nodal pattern is seen in the momentum-space density, which, for these times, fluctuates as a function of time (Figure 5a), giving rise to fluctuations in $I_\pi(t)$.

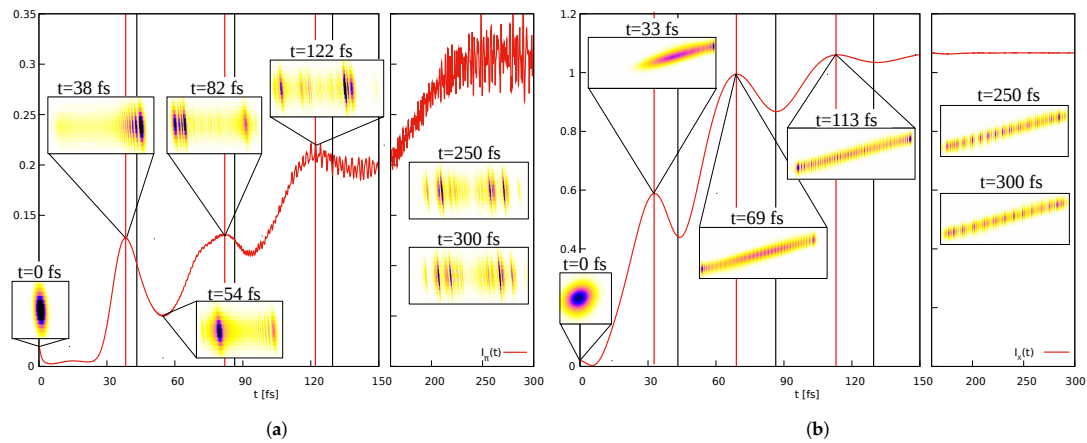


Figure 5. BO-dynamics. (a) Shown are momentum-space densities $\rho(p, P, t)$ for different times as indicated. Abscissa and ordinate correspond to the nuclear and electronic momentum, respectively. Also shown is the MI $I_\pi(t)$. The vertical red lines mark times when the MI exhibits extrema, and the black lines indicate the times when the classical turning points are reached. (b) Same as (a), but in coordinate space. The densities $\rho(r, R, t)$ (abscissa R , ordinate r) are depicted for selected times.

To support the connection between the nodal structure of the momentum-space density and the resulting MI, we developed an analytical model using the simple ansatz for the normalized density as

$$\rho_{a,b}(p, P) = \frac{2 e^{-p^2 - P^2} \cos^2\left(\frac{a}{\sqrt{1+b^2}}(P + bp)\right)}{\pi(1 + e^{-a^2})}. \quad (45)$$

Here, the parameter a determines the frequency of the cosine and thus the number of nodes. In the limit $a \rightarrow 0$, a standard non-correlated Gaussian is recovered. The second parameter $b \in [0, 1]$ determines the alignment of the nodes. The factor $\sqrt{1+b^2}$ ensures that b does not distort the density and thus influences the effective frequency/number of nodes.

Using *MATHEMATICA*, we calculate the MI as a function of the frequency (i.e., number of nodes) and for several values of b . The extensive analysis of these calculations is out of the scope of this paper, and it will be given elsewhere [44]. Here, we summarize the main results. Regarding the MI as a function of the number of nodes, we find that it grows monotonically and approaches a constant with increasing number of nodes. Furthermore, the MI vanishes for $b = 0$ and arbitrary a , and curves reach the same upper bound faster with increasing $b > 0$. The rough model explains qualitatively what is seen in the numerical results. Using the ansatz Equation (45), the covariance and correlation can be calculated analytically. These functions vanish for $b \rightarrow 0$ and $a \rightarrow 0$ as expected, but they also vanish for $a \rightarrow \infty$, whereas the MI approaches a finite non-zero limit. This finding is also in accord with what is seen in Figure 4. Here we encounter a behavior of the MI which is different from the covariance and correlation, which hints at the fact that non-linear correlations are present in the wave packet moving in momentum space.

3.2. Strong Coupling: Diabatic Dynamics

In this section, we treat the case of a strong non-adiabatic coupling, which is achieved in setting the screening parameter to $R_c = 5 \text{ \AA}$. The adiabatic potentials and the electronic eigenfunctions are illustrated in Figure 1. The nuclear wave function starts at $R_0 = -1.5 \text{ \AA}$. For an analytical approach, we take advantage of the fact that the dynamics (see right-hand

column of Figure 2) can be well described as a diabatic motion [47], where the wave function is of the form

$$\Psi(r, R, t) = \psi_d(R, t) \varphi_0(r, R_d). \tag{46}$$

Within this approximation, the nuclear component moves in the diabatic potential obtained in connecting the negative branch of $V_0(R)$ with the positive branch of $V_1(R)$, and the electronic wave function is the diabatic function calculated at a fixed value $R = R_d$.

The analytical treatment starts from the ansatz for the wave function as

$$\Psi(r, R, t) = \sqrt{\frac{\sqrt{\gamma\beta_t}}{\pi}} e^{-\frac{\beta_t}{2}(R-R_d)^2} e^{-\frac{\gamma}{2}(r-R_d)^2}. \tag{47}$$

Thus, here, the total wave function is separable, which simplifies the calculations if compared to the BO case treated in Section 3.1. As shown in Appendix B, the following entropies evolve from the diabatic ansatz of the wave function:

$$S_x(t) = \ln \left[\frac{\pi}{\sqrt{\beta_t \gamma}} \right] + 1, \tag{48}$$

$$S_\pi(t) = \ln \left[\sqrt{\gamma\beta_t} \pi \right] + 1, \tag{49}$$

$$S_r^{el}(t) = \ln \left[\sqrt{\frac{\pi}{\gamma}} \right] + \frac{1}{2}, \tag{50}$$

$$S_R^{nuc}(t) = \ln \left[\sqrt{\frac{\pi}{\beta_t}} \right] + \frac{1}{2}, \tag{51}$$

$$S_p^{el}(t) = \ln \left[\sqrt{\pi\gamma} \right] + \frac{1}{2}, \tag{52}$$

$$S_p^{nuc}(t) = \ln \left[\sqrt{\pi\beta_t} \right] + \frac{1}{2}. \tag{53}$$

Here, we determine γ from the electronic width at $t = 0$ which yields a value of $\gamma = 0.436 \text{ \AA}^{-2}$. Note that because of the separability of the diabatic wave function, the correlation, covariance and mutual information vanish in coordinate- and momentum space.

A comparison of the equations for the coordinate and momentum total entropies in the diabatic and adiabatic case (Equations (29) and (48), Equations (30) and (49)) shows that they are identical. In both situations, the nuclear dynamics takes place in a single potential. For a diabatic motion, the electron remains stationary, whereas the nucleus vibrates, being more or less localized as time goes along. In the BO case, both particles localize simultaneously.

The entropies evolving from the diabatic dynamics are presented in Figure 6. The nuclear coordinate entropy oscillates with a single frequency associated with the vibrational wave packet motion, and the analytically obtained curve tracks the numerical one perfectly. The oscillations show an increasing amplitude, which, according to Equation (51), correlates with a decrease in the width parameter β_t . The obtained curve is much more regular if compared to the BO case (Figure 3). This is due to the excellent accuracy of the diabatic approximation. Here, the nuclear motion takes place in an almost harmonic potential (which is not the case in the adiabatic situation, where the potential shows a double minimum structure). This harmonic-like motion is clearly seen in the density dynamics displayed in the right-hand column of Figure 2. The momentum space nuclear entropy $S_p^{nuc}(t)$ exhibits the same quasi-periodic time structure but is phase shifted with respect to $S_R^{nuc}(t)$, as is expected from Equation (53). In both spaces, the electronic entropy is nearly constant as is predicted within the analytical ansatz (Equations (50) and (52)). The minor numerically found deviations from a constant behavior are due to the approximate nature of the diabatic ansatz and also the variation of the electronic variance as a function of the nuclear coordinate sR .

6. INFORMATION-THEORETICAL APPROACH TO COUPLED ELECTRON-NUCLEAR DYNAMICS

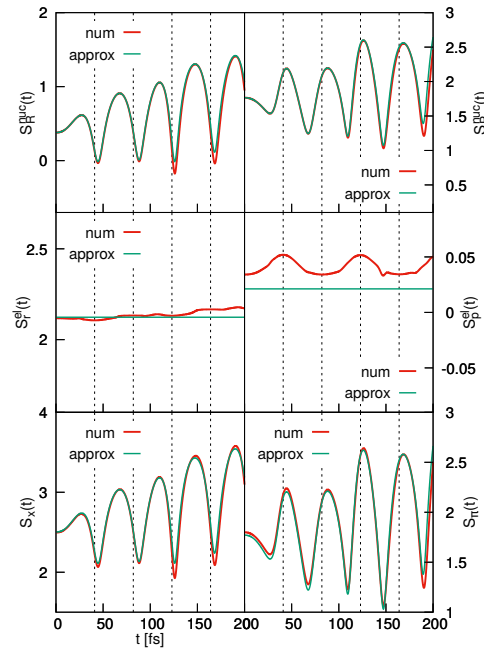


Figure 6. Same as Figure 3 but for the strong coupling case.

Whereas for the purely diabatic dynamics, all functions which measure correlations are identical to zero, the numerically calculated curves are non-zero but are small in magnitude, and thus we do not show them here.

Until now, we adopted a diabatic picture to describe the strong coupling case. It is interesting to relate the results to the adiabatic approach, where the expansion of the total wave function reads

$$\Psi(r, R, t) = \sum_{n=0}^{\infty} \psi_n(R, t) \varphi_n(r; R). \quad (54)$$

The total probability density then is

$$\rho(r, R, t) = |\Psi(r, R, t)|^2 = \sum_{n,m=0}^{\infty} \rho_{nm}(r, R, t), \quad (55)$$

with the matrix elements

$$\rho_{nm}(r, R, t) = \psi_n^*(R, t) \psi_m(R) \varphi_n(r; R) \varphi_m(r; R). \quad (56)$$

In our example, we start in the first excited electronic state, and the dynamics then leads to an almost 100% population transfer to the ground state at a time of $t_{tr} \approx 18.8$ fs. Later on, the population exchange between the two states occurs periodically. In order to illustrate the contributions of the different states to the entropies, we decompose the latter into components. Therefore, we first calculate adiabatic nuclear densities by integration as

$$\rho_{nm}^{nuc}(R, t) = \int dr \rho_{nm}(r, R, t) = |\psi_n(R, t)|^2 \delta_{nm}. \quad (57)$$

Thus, the off-diagonal elements vanish. This, in general, does not apply to the electronic case where we have

$$\rho_{nm}^{el}(r, t) = \int dR \rho_{nm}(r, R, t). \tag{58}$$

In the present numerical example, we find that the off-diagonal elements are negligible. The diagonal terms are positive semi-definite and may be interpreted as densities which are not normalized, and they are related to the populations in the electronic states as

$$\tilde{P}_n(t) = |\langle \varphi_n | \Psi(t) \rangle|^2 = \int dr \int dR \rho_{nn}(r, R, t). \tag{59}$$

Using the diagonal elements of the densities, we define state-specific entropies as follows:

$$S_{x,n}(t) = - \int dR \int dr \rho_{nn}(r, R, t) \ln[\rho_{nn}(r, R, t)], \tag{60}$$

$$S_{r,n}^{el}(t) = - \int dr \rho_{nn}^{el}(r, t) \ln[\rho_{nn}^{el}(r, t)], \tag{61}$$

$$S_{R,n}^{nuc}(t) = - \int dR \rho_{nn}^{nuc}(R, t) \ln[\rho_{nn}^{nuc}(R, t)]. \tag{62}$$

The decomposition of the entropies into different components may as well be performed in momentum space. Taking the Fourier transform of the wave function yields

$$\Psi(p, P, t) = \sum_n \Psi_n(p, P, t), \tag{63}$$

with the definition

$$\Psi_n(r, P, t) = \frac{1}{2\pi} \int dR e^{-iPR} \psi_n(R, t) \int dr e^{-ipr} \varphi_n(r; R). \tag{64}$$

The decomposition of the momentum-space densities is calculated as

$$\rho(p, P, t) = \sum_{n,m} \rho_{nm}(p, P, t), \tag{65}$$

with

$$\rho_{nm}(p, P, t) = \Psi_n^*(p, P, t) \psi_m(p, P, t). \tag{66}$$

From the latter matrix elements, we derive the electronic and nuclear matrix elements

$$\rho_{nm}^{el}(p, t) = \int dP \rho_{nm}(p, P, t), \tag{67}$$

$$\rho_{nm}^{nuc}(P, t) = \int dp \rho_{nm}(p, P, t). \tag{68}$$

The state-specific entropies are defined incorporating the diagonal elements of the densities and read

$$S_{\pi,n}(t) = - \int dP \int dp \rho_{nn}(p, P, t) \ln[\rho_{nn}(p, P, t)], \tag{69}$$

$$S_{p,n}^{el}(t) = - \int dp \rho_{nn}^{el}(p, t) \ln[\rho_{nn}^{el}(p, t)], \tag{70}$$

$$S_{P,n}^{nuc}(t) = - \int dP \rho_{nn}^{nuc}(P, t) \ln[\rho_{nn}^{nuc}(P, t)]. \tag{71}$$

In the left-hand column of Figure 7, we show the results of the decomposition of the coordinate-space entropies. The nuclear functions $S_{R,n}(t)$ for the quantum numbers $n = 0, 1$

6. INFORMATION-THEORETICAL APPROACH TO COUPLED ELECTRON-NUCLEAR DYNAMICS

are displayed in the upper left-hand panel of the figure. Also included is the sum of these two components and the numerically determined nuclear entropy $S_R(t)$. The components follow the population dynamics and also reflect the focusing and broadening of the wave packet components in the two states. The term $S_{R,1}(t)$ contributes to the entropy until the non-adiabatic transition takes place. Then, this function decreases, which goes in hand with an increase in $S_{R,0}(t)$ until the latter function becomes equal to the nuclear entropy. This behavior takes place several times in the shown interval, and, besides minor deviations, at all times, the sum of the two components equals the numerically determined nuclear entropy. To understand this, we write the latter within the approximation of two contributing states:

$$S_R^{nuc}(t) = - \int dR |\psi_0(R, t)|^2 \ln [|\psi_0(R, t)|^2 + |\psi_1(R, t)|^2] - \int dR |\psi_1(R, t)|^2 \ln [|\psi_0(R, t)|^2 + |\psi_1(R, t)|^2]. \quad (72)$$

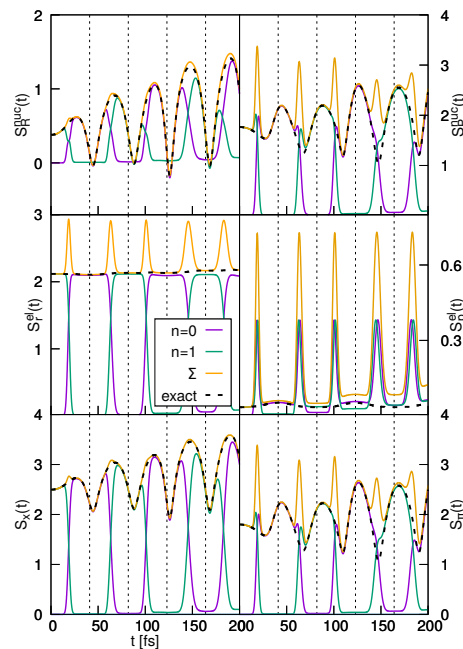


Figure 7. Decomposition of the entropies in the strong coupling case: Nuclear (**upper panels**), electronic (**middle panels**) and total entropies (**lower panels**). The coordinate-space entropies ($S_R^{nuc}(t)$, $S_R^{el}(t)$, $S_x(t)$) and the contributions of the two adiabatic electronic states ($S_{R,n}^{nuc}(t)$, $S_{R,n}^{el}(t)$, $S_{x,n}(t)$, $n = 0, 1$) are shown, and also the sum (Σ) of the state-specific entropies and the numerically exact curve. The right-hand column contains the respective quantities derived from the momentum-space density. The vertical dashed lines indicate the times when the classical turning points are reached.

From our numerical calculation, we find that the two nuclear wave functions $\psi_0(R, t)$ and $\psi_1(R, t)$ at no time have a significant spatial overlap, even around the transition times. Thus, we may set $\psi_1(R, t)$ equal to zero in the first integral appearing in Equation (72) and neglect $\psi_0(R, t)$ in the second integral. This yields

$$S_R^{nuc}(t) \approx - \sum_{n=0,1} \int dR |\psi_n(R, t)|^2 \ln [|\psi_n(R, t)|^2] = \sum_{n=0,1} S_{R,n}^{nuc}(t). \quad (73)$$

The electronic state-specific entropies (middle left panel of Figure 7) behave like the populations in the two electronic states (the curves for $\tilde{P}_n(t)$ are not included because their time variation is almost identical to the functions $S_{R,n}(t)$). This does not apply in the time intervals where the transitions take place. There, the sum of the electronic components $S_{r,n}^{el}(t)$ does not add up to the electronic coordinate entropy. Because the off-diagonal elements of the matrix $\rho_{nm}(r, t)$ are negligible, we have

$$S_r^{el}(t) = - \int dr \left[\sum_{n=0}^1 \rho_{nn}^{el}(r, t) \right] \ln \left[\sum_{n=0}^1 \rho_{nn}^{el}(r, t) \right]. \quad (74)$$

Numerically, we find that at a transition time t_{tr} , the elements $\rho_{00}^{el}(r, t)$ and $\rho_{11}^{el}(r, t)$ are approximately equal. It then follows that

$$\begin{aligned} S_r^{el}(t_{tr}) &\approx - \int dr \left[2\rho_{00}^{el}(r, t_{tr}) \right] \ln \left[2\rho_{00}^{el}(r, t_{tr}) \right] \\ &= -\ln[2] \int dr \left[2\rho_{00}^{el}(r, t_{tr}) \right] - 2 \int dr \rho_{00}^{el}(r, t_{tr}) \ln \left[\rho_{00}^{el}(r, t_{tr}) \right] \\ &= -\ln[2] + S_{0,r}(t_{tr}) + S_{1,r}(t_{tr}), \end{aligned} \quad (75)$$

where we used that at the transition time, the population takes a value of $\tilde{P}_0(t_{tr}) = 0.5$. Thus, at this time, the numerical electronic entropy and the sum of the components differ by a value of $-\ln[2]$. This is in accord with what is seen in Figure 7. In contrast, the total entropy is excellently represented by the sum of the state functions, which can be traced back to the fact that the nuclear components of the two involved states do not overlap and thus, as a result of integrating out the nuclear degree of freedom, the same applies to the diagonal elements ρ_{nm} .

In the right-hand column of Figure 7, we document the decomposition of the momentum-space entropies. Again, the nuclear state-selective entropies follow the population dynamics, but here the sum of the single components exhibits larger deviations from the total entropy around the transition times. This is because the mathematical structure of the momentum-space matrix elements (Equation (66)) is more complex than in coordinate space. Pronounced deviations are also found in the electronic momentum entropies, where large maxima are seen in the state-specific entropies, whereas the total electronic entropy remains nearly constant. The disagreement of the curves, related to the non-adiabatic transitions, is also apparent in the total momentum entropy, see lower right panel of the figure. This is because the diagonal elements ρ_{nn} overlap already in $(p - P)$ -space, and thus, the off-diagonal elements cannot be ignored.

4. Summary

We study differential entropies evolving from a coupled electron–nuclear quantum dynamics. Using the total density and single-particle densities, we calculate the respective time-dependent entropies in coordinate- and momentum space. In doing so, two situations are regarded. In the first one, the dynamics takes place in a single adiabatic electronic state so that the Born–Oppenheimer approximation applies. The second case is characterized by a strong non-adiabatic coupling, which leads to a complete population transfer between two adiabatic states. Under these conditions, one encounters a diabatic motion.

The two described dynamical situations are realized within a model for a one-dimensional motion of a single electron and nucleus, which allows to integrate the time-dependent Schrödinger equation numerically. In both cases, it is also possible to find an analytical description which explains most of the features found in the numerical calculation.

For the BO dynamics, where the electron adiabatically follows the nucleus, the time-dependence of the coordinate-space entropies is determined by the position and width of the nuclear density. In our example, the latter performs a vibrational motion, and at the classical turning points of this dynamics, the density is focused. Then, we have more information about the positions of the two particles, which is reflected in the particle

and total entropies, which all pass through minima. At the same instants of time, the momentum-space entropies exhibit maxima which are related to the Fourier properties of the coordinate- and momentum-space wave functions.

We compare three different measures for the particle entanglement, i.e., the covariance, the correlation and the mutual information. If these functions are determined from the coordinate space densities, they show a similar time dependence. In particular, when the wave packet reaches the classical turning point, they exhibit minima. This means that at these times, when the coordinate space wave function becomes more localized, the electron–nuclear correlation is small. The reason is that then the dependence of the electronic wave function on the nuclear geometry is less pronounced. A different picture evolves from the momentum-space densities. There, the MI behaves differently than the covariance and correlation. Because the latter monitor a linear particle entanglement, this hints at nonlinear effects. It is found that the behavior of the MI is related to the nodal structure of the momentum-space density. Maxima occur at times when the latter density exhibits a clear node behavior with lines oriented non-parallel to the nuclear momentum axis. An analytical model shows that with an increasing number of nodes, the MI grows until a threshold is approached.

In the situation where strong non-adiabatic couplings are present, the dynamics is most efficiently described within a diabatic picture, which means that there is no correlation between the particles present. This is clear from the form of the wave function and is seen in our numerical example. The numerical results can be well reproduced using the analytical model starting from a diabatic wave function. The nuclear wave packet motion proceeds in an almost harmonic potential, which results in a regular variation of the nuclear entropy. On the other hand, the electronic entropy is nearly constant. This holds in both coordinate- and momentum space. A decomposition of the coordinate space in terms of the adiabatic expansion of the total wave function leads to state-specific entropies. For the nuclear case, these functions add up to the total entropy. This, however, is not the case in momentum space. There, the decomposition yields non-negligible off-diagonal contributions, which cannot be ignored.

Author Contributions: Conceptualization, P.S. and V.E.; methodology, P.S. and V.E.; software, P.S.; validation, P.S. and V.E.; formal analysis, P.S.; investigation, P.S.; resources, V.E.; data curation, P.S.; writing—original draft preparation, V.E.; writing—review and editing, P.S. and V.E.; visualization, P.S.; supervision, V.E.; project administration, V.E. All authors have read and agreed to the published version of the manuscript.

Funding: This publication was supported by the Open Access Publication Fund of the University of Würzburg.

Institutional Review Board Statement: Not applicable.

Data Availability Statement: The data that support the findings of this study are available from the corresponding author upon reasonable request.

Conflicts of Interest: The authors declare no conflict of interest.

Abbreviations

The following abbreviations are used in this manuscript:

BO Born–Oppenheimer
MI Mutual information

Appendix A. Entropies in Momentum Space

To evaluate the momentum-space densities, we first take the Fourier transform of the spatial wave function Equation (27):

$$\Psi(p, P) = \frac{N_t}{2\pi} \int dR \int dr e^{-iPR - ipr} e^{-\frac{\beta_t}{2}(R-R_t)^2 - \frac{\gamma}{2}(r-R)^2}. \quad (\text{A1})$$

The Fourier integral over the electronic coordinate is a Gaussian integration. Using the coordinate $r' = r - R$, one finds

$$e^{-ipR} \int dr' e^{-ipr'} e^{-\frac{\gamma}{2}r'^2} = \sqrt{\frac{2\pi}{\gamma}} e^{-ipR - \frac{p^2}{2\gamma}}. \tag{A2}$$

With this result, and performing another Gaussian integral, the wave function is evaluated as

$$\begin{aligned} \Psi(p, P) &= \frac{N_t}{2\pi} \sqrt{\frac{2\pi}{\gamma}} e^{-\frac{\beta_t}{2}R_t^2 - \frac{p^2}{2\gamma}} \int dR e^{-\frac{\beta_t}{2}R^2 + [\beta_t R_t - i(p+P)]R} \\ &= \frac{N_t}{2\pi} \sqrt{\frac{2\pi}{\gamma}} \sqrt{\frac{2\pi}{\beta_t}} e^{-\frac{\beta_t}{2}R_t^2 - \frac{p^2}{2\gamma}} e^{\frac{[\beta_t R_t - i(p+P)]^2}{2\beta_t}} \\ &= \frac{1}{\sqrt{\pi}(\beta_t \gamma)^{1/4}} e^{-\frac{\beta_t}{2}R_t^2 - \frac{p^2}{2\gamma} + \frac{[\beta_t R_t - i(p+P)]^2}{2\beta_t}}. \end{aligned} \tag{A3}$$

In calculating the momentum-space density, the exponential containing the mean position R_t drops out and one finds

$$\rho(p, P, t) = M_t e^{-\frac{1}{\beta_t}(p+P)^2 - \frac{p^2}{\gamma}}, \tag{A4}$$

with the normalization constant

$$M_t = \frac{1}{\pi \sqrt{\beta_t \gamma}}. \tag{A5}$$

To evaluate the entropy, we take advantage of the fact that the polynomial appearing in the exponent is quadratic. Thus, the function

$$f(p, P) = -\frac{1}{\beta_t}(p+P)^2 - \frac{p^2}{\gamma}, \tag{A6}$$

using the real valued parameter λ may be written as

$$f(p', P') = \lambda f(p, P), \quad p' = \sqrt{\lambda} p, \quad P' = \sqrt{\lambda} P, \tag{A7}$$

with the scaled coordinates p' and P' . We then have the property

$$M_t \int dp \int dP e^{\lambda f(p, P)} = \frac{1}{\lambda} M_t \int dp' \int dP' e^{f(p', P')} = \frac{1}{\lambda}, \tag{A8}$$

and it follows that

$$\begin{aligned} M_t \int dp \int dP e^{f(p, P)} f(p, P) &= \lim_{\lambda \rightarrow 1} \frac{d}{d\lambda} \left[M_t \int dp \int dP e^{\lambda f(p, P)} \right] \\ &= \lim_{\lambda \rightarrow 1} \frac{d}{d\lambda} \left[\frac{1}{\lambda} \right] = -1. \end{aligned} \tag{A9}$$

We note that this result can be generalized to quadratic functions $f(y_1, y_2, \dots, y_d)$ depending on d variables y_j . Below, we need the derived property for the case of a single variable y so that

$$M_t \int dy e^{f(y)} f(y) = \lim_{\lambda \rightarrow 1} \frac{d}{d\lambda} \left[M_t \int dy e^{\lambda f(y)} \right] = \lim_{\lambda \rightarrow 1} \frac{d}{d\lambda} \left[\frac{1}{\sqrt{\lambda}} \right] = -\frac{1}{2}. \tag{A10}$$

The entropy now can be calculated as

$$S_{\pi}(t) = -\ln[M_t] - M_t \int dp \int dP e^{f(p,P)} f(p,P) = \ln[\sqrt{\gamma\beta_t\pi}] + 1. \quad (A11)$$

For the sum of the momentum and position entropy, one finds

$$\begin{aligned} S_{\pi}(t) + S_x(t) &= \ln[\sqrt{\gamma\beta_t\pi}] + 1 + \ln\left[\frac{\pi}{\sqrt{\gamma\beta_t}}\right] + 1 \\ &= 2(\ln[\pi] + 1). \end{aligned} \quad (A12)$$

This result is well known, and it reflects the relation of the differential Shannon entropies to the coordinate–momentum uncertainty relation. Next, we calculate the electronic entropy from the electronic density. The latter is obtained from a Gaussian integral as

$$\rho^{el}(p,t) = \frac{1}{\pi\sqrt{\beta_t\gamma}} \int dP e^{-\frac{1}{\beta_t}(p+P)^2 - \frac{P^2}{\gamma}} = \frac{1}{\sqrt{\pi\gamma}} e^{-\frac{p^2}{\gamma}} \quad (A13)$$

As was discussed above for the total entropy, the quadratic expression for the exponent appearing in the electronic momentum density allows to evaluate the entropy introducing the scaled coordinate $p' = \sqrt{\lambda} p$ so that the volume element transforms as $dp' = dp/\sqrt{\lambda}$. Using Equation (A10), this then leads to

$$S_p^{el}(t) = \ln[\sqrt{\pi\gamma}] + \frac{1}{2}. \quad (A14)$$

In the nuclear case, the density is

$$\begin{aligned} \rho^{nuc}(P,t) &= \frac{1}{\pi\sqrt{\beta_t\gamma}} \int dp e^{-\frac{1}{\beta_t}(p+P)^2 - \frac{P^2}{\gamma}} \\ &= \frac{1}{\pi\sqrt{\beta_t\gamma}} e^{-\frac{P^2}{\beta_t}} \int dp e^{-\frac{\gamma+\beta_t}{\beta_t\gamma} p^2 - \frac{2P}{\beta_t} p} \\ &= \frac{1}{\pi\sqrt{\beta_t\gamma}} \sqrt{\frac{\pi\gamma\beta_t}{\gamma+\beta_t}} e^{-\frac{P^2}{\beta_t}} e^{\frac{\beta_t\gamma}{\gamma+\beta_t} \frac{P^2}{\beta_t^2}} \\ &= \frac{1}{\sqrt{\pi(\beta_t+\gamma)}} e^{-\frac{P^2}{\gamma+\beta_t}}. \end{aligned} \quad (A15)$$

With the help of Equation (A10), the nuclear entropy is of the form

$$S_p^{nuc}(t) = \ln[\sqrt{\pi(\beta_t+\gamma)}] + \frac{1}{2}. \quad (A16)$$

Having calculated the total and single-particle entropies, the mutual information can be determined as

$$I_{\pi}(t) = \ln[\sqrt{\pi\gamma}] + \ln[\sqrt{\pi(\beta_t+\gamma)}] - \ln[\sqrt{\gamma\beta_t\pi}], \quad (A17)$$

which can be re-written as

$$I_{\pi}(t) = \frac{1}{2} \ln\left[1 + \frac{\gamma}{\beta_t}\right]. \quad (A18)$$

To determine the covariance in momentum space, we need the expectation values of p, P and the product pP . Regarding the momentum-space density given in Equation (A4), it follows due to symmetry that

$$\langle P \rangle_t = \langle p \rangle_t = 0. \quad (A19)$$

This can be traced back to the ansatz of the wave function (Equation (27)), which does not incorporate a mean momentum different from zero. The expectation value of the momentum product is

$$\langle pP \rangle_t = \frac{1}{\pi\sqrt{\beta_t\gamma}} \int dP \int dp P p e^{-\frac{1}{\beta_t}(P+p)^2 - \frac{p^2}{\gamma}}. \quad (\text{A20})$$

Introducing the new variable $P' = P + p$, the latter integral transforms as

$$\begin{aligned} \langle pP \rangle_t &= \frac{1}{\pi\sqrt{\beta_t\gamma}} \int dP' \int dp (P'p - p^2) e^{-\frac{1}{\beta_t}P'^2 - \frac{p^2}{\gamma}} \\ &= -\frac{1}{\sqrt{\pi\gamma}} \int dp p^2 e^{-\frac{p^2}{\gamma}} = -\frac{1}{2}\gamma, \end{aligned} \quad (\text{A21})$$

where we employed symmetry in the integration over P' , and we used the analytical result for an Gaussian integral as $\int dy y^2 e^{-y^2} = \sqrt{\pi}/2$. We then arrive at the result

$$\text{cov}_\pi(t) = -\frac{1}{2}\gamma. \quad (\text{A22})$$

Finally, to calculate the correlation, we need the variances in the two momentum variables. From Equation (A21) we realize that

$$\langle p^2 \rangle_t = \frac{\gamma}{2}. \quad (\text{A23})$$

In calculating the variance for the variable P , again the transformation $P' = P + p$ is used and properties of integrals over Gaussians are employed. One finds

$$\begin{aligned} \langle P^2 \rangle &= \frac{1}{\pi\sqrt{\beta_t\gamma}} \int dP \int dp P^2 e^{-\frac{1}{\beta_t}(P+p)^2 - \frac{p^2}{\gamma}} \\ &= \frac{1}{\pi\sqrt{\beta_t\gamma}} \int dP' \int dp (P' - p)^2 e^{-\frac{1}{\beta_t}P'^2 - \frac{p^2}{\gamma}} \\ &= \frac{1}{\pi\sqrt{\beta_t\gamma}} \int dP \int dp (P^2 + p^2) e^{-\frac{1}{\beta_t}P^2 - \frac{p^2}{\gamma}} \\ &= \frac{1}{\sqrt{\pi\beta_t}} \int dP P^2 e^{-\frac{1}{\beta_t}P^2} + \frac{1}{\sqrt{\pi\gamma}} \int dp p^2 e^{-\frac{p^2}{\gamma}} \\ &= \frac{1}{2}(\beta_t + \gamma), \end{aligned} \quad (\text{A24})$$

so that

$$\sigma_P^2 = \frac{1}{2}(\beta_t + \gamma). \quad (\text{A25})$$

Having calculated the variances, one arrives at an expression for the correlation, which reads

$$\text{corr}_\pi(t) = -\frac{1}{\sqrt{1 + \beta_t/\gamma}}. \quad (\text{A26})$$

Appendix B. Entropies for Strong Coupling

Here, the entropies for the strong coupling case are determined analytically using the ansatz of Equation (47) for the wave function. Using the nuclear density

$$\rho^{nuc}(R, t) = \sqrt{\frac{\pi}{\beta_t}} e^{-\beta_t(R-R_t)^2}, \quad (\text{A27})$$

the associated entropy is, using the result of Equation (A10),

$$S_x^{nuc}(t) = \ln \left[\sqrt{\frac{\pi}{\beta_t}} \right] + \frac{1}{2}. \quad (\text{A28})$$

With the electronic density

$$\rho^{el}(r, t) = \sqrt{\frac{\gamma}{\pi}} e^{-\gamma(r-R_0)^2} \quad (\text{A29})$$

an equivalent calculation as performed in the nuclear case yields the electronic entropy

$$S_x^{el}(t) = \ln \left[\sqrt{\frac{\pi}{\gamma}} \right] + \frac{1}{2}. \quad (\text{A30})$$

The same result is obtained in the BO case for $\beta \rightarrow \infty$, which means that the nuclear wave function is strongly localized so that the R -dependence of the electronic wave function can be neglected and one recovers the diabatic case.

For the present situation of a separable wave function, the total entropy is just the sum of the single-particle entropies, and it reads

$$S_x(t) = \ln \left[\frac{\pi}{\sqrt{\beta_t \gamma}} \right] + 1. \quad (\text{A31})$$

Because of the Fourier properties of Gaussians, the nuclear momentum density has the same functional form as the coordinate density upon the replacements $R \rightarrow P$ and $\beta_t \rightarrow 1/\beta_t$. This leads to the entropy

$$S_p^{nuc}(t) = \ln \left[\sqrt{\pi \beta_t} \right] + \frac{1}{2}. \quad (\text{A32})$$

Using the replacement $r \rightarrow p, \gamma \rightarrow 1/\gamma$ yields

$$S_p^{el}(t) = \ln \left[\sqrt{\pi \gamma} \right] + \frac{1}{2}, \quad (\text{A33})$$

and the total entropy is additive:

$$S_\pi(t) = \ln \left[\sqrt{\gamma \beta_t \pi} \right] + 1. \quad (\text{A34})$$

References

1. Cover, T.M.; Thomas, J.A. *Elements of Information Theory*, 2nd ed.; Wiley Series in Telecommunications and Signal Processing; Wiley-Interscience: Hoboken, NJ, USA, 2006.
2. Hertz, A.; Cerf, N.J. Continuous-variable entropic uncertainty relations. *J. Phys. A* **2019**, *52*, 173001. [[CrossRef](#)]
3. Hirschman, I.I. A Note on Entropy. *Am. J. Math.* **1957**, *79*, 152–156. [[CrossRef](#)]
4. Białynicki-Birula, I.; Mycielski, J. Uncertainty relations for information entropy in wave mechanics. *Commun. Math. Phys.* **1975**, *44*, 129–132. [[CrossRef](#)]
5. Beckner, W. Inequalities in Fourier Analysis. *Ann. Math.* **1975**, *102*, 159–182. [[CrossRef](#)]
6. Levine, R.D. The information theoretic approach to intramolecular dynamics. In *Photoselective Chemistry*; John Wiley & Sons, Inc.: Hoboken, NJ, USA, 1981; Volume 47, pp. 239–292. [[CrossRef](#)]
7. Quack, M. *Femtosecond Chemistry*; VCH: Weinheim, Germany, 1995; Volume II, pp. 781–818.

8. Quack, M. On the emergence of simple structures in complex phenomena: Concepts and some numerical examples. In *Advances in Chemical Physics*; John Wiley & Sons, Inc.: Hoboken, NJ, USA, 2014; Volume 157, pp. 97–118.
9. Jia, D.; Manz, J.; Yang, Y. From coherent quasi-irreversible quantum dynamics towards the second law of thermodynamics: The model boron rotor B_3^+ . *AIP Adv.* **2018**, *8*, 045222. [[CrossRef](#)]
10. Ludeña, E.V.; Torres, F.J.; Becerra, M.; Rincón, L.; Liu, S. Shannon entropy and Fisher information from a non-Born-Oppenheimer perspective. *J. Phys. Chem. A* **2020**, *124*, 386–394. [[CrossRef](#)] [[PubMed](#)]
11. Flores-Gallegos, N. Shannon Informational Entropies and Chemical Reactivity. In *Advances in Quantum Mechanics*; InTech: Rijeka, Croatia, 2013. [[CrossRef](#)]
12. Noorizadeh, S.; Shakerzadeh, E. Shannon entropy as a new measure of aromaticity, Shannon aromaticity. *Phys. Chem. Chem. Phys.* **2010**, *12*, 4742. [[CrossRef](#)]
13. Hsueh, Y.W.; Hsueh, C.H.; Wu, W.C. Thermalization in a Quantum Harmonic Oscillator with Random Disorder. *Entropy* **2020**, *22*, 855. [[CrossRef](#)]
14. Schürger, P.; Schaupp, T.; Kaiser, D.; Engels, B.; Engel, V. Wave packet dynamics in an harmonic potential disturbed by disorder: Entropy, uncertainty, and vibrational revivals. *J. Chem. Phys.* **2022**, *137*, 054303. [[CrossRef](#)]
15. Martínez-Flores, C. The information theory of the helium atom in screened Coulomb potentials. *Int. J. Quantum Chem.* **2021**, *121*, e26529. [[CrossRef](#)]
16. Nascimento, W.S.; Prudente, F.V. Shannon entropy: A study of confined hydrogenic-like atoms. *Chem. Phys. Lett.* **2018**, *691*, 401–407. [[CrossRef](#)]
17. Kumar, K.; Prasad, V. Few generalized entropic relations related to Rydberg atoms. *Sci. Rep.* **2022**, *12*, 7496. [[CrossRef](#)]
18. Saha, S.; Jose, J. Shannon entropy as a predictor of avoided crossing in confined atoms. *Int. J. Quantum Chem.* **2020**, *120*, e26374. [[CrossRef](#)]
19. González-Férez, R.; Dehesa, J.S. Shannon Entropy as an Indicator of Atomic Avoided Crossings in Strong Parallel Magnetic and Electric Fields. *Phys. Rev. Lett.* **2003**, *91*, 113001. [[CrossRef](#)] [[PubMed](#)]
20. He, Y.L.; Chen, Y.; Han, J.N.; Zhu, Z.B.; Xiang, G.X.; Liu, H.D.; Ma, B.H.; He, D.C. Shannon entropy as an indicator of atomic avoided crossings for Rydberg potassium atoms interacting with a static electric field. *Eur. Phys. J. D* **2015**, *69*, 283. [[CrossRef](#)]
21. Salazar, S.J.C.; Laguna, H.G.; Sagar, R.P. Pairwise and higher-order statistical correlations in excited states of quantum oscillator systems. *Eur. Phys. J. Plus* **2022**, *137*, 19. [[CrossRef](#)]
22. Yépez, V.S.; Sagar, R.P.; Laguna, H.G. Higher-Order Statistical Correlations and Mutual Information Among Particles in a Quantum Well. *Few-Body Syst.* **2017**, *58*, 158. [[CrossRef](#)]
23. Born, M.; Oppenheimer, R. Zur Quantentheorie der Molekeln. *Ann. Phys.* **1927**, *84*, 457–484. [[CrossRef](#)]
24. Born, M.; Huang, K. *Theory of Crystal Lattices*; Oxford University Press: Oxford, UK; London, UK, 1954.
25. Baer, M. *Beyond Born-Oppenheimer: Electronic Nonadiabatic Coupling Terms and Conical Intersections*; Wiley: Hoboken, NJ, USA, 2006.
26. Child, M.S. *Semiclassical Mechanics with Molecular Applications*; Clarendon Press: Oxford, UK, 1991.
27. Nakamura, H. *Nonadiabatic Transition*, 2nd ed.; World Scientific: Singapore, 2012.
28. Yarkony, D.R. Diabolical conical intersections. *Rev. Mod. Phys.* **1996**, *68*, 985. [[CrossRef](#)]
29. Köppel, H. *Conical Intersections: Electronic Structure, Dynamics and Spectroscopy*; Domcke, W., Yarkony, D.R., Köppel, H., Eds.; World Scientific: Singapore, 2004; pp. 175–204, 429–472.
30. Paterson, M.J.; Bearpark, M.J.; Robb, M.A.; Blancafort, L.; Worth, G.A. Conical Intersections: A Perspective on the Computation of Spectroscopic Jahn-Teller Parameters and the Degenerate Intersection Space. *Phys. Chem. Chem. Phys.* **2005**, *7*, 2100–2115. [[CrossRef](#)]
31. Shannon, C.E. A mathematical theory of communication. *Bell Syst. Tech. J.* **1948**, *27*, 379–423. [[CrossRef](#)]
32. Schürger, P.; Engel, V. Information Theoretical Approach to Coupled Electron-Nuclear Wave Packet Dynamics: Time-Dependent Differential Shannon Entropies. *J. Phys. Chem. Lett.* **2023**, *14*, 334–339. [[CrossRef](#)] [[PubMed](#)]
33. Shin, S.; Metiu, H. Multiple time scale quantum wavepacket propagation: Electron-nuclear Dynamics. *J. Phys. Chem.* **1996**, *100*, 7867–7872. [[CrossRef](#)]
34. Shin, S.; Metiu, H. Nonadiabatic effects on the charge transfer rate constant: A numerical study of a simple model system. *J. Chem. Phys.* **1995**, *102*, 9285–9295. [[CrossRef](#)]
35. Erdmann, M.; Marquetand, P.; Engel, V. Combined electronic and nuclear dynamics in a simple model system. *J. Chem. Phys.* **2003**, *119*, 672–679. [[CrossRef](#)]
36. Erdmann, M.; Gross, E.K.U.; Engel, V. Time-dependent electron localization functions for coupled nuclear-electronic motion. *J. Chem. Phys.* **2004**, *121*, 9666–9670. [[CrossRef](#)]
37. Falge, M.; Engel, V.; Gräfe, S. Time-resolved PES of coupled electron-nuclear motion. *J. Chem. Phys.* **2011**, *134*, 184307. [[CrossRef](#)]
38. Min, S.K.; Abedi, A.; Kim, K.; Gross, E.K.U. Is the Molecular Berry Phase an Artifact of the Born-Oppenheimer Approximation? *Phys. Rev. Lett.* **2014**, *113*, 263004. [[CrossRef](#)]
39. Hader, K.; Albert, J.; Gross, E.K.U.; Engel, V. Electron-nuclear wave-packet dynamics through a conical intersection. *J. Chem. Phys.* **2017**, *146*, 074304. [[CrossRef](#)]
40. Schaupp, T.; Engel, V. Correlated three-dimensional electron-nuclear motion: Adiabatic dynamics vs passage of conical intersections. *J. Chem. Phys.* **2022**, *156*, 074302. [[CrossRef](#)]

6. INFORMATION-THEORETICAL APPROACH TO COUPLED ELECTRON-NUCLEAR DYNAMICS

41. Feit, M.D.; Fleck, J.A.; Steiger, A. Solution of the Schrödinger equation by a spectral method. *J. Comput. Phys.* **1982**, *47*, 412–433. [[CrossRef](#)]
42. Kosloff, R.; Tal-Ezer, H. A direct relaxation method for calculating eigenfunctions and eigenvalues of the Schrödinger equation on a grid. *Chem. Phys. Lett.* **1986**, *127*, 223–230. [[CrossRef](#)]
43. Mandel, E.; Wolf, E. *Optical Coherence and Quantum Optics*; Cambridge University Press: Cambridge, UK, 1995.
44. Schürger, P.; Engel, V. Institute of Physical and Theoretical Chemistry, Würzburg, Germany. 2023, *to be published*.
45. Tannor, D.J. *Introduction to Quantum Mechanics: A Time-Dependent Perspective*; University Science Books: Sausalito, CA, USA, 2007.
46. Schaupp, T.; Engel, V. Born–Oppenheimer and non-Born–Oppenheimer contributions to time-dependent electron momenta. *J. Chem. Phys.* **2020**, *152*, 204310. [[CrossRef](#)] [[PubMed](#)]
47. Albert, J.; Kaiser, D.; Engel, V. Adiabatic and non-adiabatic electron-nuclear motion: Quantum and classical dynamics. *J. Chem. Phys.* **2016**, *144*, 171103. [[CrossRef](#)] [[PubMed](#)]

Disclaimer/Publisher’s Note: The statements, opinions and data contained in all publications are solely those of the individual author(s) and contributor(s) and not of MDPI and/or the editor(s). MDPI and/or the editor(s) disclaim responsibility for any injury to people or property resulting from any ideas, methods, instructions or products referred to in the content.




6.3.4 On the relation between nodal structures in quantum wave functions and particle correlation [6]



Reprinted from "P. Schürger, V. Engel, AIP Advances 2023, 13, 125307"; licensed under a Creative Commons Attribution (CC BY) license (CC BY 4.0).

AIP Advances
ARTICLE
pubs.aip.org/aip/adv

On the relation between nodal structures in quantum wave functions and particle correlation

Cite as: AIP Advances **13**, 125307 (2023); doi: [10.1063/5.0180004](https://doi.org/10.1063/5.0180004)
Submitted: 6 October 2023 • **Accepted:** 14 November 2023 •
Published Online: 7 December 2023

 View Online
 Export Citation
 CrossMark

Peter Schürger^{a1}  and **Volker Engel**^{a1} 

AFFILIATIONS

Universität Würzburg Institut für Physikalische und Theoretische Chemie, Emil-Fischer-Str. 42, 97074 Würzburg, Germany

^{a1}Authors to whom correspondence should be addressed: peter.schuerger@uni-wuerzburg.de and volker.engel@uni-wuerzburg.de

ABSTRACT

We study the influence of nodal structures in two-dimensional quantum mechanical densities on wave packet entanglement. This is motivated by our recent study [Entropy, 25, 970 (2023)], which showed that the mutual information derived from the momentum-space probability density of a coupled two-particle system exhibits an unusual time dependence, which is not encountered if the position-space density is employed in the calculation. In studying a model density, here, we identify cases where the mutual information increases with the number of nodes in the wave function and approaches a finite value, whereas in this limit, the linear correlation vanishes. The results of the analytical model are then applied to interpret the correlation measures for coupled electron-nuclear dynamics, which are treated by numerically solving the time-dependent Schrödinger equation.

© 2023 Author(s). All article content, except where otherwise noted, is licensed under a Creative Commons Attribution (CC BY) license (<http://creativecommons.org/licenses/by/4.0/>). <https://doi.org/10.1063/5.0180004>

I. INTRODUCTION

Nodes appearing in quantum mechanical wave functions are closely related to the excitation state of the system under consideration. For example, the number of nodes in the radial functions of the hydrogen atom equals the principal quantum number plus one.¹ In addition, regarding normal modes of vibrations, the nodes, being directly related to the quantum numbers, determine the symmetry selection rules for infrared transitions.² Another aspect of zeros that are present in probability densities is that they cause problems in applying classical approximations to the density, e.g., in quantum diffusion calculations.^{3,4}

Nodal structures in wave functions influence the appearance of different observables if detected as a function of a single parameter. For example, using the "reflection principle,"⁵ structures appearing in absorption spectra can be traced back to the nodes of the initial vibrational wave functions,⁶ and the same applies to resonance Raman spectra.⁷ As another example, we mention the power of time-resolved photoelectron spectroscopy to detect quantum topologies in vibrational wave packets.⁸ In this paper, we are concerned with

densities from which the correlation between two variables can be inferred. The focus is to investigate how nodes, being present in such densities, are related to the correlation. Although our numerical example treats the wave-packet entanglement between electronic and nuclear degrees of freedom, the derived results are more general, and they apply also to other types of correlation effects. This, in particular, is the case for many-body electronic systems where, due to their fermionic character, nodes arise naturally. Electron-electron correlation plays a prominent role in quantum chemistry, and it is thus important to characterize such collective effects. Electronic structure calculations are static and do not yield information on the time evolution of the correlation. Here, we treat dynamical effects that arise from the correlated motion of electrons and nuclei. Because the solution of the time-dependent Schrödinger equation for molecules is, in general, not possible without imposing restrictive approximations, a simple numerical model is employed. The results may serve as a starting point for further work on more complex systems. Within the employed model, it is possible to determine electron-nuclear wave packets in position- and momentum-space. The respective densities exhibit distinct quantum structures and,

AIP Advances **13**, 125307 (2023); doi: [10.1063/5.0180004](https://doi.org/10.1063/5.0180004)
 © Author(s) 2023

13, 125307-1

13 December 2023 12:10:38

at certain times, are characterized by different node patterns. We address the following question: how do these time-dependent patterns influence particle correlations? This is of importance regarding molecules because chemical bonding and reactivity are determined by such correlations. It is then necessary to find reasonable ways to characterize the latter.

There are different measures that are used to estimate entanglement; for applications in the context of chemical reactions and electronic structure theory, see, e.g., Refs. 9–20. We consider two of such functions, namely, the mutual information (MI)^{21,22} and the linear correlation coefficient,²³ and investigate their time dependence arising from nuclear-electron dynamics.

The mutual information has been calculated to characterize correlation effects in atoms and molecules.^{11,14,15,19} It is important, however, to emphasize that the MI and the correlation coefficient are not observables but measures to visualize and quantify correlation.

The paper is organized as follows: In Sec. II, we summarize the main definitions. The results are given in Sec. III, where analytical expressions for the correlation measures are derived for a parameterized model density (Sec. III A). A numerical example is presented in Sec. III B. The latter treats the adiabatic motion of an electron and a nucleus, which are coupled through screened Coulomb interactions. Using the analytical results, the behavior of the MI and the correlation coefficients derived from the coordinate-space and momentum-space densities, respectively, is interpreted. The article is closed with a summary given in Sec. IV.

II. THEORY

Our considerations are limited to two variables x and y and a probability density $\rho(x, y)$, which may also depend on time. Although this describes a more general situation, we will, in what follows, refer to a nucleus and an electron having nuclear (*nuc*) and electronic (*el*) degrees of freedom of x and y , respectively.

The non-linear correlation between the two particles is measured using the mutual information (MI).^{21,22} It is a functional that is related to the difference between the probability density $\rho(x, y)$ and the density built from the single particles, which are defined as

$$\rho^{nuc}(x) = \int dy \rho(x, y), \quad (1)$$

$$\rho^{el}(y) = \int dx \rho(x, y). \quad (2)$$

Then the MI is

$$I = \int dx dy \rho(x, y) \ln \left[\frac{\rho(x, y)}{\rho^{nuc}(x)\rho^{el}(y)} \right]. \quad (3)$$

Equivalently, this function can be written as

$$I = S^{nuc} + S^{el} - S. \quad (4)$$

Here appear the (differential) Shannon entropies^{24,25} determined from the total density,

$$S = - \int dx dy \rho(x, y) \ln [\rho(x, y)], \quad (5)$$

and the single-particle entropies,

$$\begin{aligned} S^{nuc} &= - \int dx \rho^{nuc}(x) \ln [\rho^{nuc}(x)], \\ S^{el} &= - \int dy \rho^{el}(y) \ln [\rho^{el}(y)]. \end{aligned} \quad (6)$$

If the Shannon entropy is regarded as a measure of information, the MI can be interpreted as the amount of information lost when comparing what is inferred from the densities $\rho^{nuc}(x)$ and $\rho^{el}(y)$ with the information extracted from the total density $\rho(x, y)$.

As another measure for entanglement, we define the linear correlation coefficient as²³

$$corr = \frac{cov}{\sigma_x \sigma_y}, \quad (7)$$

where the nominator is the covariance function,

$$cov = \langle xy \rangle - \langle x \rangle \langle y \rangle, \quad (8)$$

and the denominator contains the variances,

$$\sigma_x^2 = \langle x^2 \rangle - \langle x \rangle^2, \quad \sigma_y^2 = \langle y^2 \rangle - \langle y \rangle^2. \quad (9)$$

In the latter equations, the brackets denote the expectation values taken with respect to the density $\rho(x, y)$. The correlation coefficient takes a value between -1 and 1 , and its absolute value determines how well the density $\rho(x, y)$ is approximated by a straight line.²³ This means that, approximately, we find a linear relationship $\langle y \rangle \approx \lambda_0 + \lambda_1 \langle x \rangle$, with λ_0 and λ_1 being numbers. The sign determines if this line has a negative or positive gradient. For a vanishing function, i.e., $corr = 0$, no linear correlation between the variables exists, but higher order correlations may be present in the MI.²⁶

III. RESULTS

A. Analytical considerations

In this section, we start from a density of a particular form, and the reason for its choice will become apparent when the numerical example presented in Sec. III B is discussed. The density is

$$\rho_{a,b}(x, y) = \frac{2 e^{-(x^2+y^2)} \cos^2 \left[\frac{a}{\sqrt{1+b^2}} (x + by) \right]}{\pi (1 + e^{-a^2})}, \quad (10)$$

where a and b are real valued parameters. From the total density, the single-particle densities are determined using *MATHEMATICA*,²⁷ and the results are

$$\rho_{a,b}^{nuc}(x) = \frac{e^{\frac{x^2}{b^2+1} - x^2} \left(e^{\frac{a^2 b^2}{b^2+1}} + \cos \left[\frac{2ax}{\sqrt{b^2+1}} \right] \right)}{\sqrt{\pi} (e^{a^2} + 1)}, \quad (11)$$

$$\rho_{a,b}^{el}(y) = \frac{e^{\frac{a^2 b^2}{b^2+1} - y^2} \left(e^{\frac{a^2}{b^2+1}} + \cos \left[\frac{2aby}{\sqrt{b^2+1}} \right] \right)}{\sqrt{\pi} (e^{a^2} + 1)}. \quad (12)$$

The total density is a Gaussian multiplied by a \cos^2 function, and it is normalized to a value of one. The number of nodes that

fall into the region where the Gaussian is located can be controlled by the variation in the parameter a , where in the limit of $a \rightarrow 0$, a standard non-correlated Gaussian is obtained. For non-zero values of the second parameter b , the Gaussian is rotated in the (x, y) plane, and the rotation angle is given by $\alpha = \tan^{-1}[b]$. The factor $\sqrt{1 + b^2}$, which is included in the argument of the \cos^2 function, ensures that b does not distort the overall shape of the density.

Examples for densities $\rho_{a,b}(x, y)$ obtained for different choices of the parameters a and b are displayed in Fig. 1. Also included are the respective nuclear densities $\rho_{a,b}^{nuc}(x)$ (blue lines) and electronic densities $\rho_{a,b}^{el}(y)$ (red lines). The upper panels contain functions for a fixed value of $a = 7$ and different values of b taken from the interval $b \in [0, 1]$. As it is seen in the figure, with the variation in b , the nodal lines change their orientation with respect to the x -axis, but the frequency with which they appear is not influenced. In the case of $b = 1$, the nodes are parallel to the $x = -y$ diagonal. Here, electronic and nuclear densities are nodeless and of equal shape.

The influence of the parameter a on the density is illustrated in the lower panels of Fig. 1, where we set $b = 0.2$. With increasing values of a , more nodes appear in the density. It is also seen that the nuclear particle density exhibits structures that can be traced back to the nodes, whereas for the present choice of parameters, the electronic particle densities do not, and they appear to be nearly identical.

The mutual information $I_{a,b}$ is calculated numerically from the densities given in Eqs. (10)–(12) as a function of the two parameters a and b . Representative curves are shown in the upper panel of Fig. 2. The curves are displayed as a function of the frequency factor a and for selected values of b . Note that for $b = 0$, the total density factorizes and the MI vanishes so that $I_{a,0} = 0$, which is independent of the value of a . All curves start at zero and grow monotonically. They approach an upper bound at $I_{a,b} \approx 0.31$, and this limit is reached faster with the increasing value of b . The functions illustrate that the MI is directly related to the number of nodes in the density. Note that this number is not a well-defined concept for the model density $\rho_{a,b}(x, y)$ because, technically, there exist an infinite number of zeros. As mentioned before, here, we mean the zeros that fall

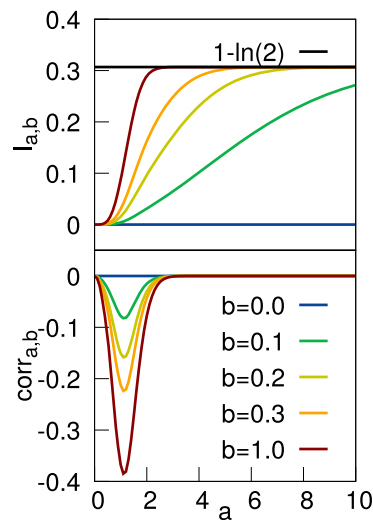


FIG. 2. Mutual information (upper panel) and correlation (lower panel) as a function of the parameter a for selected values of b , as indicated. The black line in the upper panel corresponds to the analytical limit of $a \rightarrow \infty$ ($b = 1$).

into the region where the Gaussian envelope is of non-negligible intensity. Approximately, it holds that $I_{a,b}$ is proportional to this number, where the proportionality factor itself is proportional to b . The asymptotic value for $a \rightarrow \infty$ and $b = 1$ can be calculated analytically, see the Appendix, and one finds that

$$\lim_{a \rightarrow \infty} I_{a,1} = 1 - \ln[2] \approx 0.3069, \quad (13)$$

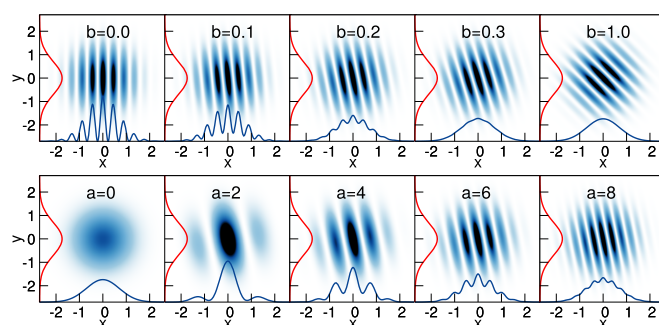


FIG. 1. Densities $\rho_{a,b}(x, y)$, as defined in Eq. (10). The upper panels show functions for $a = 7$ and selected values of the parameter b . In the lower panel, $b = 0.2$ is used, and a is varied, as indicated. Also shown are nuclear particle densities $\rho_{a,b}^{nuc}(x)$ (blue lines) and electronic particle densities $\rho_{a,b}^{el}(y)$ (red lines).

13 December 2023 12:10:38

which excellently agrees with the numerical results. The latter suggests that this limit does not depend on the particular value of b .

We next calculate the covariance (again using *MATHEMATICA*) with the result

$$cov_{a,b} = -\frac{a^2 b}{(e^{a^2} + 1)(b^2 + 1)}. \quad (14)$$

The variances in the two variables are determined as

$$\sigma_x^2 = \frac{1}{2} - \frac{a^2}{(e^{a^2} + 1)(b^2 + 1)}, \quad (15)$$

$$\sigma_y^2 = \frac{1}{2} - \frac{a^2 b^2}{(e^{a^2} + 1)(b^2 + 1)}. \quad (16)$$

Both functions are bounded by a value of 0.5, and they are identical for $b = 1$. By inserting the obtained results into the definition of the linear correlation coefficient, one finds that

$$corr_{a,b} = -\frac{a^2 b}{(e^{a^2} + 1)(b^2 + 1)} \times \left(-\frac{a^2}{2(e^{a^2} + 1)} + \frac{a^4 b^2}{(e^{a^2} + 1)^2 (b^2 + 1)^2} + \frac{1}{4} \right)^{-\frac{1}{2}}. \quad (17)$$

In the considered parameter regime ($be[0, 1]$), the covariance and correlation are negative semidefinite. By considering them as a function of the parameter a , i.e., as a function of the number of nodes, they exhibit a single minimum (obtained by symbolic differentiation employing *MATHEMATICA*) at

$$a_{\min} = \sqrt{W\left(\frac{1}{e}\right) + 1} \approx 1.13, \quad (18)$$

where W is the Lambert W -function.²⁸ Both the covariance and correlation are zero in the limit of vanishing parameters a and b , respectively. This is expected because in both cases, the density equals an uncorrelated Gaussian. In addition, we find that they also approach zero for $a \rightarrow \infty$.

The functions $corr_{a,b}$ are shown in the lower panel of Fig. 2 for different values of b . As predicted, extrema are found at $a_{\min} \approx 1.13$ for all values of b . They occur when the wavelength of the oscillations is comparable to the variance of the density. This approximately is the case for a value of $a = 2$, as can be seen in Fig. 1. There, the Gaussian shape-function suppresses all maxima of the \cos^2 function except the central one. This has the consequence that the density is located in a restricted region around the line with orientation angle $\tan^{-1}(b = 0.2)$. Furthermore, the smaller the value of b , the smaller the value of $corr_{a,b}$ because the orientation angle diminishes. In addition, if compared to the MI, the correlation approaches its asymptotic limit already for lower values of a .

What we have shown so far is that, for a model Gaussian density $\rho_{a,b}(x, y)$, which is modulated with a periodic function, the MI and correlation coefficient behave rather differently as a function of the

number of occurring nodes. The correlation coefficient shows a single extremum and quickly reaches a value of zero. This feature does not depend on the orientation of the nodal lines in the (x, y) -plane. On the other hand, the MI is a monotonous function of the number of nodes, and it converges, for all values of $b \neq 0$, to a finite limit of $\ln[e/2]$. This limit is reached for much larger values of a than the asymptotic value of zero reached by $corr_{a,b}$.

B. A numerical example: Electron-nuclear dynamics in the Born-Oppenheimer case

We now treat coupled electron-nuclear wave packet dynamics as a non-trivial example, where the analytical results of Sec. III A can be used for interpretation. The model consists of an electron (coordinate r) and a proton (coordinate R) moving in one dimension.^{29,30} They interact with each other and two fixed nuclei at positions of $R_{1,2} = \pm 5 \text{ \AA}$ through screened Coulomb interactions. The interaction potential is (in atomic units)

$$V(r, R) = \frac{1}{|R_1 - R|} + \frac{1}{|R_2 - R|} - \frac{erf[|R_1 - r|/R_f]}{|R_1 - r|} - \frac{erf[|R_2 - r|/R_f]}{|R_2 - r|} + \Delta, \quad (19)$$

where erf denotes the error function. For the screening parameters, we use $R_f = 1.5 \text{ \AA}$ and $R_c = 1.0 \text{ \AA}$, and Δ is the energy shift adjusted such that the potential minimum occurs at zero energy in the region of our spatial grid.

The time-dependent Schrödinger equation for the coupled motion reads

$$i\hbar \frac{\partial}{\partial t} \Psi(r, R, t) = \hat{H} \Psi(r, R, t), \quad (20)$$

with the Hamiltonian

$$\hat{H} = \frac{\hat{p}_R^2}{2M} + \frac{\hat{p}_r^2}{2m_e} + V(r, R). \quad (21)$$

The momentum operators for the electron and the nucleus are denoted as \hat{p}_r and \hat{p}_R , respectively, the mass of the proton is M , and m_e is the electron mass.

We solve Eq. (20) numerically with the split-operator method.³¹ The grid ranges from -12 to $+12 \text{ \AA}$ and from -6 to $+6 \text{ \AA}$ for the coordinates r and R , respectively. The number of grid points is taken as 512 for both coordinates, and a time step of $\Delta t = 0.0024 \text{ fs}$ is employed. The initial condition is chosen as

$$\Psi(r, R, 0) = N_0 e^{-\frac{\beta_0}{2}(R-R_0)^2} \varphi_0(r; R), \quad (22)$$

with the normalization factor N_0 , and the Gaussian is parameterized with $R_0 = -3.5 \text{ \AA}$ and $\beta_0 = 7.14 \text{ \AA}^{-2}$. The function $\varphi_0(r; R)$ is the electronic ground state wave function, which parametrically depends on the nuclear coordinate, and it is the solution of the electronic Schrödinger equation

$$\left[\frac{\hat{p}_r^2}{2m_e} + V(r, R) \right] \varphi_0(r, R) = V_0(R) \varphi_0(r, R), \quad (23)$$

where $V_0(R)$ is the ground state potential curve. Equation (23) is solved numerically using imaginary time propagation.³²

In Sec. II, the mutual information and the correlation are defined with respect to the variables y and x . We first identify these variables with the coordinates r and R , respectively, and the density $\rho(r, R, t) = |\Psi(r, R, t)|^2$ in the coordinate space is obtained from the time-dependent wave function. Taking the Fourier transform of the latter, one arrives at the momentum-space wave function $\Psi(k, K, t)$, where y and x now correspond to the electronic (k) and nuclear (K) momenta, respectively, and the density is $\rho(k, K, t) = |\Psi(k, K, t)|^2$. From the two densities, the MI in coordinate space ($I_\xi(t)$) and in momentum space ($I_\pi(t)$) is readily calculated. Likewise, the correlations $corr_\xi(t)$ and $corr_\pi(t)$ are determined.

Instead of using either position-space or momentum-space densities, one can think of using the Wigner function to obtain the MI from a phase-space distribution. This is not straightforward because it may assume negative values³³ so that the logarithm cannot be calculated. There have been attempts to circumvent the associated difficulties. We will not follow this route and refer the reader to the literature.^{34,35}

For the given parameterization of the interaction potential and the chosen initial wave function, the electronic ground state potential $V_0(R)$ is separated by a large energy gap from the excited state potentials.³⁶ Accordingly, the Born–Oppenheimer (BO) approximation applies, and the wave function can be written as a product of $\phi_0(r; R)$ and the nuclear wave function $\psi(R, t)$ depending on time. In a previous work on the present model,^{37,38} we found that information theoretical properties derived from coordinate dependent densities can be predicted analytically if the numerically propagated wave function is approximated as

$$\Psi(r, R, t) = N_t e^{-\frac{\beta_t}{2}(R-R_t)^2} e^{-\frac{\gamma_t}{2}(r-R)^2}, \quad (24)$$

which is of the BO form. Here appear the normalization factor N_t , the Gaussian width parameter β_t , and the center of the Gaussian R_t , where the subscripts indicate that these parameters depend on time. However, significant deviations were found in the momentum space MI³⁸ so that its time dependence cannot be explained within the ansatz of Eq. (24). One reason is that the BO Gaussian function does not incorporate nodal structures of the nuclear–electron wave packet. In what follows, we will take up this point and address their importance.

The time-dependent mutual information obtained for times up to 300 fs is displayed in the upper two panels of Fig. 3. It is seen that the spatial MI exhibits an overall increase, superposed by oscillations that are related to the vibrational wave packet dynamics. Adopting the BO ansatz of Eq. (24), it can be shown³⁷ that the coordinate space MI takes the form

$$I_\xi^{appr}(t) = \frac{1}{2} \ln [1 + 2\gamma\sigma_R^2(t)], \quad (25)$$

where the time-dependent variance $\sigma_R^2(t)$ enters the nuclear coordinate. This curve is also included in Fig. 3. The values for $\sigma_R^2(t)$ are extracted from the numerical propagation, and an average value of $\gamma = 0.733 \text{ \AA}^{-2}$ is used, which is determined from the electronic wave function $\phi_0(r; R)$. It is seen that $I_\xi^{appr}(t)$ reproduces the numerically obtained MI accurately, emphasizing the quality of the Gaussian approximation.

The function $corr_\xi(t)$ is shown in Fig. 3, second panel from below. It increases as a function of time and converges to a value

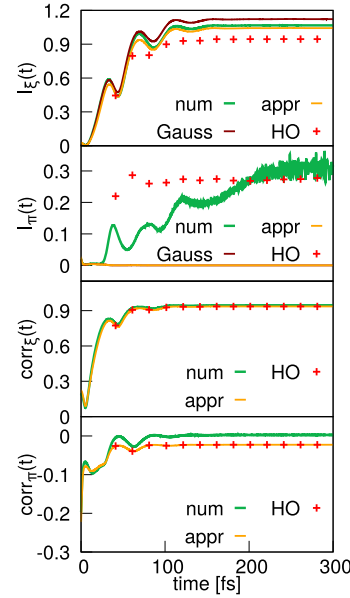


FIG. 3. Mutual information (upper two panels) and correlation coefficients (lower two panels) calculated from the coordinate-space (subscript ξ) and momentum-space densities (subscript π). The numerically derived curves (num) are compared to the ones obtained from the simplified ansatz for the BO wave function [Eqs. (25), (26), (28) and (29)]. In addition, the MI determined from Eq. (27) is shown in the two upper panels (Gauss). The red crosses correspond to functions derived within the harmonic ansatz (HO) for the nuclear density, as described in the text.

of ≈ 0.9 after about 100 fs. The curve is compared to the analytical function derived from the BO ansatz, which reads³⁷

$$corr_\xi^{appr}(t) = \sqrt{\frac{\sigma_R^2(t)}{\sigma_R^2(t) + \frac{1}{2\gamma}}}. \quad (26)$$

From the figure, it emerges that this formula presents an excellent approximation to the numerical result.

There is a relationship between the linear correlation coefficient and the mutual information for two-dimensional Gaussians,^{24,39} which is

$$I^{Gauss} = -\frac{1}{2} \ln [1 - corr^2]. \quad (27)$$

The curve for $I_\xi^{Gauss}(t)$, determined from the numerically derived function $corr_\xi(t)$ and using Eq. (27), is also included in Fig. 3. Inserting Eq. (26) in Eq. (27) yields the result of Eq. (25). However, the numerical curves show minor deviations, which are due to the Gaussian approximation. These findings mean that the coordinate-space MI is mainly determined by linear correlations between the two moving particles. In particular, because the wave function in Eq. (24)

does not include nodal patterns but is just the product of two correlated Gaussians, such nodes do not influence the spatial MI and the spatial correlation coefficient.

The numerically calculated momentum space MI is displayed in Fig. 3 (second panel from the top). In addition, we show the function that is derived from the analytical ansatz, which reads³⁸

$$I_{\pi}^{\text{appr}}(t) = -\frac{1}{2} \ln \left[1 - \frac{\gamma}{2\sigma_K^2(t)} \right], \quad (28)$$

with the nuclear variance in momentum space being $\sigma_K^2(t)$. The latter is determined numerically from the propagated wave function $\Psi(k, K, t)$, and γ is chosen as specified above. The curves agree only for short times (this is not seen in the figure because of their low magnitude), and afterward, no agreement is found. The MI seems to saturate for later times at values slightly above a value of $I_{\pi} \approx 0.30$, where the appearing fluctuations are not due to numerical errors. We note that this value is close to what is found for the MI derived from the model density (Sec. III A) in the limit of a large number of nodes.

The momentum-space correlation is shown in the lower panel of Fig. 3. It exhibits some oscillations related to the nuclear dynamics and, for longer times, remains at a value of zero. The approximate expression for the correlation coefficient, which is³⁸

$$\text{corr}_{\pi}^{\text{appr}}(t) = -\sqrt{\frac{\gamma}{2\sigma_K^2(t)}}, \quad (29)$$

is able to reproduce the main features of the numerical results. Thus, here, the assumption of an unstructured Gaussian wave packet is appropriate. We emphasize that the values of the various functions obtained for longer times do not necessarily remain constant over time. In particular, if the level structure of the quantum system allows for a wave-packet revival,^{40–44} the initial values will be recovered.

From the discussion of the results presented in Fig. 3, it emerges that the time-evolution of the position-space MI and correlation as well as the momentum-space correlation is not sensitive to an eventually existing node pattern in the probability densities. Only the momentum-space MI cannot be explained within an ansatz of nodeless Gaussians. In analyzing the density $\rho(k, K, t)$, one finds that the deviations between the numerically and approximately calculated MI are accompanied by the appearance of nodal patterns. In particular, the maxima seen in $I_{\pi}(t)$ occur when clear nodal lines are detectable. To illustrate these patterns, we show in Fig. 4 the coordinate- and momentum-space densities for two selected times. It is seen that in position space, the nodes are oriented vertically (visualized by a green line) and the density is oriented along the diagonal ($r = R$), as is indicated by the red line. Due to wave-packet dispersion, the density becomes more de-localized over time, and more structures are seen. In momentum space, the nodes appear parallel to the line, defined by $k = -K$, and the density is located along the horizontal axis with $k = 0$. As is the case in position space, a richer node pattern is encountered at a later time, and the density becomes more extended along the horizontal axis. This explains why the correlation coefficient is small (see Fig. 3).

The densities shown in Fig. 4 exhibit characteristics that we encountered in those of the model system studied in Sec. III A.

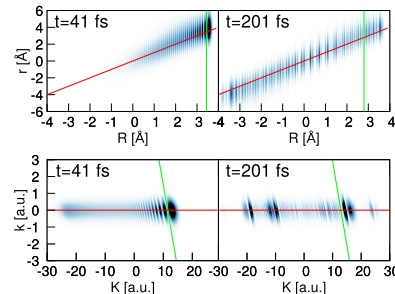


FIG. 4. Coordinate-space (upper panels) and momentum-space densities (lower panels) of the electron-nuclear wave packets shown for times of $t = 41$ fs and $t = 201$ fs. As a guide to the eye, the red and green lines indicate the overall orientation of the densities and the nodal lines, respectively.

Regarding the density $\rho_{a,b}(x, y)$ with the parameter $b = 0$, the nodal lines are oriented vertically (see Fig. 1), as is also seen in the spatial densities of Fig. 4, and for $b \neq 0$, they are rotated in the plane, as is found for the momentum densities. In the model, the $b = 0$ case leads to an uncorrelated wave function so that both, the MI and the correlation coefficient, are zero. In our numerical example, the orientation of the position space density is along the diagonal and not along one of the axis, which can be traced back to the particular form of the BO wave function. This leads to a non-zero MI and correlation, with the latter approaching the value of one, which are not (or only weakly) influenced by the vertical nodes.

To find an appropriate approximation to what is found numerically and explicitly address the role of the nodes, we proceed as follows: The ground state electronic eigenfunction, which enters the Born–Oppenheimer ansatz [Eq. (24)], is, to a good approximation a Gaussian for all values of R ,³⁷ and the dynamics are described by temporal changes in the nuclear wave packet $\psi(R, t)$. Let us assume that the motion of this wave packet is harmonic where the harmonic eigenfunctions are denoted as $\chi_m(R)$. Expansion of the nuclear density then yields

$$\rho^{\text{nuc}}(R, t) = \left| \sum_m c_m e^{-\frac{i}{\hbar} E_m t} \chi_m(R) \right|^2, \quad (30)$$

with coefficients c_m and harmonic eigenenergies E_m . In order to get a hand on the number of nodes in the nuclear density, we assume that at a time t_s , the density is dominated by a single term in Eq. (30) (with quantum number $m = n$) so that it can be written as

$$\rho^{\text{nuc}}(R, t_s) \approx |\chi_n(R)|^2. \quad (31)$$

The normalized density then is

$$\rho_n^{\text{HO}}(r, R, t_s) = \frac{2^{-n} \sqrt{\beta_t} \gamma}{\pi n!} e^{-\beta_t R^2 - \gamma(R-r)^2} \left(H_n(\sqrt{\beta_t} R) \right)^2, \quad (32)$$

with the Hermite polynomials H_n . Examples for these spatial densities are shown in the upper panels of Fig. 5 for different values of the quantum number n . Here, the values of $\beta = \gamma = 1 \text{ \AA}^{-2}$ are employed. It is seen that the displayed functions have the same properties as the

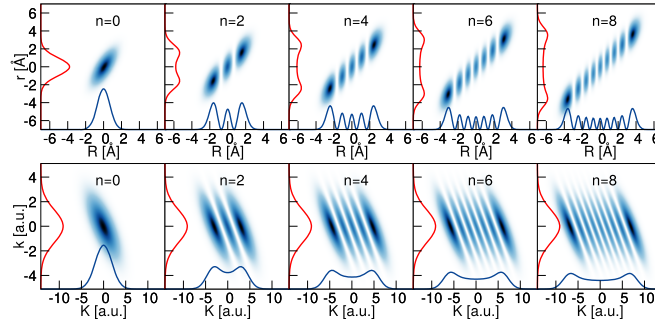


FIG. 5. Representative Born-Oppenheimer densities involving the harmonic approximation for the nuclear motion. The upper and lower panels depict the coordinate-space and momentum-space densities as defined in Eqs. (32) and (33), respectively. Shown are functions for different quantum numbers n . The nuclear (blue lines) and electronic (red lines) particle densities are also included.

numerically determined ones shown in Fig. 4. That is to say, they are oriented along the diagonal and show vertical nodes. From the findings presented in Sec. III A, it is expected that both $I_{\xi}(t)$ and $corr_{\xi}(t)$ are not influenced by such oriented nodes. In addition, the densities become more extended along the diagonal, which implies a linear relationship between r and R , and thus, the MI and the correlation here contain the same information (see below).

To arrive at the momentum space densities, the Fourier transformation of the coordinate space wave function is calculated, which then leads to the density as follows:

$$\rho^{HO}(k, K, t_s) = \frac{2^{-n}}{\pi n! \sqrt{\beta_t} \gamma} e^{-\frac{1}{2}k^2 - \frac{1}{2\beta_t}(K+k)^2} \times \left(H_n \left(\frac{1}{\sqrt{\beta_t}}(K+k) \right) \right)^2. \quad (33)$$

The relation between the electronic and nuclear degrees of freedom is different from what is encountered in coordinate space. In particular, the Hermite polynomials, which are responsible for the nodes, are dependent on the sum of the electron and nuclear momenta.

Momentum space densities are shown in the bottom panels of Fig. 5. They very much reproduce the characteristics of the numerical densities depicted in Fig. 4. The orientation of the overall density and of the nodal lines are the same. With the increasing value of the quantum number n , the density spreads along the $k = 0$ axis, whereas the width in the direction of the electron momentum is constant. This has a consequence that the correlation becomes smaller with increasing values of n . On the other hand, because the nodal lines follow the direction of the line $k = -K$, they are not visible in the single particle densities so that this information encoded in the total density is lost and the MI (which measures the loss of information) is non-zero. This is in line with the discussion about the properties of the model density in Sec. III A.

Although the harmonic-like densities reproduce features of the numerically obtained electron-nuclear densities, it is unclear if they are useful in describing the correlation measures we are interested in.

To answer this question, we choose a set of times $t = t_s$ and estimate the number of nodes n appearing in the spatial density $\rho(r, R, t_s)$. This is possible only approximately because the densities do not always show clearly defined nodes (in particular, in momentum-space). Rather, more or less pronounced minima are seen. However, the MI and correlations are not too sensitive with respect to the exact number of nodes. The variances of the position- and momentum-space densities, as defined in Eqs. (32) and (33), can be calculated analytically, and they are

$$\sigma_R^2(n) = \frac{2n+1}{2\beta_s}, \quad (34)$$

$$\sigma_K^2(n) = \frac{2n+1}{2}\beta_t + \frac{\gamma}{2}. \quad (35)$$

Inserting the numerically derived variances into the latter equations, i.e., $\sigma_R^2(n) = \sigma_R^2(t_s)$ and $\sigma_K^2(n) = \sigma_K^2(t_s)$, leads to two different values of the parameter β (namely, β_R and β_K), which are then used in the equations for the approximate densities. As before, a value of $\gamma = 0.733 \text{ \AA}^{-2}$ is chosen. In this way, we obtain approximate densities in position- and in momentum-space, which have the widths and the number of nodes similar to the numerical ones. The thus constructed functions are used to calculate the MI and correlation coefficients, and the results are included in Fig. 3 as red crosses. In what follows, they are referred to as I_{ξ}^{HO} , I_{π}^{HO} , $corr_{\xi}^{HO}$ and $corr_{\pi}^{HO}$, respectively. It is seen that in position-space, the approximate MI (I_{ξ}^{HO}) and correlation ($corr_{\xi}^{HO}$) agree well with the numerical curves. The same applies to the momentum-space correlation ($corr_{\pi}^{HO}$). In all three cases, the nodes of the wave functions do not play a role because the Gaussian ansatz, which neglects the node structure, yields about the same results. The only exception is the function $I_{\pi}(t)$. There, the assumption of a Gaussian form of the wave function fails completely. Including the nodes as described above yields a curve that deviates at shorter times but gives a reasonable prediction of the overall time dependence. The deviations occur at times when the wave packet is fairly localized, so the representation of its R -dependence by a single harmonic wave function is not very

accurate. The curve increases and, for longer times, converges to a constant. This trend is in accordance with the results derived for the model density shown in Sec. III A. Thus, we have found that the momentum-space MI reflects non-linear electron-nuclear correlations, which are strongly influenced by the nodal structure of the underlying momentum density.

Let us now discuss the limit of longer times in the regarded interval. The numerically calculated spatial- and momentum-densities for a time of $t_n = 281$ fs are displayed in the left hand panels of Fig. 6. Counting the number of nodes in the coordinate space density yields an approximate value of $n = 65$. The respective densities obtained within the harmonic approximation [i.e., Eqs. (32) and (33)] are also shown in the figure (right hand panels). They are obtained for the parameters $\beta_R = 13.63 \text{ \AA}^{-2}$, $\beta_K = 3.01 \text{ au}^{-2}$, and $\gamma = 0.733 \text{ \AA}^{-2}$. As can be seen in the figure, they reproduce the main characteristics of the numerical densities. This opens up the possibility to directly study the influence of the number of nodes on the MI and the correlation coefficients at the considered fixed time. These functions are calculated by keeping the chosen parameters fixed (i.e., β_R, β_K , and γ) and varying the quantum number n of the harmonic functions. In the upper two panels of Fig. 7, the MI in position- and momentum-space is shown. Both curves grow monotonically in the displayed range of quantum numbers, while the gradient decreases slowly. They start at the same value because for zero nodes, the correlation of the model is linear. The momentum-space MI increases with a large gradient at lower quantum numbers and then levels slowly. This is exactly what is found in the $b = 1$ case, which corresponds to the orientation encountered here along the line $k = -K$ of the model density $\rho_{a,b}(x, y)$ shown in Sec. III A. However, it does not converge in the presented regime. Taking the estimated value of $n = 65$, marked in Fig. 7 as a vertical line, we find the following numbers, $I_\xi(281) = 1.07$, $I_\xi^{HO} = 0.95$, $I_\pi(281) = 0.31$, and $I_\pi^{HO} = 0.28$, so that good agreement is found. Figure 7 also contains the MI as obtained from Eq. (27) and using the correlations depicted in the lower panels of the figure. In position space, this is a good approximation, but it completely fails in

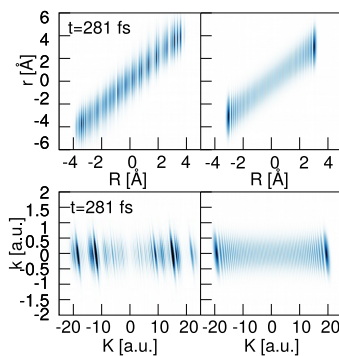


FIG. 6. Comparison of the propagated coordinate-space and momentum-space densities (left hand panels) and their harmonic approximations (right hand panels) at a time of $t = t_s = 281$ fs.

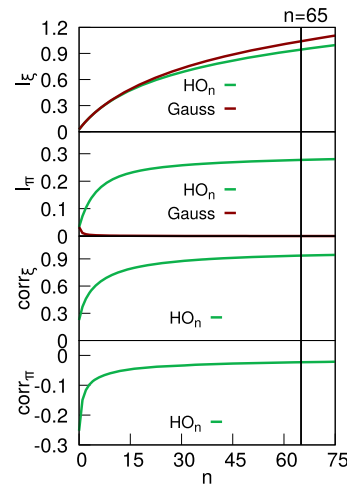


FIG. 7. Mutual information (upper two panels) and linear correlation coefficients in position- and momentum space (lower two panels). The curves (HO_n , interpolated by straight lines) are calculated using the densities ρ_ξ^{HO} and ρ_π^{HO} constructed for a time of $t_s = 281$ fs, as described in the text. They are shown for fixed parameters as a function of the quantum number n . For comparison, the MI determined from Eq. (27) using the correlations depicted in the two lower panels is also included (red curves). The horizontal line indicates the quantum number $n = 65$, which is determined from the numerical derived density at $t = 281$ fs.

momentum space. There, the curve approaches zero because the linear correlation vanishes. This again emphasizes that in calculating the function I_π , the nodes of the quantum wave functions are of great importance.

Note that the correlations $corr_\xi(t)$ and $corr_\pi(t)$ do not exhibit extrema, as is found for the model density $\rho_{a,b}(x, y)$ (see Fig. 2). This is because the variance of the densities is larger than the wavelength of the oscillations for all quantum numbers. Thus, here, we are in a regime of values above the critical number of a_{min} [Eq. (13)].

IV. SUMMARY

The focus of this work is on the analysis of how nodal structures in quantum wave functions influence particle correlations. Therefore, we consider two measures of such an entanglement. One is the mutual information, and the other is the linear correlation coefficient. These functions are derived from probability densities for systems with two degrees of freedom.

We first analyze model densities with a Gaussian shape function, where nodes are introduced by a cosine function. Here, two parameters (a and b) enter. The first one (a) determines the frequency with which the nodes appear, and the other (b) defines the orientation of the nodal lines in the plane. It is shown that the MI behaves as a monotonously increasing function converging to the same limit for all values of b . The latter determines the rate with

which the asymptotic value is reached. On the other hand, the linear correlation coefficient shows an extremum for all values of b and approaches zero for larger numbers of the frequency. This means that, opposite to the behavior of the MI, the latter is only sensitive to the number of nodes within a region where the wavelength of the oscillations in the density is larger or comparable to the variance of the density.

Having the analytical results at hand, we apply them to the motion in a system consisting of an electron and a nucleus, which show the typical dynamics encountered in the Born-Oppenheimer regime. In integrating the time-dependent Schrödinger equation for the coupled motion, the MI and the correlation coefficients are determined as a function of time. The numerical results are compared to those derived using a Gaussian ansatz for the BO wave function, which does not account for the node patterns in the probability density. It is found that the correlation measures derived from the coordinate-space density show excellent agreement with the numerically exact results. This hints at the fact that, here, the nodal structure of the density does not play an important role. As is inferred from the analytical considerations, the reason is that nodal lines present in the spatial densities are oriented perpendicular to the electronic coordinate axis. This is related to the BO wave function where the dynamics and thus the node structure are contained in the nuclear wave function whereas the electronic wave function remains of approximately constant shape.

Another picture evolves from the momentum-space dynamics. There, the quantum density exhibits nodal lines, which are oriented and non-parallel to the nuclear momentum axis. Here, the particular form of the BO wave function puts these lines at an angle of $-\pi/4$ to the axis. This has the consequence that the MI strongly depends on the number of nodes. Because the linear correlation coefficient does not show this dependence, we identify non-linear contributions to the particle correlation which, however, are only seen if the momentum-space density is used in the calculation. To explicitly address the influence of the number of nodes, we calculate the correlation measures, assuming harmonic wave functions for the nuclear degree of freedom at different times. The then obtained densities in position- and momentum-space are a good approximation to the numerically derived ones at selected times. By increasing the number of zeros in the nuclear harmonic density, it is documented that, for the regarded BO dynamics where the electron adiabatically adapts to the nuclear geometry, it is only the momentum-space mutual information that is sensitive to structures in the quantum mechanical wave function. We thus conclude that these nodal structures increase the wave packet entanglement in a non-linear fashion, which can be visualized by calculating the mutual information between the particles.

Finally, we point out that even though the nodal structures in our example influence only the momentum-space MI, one can find examples where the nodes strongly influence both the momentum- and the position-space MI. However, the results presented here illustrate the general effect, which, to the best of our knowledge, has not been discussed in detail before.

AUTHOR DECLARATIONS

Conflict of Interest

The authors have no conflicts to disclose.

Author Contributions

Peter Schürger: Conceptualization (equal); Formal analysis (lead); Software (lead); Visualization (lead); Writing – original draft (equal). **Volker Engel:** Conceptualization (equal); Formal analysis (supporting); Visualization (supporting); Writing – original draft (equal); Writing – review & editing (equal).

DATA AVAILABILITY

The data that support the findings of this study are available from the corresponding authors upon reasonable request.

APPENDIX: LIMIT OF A LARGE NUMBER OF NODES

In what follows, we provide a proof of Eq. (13), which gives the value of the MI in the limit of large values of the parameter a . This is equivalent to a large number of nodes in the model density appearing in Eq. (10). Here, we treat the special case where the parameter b assumes the value of $b = 1$. The density then reads

$$\rho_a(x, y) = \frac{2e^{-x^2-y^2} \cos^2(ax + ay)}{\pi(e^{-2a^2} + 1)}, \quad (A1)$$

where we have, for simplicity of notation, the replacement $a \rightarrow a\sqrt{2}$.

In the case of $b = 1$, because the nodes are aligned along the line $x = -y$, the electronic and nuclear densities have the same functional dependence on their respective coordinates. Regarding (exemplarily) the nuclear density and using symbolic integration, its analytic expression is determined as

$$\rho_a^{nuc}(x) = \frac{e^{a^2-x^2} (e^{a^2} + \cos(2ax))}{\sqrt{\pi}(e^{2a^2} + 1)}. \quad (A2)$$

We next apply a coordinate transformation as $(x, y) \rightarrow (x - y, y)$ so that the density takes the form

$$\rho_a(x, y) \rightarrow \frac{2e^{-(x-y)^2-y^2} \cos^2(ax)}{\pi(e^{-2a^2} + 1)}. \quad (A3)$$

This simplifies the integration over the variable y , which is performed with MATHEMATICA and yields

$$\begin{aligned} \int dx f(x, a) &= - \int dx dy \rho_a(x, y) \ln[\rho_a(x, y)] \\ &= - \int dx \frac{e^{2a^2-\frac{x^2}{2}} \cos^2(ax)}{\sqrt{2\pi}(e^{2a^2} + 1)} \\ &\quad \times \left[4a^2 - 2 \ln(\pi(e^{2a^2} + 1)) \right. \\ &\quad \left. - \ln(\sec^4(ax)) - x^2 - 1 + \ln(4) \right]. \quad (A4) \end{aligned}$$

In order to obtain the MI, the remaining integrals over the variable x are to be solved, i.e.,

$$I_a = \int dx [-2\rho_a^{nuc}(x) \ln[\rho_a^{nuc}(x)] - f(x, a)]. \quad (A5)$$

The integrand appearing in the latter equation can be decomposed into eight different terms $T_n(x, a)$ as

$$[-2\rho_a^{nuc}(x) \ln[\rho_a^{nuc}(x)] - f(x, a)] = \sum_{n=1}^8 T_n(x, a), \quad (A6)$$

with

$$T_1(x, a) = \frac{2\sqrt{\frac{2}{\pi}} a^2 e^{2a^2 - \frac{x^2}{2}} \cos^2(ax)}{e^{2a^2} + 1}, \quad (A7)$$

$$T_2(x, a) = -\frac{e^{2a^2 - \frac{x^2}{2}} \cos^2(ax)}{\sqrt{2\pi}(e^{2a^2} + 1)}, \quad (A8)$$

$$T_3(x, a) = -\frac{x^2 e^{2a^2 - \frac{x^2}{2}} \cos^2(ax)}{\sqrt{2\pi}(e^{2a^2} + 1)}, \quad (A9)$$

$$T_4(x, a) = \frac{\ln(4) e^{2a^2 - \frac{x^2}{2}} \cos^2(ax)}{\sqrt{2\pi}(e^{2a^2} + 1)}, \quad (A10)$$

$$T_5(x, a) = -\frac{\sqrt{\frac{2}{\pi}} e^{2a^2 - \frac{x^2}{2}} \cos^2(ax)}{e^{2a^2} + 1} \ln(\pi(e^{2a^2} + 1)), \quad (A11)$$

$$T_6(x, a) = -\frac{2e^{2a^2 - x^2}}{\sqrt{\pi}(e^{2a^2} + 1)} \ln\left(\frac{e^{a^2 - x^2}(e^{a^2} + \cos(2ax))}{\sqrt{\pi}(e^{2a^2} + 1)}\right), \quad (A12)$$

$$T_7(x, a) = -\frac{2e^{a^2 - x^2} \cos(2ax)}{\sqrt{\pi}(e^{2a^2} + 1)} \ln\left(\frac{e^{a^2 - x^2}(e^{a^2} + \cos(2ax))}{\sqrt{\pi}(e^{2a^2} + 1)}\right), \quad (A13)$$

$$T_8(x, a) = -\frac{e^{2a^2 - \frac{x^2}{2}} \cos^2(ax) \ln(\sec^4(ax))}{\sqrt{2\pi}(e^{2a^2} + 1)}. \quad (A14)$$

Direct symbolic integration can be performed for the terms $T_1(x, a)$, $T_2(x, a)$, $T_3(x, a)$, $T_4(x, a)$, and $T_5(x, a)$, and one finds

$$\int dx T_1(x, a) = 2a^2, \quad (A15)$$

$$\int dx T_2(x, a) = -\frac{1}{2}, \quad (A16)$$

$$\int dx T_3(x, a) = a^2 - a^2 \tanh(a^2) - \frac{1}{2}, \quad (A17)$$

$$\int dx T_4(x, a) = \ln(2), \quad (A18)$$

$$\int dx T_5(x, a) = -\ln(\pi(e^{2a^2} + 1)). \quad (A19)$$

The terms $T_6(x, a)$ and $T_7(x, a)$ are obtained by first using

$$\lim_{a \rightarrow \infty} \int dx T_n(x, a) = \int dx \lim_{a \rightarrow \infty} T_n(x, a). \quad (A20)$$

We therefore calculate these limits, which are

$$\lim_{a \rightarrow \infty} T_6(x, a) = -\frac{e^{-x^2}(2x^2 + \ln(\pi))}{\sqrt{\pi}}, \quad (A21)$$

$$\lim_{a \rightarrow \infty} T_7(x, a) = 0. \quad (A22)$$

Thus, $T_7(x, a)$ vanishes and does not contribute to the MI in the considered limit. The term of Eq. (A21) can be integrated, which yields

$$\int dx \lim_{a \rightarrow \infty} T_6(x, a) = 1 + \ln \pi. \quad (A23)$$

For the last term $T_8(x, a)$, MATHEMATICA does not provide a solution, so we need to analyze it in more detail. It can be written as

$$T_8(x, a) = \frac{e^{2a^2}}{(e^{2a^2} + 1)} \frac{e^{-\frac{x^2}{2}}}{\sqrt{2\pi}} [\cos^2(ax) \ln(\cos^4(ax))]. \quad (A24)$$

First we note that

$$\lim_{a \rightarrow \infty} \frac{e^{2a^2}}{(e^{2a^2} + 1)} = 1. \quad (A25)$$

The remaining part being present in $T_8(x, y)$ consists of a product of a Gaussian and an oscillating function having a period of $P = \pi/a$. Thus, for large values of a , the oscillations become arbitrarily fast if compared to the scale on which the Gaussian changes, and, effectively, the Gaussian only sees an average value, which is determined as

$$\frac{1}{P} \int_0^{P=\pi/a} dx \cos^2(ax) \ln(\cos^4(ax)) = \ln(4) - 1. \quad (A26)$$

Inserting this average value and the limit Eq. (A25) into the integral containing $T_8(x, a)$ yields

$$\int dx \lim_{a \rightarrow \infty} T_8(x, a) = \int dx \frac{e^{-\frac{x^2}{2}}}{\sqrt{2\pi}} [1 - \ln(4)] = 1 - \ln(4). \quad (A27)$$

We now sum over all contributions to obtain

$$\begin{aligned} \sum_{n=1}^8 \int dx T_n(x, a) &= 2a^2 - \frac{1}{2} + a^2 - a^2 \tanh(a^2) - \frac{1}{2} + \ln(2) \\ &\quad - \ln(\pi(e^{2a^2} + 1)) + 1 + \ln(\pi) + 1 - \ln(4), \end{aligned} \quad (A28)$$

which simplifies to

$$\sum_{n=1}^8 \int dx T_n(x, a) = 3a^2 - \ln(2e^{2a^2} + 2) - a^2 \tanh(a^2) + 1. \quad (A29)$$

This equation indeed converges in the limit of $a \rightarrow \infty$, and the asymptotic value of the MI is calculated as

$$\begin{aligned} \lim_{a \rightarrow \infty} I_a &= \lim_{a \rightarrow \infty} \sum_{n=1}^8 \int dx T_n(x, a) = 1 - \ln(2) \\ &= \ln\left(\frac{e}{2}\right) \approx 0.306852. \end{aligned} \quad (\text{A30})$$

REFERENCES

- ¹E. Merzbacher, *Quantum Mechanics* (Wiley, New York, 1998).
- ²S. Califano, *Vibrational States* (Wiley, New York, 1976).
- ³P. J. Reynolds, D. M. Ceperley, B. J. Alder, and W. A. Lester, *J. Chem. Phys.* **77**, 5593 (1982).
- ⁴J. B. Anderson, in *Quantum Mechanical Electronic Structure Calculations with Chemical Accuracy*, edited by S. R. Langhoff (Springer, Netherlands, Dordrecht, 1995), pp. 1–45.
- ⁵J. Tellinghuisen, in *Photodissociation and Photoionization*, 3rd ed., edited by K. P. Lawley (Wiley, New York, 1985).
- ⁶R. Schinke, *Photodissociation Dynamics* (Cambridge University Press, Cambridge, 1993).
- ⁷M. Eichelsdörfer and V. Engel, *Chem. Phys. Lett.* **263**, 640 (1996).
- ⁸H. Katsuki, H. Chiba, B. Girard, C. Meier, and K. Ohmori, *Science* **311**, 1589 (2006).
- ⁹W. Kutzelnigg, G. Del Re, and G. Berthier, *Phys. Rev.* **172**, 49 (1968).
- ¹⁰R. F. W. Bader and M. E. Stephens, *J. Am. Chem. Soc.* **97**, 7391 (1975).
- ¹¹R. Grobe, K. Rzazewski, and J. H. Eberly, *J. Phys. B: At., Mol. Opt. Phys.* **27**, L503 (1994).
- ¹²P. Ziesche, *Int. J. Quantum Chem.* **56**, 363 (1995).
- ¹³R. P. Sagar and N. L. Guevara, *J. Chem. Phys.* **123**, 044108 (2005).
- ¹⁴R. P. Sagar and N. L. Guevara, *J. Chem. Phys.* **124**, 134101 (2006).
- ¹⁵R. F. Nalewajski, *Found. Chem.* **16**, 27 (2014).
- ¹⁶E. V. Ludeña, F. J. Torres, M. Becerra, L. Rincón, and S. Liu, *J. Phys. Chem. A* **124**, 386 (2020).
- ¹⁷S. López-Rosa, R. O. Esquivel, J. C. Angulo, J. Antolin, J. S. Dehesa, and N. Flores-Gallegos, *J. Chem. Theory Comput.* **6**, 145 (2010).
- ¹⁸S. López-Rosa, A. L. Martín, J. Antolin, and J. C. Angulo, *Int. J. Quantum Chem.* **119**, e25861 (2019).
- ¹⁹J. C. Angulo and S. López-Rosa, *Entropy* **24**, 233 (2022).
- ²⁰R. O. Esquivel, M. Molina-Espiritu, and S. López-Rosa, *J. Phys. Chem. A* **127**, 6159 (2023).
- ²¹C. E. Shannon, *Bell Syst. Tech. J.* **27**, 379 (1948).
- ²²S. J. C. Salazar, H. G. Laguna, and R. P. Sagar, *Eur. Phys. J. Plus* **137**, 19 (2022).
- ²³E. Mandel and E. Wolf, *Optical Coherence and Quantum Optics* (Cambridge University Press, Cambridge, 1995).
- ²⁴T. M. Cover and J. A. Thomas, *Elements of information theory*, *Wiley Series in Telecommunications and Signal Processing*, 2nd ed. (Wiley-Interscience, 2006).
- ²⁵A. Hertz and N. J. Cerf, *J. Phys. A: Math. Theor.* **52**, 173001 (2019).
- ²⁶W. Li, *J. Stat. Phys.* **60**, 823 (1990).
- ²⁷W. R. Inc, *Mathematica, Version 12.3*, Champaign, IL, p. 2021.
- ²⁸R. M. Corless, G. H. Gonnet, D. E. G. Hare, D. J. Jeffrey, and D. E. Knuth, *Adv. Comput. Math.* **5**, 329 (1996).
- ²⁹S. Shin and H. Metiu, *J. Phys. Chem.* **100**, 7867 (1996).
- ³⁰S. Shin and H. Metiu, *J. Chem. Phys.* **102**, 9285 (1995).
- ³¹M. D. Feit, J. A. Fleck, and A. Steiger, *J. Comput. Phys.* **47**, 412 (1982).
- ³²R. Kosloff and H. Tal-Ezer, *Chem. Phys. Lett.* **127**, 223 (1986).
- ³³W. P. Schleich, *Quantum Optics in Phase Space* (Wiley VCH, Berlin, 2001).
- ³⁴H. G. Laguna and R. P. Sagar, *Entropy* **15**, 1516 (2013).
- ³⁵J. F. Santos, C. H. Vieira, and P. R. Dieguez, *Physica A* **579**, 125937 (2021).
- ³⁶P. Schürger and V. Engel, *J. Phys. Chem. Lett.* **14**, 334 (2023).
- ³⁷P. Schürger and V. Engel, *Phys. Chem. Chem. Phys.* **25**, 28373 (2023).
- ³⁸P. Schürger and V. Engel, *Entropy* **25**, 970 (2023).
- ³⁹D.-J. Jwo, T.-S. Cho, and A. Biswal, *Entropy* **25**, 1177 (2023).
- ⁴⁰J. H. Eberly, N. B. Narozhny, and J. J. Sanchez-Mondragon, *Phys. Rev. Lett.* **44**, 1323 (1980).
- ⁴¹I. S. Averbukh and N. F. Perelman, *Phys. Lett. A* **139**, 449 (1989).
- ⁴²R. W. Robinett, *Phys. Rep.* **392**, 1 (2004).
- ⁴³O. Knospe and R. Schmidt, *Phys. Rev. A* **54**, 1154 (1996).
- ⁴⁴C. Leichtle, I. S. Averbukh, and W. P. Schleich, *Phys. Rev. A* **54**, 5299 (1996).

7 Summary

In the course of this work, information-theoretical measures have been applied to different systems.

First, differential Shannon entropies were calculated from position and momentum densities of an harmonic oscillator with and without disorder. Analytical expressions for the entropy of coherent and squeezed states in an undisturbed harmonic oscillator have been computed. They reveal the dependence of the entropy on the width of the probability density in the respective space, highlighting the relationship between the entropy and the localization of the wave function. The entropy of the harmonic eigenstates has been approximated by a fit function which gives excellent agreement with the numerical results. Entropies for the classical harmonic oscillator in the microcanonical ensemble were also calculated and compared with the quantum entropy of harmonic eigenstates. Static disorder was added to the harmonic potential and the short- and long-time behavior of the entropy was investigated for quantum and classical dynamics. The such obtained entropies behave harmonically for short times and, due to dispersion, increase to larger values for later times until they reach a plateau value. Quantum entropies exhibit irregular oscillations, with minima associated with wave function revivals related to the most contributing energy eigenstates. Classical entropies behave similarly to quantum entropies, but show much smaller oscillations and increase to higher values. The energy dependence of the entropy plateau values was studied. It was found that the classical plateau values can be predicted by the entropy of a dephased density, while the quantum ones follows that of the harmonic eigenstates.

Information-theoretical measures were also applied to a model of coupled electron-nuclear dynamics, which consists of two fixed and one mobile nucleus and one mobile electron in one dimension. In this model, two distinct scenarios were considered: weak and strong non-adiabatic coupling. In the weakly coupled case, the electron closely follows the mobile nucleus, while for strong coupling the electron remains at a fixed nucleus. The information-theoretical properties of the wave function were benchmarked. For this the total, electron and nuclear entropies were analyzed, and the mutual information was computed as a measure for particle correlation. Notably, entropy values for both electron and nucleus correlate with the width of their densities, particularly at turning points where the density refocuses.

The total entropy was found primarily related to the nuclear density, while the electrons influence on total entropy was comparatively less. Mutual information increases over time, reaching maxima and minima due to dispersion and the classical turning points. In the strongly coupled case, the electron's width and entropy remains nearly constant.

Here, the mutual information vanishes, indicating no significant correlation between the electron and the nucleus. State-dependent entropies were introduced for strong adiabatic coupling, revealing insights into the population transfer and the form of the density matrix elements in the respective adiabatic states. Comparing the sums of these decomposed entropies to the total entropies provides information about transitions between electronic states at the avoided crossings.

An analytical ansatz was applied to describe the two coupling regimes. In the weakly coupled case, the Born-Oppenheimer ansatz yielded excellent results in position space. The analytical model successfully predicted various entropies and correlation measures, indicating that the nuclear width determines the information dynamics. In momentum space, the analytical ansatz shows good agreement for early times, particularly in predicting the linear correlation coefficient. However, it does not reproduce densities with nodal patterns, so it fails to describe the increasing mutual information in momentum space. We traced this effect back to the number of nodes occurring in the momentum density. The analytical ansatz was modified to describe the diabatic dynamics. The analytic results demonstrated excellent agreement with the numerical derived ones due to the simplicity of the dynamics in this coupling case.

Finally, the relation of nodal patterns and particle correlation was investigated. For this, an example density was employed, where we showed that the mutual information is dependent on the number and the alignment of nodes. The observations were applied to improve the analytical ansatz and in this way it became possible reproduce the previously found increasing momentum-space mutual information.

8 Zusammenfassung

Im Rahmen dieser Arbeit wurden informationstheoretische Maße auf verschiedene Systeme angewendet.

Zunächst wurden differentielle Shannon-Entropien aus Orts- und Impulsdichten in einem harmonischen Oszillator mit und ohne Störung berechnet. Dafür wurden analytische Ausdrücke für die Entropie von kohärenten und gestauchten Zuständen in einem ungestörten harmonischen Oszillator berechnet. Sie zeigen, dass die Entropien von der Breite im jeweiligen Raum abhängen und verdeutlichen die Beziehung zwischen Entropie und Lokalisierung der Wellenfunktion. Die Entropie der harmonischen Eigenzustände wurde durch eine Fit-Funktion angenähert, die eine exzellente Übereinstimmung mit den numerischen Ergebnissen zeigt. Die Entropien für den klassischen harmonischen Oszillator im mikrokanonischen Ensemble wurden ebenfalls berechnet und mit denen der harmonischen Eigenzustände verglichen. Dem harmonischen System wurde statische Unordnung hinzugefügt und das Kurz- und Langzeitverhalten der Entropie wurde für Quanten- und klassische Dynamik untersucht. Die Entropien verhalten sich für kurze Zeit harmonisch und steigen für spätere Zeiten aufgrund der Dispersion auf größere Werte an, bis sie einen Plateauwert erreichen. Quantenentropien weisen unregelmäßige Oszillationen auf, wobei die Minima mit dem Wiederaufleben der Anfangswellenfunktion verbunden sind, die aufgrund der signifikant beitragenden Energieeigenzuständen entstehen. Die klassische Entropie verhält sich ähnlich wie die Quantenentropie, weist jedoch wesentlich geringere Oszillationen auf und steigt auf einen höheren Plateauwert. Die Energieabhängigkeit der Entropie-Plateauwerte wurde untersucht. Es wurde festgestellt, dass die klassischen Plateauwerte durch die Entropie einer dephasierten Dichte vorhergesagt werden können, während die Quantenwerte denen der harmonischen Eigenzustände folgen.

Informationstheoretische Maße wurden auch auf gekoppelte Elektron-Kern-Dynamik angewandt. Das betrachtete eindimensionale System besteht aus zwei festen und einem beweglichen Kern und einem beweglichen Elektron. Das System wurde unter schwacher und starker nicht-adiabatischer Kopplung betrachtet. Im Fall der schwachen Kopplung folgt das Elektron dem beweglichen Kern, während bei starker Kopplung das Elektron am festen Kern lokalisiert bleibt. Es wurden die Gesamt-, Elektronen- und Kernentropie sowie die Transinformation als Maß für die Teilchenkorrelation berechnet. Die Entropiewerte sowohl für Elektronen als auch für Kerne korrelieren mit der jeweiligen Breiten ihrer Dichten. Dies geschieht insbesondere an Wendepunkten, da die Dichten hier fokussiert werden.

Die Gesamtentropie hängt insbesondere von der Kerndichte ab, während der Einfluss der Elektronen auf diese vergleichsweise gering ist. Die Transinformation nimmt aufgrund der

Dispersion mit der Zeit zu und erreicht Maxima und aufgrund Reflexionen an den klassischen Wendepunkten. Im stark gekoppelten Fall bleiben die Breite und die Entropie des Elektrons nahezu konstant. In diesem Fall ist die Transinformation in guter Näherung gleich null, weil keine Korrelation zwischen dem Elektron und dem Kern besteht.

Im Falle der starken nicht-adiabatischen Kopplung wurden zustandsabhängige Entropien eingeführt, die Aufschluss über den Populationstransfer und die Form der Dichtematrixelemente in den jeweiligen adiabatischen Zuständen geben. Der Vergleich der Summen dieser zerlegten Entropien mit den Gesamtentropien liefert Einblick in Übergänge zwischen adiabatischen Zuständen an den vermiedenen Kreuzungen. Für beide Fälle wurde ein analytischer Ansatz formuliert. Im Fall der schwachen Kopplung wurde ein Born-Oppenheimer-Ansatz gewählt, der sehr gute Ergebnisse im Ortsraum liefert. Das analytische Modell sagt Entropien und Korrelationsmaße erfolgreich vorher, was bestätigt, dass die Informationsdynamik von der Breite der Kerndichte bestimmt wird. Im Impulsraum liefert der analytische Ansatz zu Beginn der Propagation gute Ergebnisse, insbesondere für den linearen Korrelationskoeffizienten. Allerdings kann er den Anstieg der Transinformation im Impulsraum nicht reproduzieren. Dieser Effekt wurde auf die Anzahl der in der Impulsdichte vorkommenden Knoten zurückgeführt.

Der analytische Ansatz wurde auf den diabatischen Fall angepasst. Die Ergebnisse zeigen aufgrund der Einfachheit der Dynamik in diesem Szenario eine exzellente Übereinstimmung mit den numerisch exakten Daten.

Schließlich wurde die Beziehung zwischen Knotenstrukturen und Teilchenkorrelation untersucht. Dazu wurde zuerst eine Beispieldichte benutzt, bei der deutlich wurde, dass die Transinformation von Ausrichtung und Anzahl der Knoten abhängt. Diese Beobachtungen wurden angewendet, um die zuvor beobachtete Zunahme der Transinformation im Impulsraum zu reproduzieren.

9 References

- [1] P. Schürger, T. Schaupp, D. Kaiser, B. Engels, V. Engel, *The Journal of Chemical Physics* **2022**, *156*, 054303.
- [2] P. Schürger, K. Renziehausen, T. Schaupp, I. Barth, V. Engel, *The Journal of Physical Chemistry A* **2022**, *126*, 8964–8975.
- [3] P. Schürger, V. Engel, *The Journal of Physical Chemistry Letters* **2023**, *14*, 334–339.
- [4] P. Schürger, V. Engel, *Entropy* **2023**, *25*, 970.
- [5] P. Schürger, V. Engel, *Phys. Chem. Chem. Phys.* **2023**, *25*, 28373–28381.
- [6] P. Schürger, V. Engel, *AIP Advances* **2023**, *13*, 125307.
- [7] P. Schürger, V. Engel, *J. Chem. Theory Comput.* **2024**, (to be published).
- [8] L. Endres, J. Klopff, P. Schürger, H. Braunschweig, H. Helten, M. Finze, F. Fantuzzi, B. Engels, **2024**, (to be published).
- [9] E. Schrödinger, *Phys. Rev.* **1926**, *28*, 1049–1070.
- [10] F. Jensen, *Introduction to computational chemistry*, 3rd ed., John Wiley & Sons, Nashville, TN, **2017**.
- [11] W. Nolting, *Grundkurs theoretische Physik 6*, 6th ed., Springer, Berlin, Germany, **2007**.
- [12] D. J. Tannor, *Introduction to Quantum Mechanics - a Time-Dependent Perspective*, University Science Books, Sausalito, California, **2007**.
- [13] Y. W. Hsueh, C. H. Hsueh, W. C. Wu, *Entropy* **2020**, *22*, 855.
- [14] J. M. Deutsch, *Reports on Progress in Physics* **2018**, *81*, 082001.
- [15] C. E. Shannon, *The Bell System Technical Journal* **1948**, *27*, 379–423.
- [16] Thomas M. Cover, J. A. Thomas, *Elements of Information Theory*, 2nd ed., John Wiley & Sons, Nashville, TN, **2006**.
- [17] B. Zolfaghari, K. Bibak, T. Koshiha, *Entropy* **2022**, *24*, 266.
- [18] A. Loi, S. Matta, *Journal of Mathematical Economics* **2021**, *97*, 102555.
- [19] N. Flores-Gallegos in *Advances in Quantum Mechanics*, (Ed.: P. Bracken), IntechOpen, Rijeka, **2013**, Chapter 29.
- [20] R. F. Nalewajski, *Applied Sciences* **2019**, *9*, 1262.
- [21] R. F. Nalewajski, *Entropy* **2020**, *22*, 749.

-
- [22] S. Noorizadeh, E. Shakerzadeh, *Phys. Chem. Chem. Phys.* **2010**, *12*, 4742–4749.
- [23] D. S. Sabirov, I. S. Shepelevich, *Entropy* **2021**, *23*, 1240.
- [24] R. D. Levine in *Advances in Chemical Physics*, John Wiley & Sons, Ltd, **1981**, pp. 239–292.
- [25] D. Jia, J. Manz, Y. Yang, *AIP Advances* **2018**, *8*, 045222.
- [26] E. V. Ludeña, F. J. Torres, M. Becerra, L. Rincón, S. Liu, *J. Phys. Chem. A* **2020**, *124*, 386–394.
- [27] R. Atre, A. Kumar, N. Kumar, P. K. Panigrahi, *Phys. Rev. A* **2004**, *69*, 052107.
- [28] C. Martínez-Flores, *International Journal of Quantum Chemistry* **2021**, *121*, e26529.
- [29] W. S. Nascimento, F. V. Prudente, *Chem. Phys. Lett.* **2018**, *691*, 401–407.
- [30] K. Kumar, V. Prasad, *Scientific Reports* **2022**, *12*, 7496.
- [31] S. Saha, J. Jose, *International Journal of Quantum Chemistry* **2020**, *120*, e26374.
- [32] R. González-Férez, J. S. Dehesa, *Phys. Rev. Lett.* **2003**, *91*, 113001.
- [33] Y. L. He, Y. Chen, J. N. Han, Z. B. Zhu, G. X. Xiang, H. D. Liu, B. H. Ma, D. C. He, *Eur. Phys. J. D* **2015**, *69*, 1434–6079.
- [34] R. P. Sagar, N. L. Guevara, *The Journal of Chemical Physics* **2005**, *123*, 044108.
- [35] R. P. Sagar, N. L. Guevara, *The Journal of Chemical Physics* **2006**, *124*, 134101.
- [36] H. Peng, Y. Ho, *Entropy* **2015**, *17*, 1882–1895.
- [37] V. S. Yépez, R. P. Sagar, H. G. Laguna, *Few-Body Systems* **2017**, *58*, 158.
- [38] S. J. C. Salazar, H. G. Laguna, R. P. Sagar, *Phys. Rev. A* **2020**, *101*, 042105.
- [39] S. J. C. Salazar, H. G. Laguna, R. P. Sagar, *Eur. Phys. J. Plus* **2022**, *137*.
- [40] J. C. Angulo, S. López-Rosa, *Entropy* **2022**, *24*, 233.
- [41] C. S. Lent, *Physical Review E* **2019**, *100*, 012101.
- [42] D. Kaiser, doctoral thesis, Universität Würzburg, **2022**.
- [43] M. Born, R. Oppenheimer, *Annalen der Physik* **1927**, *389*, 457–484.
- [44] B. T. Sutcliffe in *Computational Techniques in Quantum Chemistry and Molecular Physics*, Springer Netherlands, **1975**, pp. 1–105.
- [45] A. Szabo, N. S. Ostlund, *Modern quantum chemistry*, Dover Publications, Mineola, NY, **1996**.
- [46] M. Hillery, R. O’Connell, M. Scully, E. Wigner, *Physics Reports* **1984**, *106*, 121–167.
-

- [47] E. Wigner, *Physical Review* **1932**, *40*, 749–759.
- [48] W. B. Case, *American Journal of Physics* **2008**, *76*, 937–946.
- [49] C. W. Gardiner, *Handbook of Stochastic Methods - For Physics, Chemistry and the Natural Sciences*, Springer, Berlin, Heidelberg, **1985**.
- [50] J. V. Michalowicz, J. M. Nichols, F. Bucholtz, *Handbook of differential entropy*, Chapman & Hall/CRC, Philadelphia, PA, **2018**.
- [51] I. I. Hirschman, *American Journal of Mathematics* **1957**, *79*, 152.
- [52] W. Beckner, *The Annals of Mathematics* **1975**, *102*, 159.
- [53] I. Białynicki-Birula, J. Mycielski, *Communications in Mathematical Physics* **1975**, *44*, 129–132.
- [54] A. Hertz, M. G. Jabbour, N. J. Cerf, *Journal of Physics A: Mathematical and Theoretical* **2017**, *50*, 385301.
- [55] A. Hertz, N. J. Cerf, *Journal of Physics A: Mathematical and Theoretical* **2019**, *52*, 173001.
- [56] R. Kosloff, *Annual Review of Physical Chemistry* **1994**, *45*, 145–178.
- [57] M. Frigo, S. Johnson, *Proceedings of the IEEE* **2005**, *93*, 216–231.
- [58] T. Schaupp, doctoral thesis, Universität Würzburg, **2022**.
- [59] M. Feit, J. Fleck, A. Steiger, *Journal of Computational Physics* **1982**, *47*, 412–433.
- [60] M. D. Feit, J. A. Fleck, *The Journal of Chemical Physics* **1983**, *78*, 301–308.
- [61] R. Kosloff, H. Tal-Ezer, *Chemical Physics Letters* **1986**, *127*, 223–230.
- [62] L. Verlet, *Physical Review* **1967**, *159*, 98–103.
- [63] M. P. Allen, D. J. Tildesley, *Computer Simulation of Liquids*, Clarendon Press, Oxford, England, **1989**.
- [64] W. C. Swope, H. C. Andersen, P. H. Berens, K. R. Wilson, *The Journal of Chemical Physics* **1982**, *76*, 637–649.
- [65] B. H. Bransden, C. J. Joachain, *Physics of atoms and molecules*, Prentice-Hall, London, England, **1982**.
- [66] P. W. Atkins, R. S. Friedman, *Molecular Quantum Mechanics*, 5th ed., Oxford University Press, London, England, **2010**.
- [67] A. Nitzan, *Chemical dynamics in condensed phases*, Oxford University Press, London, England, **2013**.

-
- [68] D. Dries, S. E. Pollack, J. M. Hitchcock, R. G. Hulet, *Phys. Rev. A* **2010**, *82*, 033603.
- [69] J. Fortágh, H. Ott, S. Kraft, A. Günther, C. Zimmermann, *Phys. Rev. A* **2002**, *66*, 041604.
- [70] A. E. Leanhardt, Y. Shin, A. P. Chikkatur, D. Kielpinski, W. Ketterle, D. E. Pritchard, *Phys. Rev. Lett.* **2003**, *90*, 100404.
- [71] M. P. A. Jones, C. J. Vale, D. Sahagun, B. V. Hall, E. A. Hinds, *Phys. Rev. Lett.* **2003**, *91*, 080401.
- [72] J. Estève, C. Aussibal, T. Schumm, C. Figl, D. Maily, I. Bouchoule, C. I. Westbrook, A. Aspect, *Phys. Rev. A* **2004**, *70*, 043629.
- [73] C. H. Hsueh, R. Ong, J. F. Tseng, M. Tsubota, W. C. Wu, *Phys. Rev. A* **2018**, *98*, 063613.
- [74] C. H. Hsueh, M. Tsubota, W. C. Wu, *Journal of Low Temperature Physics* **2019**, *196*, 13–20.
- [75] C. H. Hsueh, C. H. Cheng, T. L. Horng, W. C. Wu, *Entropy* **2022**, *24*, 1163.
- [76] E. Romera, F. de los Santos, *Phys. Rev. Lett.* **2007**, *99*, 263601.
- [77] T. Abbas, F. Saif, *International Journal of Theoretical Physics* **2014**, *53*, 1961–1970.
- [78] B. Talukdar, A. Saha, S. Chatterjee, G. Ali Sekh, *The European Physical Journal Plus* **2018**, *133*, 480.
- [79] H. J. W. Muller-Kirsten, *Introduction to quantum mechanics: Schrodinger equation and path integral*, 2nd ed., World Scientific Publishing, Singapore, Singapore, **2012**.
- [80] R. J. Yáñez, W. Van Assche, J. S. Dehesa, *Physical Review A* **1994**, *50*, 3065–3079.
- [81] V. Majernik, L. Richterek, *European Journal of Physics* **1999**, *18*, 79.
- [82] W. Van Assche, R. J. Yáñez, J. S. Dehesa, *Journal of Mathematical Physics* **1995**, *36*, 4106–4118.
- [83] R. Lustig, *The Journal of Chemical Physics* **1994**, *100*, 3048–3059.
- [84] I. M. Lifshits, S. A. Gredeskul, L. A. Pastur, *Introduction to the theory of disordered systems*, John Wiley & Sons, Nashville, TN, **1988**.
- [85] E. Rebhan, *Theoretische Physik, Band 1*, Springer, New York, NY, **1999**.
- [86] J. M. Deutsch, *Physical Review A* **1991**, *43*, 2046–2049.
- [87] M. Rigol, V. Dunjko, M. Olshanii, *Nature* **2008**, *452*, 854–858.
-

9. REFERENCES

- [88] S. Goldstein, J. L. Lebowitz, R. Tumulka, N. Zanghì, *The European Physical Journal H* **2010**, *35*, 173–200.
- [89] M. Rigol, M. Srednicki, *Phys. Rev. Lett.* **2012**, *108*, 110601.
- [90] D. Kohen, D. J. Tannor, *Journal of Chemical Physics* **1997**, *107*, 5141–5153.
- [91] J. Mostowski, J. Pietraszewicz, Wigner Function for Harmonic Oscillator and The Classical Limit, arXiv preprint, arXiv:2104.06638, **2021**.
- [92] E. Jafarov, S. Lievens, J. V. d. Jeugt, *Journal of Physics A: Mathematical and Theoretical* **2008**, *41*, 235301.
- [93] William H. Press and Flannery, Brian P and Teukolsky, Saul A and Vetterling, William T, *Numerical recipes in FORTRAN 77: Volume 1 of FORTRAN numerical recipes volume 1*, 2nd ed., Cambridge University Press, Cambridge, England, **1992**.
- [94] W. R. Inc., Mathematica, Version 12.3, Champaign, IL, 2023.
- [95] E. A. Arsenault, A. J. Schile, D. T. Limmer, G. R. Fleming, *The Journal of Chemical Physics* **2021**, *155*, 054201.
- [96] K. M. Ziems, J. Bruhnke, V. Engel, S. Gräfe, *Frontiers in Chemistry* **2022**, *10*, 942633.
- [97] M. V. Pak, S. Hammes-Schiffer, *Physical Review Letters* **2004**, *92*, 103002.
- [98] S. A. González, A. Reyes, *International Journal of Quantum Chemistry* **2009**, *110*, 689–696.
- [99] F. Agostini, E. Gross, B. F. Curchod, *Computational and Theoretical Chemistry* **2019**, *1151*, 99–106.
- [100] J. Stetzler, V. A. Rassolov, *Molecular Physics* **2022**, *121*, e2106321.
- [101] S. Shin, H. Metiu, *The Journal of Chemical Physics* **1995**, *102*, 9285–9295.
- [102] S. Shin, H. Metiu, *The Journal of Physical Chemistry* **1996**, *100*, 7867–7872.
- [103] M. Erdmann, P. Marquetand, V. Engel, *The Journal of Chemical Physics* **2003**, *119*, 672–679.
- [104] M. Falge, V. Engel, S. Gräfe, *The Journal of Chemical Physics* **2011**, *134*, 184307.
- [105] M. Falge, V. Engel, S. Gräfe, *The Journal of Physical Chemistry Letters* **2012**, *3*, 2617–2620.
- [106] J. Albert, M. Falge, S. Gomez, I. R. Sola, H. Hildenbrand, V. Engel, *The Journal of Chemical Physics* **2015**, *143*, 041102.

- [107] F. G. Fröbel, K. M. Ziem, U. Peschel, S. Gräfe, A. Schubert, *Journal of Physics B: Atomic Molecular and Optical Physics* **2020**, *53*, 144005.
- [108] T. Schaupp, V. Engel, *The Journal of Chemical Physics* **2020**, *152*, 204310.

10 Listing of Author Contributions



Erklärung zur Autorenschaft

Information Theoretical Approach to Coupled Electron-Nuclear Wave Packet Dynamics: Time-Dependent Differential Shannon Entropies, Peter Schürger, Volker Engel, J. Phys. Chem. Lett. 2023, 14, 2, 334–339

Detaillierte Darstellung der Anteile an der Veröffentlichung (in %) Angabe Autoren/innen (ggf. Haupt- / Ko- / korrespondierende/r Autor/in) mit Vorname Nachname (Initialen)

Autor/in 1 (Peter Schürger), Autor/in 2 (Volker Engel)			
Autor	A1	A2	Σ in Prozent
Conceptualization	50	50	100
Formal analysis	90	10	100
Analytic calculations	50	50	100
Implementation	100	0	100
Data curation	100	0	100
Visualization	90	10	100
Discussion of results	50	50	100
Writing - original draft	30	70	100
Writing - review and editing	40	60	100
Summe	50	50	100



Erklärung zur Autorenschaft

Differential Shannon entropies and correlation measures for Born–Oppenheimer electron–nuclear dynamics: numerical results and their analytical interpretation, Peter Schürger, Volker Engel, Phys. Chem. Chem. Phys., 2023, 25, 28373-28381

Detaillierte Darstellung der Anteile an der Veröffentlichung (in %) Angabe Autoren/innen (ggf. Haupt- / Ko- / korrespondierende/r Autor/in) mit Vorname Nachname (Initialen)

Autor/in 1 (Peter Schürger), Autor/in 2 (Volker Engel)			
Autor	A1	A2	Σ in Prozent
Conceptualization	50	50	100
Formal analysis	90	10	100
Analytic calculations	90	10	100
Implementation	100	0	100
Data curation	100	0	100
Visualization	90	10	100
Discussion of results	50	50	100
Writing - original draft	30	70	100
Writing - review and editing	40	60	100
Summe	50	50	100



Erklärung zur Autorenschaft

Differential Shannon Entropies Characterizing Electron–Nuclear Dynamics and Correlation: Momentum-Space Versus Coordinate-Space Wave Packet Motion, Peter Schürger, Volker Engel, Entropy 2023, 25(7), 970

Detaillierte Darstellung der Anteile an der Veröffentlichung (in %) Angabe Autoren/innen (ggf. Haupt- / Ko- / korrespondierende/r Autor/in) mit Vorname Nachname (Initialen)

Autor/in 1 (Peter Schürger), Autor/in 2 (Volker Engel)			
Autor	A1	A2	Σ in Prozent
Conceptualization	50	50	100
Formal analysis	90	10	100
Analytic calculations	90	10	100
Implementation	100	0	100
Data curation	100	0	100
Visualization	90	10	100
Discussion of results	50	50	100
Writing - original draft	30	70	100
Writing - review and editing	50	50	100
Summe	50	50	100



Erklärung zur Autorenschaft

On the relation between nodal structures in quantum wave functions and particle correlation, Peter Schürger, Volker Engel, AIP Advances, 2023, 13, 125307

Detaillierte Darstellung der Anteile an der Veröffentlichung (in %) Angabe Autoren/innen (ggf. Haupt- / Ko- / korrespondierende/r Autor/in) mit Vorname Nachname (Initialen)

Autor/in 1 (Peter Schürger), Autor/in 2 (Volker Engel)			
Autor	A1	A2	Σ in Prozent
Conceptualization	50	50	100
Formal analysis	90	10	100
Analytic calculations	90	10	100
Implementation	100	0	100
Data curation	100	0	100
Visualization	90	10	100
Discussion of results	50	50	100
Writing - original draft	50	50	100
Writing - review and editing	50	50	100
Summe	50	50	100

11 Acknowledgements

First of all, I would like to thank Prof. Dr. Volker Engel for being my supervisor and for giving me the possibility to write my thesis in his research group. The discussions and meetings with him really advanced my research and always lead to new ideas and insights. I had a lot of fun working together and am very grateful for his support and all the opportunities he made possible. Secondly, I would like to thank my co-supervisor Prof. Dr. Bernd Engels for the nice discussions and the collaboration, and of course the opportunity to play in his soccer team.

Further thanks are addressed to the (former) members of the Engel research group, who welcomed me well at the beginning: Thanks, Dr. Thomas Schaupp for having the patience to familiarize me with Fortran. Thanks, Dr. Fabian Glaab that you did not leave me alone with a dying server and thanks Dr. Jasmin Süß for letting me pet your dog. One of the most important people to thank is Uschi Rüppel, who helped me with organization in personal and professional aspects. I would also like to mention Dr. Dustin Kaiser, who introduced me to information theory, and Dr. Klaus Renziehausen and Dr. Ingo Barth for our successful collaborations.

Thanks also to my coworkers Luca Craciunescu, Christoph Herok and Jessica Meyr. I had a great time working with you and I will never forget the conferences that we attended. Thanks Luca for the financial consulting, thanks Chris for all the silly talk and thanks Jessi for eating my fries, when I could not. Thank you also for proofreading some sections of this work.

Vielen Dank natürlich auch an meine Eltern, meine Schwester und meine Oma, die mich schon immer unterstützt haben und ohne die ich nicht hier wäre. Ich danke auch Bernward Weigand für einen gewissen Tipp und Claudia Malcomess für das Durchhalten mit mir. Schlussendlich möchte ich noch meiner Partnerin Tabea Zmiskol danken, die mir im Endspurt den Rücken frei gehalten hat.